The Alliance of Laboratories in Europe for Education, Research and Technology

ALERT Doctoral School 2021

Constitutive Modelling in Geomaterials

Editors:

Claudio Tamagnini

David Mašín

Preface

The ALERT Doctoral School 2021 on "Constitutive Modeling in Geomaterials" will take place in Aussois, from 30th September to 2nd October, 2021. The School has been organized by Prof. Claudio Tamagnini (University of Perugia) and Prof. David Mašin (Charles University). I sincerely thank the organizers and all the contributors to this book for their effort!

The subject of the school has its roots in the fundamental objectives of our network: developing a European School of Thinking in the field of the Mechanics of Geomaterials. This was the topic of our first ALERT doctoral school in Aussois in 1994 and many following doctoral school tackled some aspects of this broad field! The ALERT Board of Director has thus decided that it was the time to organize the school on this topic, in order to contribute to the formation of all our PhD students and researchers. I am therefore convinced that this school will be beneficial to the ALERT community.

The school will run over 3 days with the first day dedicated to the Basic concepts related to Constitutive modeling. The second day will focus on specific features of geomaterials' behavior. The half-day will go towards applications and the participants will use calibration software in order to identify the parameters of some constitutive models.

As usual, the pdf file of the book can be downloaded for free from the website of ALERT Geomaterials (http://alertgeomaterials.eu/publications/) after the school.

On behalf of the ALERT Board of Directors I wish all participants a successful ALERT Doctoral School 2021!

Frédéric Collin
Director of ALERT Geomaterials
University of Liege

Contents

Foreword
Tamagnini & Mašín 1

Fundamentals of constitutive modelling for soils
Herle 3

The theory of plasticity in constitutive modeling of rate–independent soils
Tamagnini & Oliynyk 19

Hypoplasticity and other incrementally non-linear modelling approaches
Mašín 63

Modelling non-linearity, small-strain stiffness and cyclic loading
Mašín 89

Meta-stable structure, breakage and thermal effects
Mašín 121

Time and rate dependence
di Prisco & Flessati 155

Finite deformation plasticity
Oliynyk & Tamagnini 167

Numerical implementation of elastoplastic models in the Finite Element Method
Tamagnini & Oliynyk 193

Macroelement modelling
di Prisco & Flessati 227

Constitutive Modelling in Geomaterials – Foreword

Claudio Tamagnini[(1)] and David Mašín [(2)]

(1) University of Perugia, Italy
(2) Charles University, Prague, Czech Republic

Irrespectively of fast development of approaches for the analysis and design in geomechanics based on the methods for discontinuum (such as discrete element method), analysis of continua based on mesh or fast developing particle-based meshless methods still represents major means of numerical analysis in geomechanics. At the very core of such an analysis is a constitutive model: mathematical relationship converting the peculiar behaviour of particulate material, governed by the interactions between individual particles, into the behaviour of continua. As such, a properly selected and calibrated constitutive model has a critical effect on the outcomes of geotechnical simulations.

This school aims to introduce the students into the broad field of constitutive modelling of particulate materials with special emphasis on the behaviour of soils: after the introduction consisting of summary of basic features of soil behaviour, they will be introduced into fundamentals of constitutive modelling, followed by more detailed description of various modelling approaches - from the basic elastic and elasto-plastic models to more advanced frameworks of hardening plasticity, bounding surface plasticity, generalised plasticity and hypoplasticity. The second day will be focused on various specific more-advanced topics, such as simulation of small strain stiffness and cyclic loading, modelling of unsaturated soils, meta-stable structure, breakage, thermal effects, chemical effects and time and rate dependence, including formulation of finite-deformation plasticity and macroelement modelling. The last day is devoted to steps needed for adoption of models in numerical analysis tools, namely to their implementation in finite element codes. Finally, in practical hands-on sessions, students will train calibration using real experimental data themselves, using both manual and automatic freely-available calibration tools.

Claudio Tamagnini
David Mašín

Fundamentals of constitutive modelling for soils

Ivo Herle

Technische Universität Dresden, Germany

The constitutive modelling of soils is based on several basic principles enhanced with numerous advanced issues. Some basic principles can be understood even in 1D, like irreversibility of deformation or non-linearity of the stress-strain response. The standard features — soil stiffness, limit stress condition, critical state, dilatancy — are common to all modern constitutive models. Advanced features can take into account some additional effects. In spite of the progress in the field, the present state of the art of the constitutive modelling for soils is still far away from perfection.

1 Introduction

Models are simplifications of reality. They need to capture essential features of the modelling objects and neglect those of less importance. The distinction between important and negligible issues is problem- and purpose-dependent. A physical model of a house for an architecture exhibition will be different from a model house for a children playground, even if both houses are of the same scale.

Constitutive models should mathematically describe the material behaviour. An extraordinary abstraction level is required. Moreover, the model can focus on the micro-, meso- or macroscale, respectively. The material behaviour is not restricted to the stress-strain response only. In many applications the transport phenomena for liquid, gas or heat are of major interest. In other cases, chemical processes within the material need to be considered.

The constitutive modelling of soils can simulate single grains and their interactions using the framework of the discrete element method (DEM). Although impressive advances have been achieved in this field, the discrete modelling is not suitable for routine engineering applications yet. The latter remain in the domain of the continuum mechanics which profits from manifold and well-established theoretical principles.

Within constitutive models for soil as a continuum matter, single grains are smeared into an idealized material (Fig. 1). This material has, for the aspects of interest, the

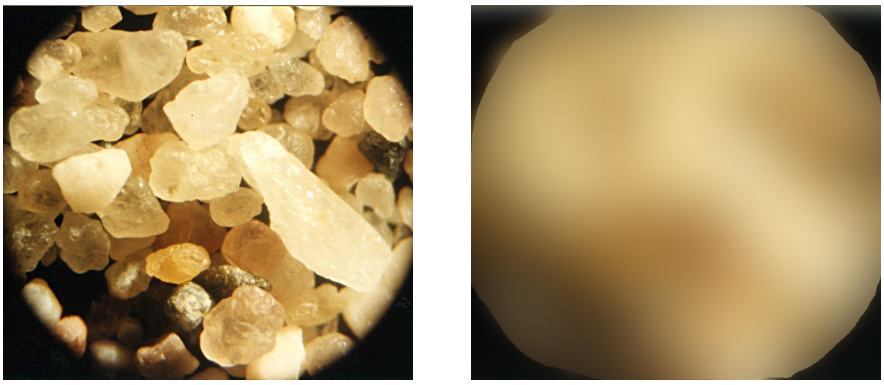

Figure 1: Single grains are not represented in constitutive models for continuum. The particulate nature of soil is smeared.

same response as a soil element. A suitable size of a representative elementary volume (REV) is being implicitly considered, although this size is not obvious. Which amount and fabric of soil grains are necessary for the REV in order to define stress and strain tensors from contact forces and mutual displacements of the grains? An objective answer is not possible since the REV is also inevitably influenced by the natural heterogeneity of soils as geological materials. What is the scale for such a heterogeneity? Where does the scatter of local quantities end and the natural heterogeneity start?

Common constitutive models for soils do not smear only the solid grains but also the liquid and gas phases between the grains. The principle of effective stresses serves as a link between those phases. Multiphase models can consider constitutive models for the phases separately. In this case, however, interaction relationships between the phases must be additionally specified. These interactions are, again, smeared over the REV and do not necessarily reflect the micromechanical response in a straightforward way.

Stress-strain relationships are typical products of constitutive models. Thus, stress-strain curves, like in Fig. 2, are related to the behaviour of a REV which, on the other hand, represents only a point in the continuum. In order to develop, calibrate and validate the constitutive models, the stress-strain curves of a REV must be accessible in experiments, at least for a few well controlled test conditions. The standard laboratory tests involve soil specimens which are definitely much larger than a corresponding REV of the tested material. Still, we interpret the specimen behaviour as identical with the one of the REV and base our constitutive models on this assumption.

Constitutive models are equations and, thus, they are composed of two different sets of quantities — constants and (state) variables. The material parameters are constants in constitutive equations and should not change their values throughout the modelled process. This requires that the material properties with respect to those parameters

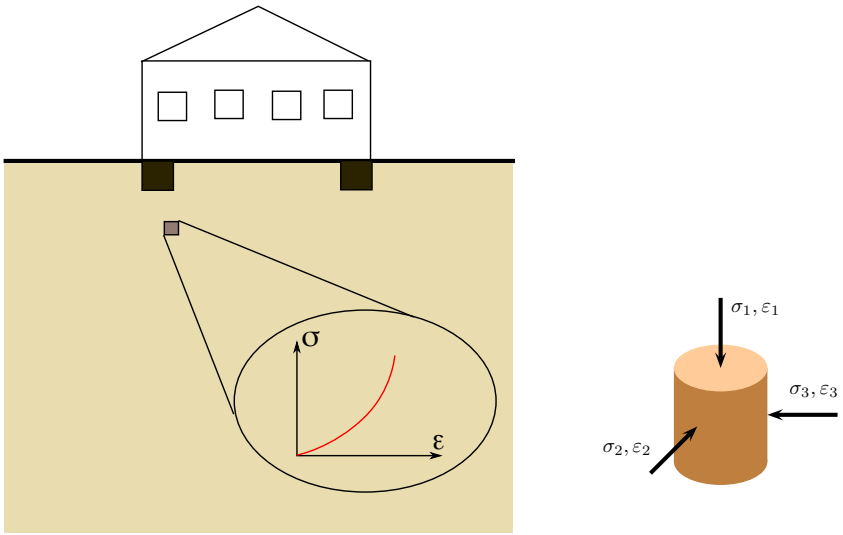

Figure 2: Soil element in situ as a REV and its representation in a laboratory test.

remain constant too. Although this requirement may seem self-evident, it is often violated in the practice of constitutive modelling.

The model variables characterize the actual soil state and, thus, can (and should) change during the modelled process. Equations for the evolution of state variables must be specified. A constitutive model for a stress-strain relationship is an example for an evolution equation for the stress as a state variable. If more (internal) variables are included in a constitutive model, evolution equations for all of them are required. Note that the strain tensor should not be considered as a state variable since soils do not possess a unique reference configuration in which strain corresponds to zero.

A determination (calibration) of the material parameters is crucial for a successful application of any constitutive model. The calibration can be seen as a fitting procedure attempting to achieve a good coincidence between the measured (observed) and calculated behaviour. Equally important is the determination of the initial values of state variables. This task can be much more difficult than the calibration of the model parameters (constants), especially for advanced constitutive models which use internal variables not accessible to measurements.

2 Basic features

Let us focus first on stress-strain relationships in one-dimensional representation. The equation

$$\sigma = E\varepsilon \tag{1}$$

describes a proportionality between the stress σ and the strain ε (Fig. 3 left). Stress should be the effective stress which controls the mechanical behaviour of soils. The constant in Eq. (1) is the material parameter E. It represents the stiffness of the material and in the model of elasticity it would be called Young's modulus.

2.1 Irreversibility

One of the most obvious soil properties is the irreversibility of deformation. With exception of extremely small deformations (e. g., during the passage of weak seismic waves through the soil), the soil skeleton does not recover its original configuration after a load reversal. Eq. (1) suggests a fully reversible behaviour with a unique relationship between stress and strain (Fig 3 left). However, for an irreversible response the stiffness must be different for loading and unloading, respectively (Fig 3 middle). Thus, a unique relationship between stress and strain does not exist (Fig 3 right).

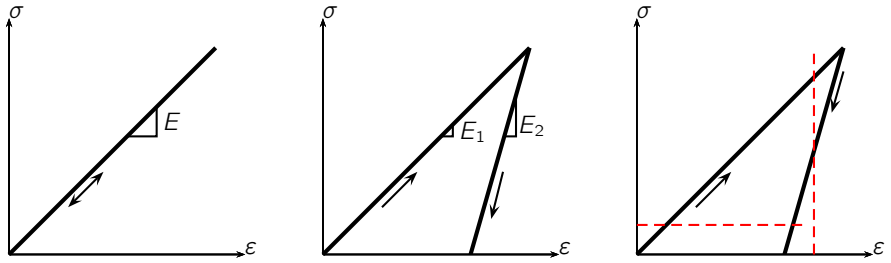

Figure 3: Reversible (elastic) and irreversible (inelastic) behaviour. Red dashed lines in the right diagram demonstrate two different strains for one stress and vice versa. Consequently, there is no unique relationship between stress and strain if the behaviour is irreversible.

Since change of the loading direction can take place in any admissible stress state, the constitutive models for soils must be formulated as incremental stress-strain relationships

$$\dot{\sigma} = E\dot{\varepsilon} \tag{2}$$

where the superimposed dots denote rates (time derivatives) of the quantities. A stress increment can be obtained by integration, e. g.,

$$\Delta\sigma = \int_{t_i}^{t_{i+1}} \dot{\sigma} dt = \dot{\sigma} \cdot \Delta t \,. \tag{3}$$

Obviously, E in Eq. (2) is not a material constant any more since it depends on the loading direction. This condition requires that $\dot{\sigma}(\dot{\varepsilon}) \neq \dot{\sigma}(-\dot{\varepsilon})$. The corresponding constitutive equation may be written as

$$\dot{\sigma} = E_1 \dot{\varepsilon} \quad \text{for } \dot{\varepsilon} > 0 \tag{4}$$

$$\dot{\sigma} = E_2 \dot{\varepsilon} \quad \text{for } \dot{\varepsilon} < 0 \tag{5}$$

It is possible to avoid the switch condition in the equations above if the absolute value $|\dot{\varepsilon}|$ is considered:

$$\dot{\sigma} = \frac{E_1 + E_2}{2} \dot{\varepsilon} + \frac{E_1 - E_2}{2} |\dot{\varepsilon}| = E_a \dot{\varepsilon} + E_b |\dot{\varepsilon}| \tag{6}$$

The latter approach is fundamental for the hypoplastic constitutive models. In elasto-plastic constitutive models, the reversible part of the deformation is usually considered elastic.

2.2 Nonlinearity

The incremental stiffness

$$E = \frac{\dot{\sigma}}{\dot{\varepsilon}} \tag{7}$$

does not depend only on loading direction but also on the stress state. It may increase with stress if we consider a compression loading (Fig. 4), or decrease if the stress approaches the limit state.

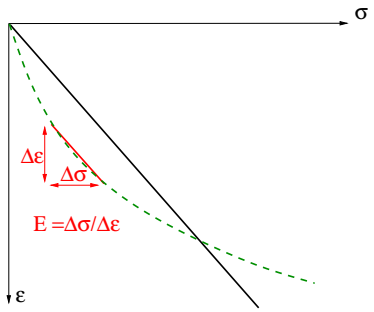

Figure 4: Nonlinear stress-strain behaviour due to stress-dependent stiffness.

In order to reproduce the nonlinear behaviour in (Fig. 4), the stiffness E can be written as a function of stress

$$\dot{\sigma} = E(\sigma)\dot{\varepsilon} \; . \tag{8}$$

The most simple is a linear dependence, i. e.,

$$E(\sigma) = C\sigma \; , \tag{9}$$

where C is a new soil parameter. The stiffness E becomes an auxiliary variable and is not a soil constant any more.

2.3 Rate-independence

The stress increment according to Eq. (3) depends on the time increment Δt. Often, however, the effects of real time on the soil behaviour are to be neglected and t should represent an integration parameter only. This requires that the constitutive equation is homogeneous of the first degree with respect to $\dot{\varepsilon}$, i. e.,

$$\dot{\sigma} = f(\sigma, k \cdot \dot{\varepsilon}) = k \cdot f(\sigma, \dot{\varepsilon}) \qquad \text{with } k > 0 \; . \tag{10}$$

The constitutive models (6) and (8) fulfil Eq. (10).

On the contrary, if time effects like creep, relaxation or dependence on the deformation velocity (rate-dependence, see Fig. 5) should be reproduced, the model must not obey Eq. (10).

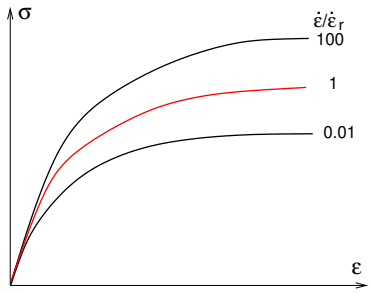

Figure 5: Rate-dependence of the stress-strain behaviour. $\dot{\varepsilon}_r$ denotes a reference strain rate.

3 Standard features

Only a few basic features of constitutive models can be outlined in an one-dimensional representation. A generalisation for at least two dimensions is necessary to capture some further standard features of the soil models. Finally, all constitutive models need

a tensorial formulation in 3D, in order to be able to implement the models into general-purpose finite elements codes. The model formulations must be independent on the reference frame and should not predict any deformation for a rigid body rotation.

In more than one spatial dimension, the understanding of stress (and strain) paths is crucial for constitutive modelling. The evolution of the stress tensor can be captured in various coordinates. The stress invariants p (mean stress) and q (stress deviator) are the most common ones. Nevertheless, some effects, like the rotation of principal stress axes, cannot be observed in the $p - q$ representation.

3.1 Stiffness

The incremental modulus defined in Eq. (8) obscures the spatial character of the stiffness. Its magnitude should depend on the direction of deformation at a particular soil state, i. e.,

$$E_{ij}(\sigma_i) = \frac{\dot{\sigma}_i}{\dot{\varepsilon}_j} \tag{11}$$

(here, the state variable is the principal effective stress σ_i). This feature can be well represented by response envelopes shown in Fig. 6.

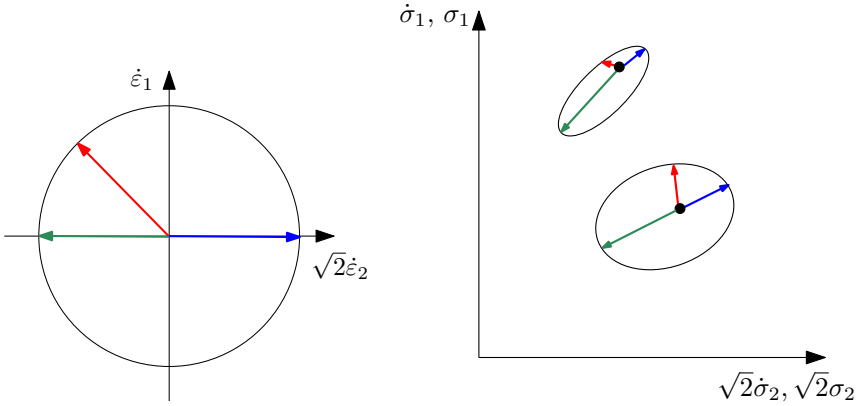

Figure 6: The concept of response envelopes. Each direction of the strain rate $|\dot{\varepsilon}| = 1$ (left) is mapped to the corresponding stress rate $\dot{\sigma}$ (right) which represents a state- and direction-dependent stiffness.

Consider a cylindrical specimen at radially symmetric (triaxial) conditions loaded in three different strain rates of the same magnitude but of different directions (Fig. 6 left): the blue arrow represents isotropic compression, the green one isotropic extension and the red one the undrained (constant volume) compression. The corresponding strain rates, as predicted by a constitutive model, are shown in Fig. 6 right. The particular stress states are marked by the big black dots. The stress ratio for isotropic extension (unloading) is higher than for isotropic loading. For the stress state with a

higher ratio of principal stresses, i. e., closer to the limit stress condition, the stiffness in shear (undrained compression) is much lower than for the stress state close to the isotropic one.

If the constitutive model is rate-independent, the magnitude of the strain rate can be considered as one, $|\dot{\varepsilon}| = \sqrt{\dot{\varepsilon}_1 + 2\dot{\varepsilon}_2} = 1$, and thus the magnitude of the stress rate $|\dot{\sigma}| = \sqrt{\dot{\sigma}_1 + 2\dot{\sigma}_2}$ corresponds to the state- and direction-dependent stiffness $\dot{\sigma}/\dot{\varepsilon}$. Connecting stress rates calculated for all strain rates at one particular state, so-called stress response envelopes (Fig. 6 right) are obtained [Gud79].

3.2 Limit stress condition

The effective stresses are bounded in the stress space. However, it is not possible to consider a unique limit stress condition for a soil. The magnitude of the limit stress depends on the amount of deformation and the soil state (Fig. 7 left). The state-dependence of the limit stress state results in a non-linear stress envelope (Fig. 7 middle). Moreover, various proposals can be found for the shape of the limit stress surface in the deviatoric plane (Fig. 7 right).

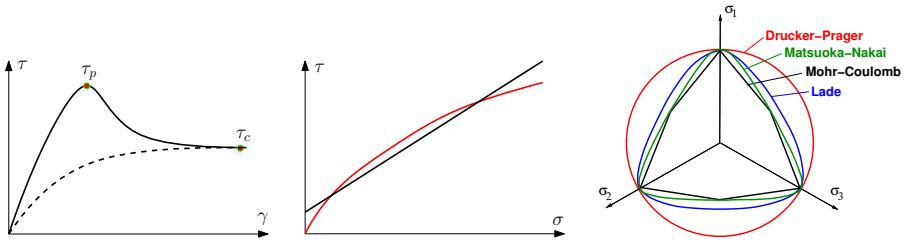

Figure 7: Various aspects of the limit stress condition: state- and strain-dependence of shear strength (left), non-linearity with respect to normal (mean) stress (middle) and cross-section in the deviatoric plane (right).

The limit stress state is characterised by vanishing stiffness, i. e., $\dot{\sigma}_i = 0$. Thus, for a particular soil state, it should be possible to calculate the limit stress from the constitutive equation analytically.

3.3 Void ratio and critical states

Void ratio e plays a crucial role for the state-dependent description of the soil behaviour. It has been established as a state variable practically in all advanced constitutive models. The evolution equation

$$\dot{e} = (1 + e)\dot{\varepsilon}_v \tag{12}$$

relates the change of e to the change of volumetric strain ε_v and, thus, implies incompressibility of soil grains.

The critical state as a steady state during constant volume deformation is a fundamental concept of the modern soil mechanics [Mui90]. It is common to assume a unique relationship between mean stress and void ratio in the critical state, although some experimental results question it [MFV98, FR03]. The critical state as an attractor during shear deformation is necessary for a robust performance of any constitutive model for soils.

3.4 Dilatancy

Dilatancy D expresses the maximum rate of the volume increase during shearing, which can be formulated, e. g., in triaxial (axially symmetric) conditions as

$$D = \frac{\dot{\varepsilon}_v}{\dot{\varepsilon}_q} = \frac{\dot{\varepsilon}_1 + 2\dot{\varepsilon}_2}{\frac{2}{3}(\dot{\varepsilon}_1 - \dot{\varepsilon}_2)} \quad . \tag{13}$$

By increasing relative soil density, the maximum shear strength and also dilatancy rise. Thus, a unique relationship between dilatancy D (for plastic strain rates in case of elasto-plastic models) and the maximum ratio of principal stresses $R = \sigma_1/\sigma_2$ is included in many constitutive equations (Fig. 8 left).

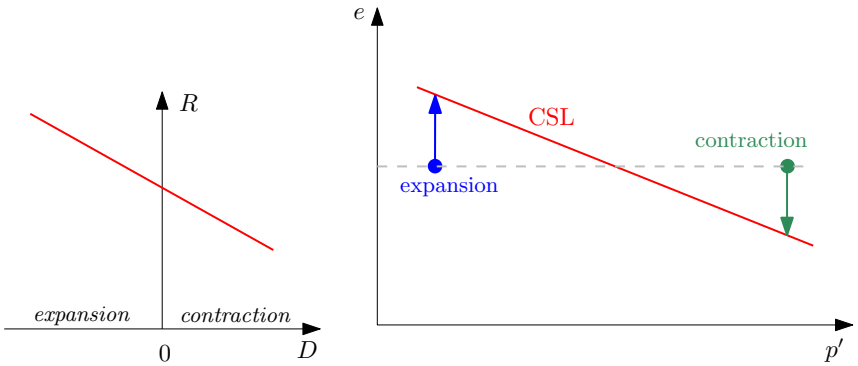

Figure 8: Dilatancy D as a function of the maximum stress ratio R (left), pressure-dependent volumetric response (right).

However, the soil state changes during deformation and is, in fact, pressure-dependent. This means that a "dense" soil at a low mean pressure can behave as a loose soil at a high mean pressure (Fig. 8 right). In (water-saturated) fine grained soils, analogous effects can be observed for water content related to consistency limits. Consequently, the relationship in Fig. 8 (left) is pressure-dependent [Bol86, LD00].

The distance between the soil state and the critical state line CSL at one particular mean pressure p' is often denoted as state parameter $\psi = e - e_c$ [BJ85]. An analogous role plays a so-called pressure-dependent relative density in hypoplastic models for

sand [Gud96]. For fine grained soils, the horizontal distance between the soil state and the critical state line, similar to the Hvorslev's equivalent pressure (e.g., [Mui90]), can be used.

3.5 Constant volume deformation

The undrained conditions are being produced in laboratory testing of fully saturated soils when the drainage is completely prohibited. Under assumption of incompressibility of water and soil grains, constant volume of the specimen, i. e. $\dot{\varepsilon}_v = 0$, is preserved during the test.

The undrained response is an important benchmark for the constitutive models. The shape of the stress path is linked to the evolution of the pore water pressure and, thus, to the dilatancy effect. The maximum stress difference $q = \sigma_1 - \sigma_2$ is essential, e. g., for analyses of liquefaction or short term slope stability. The predicted undrained shear strength should be state-dependent and should reflect the soil loading history like overconsolidation.

4 Advanced features

Recent constitutive models can take into account a number of additional features of the soil behaviour. Obviously, by adding further ingredients, the complexity of the models increases. The increased complexity results not only in more equations but also in more material parameters which may be mutually dependent. In many cases, additional state variables are introduced which, in turn, need their evolution equations.

The following list of effects, which can be implemented in advanced constitutive models (stress-strain relationships), brings only a few typical examples and does not represent a comprehensive state of the art.

- *Stress and deformation history*

  Memory of soil preserves its stress and deformation history in a manifold way. A typical scalar memory variable is the overconsolidation ratio OCR. In elastoplastic models, the latter is usually related to the size of the yield surface. The OCR can be also linked to the equivalent pressure or another similar quantity.

  Recent deformation history related to the so-called small-strain stiffness [ARS90] is often taken into account by the kinematic nature of yield surfaces [ATMW89]. Another option may be the so-called intergranular strain concept [NH97].

- *Anisotropy*

  Properties of anisotropic materials depend on the orientation with reference to the coordinate system. An essential induced anisotropy evolves with non-isotropic stress tensor since in most models stiffness depends on stress. A fabric-related anisotropy (e. g., the distribution of the grain contact normals

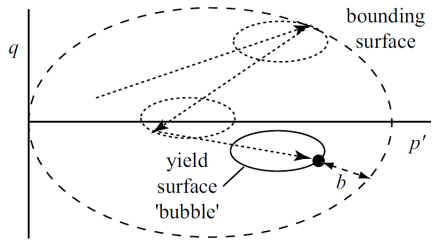

Figure 9: Kinematic yield surface of the "Bubble" model [Mui04].

in space) is reflecting the deformation history. It may be modelled by a structure tensor linked to the kinematic hardening of the yield surface(s) [WNKL03, TD08].

- *Cementation*

  In natural soils, brittle bonds at grain contacts can evolve with time due to various physical and chemical processes. Such a cementation may result in an increased apparent preconsolidation pressure. Elastoplastic constitutive models consider this effect by increasing the yield stress and thus expanding the (quasi) elastic stress range, followed by a fast structure degradation (collapse) [LN95]. The limit stress condition and further soil features can be affected by cementation as well [LT14].

- *Chemical and weathering effects*

  The modelling methodology for the degradation of bonding (cementation) can be also applied to weathering and chemical degradation [NCT03, Bus12, CdP16], sometimes in coupling with effects of partial saturation [PAV07]. Purely chemical processes can impact the mechanical properties of soils as well [HHH16].

- *Thermal effects*

  Soil behaviour is also sensitive to temperature. Constitutive models usually distinguish the effects of high temperatures (e.g., in clay barriers for the radioactive waste) [MK12, HPTC13] and freezing phenomena [NW19] separately. With respect to energy geostructures, the constitutive modelling of temperature oscillations may be of special interest, too [DL15].

- *Grain crushing*

  Usually, the soil parameters are constant for one particular soil which is characterized, among others, by its grain size distribution curve. Consequently, the grains of such a soil are considered to be permanent. However, especially coarse grains undergo degradation during soil deformation. This degradation starts with an abrasion of asperities at the grain surface at lower stresses and contin-

ues with grain breakage at higher stresses. The modelling of grain crushing and the resulting change of the grain size distribution may be linked to the consumed energy [Ein07]. The modification of the grading can be related to the classical elastoplastic concepts [KMR10].

- *Partial saturation*

  If the soil is not fully saturated, it must be considered as a three-phase material. The definition of the effective stress becomes less obvious. An additional stress variable, mostly the suction as a difference between air and water pressure, is needed in order to model the observed phenomena [GGSV03]. A short overview of the modelling concepts can be found, e. g., in [GSS06, SGFS08, NZC20].

5 Evaluation and validation

Even if there exists a perfect constitutive model for the soil behaviour, it is of no value until its parameters (constants) are known. Thus, the calibration of the material parameters is crucial for a successful application of constitutive models.

However, the constitutive models for soils are by far not perfect. They represent a compromise with respect to numerous effects which can be observed in experiments. There is a number of publications comparing the performance of advanced constitutive models, e. g., [RM10, WFT19]. They confirm the necessity for further (sometimes substantial) improvements. A unified approach for the software routines of constitutive models [GAG$^+$07] is helpful for such comparisons.

It must be also taken into account that practically all soil mechanics tests treat the soil specimens as idealized elements and attribute only unique values of the measured quantities to the whole specimen. E. g., vertical stresses and strains in a triaxial specimen are calculated from the measurements of a single force and displacement at the specimen boundary, assuming a homogeneous deformation. Thus, the scatter of the soil state (and, eventually, of the soil parameters) over the high number of REVs within the specimen is not taken into account.

The development, evaluation and validation of the constitutive models is, thus, affected by many uncertainties. A perfect coincidence between the measured and calculated curves is not necessarily admirable. Exaggerated requirements on the agreement between experimental and numerical results in element tests are not meaningful. General trends are usually much more important. During the model calibration and evaluation, a decision linked to the later application must be often made, see, e. g., Fig. 10.

6 Final remarks

The constitutive modelling of soils is a challenging discipline. Its fundamentals require a firm knowledge of soil testing and behaviour, paired with advanced mathemat-

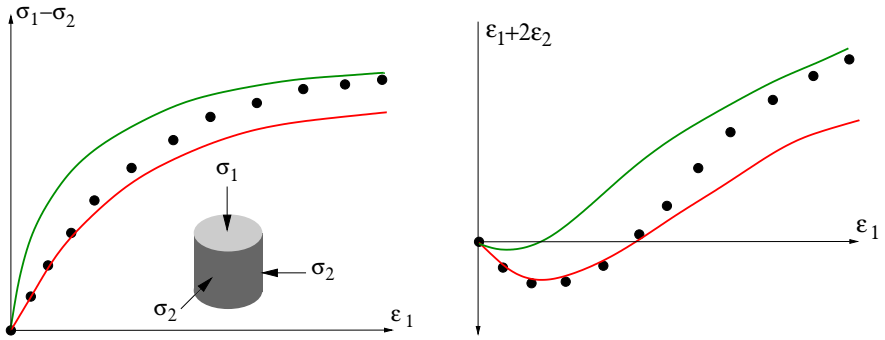

Figure 10: Which model (or parameter set) is better?

ics and a high level of abstraction. Although numerous advanced constitutive models are available for soils, their performance is not fully satisfactory under general conditions. A further research is needed.

References

[ARS90] J. H. Atkinson, D. Richardson, and S. E. Stallebrass. Effect of recent stress history on the stiffness of overconsolidated soil. *Géotechnique*, 40(4):531–540, 1990.

[ATMW89] A. Al-Tabbaa and D. Muir Wood. An experimentally based "bubble" model for clay., 1989.

[BJ85] K. Been and M. G. Jefferies. A state parameter for sands. *Géotechnique*, 35(2):99–112, 1985.

[Bol86] M. D. Bolton. The strength and dilatancy of sands. *Géotechnique*, 36(1):65–78, 1986.

[Bus12] G. Buscarnera. A conceptual model for the chemo-mechanical degradation of granular geomaterials. *Géotechnique Letters*, 2(3):149–154, 2012.

[CdP16] M. O. Ciantia and C. di Prisco. Extension of plasticity theory to debonding, grain dissolution, and chemical damage of calcarenites. *International Journal for Numerical and Analytical Methods in Geomechanics*, 40(3):315–343, 2016.

[DL15] A. Di Donna and L. Laloui. Response of soil subjected to thermal cyclic loading: Experimental and constitutive study. *Engineering Geology*, 190:65–76, 2015.

[Ein07] I. Einav. Soil mechanics: breaking ground. *Philosophical Transactions of the Royal Society A*, 365:2985–3002, 2007.

[FR03] R. J. Finno and A. L. Rechenmacher. Effects of Consolidation History on Critical State of Sand. *Journal of Geotechnical and Geoenvironmental Engineering*, 129(4):350–360, 2003.

[GAG+07] Gerd Gudehus, Angelo Amorosi, Antonio Gens, Ivo Herle, Dimitrios Kolymbas, David Mašín, David Muir Wood, Andrzej Niemunis, Roberto Nova, Manuel Pastor, Claudio Tamagnini, and Gioacchino Viggiani. The soilmodels.info project. *International Journal for Numerical and Analytical Methods in Geomechanics*, 2007.

[GGSV03] D. Gallipoli, A. Gens, R. Sharma, and J. Vaunat. An elasto-plastic model for unsaturated soil incorporating the effects of suction and degree of saturation on mechanical behaviour. *Géotechnique*, 53(1):123–135, 2003.

[GSS06] A. Gens, M. Sánchez, and D. Sheng. On constitutive modelling of unsaturated soils. *Acta Geotechnica*, 1:137–147, 2006.

[Gud79] G. Gudehus. A comparison of some constitutive laws for soils under radially symmetric loading and unloading. In *Third International Conference on Numerical Methods in Geomechanics*, pages 1309–1323, Aachen, 1979.

[Gud96] G. Gudehus. A comprehensive constitutive equation for granular materials. *Soils And Foundations*, 36(1):1–12, 1996.

[HHH16] T Hueckel, L B Hu, and M M Hu. Coupled chemo-mechanics: A comprehensive process modeling for Energy Geotechnics. In *Energy Geotechnics*, pages 25–34, 2016.

[HPTC13] P. Y. Hong, J. M. Pereira, A. M. Tang, and Y. J. Cui. On some advanced thermo-mechanical models for saturated clays. *International Journal for Numerical and Analytical Methods in Geomechanics*, 37(17):2952–2971, 2013.

[KMR10] M. Kikumoto, D. Muir Wood, and A. Russell. Particle crushing and deformation behaviour. *Soils And Foundations*, 50(4):547–563, 2010.

[LD00] X. S. Li and Y. F. Dafalias. Dilatancy for cohesionless soils. *Géotechnique*, 50(4):449–460, 2000.

[LN95] R. Lagioia and R. Nova. An experimental and theoretical study of the behaviour of a calcarenite in triaxial compression. *Geotechnique*, 45(4):633–648, 1995.

[LT14] P. V. Lade and N. Trads. The role of cementation in the behaviour of cemented soils. *Geotechnical Research*, 1(4):111–132, 2014.

[MFV98] M. A. Mooney, R. J. Finno, and G. Viggiani. A unique critical state for sand? *Journal of Geotechnical and Geoenvironmental Engineering*, 124(11):1100–1108, 1998.

[MK12] D. Mašín and N. Khalili. A thermo-mechanical model for variably saturated soils based on hypoplasticity. *International Journal for Numerical and Analytical Methods in Geomechanics*, 36:1461–1485, 2012.

[Mui90] David Muir Wood. *Soil Behaviour and Critical State Soil Mechanics*. Cambridge University Press, 1990.

[Mui04] D. Muir Wood. *Geotechnical Modelling*. Taylor & Francis, 2004.

[NCT03] R. Nova, R. Castellanza, and C. Tamagnini. A constitutive model for bonded geomaterials subject to mechanical and/or chemical degradation. *International Journal for Numerical and Analytical Methods in Geomechanics*, 27(9):705–732, 2003.

[NH97] A Niemunis and I Herle. Hypoplastic model for cohesionless soils with elastic strain range. *Mechanics of Cohesive-Frictional Materials*, 2(4):279–299, 1997.

[NW19] S. Nishimura and J. Wang. A simple framework for describing strength of saturated frozen soils as multi-phase coupled system. *Géotechnique*, 69(8):659–671, 2019.

[NZC20] C. W. W. Ng, C. Zhou, and C. F. Chiu. Constitutive modelling of state-dependent behaviour of unsaturated soils: an overview. *Acta Geotechnica*, 15(10):2705–2725, 2020.

[PAV07] N. Pinyol, E. E. Alonso, and J. Vaunat. A constitutive model for soft clayey rocks that includes weathering effects. *Géotechnique*, 57(2):137–151, 2007.

[RM10] A. R. Russell and D. Muir Wood. A comparison of critical state models for sand under conditions of axial symmetry. *Géotechnique*, 60(2):133–140, 2010.

[SGFS08] D. Sheng, A. Gens, D. G. Fredlund, and S. W. Sloan. Unsaturated soils: From constitutive modelling to numerical algorithms. *Computers and Geotechnics*, 35(6):810–824, 2008.

[TD08] M. Taiebat and Y. F Dafalias. SANISAND: Simple anisotropic sand plasticity model. *International Journal for Numerical and Analytical Methods in Geomechanics*, 32:915–948, 2008.

[WFT19] T. Wichtmann, W. Fuentes, and T. Triantafyllidis. Inspection of three sophisticated constitutive models based on monotonic and cyclic tests on fine sand: Hypoplasticity vs. Sanisand vs. ISA. *Soil Dynamics and Earthquake Engineering*, 124:172–183, 2019.

[WNKL03] S. J. Wheeler, A. Näätänen, M. Karstunen, and M. Lojander. An anisotropic elastoplastic model for soft clays. *Canadian Geotechnical Journal*, 40:403–418, 2003.

The theory of plasticity in constitutive modeling of rate–independent soils

Claudio Tamagnini[a], **Kateryna Oliynyk**[a,b]

[a)] *University of Perugia, Italy*
[b)] *University of Dundee, UK*

This chapter presents a review of the applications of the theory of plasticity to the modeling of rate–independent geomaterials, starting from classical approaches and covering some of the advanced versions of the theory designed to improve its capabilities in cyclic/dynamic loading conditions as well as to model "environmental" loading effects. In the discussion of the different approaches, particular attention is given to the incremental nature of the constitutive equations, emerging from the need of reproducing the essential features of the history–dependent behavior of soils. The relative merits and limitations of each class of models discussed are outlined with emphasis on those inherent features of their mathematical structure which might be of help in the assessment of their predictive capabilities when applied to practical geotechnical problems.

1 Introduction

In the application of continuum theories to the analysis of any solid mechanics problem, a fundamental role is played by the *constitutive equations*, which are expected to describe in precise mathematical terms the actual mechanical behavior of the material. Constitutive equations do not represent universal laws of nature. Rather, they can be considered definitions of *ideal materials*, *i.e.*, what is usually referred to as *constitutive models*. Constitutive models may possess the properties of the actual materials they are intended to model only to a limited extent. However, this do not lessen their worth, which is to produce a mathematical tool to predict the behavior of the physical system under any possible circumstance, starting from the limited knowledge gathered in a few experimental observations.

The quality of the predictions depends on the ability to define a suitable idealization for the real material which is capable to capture, from a quantitative point of view, the experimentally observed features which are thought to be of relevance for the practi-

cal problem at hand. This is particularly true in computational geomechanics, where the materials under consideration – *i.e.*, soil layers or rock masses – are usually characterized by a complex multi–phase structure and by a highly non–linear, irreversible and history–dependent response to the applied mechanical or "environmental" loading conditions.

The main objective of this chapter is to provide an outline of the different classes of constitutive equations for soils developed within the general framework of the theory of plasticity – from the early, pioneering works in perfect plasticity, to more recent developments in bounding surface and generalized plasticity, as well as in plasticity with generalized hardening laws to capture the effects of "environmental" loading conditions.

The topics covered in the following are not intended to provide a comprehensive review of the enormous amount of work which has been done in the applications of the theory of plasticity to soil mechanics over many decades. For this, the reader is referred, for example, to the following monographs [DS84, DS02, Woo04, Yu06, Bor13, Has17]. Rather, the presentation will be limited to those aspects of the general framework of the theory of which reflect the authors' own experience and interests. In particular, the discussion will be mostly focused – with the only exception of Sect. 9 – on constitutive equations for *rate–independent*, *saturated soils* in *isothermal conditions*, obeying the *principle of effective stress* as stated by Terzaghi [Ter48]. Details on how the constitutive models for saturated soils should be extended to account for partially saturated conditions can be found in the chapter by Jommi [Jom21] in this book. In the presentation of the different classes of models, we will focus on the infinitesimal theory of plasticity, suitable for small deformations and rotations. The extension of the theory to finite deformations is discussed in the chapter by Oliynyk and Tamagnini [OT21] in this book. The constitutive equations for brittle materials – *e.g.*, rocks or concrete – developed in the framework of damage mechanics are deliberately left out of this exposition. Finally, only constitutive equations for *simple materials*, according to Truesdell & Noll [TN65], will be considered in the following. Although non–local or weakly non–local theories for materials with microstructure – such as polar, second gradient or micromorphic materials – have been the subject of a considerable amount of research in geomechanics, mainly in relation to the study of strain localization into shear bands, they are outside the scope of the present work. For this interesting subject, the reader is referred to the books by Vardoulakis and Sulem [VS95, Var19], and references therein.

2 Notation

In the following, boldface lower– and upper–case letters are used to represent vector and tensor quantities. The symbols $\mathbf{1}$ and $\boldsymbol{I}^s$ are used for the second–order and fourth–order identity tensors, with components:

$$(\mathbf{1})_{ij} = \delta_{ij} \qquad\qquad (\boldsymbol{I}^s)_{ijkl} = \frac{1}{2}\left(\delta_{ik}\delta_{jl} + \delta_{il}\delta_{jk}\right) \tag{1}$$

The symmetric and skew–symmetric parts of a second–order tensor $\boldsymbol{X}$ are denoted as: $\mathrm{sym}\,\boldsymbol{X} := (\boldsymbol{X} + \boldsymbol{X}^T)/2$ and $\mathrm{skw}\,\boldsymbol{X} := (\boldsymbol{X} - \boldsymbol{X}^T)/2$, respectively. The dot product is defined as follows: $\boldsymbol{v} \cdot \boldsymbol{w} := v_i w_i$ for any two vectors $\boldsymbol{v}$ and $\boldsymbol{w}$; $\boldsymbol{X} \cdot \boldsymbol{Y} := X_{ij} Y_{ij}$ for any two second–order tensors $\boldsymbol{X}$ and $\boldsymbol{Y}$. The dyadic product is defined as follows: $[\boldsymbol{v} \otimes \boldsymbol{w}]_{ij} := v_i w_j$ for any two vectors $\boldsymbol{v}$ and $\boldsymbol{w}$; $[\boldsymbol{X} \otimes \boldsymbol{Y}]_{ijkl} := X_{ij} Y_{kl}$ for any two second–order tensors $\boldsymbol{X}$ and $\boldsymbol{Y}$. The quantity $\|\boldsymbol{X}\| := \sqrt{\boldsymbol{X} \cdot \boldsymbol{X}}$ denotes the Euclidean norm of $\boldsymbol{X}$. The usual sign convention of soil mechanics (compression positive) is adopted throughout. In line with Terzaghi's principle of effective stress, all stresses are *effective* stresses, unless otherwise stated. In the representation of stress and strain states, use will sometimes be made of the invariant quantities: p (mean stress), q (deviator stress), and θ (Lode angle), defined as:

$$p := \frac{1}{3}(\boldsymbol{\sigma} \cdot \mathbf{1})\,; \quad q := \sqrt{\frac{3}{2}}\,\|\boldsymbol{s}\|\,; \quad \sin(3\theta) := \sqrt{6}\frac{(\boldsymbol{s}^3) \cdot \mathbf{1}}{[(\boldsymbol{s}^2) \cdot \mathbf{1}]^{3/2}} \tag{2}$$

and: ϵ_v (volumetric strain), ϵ_s (deviatoric strain), $\dot{\epsilon}_v$ (volumetric strain rate), and $\dot{\epsilon}_s$ (deviatoric strain rate), defined as:

$$\begin{aligned} &\epsilon_v := \boldsymbol{\epsilon} \cdot \mathbf{1}\,; \quad \epsilon_s := \sqrt{\frac{2}{3}}\,\|\boldsymbol{e}\|\,; \quad \theta_\epsilon := \sqrt{6}\frac{(\boldsymbol{e}^3) \cdot \mathbf{1}}{[(\boldsymbol{e}^2) \cdot \mathbf{1}]^{3/2}} \\ &\dot{\epsilon}_v := \dot{\boldsymbol{\epsilon}} \cdot \mathbf{1}\,; \quad \dot{\epsilon}_s := \sqrt{\frac{2}{3}}\,\|\dot{\boldsymbol{e}}\| \qquad \dot{\theta}_\epsilon := \sqrt{6}\frac{(\dot{\boldsymbol{e}}^3) \cdot \mathbf{1}}{[(\dot{\boldsymbol{e}}^2) \cdot \mathbf{1}]^{3/2}} \end{aligned} \tag{3}$$

In eqs. (2) and (3), $\boldsymbol{s} := \boldsymbol{\sigma} - p\,\mathbf{1}$ is the deviatoric part of the stress tensor; $\boldsymbol{e} := \boldsymbol{\epsilon} - (1/3)\epsilon_v\,\mathbf{1}$ and $\dot{\boldsymbol{e}} := \dot{\boldsymbol{\epsilon}} - (1/3)\dot{\epsilon}_v\,\mathbf{1}$ are the deviatoric parts of the strain and the strain rate tensors, respectively, while $\boldsymbol{s}^2$ and $\boldsymbol{s}^3$ are the square and the cube of the deviatoric stress tensor, with components $(\boldsymbol{s}^2)_{ij} := s_{ik} s_{kj}$ and $(\boldsymbol{s}^3)_{ij} := s_{ik} s_{kl} s_{lj}$. It is worth noting that in eqs. $(3)_5$ and $(3)_6$, with a slight abuse of notation, the symbols $\dot{\epsilon}_s$ and $\dot{\theta}_\epsilon$ have been employed to denote the second and third invariants of the strain rate tensor, which generally do not coincide with the time rates of ϵ_s and θ_ϵ, as defined in in eqs. $(3)_2$ and $(3)_3$.

3 History–dependent materials modeling and the need for constitutive equations in rate–form

According to the principles of *determinism* and *local action* [TN65], the most general expression for the constitutive equation of a *simple* material is given by:

$$\boldsymbol{\sigma}(\boldsymbol{x}, t) = \overset{\infty}{\underset{\tau=0}{\boldsymbol{\mathcal{G}}}} \left[\boldsymbol{F}^{(t)}(\boldsymbol{X}, \tau)\right] \tag{4}$$

where $\boldsymbol{\mathcal{G}}$ is a *functional* of the *history* up to time t of the *deformation gradient* associated with the motion $\boldsymbol{x} = \boldsymbol{\varphi}(\boldsymbol{X}, t)$ carrying the material point $\boldsymbol{X}$ in the reference

configuration to its position $\boldsymbol{x}$ in the current configuration at time t, defined as:

$$\boldsymbol{F}^{(t)}(\boldsymbol{X}, s) := \boldsymbol{F}(\boldsymbol{X}, t-s) \qquad \boldsymbol{F}(\boldsymbol{X}, t) := \frac{\partial \boldsymbol{\varphi}}{\partial \boldsymbol{X}}(\boldsymbol{X}, t) \qquad (s \geq 0) \tag{5}$$

Eq. (4) essentially states that the (effective) stress tensor $\boldsymbol{\sigma}$ is a function of the *entire deformation history*, *i.e.*, that the knowledge of the state of strain at a given time t is in general *not sufficient* to determine the stress state. This is an essential feature of inelastic, history–dependent materials such as soils.

A third fundamental principle, the *principle of material frame indifference*, implies the following restriction to the functional $\boldsymbol{\mathcal{G}}$: for every orthogonal tensor function $\boldsymbol{Q}(\tau)$ and every history $\boldsymbol{F}^{(t)}(\boldsymbol{X}, \tau)$, the relation:

$$\boldsymbol{Q}_0 \overset{\infty}{\underset{\tau=0}{\boldsymbol{\mathcal{G}}}} \left[\boldsymbol{F}^{(t)}(\boldsymbol{X}, \tau)\right] \boldsymbol{Q}_0^T = \overset{\infty}{\underset{\tau=0}{\boldsymbol{\mathcal{G}}}} \left[\boldsymbol{Q}(\tau)\boldsymbol{F}^{(t)}(\boldsymbol{X}, \tau)\right] \qquad \boldsymbol{Q}_0 := \boldsymbol{Q}(0) \tag{6}$$

must hold. Conversely, any such functional $\boldsymbol{\mathcal{G}}$ satisfying eq. (6) can be considered as defining the constitutive equation of a particular material.

The fundamental properties of the functional $\boldsymbol{\mathcal{G}}$ should be defined according to our knowledge of the main characteristic of the mechanical behavior of the materials we intend to model. As far as geomaterials – and soils in particular – are concerned, a long standing experimental evidence indicates that the mechanical response of such materials is strongly non–linear and dependent on such factors as current state, previous loading history, load increment size and loading direction. Even the simplest and most common laboratory tests, such as a one–dimensional compression test or a axisymmetric (triaxial) drained compression test, can highlight such features in both fine and coarse–grained soils.

A main consequence of this observation is that the constitutive functional $\boldsymbol{\mathcal{G}}$ must be *non–linear* and *non–differentiable*, see [OW69]. However, working with non–linear, non–differentiable functionals poses formidable mathematical problems, even in the simplest cases. An alternative strategy, which overcomes this difficulty and is commonly adopted in nonlinear solid mechanics, is to avoid formulating the constitutive equation in *global terms*, as in eq. (4), and rather adopt an incremental (or *rate–type*) formulation, in which the (objective) stress rate is given as a *function* of the rate of deformation $\boldsymbol{d} := \operatorname{sym} \nabla \boldsymbol{v}$ ($\boldsymbol{v} := d\boldsymbol{\varphi}/dt \circ \boldsymbol{\varphi}$ being the spatial velocity) and of the current state of the material:

$$\overset{\circ}{\boldsymbol{\sigma}} = \boldsymbol{G}\left(\boldsymbol{\sigma}, \boldsymbol{q}, \boldsymbol{d}\right) \tag{7}$$

In eq. (7), $\overset{\circ}{\boldsymbol{\sigma}}$ denotes a suitable objective stress rate, such as the Jaumann–Zaremba stress rate, defined as:

$$\overset{\triangledown}{\boldsymbol{\sigma}} := \dot{\boldsymbol{\sigma}} + \boldsymbol{\sigma}\boldsymbol{\omega} - \boldsymbol{\omega}\boldsymbol{\sigma} \tag{8}$$

where $\boldsymbol{\omega} := \operatorname{skw} \nabla \boldsymbol{v}$ is the spin tensor. In eq. (7), $\boldsymbol{q}$ represents a set of *internal* state variables, which are introduced to account for the effects of the previous loading history. An additional set of rate equations is then required to define the evolution of

the internal variables in time. In classical elastoplasticity, these evolution equations are referred to as *hardening laws*.

Restricting our discussion to the infinitesimal theory, the objective stress rate $\overset{\circ}{\boldsymbol{\sigma}}$ can be replaced by the standard objective time rate $\dot{\boldsymbol{\sigma}}$, and the rate of deformation $\boldsymbol{d}$ with the (linearized) strain rate tensor $\dot{\boldsymbol{\epsilon}}$. Thus, eq. (7) can be rewritten as:

$$\dot{\boldsymbol{\sigma}} = \boldsymbol{G}\left(\boldsymbol{\sigma}, \boldsymbol{q}, \dot{\boldsymbol{\epsilon}}\right) \tag{9}$$

Rate–indepence means that a change in the time scale does not affect the material response, *e.g.*, doubling the strain rate doubles the stress rate. More generally:

$$\boldsymbol{G}\left(\boldsymbol{\sigma}, \boldsymbol{q}, \lambda\dot{\boldsymbol{\epsilon}}\right) = \lambda\boldsymbol{G}\left(\boldsymbol{\sigma}, \boldsymbol{q}, \dot{\boldsymbol{\epsilon}}\right) \qquad \forall\ \lambda > 0 \tag{10}$$

A direct consequence of the above equation is that the function $\boldsymbol{G}$ is *positively homogeneous* of degree one in $\dot{\boldsymbol{\epsilon}}$. This latter property yields the following alternative expression for the constitutive equation (9):

$$\dot{\boldsymbol{\sigma}} = \boldsymbol{D}\left(\boldsymbol{\sigma}, \boldsymbol{q}, \boldsymbol{\eta}\right)\dot{\boldsymbol{\epsilon}} \tag{11}$$

where $\boldsymbol{D}$ is the (fourth–order) tangent stiffness tensor at the current state, which depends on the strain rate only through its *direction*, defined by the unit tensor $\boldsymbol{\eta} := \dot{\boldsymbol{\epsilon}}/\left\|\dot{\boldsymbol{\epsilon}}\right\|$. Eq. (11) provides a general representation for rate–independent constitutive equations which encompasses as particular cases all the constitutive equations derived within the general framework of the theory of plasticity.

4 Non–linearity and incremental non–linearity

Let $(\boldsymbol{\sigma}_0, \boldsymbol{q}_0)$ be the initial state of the material at time $t = 0$. For a given strain path $\mathcal{E}$ from $\boldsymbol{\epsilon}_0$ to $\boldsymbol{\epsilon}(t)$, the state of stress at time t, $\boldsymbol{\sigma}(t)$, is obtained by integrating eq. (11):

$$\boldsymbol{\sigma}(t) = \hat{\boldsymbol{\sigma}}\left(\boldsymbol{\sigma}_0, \boldsymbol{q}_0, \mathcal{E}\right) = \boldsymbol{\sigma}_0 + \int_{\mathcal{E}} \boldsymbol{D}\left(\boldsymbol{\sigma}, \boldsymbol{q}, \boldsymbol{\eta}\right)\frac{d\boldsymbol{\epsilon}}{ds}\,ds \tag{12}$$

From the above equation, it is immediately apparent that the dependence of the tangent stiffness $\boldsymbol{D}$ on the current state $(\boldsymbol{\sigma}, \boldsymbol{q})$ renders the function $\hat{\boldsymbol{\sigma}}$ *non–linear*, *e.g.*, doubling the strain increment does not result in doubling the stress increment. This is the notion of non–linearity to be invoked when describing a material response for which the observed stress–strain curve (*e.g.*, in a triaxial compression path) is not a straight line.

An independent concept of non–linearity can be defined by considering the functional relation between stress rate and strain rate, as first suggested by Darve [Dar78]. If the constitutive function $\boldsymbol{G}$ is *linear* in $\dot{\boldsymbol{\epsilon}}$, then the material is said to be *incrementally linear*. In this case, the tangent stiffness tensor $\boldsymbol{D}$ does not depend on the strain rate direction $\boldsymbol{\eta}$, and eq. (11) reduces to:

$$\dot{\boldsymbol{\sigma}} = \boldsymbol{D}\left(\boldsymbol{\sigma}, \boldsymbol{q}\right)\dot{\boldsymbol{\epsilon}} \tag{13}$$

While a linear behavior implies incremental linearity, the opposite is not true. That is, incremental linearity does not imply linearity of the stress–strain response over a finite load increment. On the other hand, when $\boldsymbol{G}$ is a *non–linear* function of the strain rate, *i.e.*, for any $\dot{\boldsymbol{\epsilon}}_1$ and $\dot{\boldsymbol{\epsilon}}_2$ and $a, b \in \mathbb{R}$:

$$\boldsymbol{G}\left(\boldsymbol{\sigma}, \boldsymbol{q}, a\dot{\boldsymbol{\epsilon}}_1 + b\dot{\boldsymbol{\epsilon}}_2\right) \neq a\boldsymbol{G}\left(\boldsymbol{\sigma}, \boldsymbol{q}, \dot{\boldsymbol{\epsilon}}_1\right) + b\boldsymbol{G}\left(\boldsymbol{\sigma}, \boldsymbol{q}, \dot{\boldsymbol{\epsilon}}_2\right) \tag{14}$$

the material behavior is said to be *incrementally non–linear*. In this case, the tangent stiffness $\boldsymbol{D}$ explicitly depends on the strain rate direction, see eq. (11).

From eq. (14) it follows that:

$$\boldsymbol{G}\left(\boldsymbol{\sigma}, \boldsymbol{q}, \dot{\boldsymbol{\epsilon}}\right) \neq -\boldsymbol{G}\left(\boldsymbol{\sigma}, \boldsymbol{q}, -\dot{\boldsymbol{\epsilon}}\right) \tag{15}$$

which, in turn, implies:

$$\boldsymbol{D}(\boldsymbol{\sigma}, \boldsymbol{q}, \boldsymbol{\eta}) \neq \boldsymbol{D}(\boldsymbol{\sigma}, \boldsymbol{q}, -\boldsymbol{\eta}) \tag{16}$$

Equation (16) expresses a fundamental feature of incrementally non–linear models: for any strain rate direction, the reversal of the loading path is always associated with a change in the tangent stiffness $\boldsymbol{D}$. Indeed, such a feature is *necessary* in order to correctly describe irreversible behavior. In fact, although eq. (13) is in general non–integrable, the response of an incrementally linear material remains completely *reversible* in any closed loading–unloading program following the same path in two opposite directions.

When discussing the dependence of $\boldsymbol{D}$ on $\boldsymbol{\eta}$, it is useful to introduce the concept of *tensorial zone*, as defined by Darve [Dar78, Dar90]. A tensorial zone Z is a portion of the strain rate space in which $\boldsymbol{G}$ is a linear function of $\dot{\boldsymbol{\epsilon}}$. Accordingly, in a particular tensorial zone the tangent stiffness is *independent of* $\boldsymbol{\eta}$:

$$\boldsymbol{D}(\boldsymbol{\sigma}, \boldsymbol{q}, \boldsymbol{\eta}) = \boldsymbol{D}^{Z}(\boldsymbol{\sigma}, \boldsymbol{q}) \qquad\qquad \forall\, \boldsymbol{\eta} \in Z \tag{17}$$

As $\boldsymbol{G}$ is positively homogeneous of degree one in $\dot{\boldsymbol{\epsilon}}$, Z is a cone in the strain rate space with the vertex at the origin (*i.e.*, all strain rates $\lambda\dot{\boldsymbol{\epsilon}}$ with $\lambda > 0$ belong to the same tensorial zone as $\dot{\boldsymbol{\epsilon}}$).

Following Darve [Dar90], incrementally non–linear, rate–independent constitutive equations can be classified according to the number of associated tensorial zones. When the number of tensorial zones of $\boldsymbol{G}$ is finite, the constitutive equation is *incrementally multi–linear* (*bi–linear* in the particular case of only two zones). In incrementally multi–linear materials, an important issue is represented by the *continuity* of the response at the boundary between any two tensorial zones [Gud79]. Let ∂Z_{AB} be such a boundary between the tensorial zones Z_A and Z_B. If $\dot{\boldsymbol{\epsilon}}^* \in \partial Z_{AB}$, then, continuity of the response requires that:

$$\dot{\boldsymbol{\sigma}} = \boldsymbol{D}^{Z_A}\dot{\boldsymbol{\epsilon}}^* = \boldsymbol{D}^{Z_B}\dot{\boldsymbol{\epsilon}}^* \qquad \Rightarrow \qquad \left(\boldsymbol{D}^{Z_A} - \boldsymbol{D}^{Z_B}\right)\dot{\boldsymbol{\epsilon}}^* = \boldsymbol{0} \tag{18}$$

Equation $(18)_2$ represents a generalization of the continuity condition established by Green [Gre56] for hypoelastic materials. In the following, we will focus on models with one or two tensorial zones, leaving aside the theories of plasticity with multiple plastic mechanisms and more than two tensorial zones (*multi–surface plasticity*). Interested readers may refer to Ch. 5 of the book by Simo and Hughes [SH97] for a general treatment of this subject.

As opposed to multi–linearity, a *strictly* incrementally non–linear behavior is provided by constitutive models for which a *continuous* dependence of $\boldsymbol{D}$ on $\boldsymbol{\eta}$ is assumed. This is the case of rate–type constitutive models developed within the framework of the theory of hypoplasticity [Kol91, TVC00]. This subject is presented in the chapter by Mašín [Mas21] in this book.

5 Linear elasticity, hyperelasticity and hypoelasticity

In the early application of continuum mechanics to geotechnical engineering, the enormous analytical difficulties posed by the design of even simple geotechnical structures led to the traditional distinction between "deformation" and "failure" problems, for which different, very simple constitutive equations could be used, see *e.g.*, [TP48]. The rationale behind this approach is that only some very specific features of soil behavior are of interest for the particular problem at hand, while the others could be neglected without affecting the quality of the prediction in a substantial way. In particular, the only possible constitutive framework for which (analytical) solutions to deformation problems could be obtained at that time – in lack of suitable numerical methods and powerful computer platforms – was provided by the theory of *linear elasticity*. Its successful application then relied on the "proper" selection of the relevant soil constants (in essence, the Young's modulus), which had to be assumed to depend on such primary factors as current stress state, previous stress history, and nature of the applied stress path – in terms of magnitude and, possibly, direction.

Nowadays, the theory of elasticity still plays an important role, as it can be considered a cornerstone of any plasticity theory. For this reason, the main features of elasticity models adopted in the description of soil behavior are briefly recalled in this Section.

5.1 Linear elasticity

The simplest linear elastic model is provided by the Hooke's law for isotropic materials:

$$\dot{\boldsymbol{\sigma}} = \boldsymbol{D}\dot{\boldsymbol{\epsilon}}^e \qquad\qquad \boldsymbol{D} = K\mathbf{1}\otimes\mathbf{1} + 2G\left(\boldsymbol{I}^s - \frac{1}{3}\mathbf{1}\otimes\mathbf{1}\right) \tag{19}$$

where $\dot{\boldsymbol{\epsilon}}^e$ is the elastic strain rate – coinciding with the total strain rate if there are no irreversible deformations – while K and G are the (constant) bulk and shear moduli of the material. The two elastic constants can be replaced by other, frequently used

pairs of alternative elastic properties, such as the Young's modulus and Poisson's ratio (E, ν) related to K and G by the relations:

$$K = \frac{E}{3(1-2\nu)} \qquad\qquad G = \frac{E}{2(1+\nu)}$$

or the Lame's constants (λ, μ), linked to E and ν by the relations:

$$\lambda = \frac{E\nu}{(1+\nu)(1-2\nu)} \qquad\qquad \mu = \frac{E}{2(1+\nu)} = G$$

Linear isotropic elasticity is still widely used in a number of important geotechnical applications. However, it fails to capture an essential feature of the reversible response of granular material, *i.e.*, global non–linearity, due to the dependence of the stiffness constants on the current stress state. This feature of soils' elastic response originates from the nature of the reversible grain to grain interactions at the microscopic level [CJR13].

5.2 Hypoelasticity

Early attempts to incorporate global non–linearity in the elastic response of the soil can be traced back to the works of Kondner & Zelasko [KZ63] and Duncan & Chang [DC70]. In essence, it consists in adopting an isotropic elastic constitutive equation in the form of eq. (19), where the elastic stiffness coefficients are not constants but rather functions of the strain level and/or of the stress state. Generally speaking, all models of this kind are defined as *hypoelastic*, since the quantity:

$$d\boldsymbol{\epsilon}^e = \boldsymbol{C} d\boldsymbol{\sigma} \qquad\qquad \boldsymbol{C} := \boldsymbol{D}^{-1} \tag{20}$$

is not an exact differential, *i.e.*, it is not possible to define a one–to–one correspondence between the stress and strain tensors, and a closed stress cycle might result in the development of residual deformations.

The early hypoelastic formulations adopted an elastic tangent stiffness tensor $\boldsymbol{D}$ of the form:

$$\boldsymbol{D}\left(\boldsymbol{\sigma}, \boldsymbol{\epsilon}\right) = K_t\left(p, \epsilon_v\right) \mathbf{1} \otimes \mathbf{1} + 2G_t\left(p, \epsilon_s\right) \left(\boldsymbol{I}^s - \frac{1}{3} \mathbf{1} \otimes \mathbf{1} \right) \tag{21}$$

In constitutive models of this class, the dependence of the tangent bulk and shear moduli, $K_t\left(p, \epsilon_v\right)$, and $G_t\left(p, \epsilon_s\right)$, on the strain invariants is obtained by curve–fitting the observed stress–strain response in standard loading paths, such as drained (or undrained) triaxial compression, and isotropic compression, see for example [JPFB86, JP88, JPSJH91]. For this reason, these constitutive equations are also referred to as *variable–moduli models*.

A main drawback of variable–moduli models is the fact that, in this case, the strain invariants cannot be considered as true state variables, since the reference configuration from which the strains are defined is arbitrary. In this respect, a more sound

approach is provided by those hypoelastic models in which the stiffness coefficients depend only on the current stress state, typically through the mean stress p:

$$K_t(p) = K_{t0}\left(\frac{p}{p_{\text{atm}}}\right)^{\alpha} \qquad G_t(p) = G_{t0}\left(\frac{p}{p_{\text{atm}}}\right)^{\beta} \tag{22}$$

where p_{atm} is the atmospheric pressure, used as a scaling factor for the mean stress, and K_{t0}, G_{t0}, α and β are model constants, determined by empirically fitting stress–strain curves from conventional laboratory test results. The phenomenological nature of the relations (22) implies that the resulting elastic constitutive equation is hypoelastic and cannot be derived from a potential function. Zytynski *et al.* [ZRNW78] have discussed the necessary conditions for the stiffness coefficient to make $d\boldsymbol{\epsilon}^e$ in eq. (20) an exact differential. In particular, they observe that if both K_t and G_t depend only on p, as in eq. (22), then the resulting elastic constitutive equation in rate form cannot be integrated and is therefore hypoelastic.

Hypoelastic constitutive equations have been and still are widely used in the formulation of both classical and advanced plasticity theories for soils. However, their use should remain limited to monotonic loading conditions or to situations where the soil undergoes only a small number of cycles, as pointed out in [BTA97].

5.3 Hyperelasticity

A material is said to be *hyperelastic* (or *Green elastic* [Ogd97]) when there exists an elastic potential function $\psi(\boldsymbol{\epsilon}^e)$ such that:

$$\boldsymbol{\sigma} = \frac{\partial \psi}{\partial \boldsymbol{\epsilon}^e}(\boldsymbol{\epsilon}^e) \tag{23}$$

Eq. (23) defines a hyperelastic constitutive equation, which implies the existence of a direct functional relation between the stress tensor $\boldsymbol{\sigma}$ and the elastic strain tensor $\boldsymbol{\epsilon}^e$. This relation can be recast in rate form by differentiating both sides of eq. (23), obtaining:

$$\dot{\boldsymbol{\sigma}} = \boldsymbol{D}(\boldsymbol{\epsilon}^e)\dot{\boldsymbol{\epsilon}}^e \qquad \boldsymbol{D}(\boldsymbol{\epsilon}^e) := \frac{\partial^2 \psi}{\partial \boldsymbol{\epsilon}^e \otimes \partial \boldsymbol{\epsilon}^e}(\boldsymbol{\epsilon}^e) \tag{24}$$

where the elastic tangent stiffness is obtained as the second derivative of ψ with respect of its argument. This time, $\dot{\boldsymbol{\sigma}}$ is an exact differential, and no permanent stress changes may occur in any closed elastic strain cycle.

The dual formulation of the hyperelastic constitutive equation (23) is obtained by postulating the existence of a complementary energy function $g(\boldsymbol{\sigma})$, such that:

$$\boldsymbol{\epsilon}^e = \frac{\partial g}{\partial \boldsymbol{\sigma}}(\boldsymbol{\sigma}) \tag{25}$$

By differentiating eq. (25) we obtain the following complementary hyperelastic constitutive equation in rate–form:

$$\dot{\boldsymbol{\epsilon}}^e = \boldsymbol{C}(\boldsymbol{\sigma})\dot{\boldsymbol{\sigma}} \qquad \boldsymbol{C}(\boldsymbol{\sigma}) := \frac{\partial^2 g}{\partial \boldsymbol{\sigma} \otimes \partial \boldsymbol{\sigma}}(\boldsymbol{\sigma}) \tag{26}$$

where $\boldsymbol{C} = \boldsymbol{D}^{-1}$ is the material tangent compliance tensor. The two potentials ψ and g are related one another as g can be considered the Legendre transform of ψ, see, *e.g.*, [HP07]. As a consequence of the principle of material frame indifference, ψ and g must depend on their tensorial arguments only through their invariants [SH97], *i.e.*:

$$\psi(\boldsymbol{\epsilon}^e) = \hat{\psi}(\epsilon_v^e, \epsilon_s^e, \theta_\epsilon) = \bar{\psi}(\epsilon_1^e, \epsilon_2^e, \epsilon_3^e) \tag{27}$$

$$g(\boldsymbol{\sigma}) = \hat{g}(p, q, \theta) = \bar{g}(\sigma_1, \sigma_2, \sigma_3) \tag{28}$$

The hyperelastic constitutive equations (23) and (25) allow to describe a non–linear elastic behavior, whenever the two elastic potentials are not quadratic functions of their arguments. However, it is worth noting that hyperelasticity (which includes linear elasticity as a special case) as well as hypoelasticity are both incrementally linear theories, with only one tensorial zone. Examples of hyperelastic formulations for isotropic granular materials are provided in the works of [Hou85, BTA97, HP07].

6 Thermodynamics–based approach: the theory of hyperplasticity

The most important case of constitutive equations with two tensorial zones is provided by the classical *theory of plasticity* with a *single plastic mechanism*, and its various generalizations to describe, for example, induced anisotropy and cyclic behavior. The general framework of the theory of plasticity is now well established and a thorough treatment of this subject can be found in many excellent textbooks, *e.g.*, [Lub90, SH97, JB02]. As for plasticity in soil mechanics, good references are provided, *e.g.*, by [DS84, DS02, Yu06, Bor13, Has17]. As compared to those references, in the presentation of the basic principles of the theory we have adopted a slightly different point of view, starting from the basic principles of the thermodynamics of continuous media and following the approach of the so–called *theory of hyperplasticity*, as defined by Houlsby and Puzrin [HP07]. Then, the classical approach is presented as a generalization of the basic concepts of hyperplasticity.

The attempts to derive the evolution equations of the infinitesimal rate–independent plasticity from basic thermodynamics principles can be traced back to the early works of the French school [Mor70, HN75, GNS83]. Important contributions to the understanding of the thermo–mechanics of solid materials have been provided, *e.g.*, in the works of [Zie83, ZW87, Mau92, RM93, HR99]. The advantages of ensuring thermodynamic consistency when dealing with the inelastic behavior of geomaterials have been emphasized by Houlsby [Hou81] and Collins and Houlsby [CH97], in view of the potential drawbacks associated with purely phenomenological modeling of materials featuring stress–dependent stiffness, non–associative behavior and dilatant plastic flow. Significant contributions to the development of infinitesimal elastoplastic models for soils within the framework of continuum thermo–mechanics have been given, for example, by [MLA94, HP00, PH01, CK02, CH02, CM03, EP04, DT05, EHN07, OT20].

6.1 Free energy and dissipation functions

In the framework of infinitesimal elastoplasticity, we assume the customary additive decomposition of the total strain tensor into an elastic, reversible part and an inelastic part:

$$\boldsymbol{\epsilon} = \boldsymbol{\epsilon}^e + \boldsymbol{\epsilon}^p \qquad\qquad \dot{\boldsymbol{\epsilon}} = \dot{\boldsymbol{\epsilon}}^e + \boldsymbol{\epsilon}^p \tag{29}$$

By limiting the set of state variables $\mathcal{S}$ to the elastic strain tensor $\boldsymbol{\epsilon}^e$ and to a pseudo–vector of strain–like internal variables $\boldsymbol{\alpha}$ (the components of which could be scalars or second–order tensors), we postulate the existence of a Helmholtz free energy function per unit volume of the form:

$$\psi(\boldsymbol{\epsilon}^e, \boldsymbol{\alpha}) = \psi^e(\boldsymbol{\epsilon}^e) + \psi^p(\boldsymbol{\alpha}) \tag{30}$$

This assumption is equivalent to consider the contributions to the free energy function of elastic strains and plastic internal variables as fully uncoupled. This could represent a somewhat restrictive assumption, but it can be considered sufficiently general for the scope of this work.

For isothermal processes, the second principle of thermodynamics requires that the dissipation function $\mathcal{D}$, defined as:

$$\mathcal{D} := \boldsymbol{\sigma} \cdot \dot{\boldsymbol{\epsilon}} - \dot{\psi} \geq 0 \tag{31}$$

is non–negative. Taking into account the definition of the free energy function given in eq. (30), and introducing the set of *generalized stresses* $\overline{\mathcal{K}} = \{\overline{\boldsymbol{\chi}}, \overline{\boldsymbol{\chi}}_\alpha\}$, defined by:

$$\overline{\boldsymbol{\chi}} = \frac{\partial \psi^e}{\partial \boldsymbol{\epsilon}^e} \qquad\qquad \overline{\boldsymbol{\chi}}_\alpha = -\frac{\partial \psi^p}{\partial \boldsymbol{\alpha}} \tag{32}$$

we have:

$$\begin{aligned} \mathcal{D} &= \boldsymbol{\sigma} \cdot \dot{\boldsymbol{\epsilon}} - \left\{ \frac{\partial \psi^e}{\partial \boldsymbol{\epsilon}^e} \cdot \dot{\boldsymbol{\epsilon}}^e + \frac{\partial \psi^p}{\partial \boldsymbol{\alpha}} \dot{\boldsymbol{\alpha}} \right\} \\ &= \boldsymbol{\sigma} \cdot \dot{\boldsymbol{\epsilon}} - \overline{\boldsymbol{\chi}} \cdot (\dot{\boldsymbol{\epsilon}} - \dot{\boldsymbol{\epsilon}}^p) + \overline{\boldsymbol{\chi}}_\alpha \cdot \dot{\boldsymbol{\alpha}} \\ &= (\boldsymbol{\sigma} - \overline{\boldsymbol{\chi}}) \cdot \dot{\boldsymbol{\epsilon}} + \overline{\boldsymbol{\chi}} \cdot \dot{\boldsymbol{\epsilon}}^p + \overline{\boldsymbol{\chi}}_\alpha \cdot \dot{\boldsymbol{\alpha}} \geq 0 \end{aligned} \tag{33}$$

For this inequality to hold for any possible non–dissipative processes, for which $\dot{\boldsymbol{\epsilon}}^p = \mathbf{0}$ and $\dot{\boldsymbol{\alpha}} = \mathbf{0}$, we must have:

$$\boldsymbol{\sigma} = \overline{\boldsymbol{\chi}} = \frac{\partial \psi}{\partial \boldsymbol{\epsilon}^e} \tag{34}$$

Eq. (34) is the hyperelastic constitutive equation of the material, establishing a functional relation between the stress tensor $\boldsymbol{\sigma}$ and the elastic strain tensor $\boldsymbol{\epsilon}^e$. Substituting this last result into eq. (33), we obtain the following reduced dissipation inequality:

$$\mathcal{D} = \boldsymbol{\sigma} \cdot \dot{\boldsymbol{\epsilon}}^p + \overline{\boldsymbol{\chi}}_\alpha \cdot \dot{\boldsymbol{\alpha}} \geq 0 \tag{35}$$

Eqs. (32) and (35) suggest the following functional dependence for the dissipation function $\mathcal{D}$ on both the set $\mathcal{S}$ of the state variables and the set of dissipative flows $\mathcal{F} := \{\dot{\boldsymbol{\epsilon}}^p, \dot{\boldsymbol{\alpha}}\}$:

$$\mathcal{D}(\mathcal{S}, \mathcal{F}) = \mathcal{D}\left(\boldsymbol{\epsilon}^e, \boldsymbol{\alpha}, \dot{\boldsymbol{\epsilon}}^p, \dot{\boldsymbol{\alpha}}\right) \tag{36}$$

To describe the behavior of a rate–independent material, we postulate that the dissipation function $\mathcal{D}$ is homogeneous of degree one in the elements of $\mathcal{F}$. Euler's theorem for homogeneous functions then requires that:

$$\mathcal{D} = \frac{\partial \mathcal{D}}{\partial \dot{\boldsymbol{\epsilon}}^p} \cdot \dot{\boldsymbol{\epsilon}}^p + \frac{\partial \mathcal{D}}{\partial \dot{\boldsymbol{\alpha}}} \cdot \dot{\boldsymbol{\alpha}} \tag{37}$$

By introducing the set of *generalized dissipative stresses* $\mathcal{K} := \{\boldsymbol{\chi}, \boldsymbol{\chi}_\alpha\}$, defined as:

$$\boldsymbol{\chi} = \frac{\partial \mathcal{D}}{\partial \dot{\boldsymbol{\epsilon}}^p} \qquad\qquad \boldsymbol{\chi}_\alpha = \frac{\partial \mathcal{D}}{\partial \dot{\boldsymbol{\alpha}}} \tag{38}$$

eq. (37) can be rewritten as:

$$\mathcal{D} = \boldsymbol{\chi} \cdot \dot{\boldsymbol{\epsilon}}^p + \boldsymbol{\chi}_\alpha \cdot \dot{\boldsymbol{\alpha}} \tag{39}$$

Comparing eqs. (37) and (39) we observe that generalized stresses and generalized dissipative stresses must fulfill the following relation:

$$(\boldsymbol{\chi} - \overline{\boldsymbol{\chi}}) \cdot \dot{\boldsymbol{\epsilon}}^p + (\boldsymbol{\chi}_\alpha - \overline{\boldsymbol{\chi}}_\alpha) \cdot \dot{\boldsymbol{\alpha}} = 0 \tag{40}$$

This equality is trivially satisfied if Ziegler's orthogonality conditions – see [HP07] – are assumed:

$$\boldsymbol{\chi} = \overline{\boldsymbol{\chi}} \qquad\qquad \boldsymbol{\chi}_\alpha = \overline{\boldsymbol{\chi}}_\alpha \tag{41}$$

Eq. (41) is a sufficient condition for eq. (40) to hold, but not a necessary one. Therefore, Ziegler's orthogonality condition must be considered as a (weak) restrictive constitutive assumption, yet compatible with realistic descriptions of many classes of granular materials characterized by frictional dissipation, see *e.g.*, [CH97, HP07].

6.2 Yield function and evolution equations

The homogeneity of degree one of $\mathcal{D}$ in the dissipative flows implies that the (degenerate) partial Legendre transformation of $\mathcal{D}$ with respect to the arguments in $\mathcal{F}$ is a scalar function $\hat{f}$, called *yield function*, such that:

$$\dot{\gamma}\hat{f}(\mathcal{S}, \mathcal{K}) := \boldsymbol{\chi} \cdot \dot{\boldsymbol{\epsilon}}^p + \boldsymbol{\chi}_\alpha \cdot \dot{\boldsymbol{\alpha}} - \mathcal{D} = 0 \tag{42}$$

for dissipative processes, *i.e.*, when the elements of $\mathcal{F}$ are non–zero. In the LHS of eq. (42), the scalar $\dot{\gamma} \geq 0$ is the so–called *plastic multiplier*. The set:

$$\mathbb{E} := \left\{(\boldsymbol{\epsilon}^e, \boldsymbol{\alpha}, \boldsymbol{\chi}, \boldsymbol{\chi}_\alpha) \in \mathcal{S} \times \mathcal{K} \;\middle|\; \hat{f}(\boldsymbol{\epsilon}^e, \boldsymbol{\alpha}, \boldsymbol{\chi}, \boldsymbol{\chi}_\alpha) < 0\right\} \tag{43}$$

is the *elastic domain* of the material, where the plastic multiplier is zero and all the processes are non dissipative ($\dot{\boldsymbol{\epsilon}}^p = \mathbf{0}$, $\dot{\boldsymbol{\alpha}} = \mathbf{0}$). The boundary of $\mathbb{E}$:

$$\partial\mathbb{E} := \left\{ (\boldsymbol{\epsilon}^e, \boldsymbol{\alpha}, \boldsymbol{\chi}, \boldsymbol{\chi}_\alpha) \in \mathcal{S} \times \mathcal{K} \;\middle|\; \hat{f}(\boldsymbol{\epsilon}^e, \boldsymbol{\alpha}, \boldsymbol{\chi}, \boldsymbol{\chi}_\alpha) = 0 \right\} \tag{44}$$

is the *yield surface*, on which $\dot{\gamma}$ may be positive and irreversible processes may occur.

It is worth noting that, due to the orthogonality conditions (41) and the constitutive equations (32), the yield function f can be considered as a function of $\boldsymbol{\epsilon}^e$ and $\boldsymbol{\alpha}$:

$$\hat{f}(\boldsymbol{\epsilon}^e, \boldsymbol{\alpha}, \boldsymbol{\chi}, \boldsymbol{\chi}_\alpha) = f^*(\boldsymbol{\epsilon}^e, \boldsymbol{\alpha}) = 0 \tag{45}$$

i.e., of the elastic strain and the strain–like internal variables. Therefore, the elastic domain and the yield function provided by eqs. (43) and (44) are defined in *strain space*. The stress–space counterparts of $\mathbb{E}$ and f is recovered by noting that the stress tensor $\boldsymbol{\sigma}$ and the stress–like internal variables $\overline{\boldsymbol{\chi}}_\alpha$ are given functions of $(\boldsymbol{\epsilon}^e, \boldsymbol{\alpha})$ through the constitutive equations (32). The yield function in stress space then reads:

$$f(\boldsymbol{\sigma}, \overline{\boldsymbol{\chi}}_\alpha) = f^* \left\{ \boldsymbol{\epsilon}^e(\boldsymbol{\sigma}), \boldsymbol{\alpha}(\overline{\boldsymbol{\chi}}_\alpha) \right\} = 0 \tag{46}$$

From the properties of the Legendre transform of eq. (42) the following *associative flow rules* for the elements of $\mathcal{F}$ can be obtained:

$$\dot{\boldsymbol{\epsilon}}^p = \dot{\gamma} \frac{\partial \hat{f}}{\partial \boldsymbol{\chi}} = \dot{\gamma} \frac{\partial f}{\partial \boldsymbol{\sigma}} \tag{47a}$$

$$\dot{\boldsymbol{\alpha}} = \dot{\gamma} \frac{\partial \hat{f}}{\partial \boldsymbol{\chi}_\alpha} = \dot{\gamma} \frac{\partial f}{\partial \overline{\boldsymbol{\chi}}_\alpha} \tag{47b}$$

Eq. (47a) is the standard associative flow rule for the plastic strain rate, while eq. (47b) provides the associative hardening law for the internal variable $\boldsymbol{\alpha}$. It is worth noting that the associativity of the flow rule (47a) holds in the generalized dissipative stress space. Thus, this result does not prevent the possibility of modeling non–associative plastic flow in standard Cauchy stress space for free energy functions different from the one adopted in eq. (30), see [CH97, HP07].

6.3 Consistency conditions and constitutive equations in rate–form

The yield function and the plastic multiplier are subjected to the *Kuhn–Tucker complementarity conditions*:

$$\dot{\gamma} \geq 0 \qquad f(\boldsymbol{\sigma}, \overline{\boldsymbol{\chi}}_\alpha) \leq 0 \qquad \dot{\gamma} f(\boldsymbol{\sigma}, \overline{\boldsymbol{\chi}}_\alpha) = 0 \tag{48}$$

stating that plastic flow may occur only for stress states on the yield surface (yield state). However, these conditions do not allow to distinguish which deformation processes taking place from a yield state are actually plastic, *i.e.*, cause the development of plastic deformations. Moreover, no information is yet provided on how the plastic multiplier depends on the current state and the imposed deformation rate.

These issues are addressed by the so–called *Prager's consistency condition*, stating that for a plastic process taking place from a state on the yield surface the value of f must remain zero, *i.e.*:

$$\dot{f} = \frac{\partial f}{\partial \boldsymbol{\sigma}} \cdot \dot{\boldsymbol{\sigma}} + \frac{\partial f}{\partial \overline{\boldsymbol{\chi}}_\alpha} \cdot \dot{\overline{\boldsymbol{\chi}}}_\alpha = 0 \tag{49}$$

From eqs. (32) and (47) we can derive the following expressions for $\dot{\boldsymbol{\sigma}}$ and $\dot{\overline{\boldsymbol{\chi}}}_\alpha$:

$$\dot{\boldsymbol{\sigma}} = \boldsymbol{D}^e \left(\dot{\boldsymbol{\epsilon}} - \dot{\boldsymbol{\epsilon}}^p\right) = \boldsymbol{D}^e \left(\dot{\boldsymbol{\epsilon}} - \dot{\gamma} \frac{\partial f}{\partial \boldsymbol{\sigma}}\right) \qquad \boldsymbol{D}^e := \frac{\partial^2 \psi^e}{\partial \boldsymbol{\epsilon}^e \otimes \partial \boldsymbol{\epsilon}^e}(\boldsymbol{\epsilon}^e) \tag{50a}$$

$$\dot{\overline{\boldsymbol{\chi}}}_\alpha = -\boldsymbol{\Xi}\, \dot{\boldsymbol{\alpha}} = -\dot{\gamma}\, \boldsymbol{\Xi} \frac{\partial f}{\partial \overline{\boldsymbol{\chi}}_\alpha} \qquad \boldsymbol{\Xi} := \frac{\partial^2 \psi^p}{\partial \boldsymbol{\alpha} \otimes \partial \boldsymbol{\alpha}} \tag{50b}$$

which, inserted in eq. (49) provide the following expression for the plastic multiplier:

$$\dot{\gamma} = \frac{1}{K_p} \left\langle \frac{\partial f}{\partial \boldsymbol{\sigma}} \cdot \boldsymbol{D}^e \dot{\boldsymbol{\epsilon}} \right\rangle \tag{51}$$

where the McCauley brackets $\langle x \rangle := (x + |x|)/2$ are used to denote the positive part of their argument (as by definition the plastic multiplier cannot be negative) and the positive scalar K_p is given by:

$$K_p := \frac{\partial f}{\partial \boldsymbol{\sigma}} \cdot \boldsymbol{D}^e \frac{\partial f}{\partial \boldsymbol{\sigma}} + H_p > 0 \qquad H_p := \frac{\partial f}{\partial \overline{\boldsymbol{\chi}}_\alpha} \cdot \boldsymbol{\Xi} \frac{\partial f}{\partial \overline{\boldsymbol{\chi}}_\alpha} \tag{52}$$

in which H_p is known as the *plastic modulus*. A positive value of H_p denotes *hardening*, a negative value indicates *softening*, while $H_p = 0$ characterize the special case of *perfect plasticity*. As thoroughly discussed in, *e.g.*, [SH97, JB02], the constitutive assumption that $K_p > 0$ is crucial in the establishment of the correct formulation of the loading/unloading conditions in presence of softening. Its effect is essentially to place a restriction on the amount of allowable softening.

Substituting the expression (51) for the plastic multiplier in eqs. (50a) and (50b), we obtain the following constitutive equations and hardening laws in rate form:

$$\dot{\boldsymbol{\sigma}} = \boldsymbol{D}^{ep} \dot{\boldsymbol{\epsilon}} \qquad \dot{\overline{\boldsymbol{\chi}}}_\alpha = \boldsymbol{H}^p \dot{\boldsymbol{\epsilon}} \tag{53}$$

where:

$$\boldsymbol{D}^{ep} := \boldsymbol{D}^e - \frac{\mathcal{H}(\dot{\gamma})}{K_p} \left(\boldsymbol{D}^e \frac{\partial f}{\partial \boldsymbol{\sigma}}\right) \otimes \left(\frac{\partial f}{\partial \boldsymbol{\sigma}}\, \boldsymbol{D}^e\right) \tag{54a}$$

$$\boldsymbol{H}^p := \frac{\mathcal{H}(\dot{\gamma})}{K_p} \left(\boldsymbol{\Xi} \frac{\partial f}{\partial \overline{\boldsymbol{\chi}}_\alpha}\right) \otimes \left(\frac{\partial f}{\partial \boldsymbol{\sigma}} \boldsymbol{D}^e\right) \tag{54b}$$

where $\mathcal{H}(x)$ denotes the Heaviside step function, equal to one if $x > 0$ and zero otherwise.

The constitutive equations in rate–form given by eqs. (53) are incrementally bi–linear. In fact, according to the expression (51) for the plastic multiplier, the tangent stiffness $\boldsymbol{D}$ assumes two possible values depending on the direction of $\dot{\boldsymbol{\epsilon}}$:

$$\boldsymbol{D} = \begin{cases} \boldsymbol{D}^{ep} & \text{if} \quad (\partial f/\partial \boldsymbol{\sigma}) \cdot \boldsymbol{D}^e \dot{\boldsymbol{\epsilon}} > 0 \quad \text{(plastic loading conditions)} \\ \boldsymbol{D}^{e} & \text{if} \quad (\partial f/\partial \boldsymbol{\sigma}) \cdot \boldsymbol{D}^e \dot{\boldsymbol{\epsilon}} = 0 \quad \text{(neutral loading conditions)} \\ \boldsymbol{D}^{e} & \text{if} \quad (\partial f/\partial \boldsymbol{\sigma}) \cdot \boldsymbol{D}^e \dot{\boldsymbol{\epsilon}} < 0 \quad \text{(elastic unloading conditions)} \end{cases} \tag{55}$$

The continuity at the boundary between the two tensorial zones (the neutral loading conditions) is guaranteed by the fact that $\dot{\gamma} \to 0$ as the neutral loading condition is approached from the plastic loading zone.

7 Non–associative phenomenological plasticity

The evolution equations of the theory of hyperplasticity – eqs. (53) – are developed from the knowledge of the two scalar functions ψ (free energy function) and $\mathcal{D}$ (dissipation function), in such a way to guarantee the consistency with the second principle of thermodynamics. In this respect, the name hyperplasticity is adopted to distinguish it from classical phenomenological plasticity in the same way as hyperelasticity is distinguished from hypoelasticity based on the existence of a potential function.

Historically, however, the classical theory of rate–independent plasticity has been developed following a different strategy, in which the various elements of the theory are chosen ad–hoc, based on the available experimental evidence. This phenomenological approach has led to the most successful applications of plasticity to the modeling of the inelastic and history–dependent behavior of soils, and it is, by far, still the most widely used in soil mechanics.

The main assumption of the classical phenomenological theory of plasticity will be presented in the following, pointing out the main differences with hyperplasticity.

7.1 Basic assumptions and general formulation

Starting from the additive split of the strain rate into an elastic and a plasic part, eq. (29), the elastic strain rate is linked to the stress rate by assuming a hypoelastic constitutive equation:

$$\dot{\boldsymbol{\sigma}} = \boldsymbol{D}^e(\boldsymbol{\sigma})\,\dot{\boldsymbol{\epsilon}}^e = \boldsymbol{D}^e(\boldsymbol{\sigma})\,(\dot{\boldsymbol{\epsilon}} - \dot{\boldsymbol{\epsilon}}^p) \tag{56}$$

in which the elastic tangent stiffness tensor $\boldsymbol{D}^e$ generally depends on the current stress state.

Irreversibility is introduced by requiring that the state of the material $(\boldsymbol{\sigma}, \boldsymbol{q})$ belongs to the convex set:

$$\mathbb{E} := \Big\{ (\boldsymbol{\sigma}, \boldsymbol{q}) \;\Big|\; f(\boldsymbol{\sigma}, \boldsymbol{q}) \leq 0 \Big\} \tag{57}$$

defined in terms of a phenomenologically derived yield function f, depending on the current stress and on a set of internal variables $\boldsymbol{q}$ which account for the effects of the previous loading history.

The plastic strain rate is prescribed, as in hyperplasticity, by a suitable flow rule:

$$\dot{\boldsymbol{\epsilon}}^p = \dot{\gamma}\,\frac{\partial g}{\partial \boldsymbol{\sigma}}(\boldsymbol{\sigma}, \boldsymbol{q}) \tag{58}$$

in which $g(\boldsymbol{\sigma}, \boldsymbol{q})$ is a prescribed *plastic potential* function, chosen in order to match available experimental observations – *e.g.*, stress–dilatancy relations. In general, the plastic potential function is independent of the yield function f. When g and f do not coincide, the flow rule is said to be *non–associative*. Associative plastic flow is recovered when $g \equiv f$, as in eq. (47a).

The evolution of the internal variables is provided by assigning a suitable *hardening law*:

$$\dot{\boldsymbol{q}} = \dot{\gamma}\boldsymbol{h}(\boldsymbol{\sigma}, \boldsymbol{q}) \tag{59}$$

where $\boldsymbol{h}(\boldsymbol{\sigma}, \boldsymbol{q})$ is a prescribed hardening function. Although the structure of the hardening law (59) is similar to the hardening law of hyperplasticity – eq. (47b) – and allows changes in the internal variables to take place only during plastic loading processes (for which $\dot{\gamma} > 0$), eq. (59) is *non–associative*, in the sense that the hardening function $\boldsymbol{h}$ is not derived from $\partial f / \partial \boldsymbol{q}$.

Again, the yield function and the plastic multiplier are subjected to the Kuhn–Tucker complementarity conditions of eq. (48), stating that plastic deformations may occur only for states on the yield surface. The consistency condition for plastic loading processes ($\dot{f} = 0$) allows to derive the following expression for the plastic multiplier:

$$\dot{\gamma} = \frac{1}{K_p}\left\langle \frac{\partial f}{\partial \boldsymbol{\sigma}} \cdot \boldsymbol{D}^e \dot{\boldsymbol{\epsilon}} \right\rangle \tag{60}$$

formally identical to eq. (51) but in which:

$$K_p := \frac{\partial f}{\partial \boldsymbol{\sigma}} \cdot \boldsymbol{D}^e \frac{\partial g}{\partial \boldsymbol{\sigma}} + H_p > 0 \qquad\qquad H_p := -\frac{\partial f}{\partial \boldsymbol{q}} \cdot \boldsymbol{h} \tag{61}$$

Substituting eq. (60) in eqs. (56) and (59), we obtain:

$$\dot{\boldsymbol{\sigma}} = \boldsymbol{D}^{ep} \dot{\boldsymbol{\epsilon}} \qquad\qquad \dot{\boldsymbol{q}} = \boldsymbol{H}^p \dot{\boldsymbol{\epsilon}} \tag{62}$$

where:

$$\boldsymbol{D}^{ep} := \boldsymbol{D}^e - \frac{\mathcal{H}(\dot{\gamma})}{K_p}\left(\boldsymbol{D}^e \frac{\partial g}{\partial \boldsymbol{\sigma}}\right) \otimes \left(\frac{\partial f}{\partial \boldsymbol{\sigma}} \boldsymbol{D}^e\right) \tag{63a}$$

$$\boldsymbol{H}^p := \frac{\mathcal{H}(\dot{\gamma})}{K_p} \boldsymbol{h} \otimes \left(\frac{\partial f}{\partial \boldsymbol{\sigma}} \boldsymbol{D}^e\right) \tag{63b}$$

where K_p is provided by eq. (61).

For the developments of Sect. 8, it is useful to recast the evolution equations (58) and (62) in terms of the unit tensors:

$$\boldsymbol{n}_f := \left\| \frac{\partial f}{\partial \boldsymbol{\sigma}} \right\|^{-1} \frac{\partial f}{\partial \boldsymbol{\sigma}} \qquad\qquad \boldsymbol{n}_g := \left\| \frac{\partial g}{\partial \boldsymbol{\sigma}} \right\|^{-1} \frac{\partial g}{\partial \boldsymbol{\sigma}} \tag{64}$$

providing the *loading direction* and the *plastic flow direction*, respectively. The flow rule, hardening law, plastic multiplier and elastoplastic tangent stiffness then assume the following alternative expressions:

$$\dot{\boldsymbol{\epsilon}}^p = \dot{\lambda}\, \boldsymbol{n}_g \qquad\qquad \dot{\boldsymbol{q}} = \dot{\lambda} \hat{\boldsymbol{h}} \tag{65}$$

$$\dot{\lambda} = \frac{1}{\widehat{K}_p} \langle \boldsymbol{n}_f \cdot \boldsymbol{D}^e \dot{\boldsymbol{\epsilon}} \rangle = \left\| \frac{\partial g}{\partial \boldsymbol{\sigma}} \right\| \dot{\gamma} \tag{66}$$

$$\boldsymbol{D}^{ep} = \boldsymbol{D}^e - \frac{\mathcal{H}(\dot{\lambda})}{\widehat{K}_p} (\boldsymbol{D}^e\, \boldsymbol{n}_g) \otimes (\boldsymbol{n}_f\, \boldsymbol{D}^e) \tag{67}$$

where:

$$\widehat{K}_p := \boldsymbol{n}_f \cdot \boldsymbol{D}^e \boldsymbol{n}_g + \widehat{H}_p \qquad\qquad \widehat{H}_p := \left(\left\| \frac{\partial f}{\partial \boldsymbol{\sigma}} \right\| \left\| \frac{\partial g}{\partial \boldsymbol{\sigma}} \right\| \right)^{-1} H_p \tag{68}$$

are the corresponding plastic moduli.

7.2 Perfect plasticity

The particular case in which the set of state variables contains the Cauchy stress only (*i.e.*, $\boldsymbol{q} = \boldsymbol{0}$) is known as *perfect plasticity*. In perfect plasticity the yield function and the plastic potential are given functions of the stress tensor $\boldsymbol{\sigma}$ only. The constitutive equations for perfect plasticity are recovered from eqs. $(62)_1$ and (63a), setting $H_p = 0$ in eq. (61). Due to this specific feature, in perfect plasticity yielding along a predefined stress path occurs at constant stress and constant plastic strain rate:

$$\dot{\boldsymbol{\sigma}} = \boldsymbol{0} \qquad\qquad \dot{\boldsymbol{\epsilon}}^e = \boldsymbol{0} \qquad\qquad \dot{\boldsymbol{\epsilon}}^p = \text{const.}$$

i.e., yield states are also *failure states*.

The early applications of perfect plasticity to soil mechanics can be traced back to the various solutions of failure problems for foundations, retaining walls, or slopes obtained through the method of characteristics (slip line theory) [Sok65], or the application of the upper and lower bound theorems of limit analysis [Che76]. In both these approaches, the soil is modelled as a rigid–perfectly plastic medium, with a failure condition provided, *e.g.*, by the so–called *Mohr–Coulomb* yield function:

$$f(\boldsymbol{\sigma}) = (\sigma_1 - \sigma_3) - 2c\cos\phi - (\sigma_1 + \sigma_3)\sin\phi = 0 \tag{69}$$

where σ_1 and σ_3 are the maximum and minimum principal stresses, and c and ϕ are two material constants defining the *cohesion* and the *friction angle* of the soil, respectively.

In these applications, the emphasis was placed in the determination of the stress field in limit conditions, in order to evaluate the stability of the system with respect to a particular collapse mechanism. The success of this simple and elegant approach to failure problems is witnessed by the fact that most of the design methods currently in use for geotechnical structures are still based on such limit solutions, and specific numerical techniques have been developed to extend limit analysis to those cases for which no sufficiently accurate analytic solution can be found, see, *e.g.*, [SK95, PBZL97, LS02].

Extension of the above concepts to the analysis of more complex deformation problems, such as soil–structure interaction or the modelling of the transition from the small–strain regime up to failure conditions, had to wait until the pioneering application of the finite element method to soil mechanics. Examples of the use of elastic–perfectly plastic models with pressure–dependent yield functions such as those of Mohr–Coulomb and Drucker–Prager models, are given, *e.g.*, in [ZH77, SD83] for shallow foundations, [ZHL75] for slopes, [SH92, SGvW95] for flexible retaining structures, and [RK83, WK91] for tunnels.

7.3 Isotropic hardening plasticity

The experience gathered in using classical perfect plasticity in the analysis of deformation problems has shown how these formulations provide a too crude description of the actual behavior of natural soils in pre–failure conditions. A radical change of perspective in soil plasticity occurred after the pioneering work of Roscoe and coworkers in Cambridge, which lead, in the sixties, to the basic principles of the so–called "Critical State Soil Mechanics" (CSSM) [RB68, SW68]. The practical use of CSSM in geotechnical applications started in the early seventies, when CSSM was interpreted as a particular application of isotropic hardening plasticity, see *e.g.*, [ZN71], and generalized to full six–dimensional stress and strain states. The road was then open to a new approach to geotechnical engineering practice, in which no such distinction between failure and deformation problems, or elastic response and plastic collapse was needed any longer.

Isotropic hardening plasticity is obtained from the general formulation of Sect. 7.1 when all the elements of the pseudo–vector $\boldsymbol{q}$ collecting the internal variables are *scalar quantities*, and, as such do not provide any information about the orientation of the microstructure.

The prototype of isotropic hardening elastoplastic models for cohesive soils is the so–called "Modified Cam–Clay" (MCC) [RB68], which assumes an associative flow rule. The yield surface adopted in the original MCC model is given by:

$$f(p, q, p_s) = p(p - p_s) + \frac{q^2}{M^2} = 0 \tag{70}$$

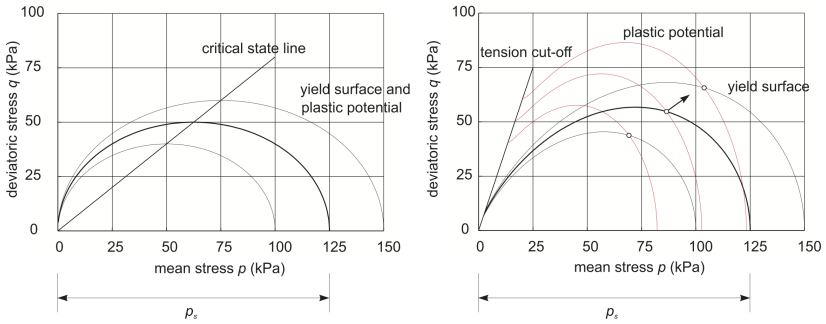

Figure 1: Yield surfaces and plastic potentials for isotropic hardening elastoplastic models: a) Modified Cam–Clay [RB68]; b) Sinfonietta Classica [Nov88].

In the q:p stress invariant space, it has the shape of an ellipse passing through the origin, with its principal axes parallel to the coordinate axes. The scalar quantity p_s (*preconsolidation pressure*) controls the size of the yield surface, and represents the only internal state variable of the material. For any possible value of p_s, eq. (70) describes a family of such ellipses, see fig. 1a. In eq. (70) M is a material constant defining the aspect ratio of the ellipse.

The evolution equation for the preconsolidation pressure is provided by an empirically derived logarithmic law of the type[1]:

$$\dot{p}_s = \rho_s \, p_s \, \dot{\epsilon}_v^p \tag{71}$$

with $\rho_s = \text{const}$. The hardening law provided by eq. (71) is purely volumetric, *i.e.*, p_s may change only when plastic volumetric strains occur. Positive (contractant) plastic volumetric strains cause an increase in p_s (expansion of the elastic domain), while negative (dilatant) plastic volumetric strains induce a reduction of p_s and the shrinkage of the elastic domain.

In the notation of eqs. (59) and $(61)_2$:

$$\dot{p}_s = \dot{\gamma} \, h_s(p, q, p_s) \qquad h_s := \rho_s \, p_s \, \frac{\partial f}{\partial p} \qquad H_p = -\rho_s \, p_s \, \frac{\partial f}{\partial p} \, \frac{\partial f}{\partial p_s} \tag{72}$$

From eq. (72) it is clear that the "failure" conditions for the material (which occur when $p_s = \text{const.}$ and $H_p = 0$) are characterized by purely distortional plastic strain rates, *i.e.*, the material can be deformed indefinitely at *constant stress and constant volume*. Such particular failure states, the existence of which is experimentally observed in both fine– and coarse–grained soils, are defined *critical states*, and form the basis of almost all subsequent modern treatments of hardening plasticity for soils.

[1]Note that, to avoid using too many different symbols, the notations employed in this work can sometimes be different from the one adopted in the original works cited.

Modifications of MCC to improve its predictive capabilities have been discussed by numerous authors. Among them, we recall the extension of the yield function (70) to include the third stress invariant θ [ZN73], the adoption of a composite yield surface to include the so called *Hvorslev surface* for yield points on the "supercritical side" of the critical state line [ZN73, HWW84], and the adoption of a hyperelastic constitutive equation [Hou85, BTA97]. The isotropic hardening models known in the literature as *cap models* [DMS71, SDMB76] can be considered essentially as Critical State models with a modified supercritical yield function, the position of which, however, does not change with plastic strains.

In the application of the concepts of isotropic hardening plasticity to coarse–grained soils, two major limitations of classical critical state models have been pointed out. First, the assumption of an associated flow rule is generally not supported by available experimental data on sand dilatancy, see *e.g.*, [PHS66, PHS67]. In addition, the modeling of *static liquefaction* in the *hardening regime*, observed in loose sands under undrained conditions is not possible adopting an associative flow rule [Nov96]. Second, the hypothesis of purely volumetric hardening does not allow to describe the so–called *phase transition* effect – *i.e.*, the transition from contractant to dilatant behavior – typically observed in dense sand under undrained compression.

Non–associative isotropic hardening models for sands have been proposed since the pioneering work of Pooroshasb *et al.* [PHS66, PHS67], who coupled a Cam–Clay type plastic potential with a classical Mohr–Coulomb yield locus. Subsequent improvements were proposed, *e.g.*, by Nova & Wood [NW79] and Kim & Lade [KL88, LK88]. As for the hardening function, Nova [Nov77] and Wilde [Wil77] independently proposed an extension of the volumetric hardening rule (71) which incorporates the effect of deviatoric plastic strain rate:

$$\dot{p}_s = \rho_s \, p_s \, \{\dot{\epsilon}_v^p + \xi_s \dot{\epsilon}_s^p\} \qquad H_p := -\rho_s \, p_s \left\{ \frac{\partial g}{\partial p} + \xi_s \, \frac{\partial g}{\partial q} \right\} \frac{\partial f}{\partial p_s} \tag{73}$$

The scalar quantity ξ_s appearing in eq. (73) can be considered either a constant, as in [Nov77], or a monotonically decreasing function of the accumulated plastic deviatoric strains, as in [Wil77]. In this last case, a critical state is recovered in the ultimate conditions at very large plastic strains.

An example of isotropic hardening models for sands – which combines good predictive capabilities for monotonic loading with a limited number of material constants easily linked to observed material behavior in standard tests – is provided by the model proposed by Nova under the name *Sinfonietta Classica* [Nov88]. For this model, the adopted yield function and plastic potential are given by the following equations:

$$f(p, \boldsymbol{r}, p_s) = 3\beta \, (\gamma - 3) \, \ln\left(\frac{p}{p_s}\right) - \gamma \, \mathrm{tr}\left(\boldsymbol{r}^3\right) + \frac{9}{4} \, (\gamma - 1) \, \mathrm{tr}\left(\boldsymbol{r}^2\right) = 0 \tag{74}$$

$$g(p, \boldsymbol{r}, p_s^*) = 9 \, (\gamma - 3) \, \ln\left(\frac{p}{p_s^*}\right) - \gamma \, \mathrm{tr}\left(\boldsymbol{r}^3\right) + \frac{9}{4} \, (\gamma - 1) \, \mathrm{tr}\left(\boldsymbol{r}^2\right) = 0 \tag{75}$$

where $\boldsymbol{r} := \boldsymbol{s}/p$ is the stress–ratio tensor while β and γ are material parameters ($\beta \neq 3$ denotes non–associative behavior). The corresponding surfaces in the $q : p$ plane are shown in Fig. 1b. An hardening law with volumetric and deviatoric hardening similar to eq. (73) is assumed for the internal variable p_s, which controls the size of the yield surface.

Subsequent developments gave rise to a number of constitutive models which progressively diverged from the basic assumptions of CSSM in the attempt of covering further aspects of experimentally observed soil behavior, as well as to tackle other, more challenging classes of engineering problems. The breath and depth of such scientific production is well portrayed, for example, by the proceedings of the workshops held in Grenoble in 1982 [GDV84], Cleveland in 1988 [SB89], and Horton in 1992 [Kol93]. Another useful source of references is provided by the special volume published on the occasion of the XI ICSMFE [Mur85].

7.4 Anisotropic hardening plasticity

Almost all geotechnical materials such as rocks, coarse–grained soils and fine–grained soils are characterized – to a certain extent – by the existence of some preferential orientations at the microstructural level. In granular soils such preferential orientations can be associated to the spatial distributions of the contact normals, to grain shape and to void shape, see [ONNK85]. Moreover, the directional properties of the microstructure might remain more or less stable during the deformation of the solid skeleton (as, *e.g.*, the distribution of grain orientations in the tests performed by Oda *et al.* [ONNK85]), or they might evolve as a consequence of grain rearrangements upon applied loading (as, *e.g.*, the distribution of contact normals [ONNK85]). From this observations, it follows naturally that the macroscopic response of the material – reflecting the properties of the microstructure – can be characterized by a more or less marked *anisotropy*, both in terms of stress–strain response in pre–failure conditions, and in terms of shear strength.

According to the possibility that superimposed loading histories may change the directional properties of the microstructure, two different kind of anisotropy can be distinguished at the macroscopic level, see [CC44]:

- *inherent anisotropy*, "[...] a physical characteristics inherent in the material and entirely independent of the applied strains";
- *induced anisotropy*, "[...] a physical characteristic due exclusively to the strain associated with the applied stress".

Inherent anisotropy is usually relevant in hard, heavily overconsolidated soils and stratified rocks, where strong intergranular bonds prevent the occurrence of significant rearrangements of the microstructure, or in coarse–grained soils with strongly non–circular particles, the orientation of which cannot be modified easily unless a substantial amount of grain crushing occurs. On the contrary, induced anisotropy plays a major role in non–cemented granular soils with rounded particles, or in clays

where the applied loading can modify and, in some cases, even erase the effects of the previous loading history. Direct and indirect experimental evidence of inherent and induced anisotropy is reported, *e.g.*, in [ABS77] for soft rocks, in [OKH78, WA85, YMH91, YIV98] for sands, and in [DS66, Mit70, TL77, GNL83, SJH92] for clays.

In the framework of the classical theory of plasticity, inherent anisotropy can be dealt with in the formulation of the elastic constitutive equation – as in, *e.g.*, [Boe75, GH83] – and/or in the definition of yield and plastic potential functions. Constitutive equations for inherent anisotropy have been proposed, *e.g.*, by Nova [Nov86], Pastor [Pas91] and Semnani *et al.* [SWB16], based on a approach first suggested by Hill [Hil50]. Essentially, these models are derived from existing isotropic hardening formulations by replacing the standard invariants of the stress tensor with corresponding anisotropic invariants defined by means of suitably chosen (constant) *structure tensors*, which are employed as metric tensors in the construction of the scalar invariants entering in the constitutive functions. An alternative strategy to incorporate inherent anisotropy, based on the use of a microstructure tensor in the definition of the yield surface, has been proposed in [PM00, PLS02, OKKA02].

The description of induced anisotropy – *i.e.*, the evolution of the directional properties of the material with the loading history – requires the set of internal state variables $\boldsymbol{q}$ to include at least one tensor–valued quantity. In most of the existing anisotropic hardening plasticity models, this is usually assumed to be a symmetric second–order tensor, with the character of a *microstructure tensor*. Although this limits the degree of symmetry of the material to *orthotropy*, see [Boe87], it is considered sufficient for most geomaterials of relevant practical interest.

In presence of a symmetric second–order microstructure tensor among the internal variables, the general restrictions imposed to the yield and plastic potential functions by the principle of material frame indifference, as well as the consequences of induced anisotropy on the relative orientation between the principal directions of the stress and the plastic strain tensors are discussed in detail in [BD84]. Plasticity models with anisotropic hardening can be broadly grouped into two different classes, according to the experimental evidence which they were intended to reproduce, namely:

a) constitutive models with *kinematic hardening*, capable of modelling soil behavior under cyclic loading paths, see, *e.g.*, [Woo82] and references therein;

b) constitutive models with *rotational hardening*, which are capable of describing the changes in the orientation of the yield surface with the evolution of plastic strains, as observed, *e.g.*, in [YMH91, TL77, GNL83, SJH92].

Kinematic hardening models for soils originate from the pioneering work of Mroz [Mro67], Iwan [Iwa67], and Dafalias & Popov [DP75]. In such models, a yield function of the form:

$$f(\boldsymbol{\sigma}, \boldsymbol{\alpha}, q_k) = \hat{f}(\hat{\boldsymbol{\sigma}}, q_k) = 0 \qquad\qquad \hat{\boldsymbol{\sigma}} := \boldsymbol{\sigma} - \boldsymbol{\alpha} \tag{76}$$

is assumed, in which the so–called *back–stress* $\boldsymbol{\alpha}$ is the microstructure tensor, responsible for the induced anisotropy, and the scalars q_k ($k = 1, \ldots, n$) denote the

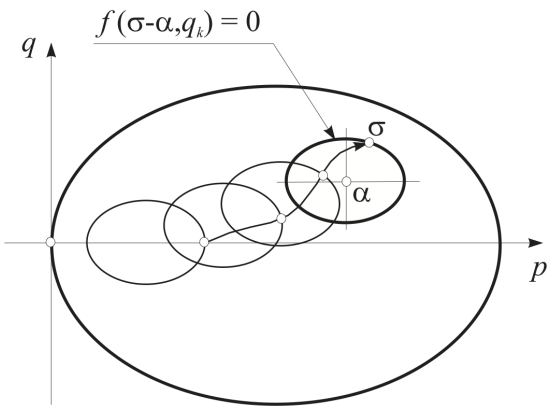

Figure 2: Kinematic hardening inside the Bounding Surface.

other internal variables. As $\boldsymbol{\alpha}$ changes during the loading process, the yield surface is dragged by the stress–path as indicated qualitatively in Fig. 2. The motion of the yield surface in stress space is typically restricted by a larger, outer surface, referred to as *Bounding Surface* (BS), of equation:

$$F(\boldsymbol{\sigma}, \overline{q}_k) = 0 \qquad\qquad \{\overline{q}_k\} \subset \{q_k\} \tag{77}$$

In classical anisotropic plasticity, the BS – generally similar in shape to the yield surface – provides a limit to the possible evolution of the back–stress $\boldsymbol{\alpha}$. Models of this kind have been proposed by various authors. Among them we recall the works of Prevost [Pre77, Pre86], Mroz *et al.* [MNZ78, MNZ81], Hashiguchi [Has85, Has88], Wood and coworkers [ATW89, GW99, RW00] and Stallebrass and Taylor [ST97].

Most of these works represent a straightforward extension of classical Modified Cam–Clay, see Sect. 7.3. As an example, in the model of Al–Tabbaa & Wood [ATW89], the yield and Bounding Surface functions are given by:

$$F(\boldsymbol{\sigma}, p_c) = \frac{3}{2M_\theta}\, \boldsymbol{s} \cdot \boldsymbol{s} + (p - p_c)^2 - p_c^2 = 0 \tag{78}$$

$$f(\boldsymbol{\sigma}, p_c) = \frac{3}{2M_\theta}\, (\boldsymbol{s} - \operatorname{dev} \boldsymbol{\alpha}) \cdot (\boldsymbol{s} - \operatorname{dev} \boldsymbol{\alpha}) + (p - p_\alpha)^2 - R^2 p_c^2 = 0 \tag{79}$$

where $p_c = p_s/2$, $p_\alpha = \operatorname{tr} \boldsymbol{\alpha}/3$ and $R \ll 1$ is a material constant representing the ratio between the sizes of the two surfaces.

In this class of models, the hardening function adopted for p_c (or p_s) is similar to the one adopted in critical state models, see eq. (71). As for the tensor $\boldsymbol{\alpha}$, rather than prescribing explicitly the hardening function, the hardening modulus H_p is assigned as a monotonically decreasing function of the distance δ between the current state and a *image state* $\overline{\boldsymbol{\sigma}}$ on the BS, defined as the point at which the unit normals to $f = 0$ and

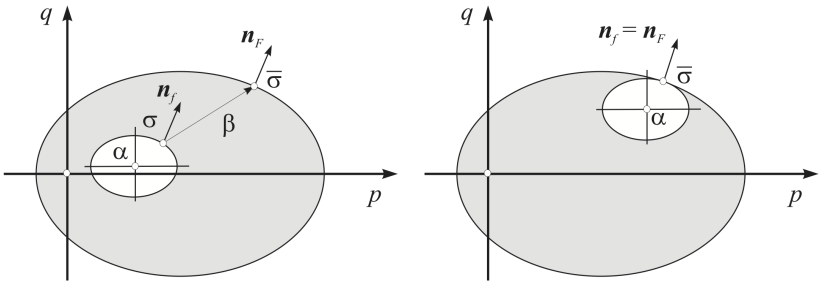

Figure 3: Kinematic hardening models: definition of the image point.

$F = 0$ have the same direction (see Fig. 3a):

$$H_p = \widehat{H}\left(\overline{H}_p, \delta\right) \qquad \frac{\partial \widehat{H}}{\partial \delta} > 0 \qquad \widehat{H}\left(\overline{H}_p, 0\right) = \overline{H}_p \tag{80}$$

In eq. (80), $\delta := \|\overline{\boldsymbol{\sigma}} - \boldsymbol{\sigma}\|$ and $\overline{H}_p$ is the plastic modulus at $\overline{\boldsymbol{\sigma}}$:

$$\overline{H}_p := -\frac{\partial F}{\partial p_c}\, h_c \tag{81}$$

obtained from the consistency condition on the BS:

$$\dot{F}(\overline{\boldsymbol{\sigma}}, \overline{q}_k) = 0$$

When the stress–path touches the BS, the two surfaces must share the same tangent, otherwise some admissible states would fall *outside* the BS, see Fig. 3b. As shown by Hashiguchi [Has85], this is obtained through an appropriate definition of the evolution equation for $\boldsymbol{\alpha}$. For the Al–Tabbaa & Wood model [ATW89], the non–intersection condition requires that:

$$\dot{\boldsymbol{\alpha}} = \dot{\overline{\boldsymbol{\alpha}}} + (\boldsymbol{\alpha} - \overline{\boldsymbol{\alpha}})\, \frac{\dot{p}_c}{p_c} + \frac{\boldsymbol{n} \cdot \left[\dot{\overline{\boldsymbol{\sigma}}} - (\dot{p}_c/p_c)\, \overline{\boldsymbol{\sigma}}\right]}{\boldsymbol{n} \cdot (\overline{\boldsymbol{\sigma}} - \boldsymbol{\sigma})}\, (\overline{\boldsymbol{\sigma}} - \boldsymbol{\sigma}) \tag{82}$$

In eq. (82), the first term is related to the translation of the center of the BS, the second represents the effect of the change in size of the BS (and of the yield surface), and the third a net translation in the direction of the tensor $\boldsymbol{\beta} := \overline{\boldsymbol{\sigma}} - \boldsymbol{\sigma}$, see Fig. 3a.

Anisotropic plasticity models with rotational hardening are more suitable for describing the anisotropy induced by loading histories associated to depositional processes in natural deposits, such as one–dimensional compression and, possibly, swelling. These models can be traced back to the pioneering works of Sekiguchi & Ohta [SO77] for clays, or Ghaboussi & Momen [GM82] for sands. Constitutive equations of this kind

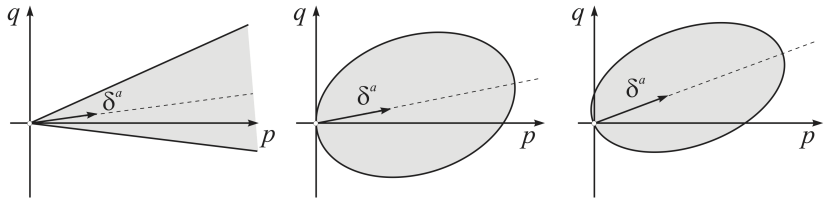

Figure 4: Typical yield surfaces adopted in rotational hardening models.

proposed for sands are usually intended to model irreversible processes associated with deviatoric loading paths, and therefore adopt conical–shaped yield surfaces, *open* towards the range of high mean pressures (fig. 4a). Among them, we recall the models proposed in refs. [GM82, PP85, MD97, GW99, DM04, TD08].

Rotational hardening models for fine–grained soils, on the contrary, adopt *closed* yield surfaces (fig. 4b,c), in order to reproduce the irreversible deformations usually observed in these materials along isotropic or proportional loading paths ($q/p = \text{const.}$). Examples of rotational hardening models for clays are given in the works of [Has79, BY86, AD86, WNKL03, DMP06, TDP10].

Exceptions to this general trend are provided, for example, by the models of di Prisco *et al.* [dPNL93] – actually a generalization of the Sinfonietta Classica model discussed in the previous section – and Pestana & Whittle [PW99], which can be employed for coarse as well as fine–grained materials. It is worth noting that in most of the aforementioned models, the rotational anisotropy is employed in connection to some form of generalized plasticity allowing plastic flow inside the main state boundary surface, which will be discussed in Sect. 8.

Rotational hardening models can be easily derived as generalizations of classical isotropic hardening formulations (*e.g.*, Modified Cam–Clay) by simply replacing the stress invariants entering in the yield and plastic potential functions with appropriate *mixed invariants* which take into due account the microstructure tensor. Possible ways of defining such mixed invariants are provided, for example, by Anandarajah and Dafalias [AD86] (slightly modified):

$$p^a := \frac{1}{3}\,\boldsymbol{\sigma}\cdot\boldsymbol{\delta}^a \qquad q^a := \sqrt{\frac{3}{2}}\,\|\boldsymbol{s}^a\| \qquad \sin(3\theta^a) := \sqrt{6}\frac{(\boldsymbol{d}^a)^3\cdot\mathbf{1}}{[(\boldsymbol{d}^a)^2\cdot\mathbf{1}]^{3/2}} \tag{83}$$

where $\boldsymbol{\delta}^a$ is the microstructure tensor, and:

$$\boldsymbol{s}^a := \boldsymbol{\sigma} - p^a\,\boldsymbol{\delta}^a \qquad \boldsymbol{d}^a := \operatorname{dev}(\boldsymbol{s}^a) \qquad \boldsymbol{\delta}^a\cdot\boldsymbol{\delta}^a = 3 \tag{84}$$

or by Wheeler *et al.* [WNKL03]:

$$p^a := \frac{1}{3}\,\boldsymbol{\sigma}\cdot\mathbf{1} = p \qquad q^a := \sqrt{\frac{3}{2}}\,\|\boldsymbol{s}^a\| \qquad \sin(3\theta^a) := \sqrt{6}\frac{(\boldsymbol{s}^a)^3\cdot\mathbf{1}}{[(\boldsymbol{s}^a)^2\cdot\mathbf{1}]^{3/2}} \tag{85}$$

where $\boldsymbol{\delta}^a$ is a purely deviatoric microstructure tensor, and:

$$\boldsymbol{s}^a := \boldsymbol{s} - p\,\boldsymbol{\delta}^a \qquad \boldsymbol{s} := \mathrm{dev}\,(\boldsymbol{\sigma}) \qquad \boldsymbol{\delta}^a \cdot \mathbf{1} = 0 \tag{86}$$

In eqs. (83) and (84), the projection of $\boldsymbol{\sigma}$ on the isotropic axis, commonly used to construct the isotropic and deviatoric invariants of the stress tensor, are replaced by the corresponding projection on the microstructure tensor $\boldsymbol{\delta}^a$, now playing the role of the unit tensor – compare eqs. (83) with eqs. (2) – and, in fact, defining the rotation of the surface with respect to the isotropic axis, see fig. 4c.

In eqs. (85) and (86) the yield surface is distorted in the direction of the deviatoric axis, rather than rotated around the origin of the stress space. This effect is obtained by shifting the deviatoric stress by a quantity proportional to the deviatoric microstructure tensor and the current mean stress, see fig. 4b.

Several alternative strategies have been proposed to link the evolution of the microstructure tensor (*i.e.*, the rotation of the yield surface) with the plastic strain rate. All of them must, however, satisfy the orthogonality condition $\dot{\boldsymbol{\delta}}^a \cdot \boldsymbol{\delta}^a = 0$, required by the assumption $(84)_3$, or the requirement set by eq. $(86)_3$. A thorough discussion on the different rotational hardening mechanisms adopted for fine–grained soils has been presented by Dafalias and Taiebat [DT13].

8 Bounding Surface models and generalized plasticity

An important limitation of classical elastoplasticity as applied to geomaterials is represented by the assumption of a large elastic domain, inside which the response of the material is purely reversible. In light of the concepts introduced in Sects. 6 and 7, classical elastoplasticity is characterized by an incrementally bi–linear constitutive equation *only* for states *on the yield surface*. All elastic states are, by definition, endowed with an incrementally linear response. However, a large body of experimental evidence suggests that soil behavior can be irreversible and path–dependent *even for strongly preloaded states*, and that plastic yielding is a rather gradual process. Although such effects can be considered of secondary importance in the simulation of monotonic loading paths, it must be noted that a strong dependence of the small–strain stiffness on the loading path direction has been observed, *e.g.*, by [ARS86, Sta90] in heavily overconsolidated soils, and that such a feature of soil behavior – which cannot be reproduced by any incrementally linear model – can be of great importance in all practical applications in which strong variations of the stress–path direction are expected in different zones of the soil mass, *e.g.*, in the analysis of excavations. Moreover, irreversible (plastic) strains occurring well inside the locus of admissible stress states are obviously of great importance in cyclic loading processes, and the accurate description of such phenomena as cyclic mobility or liquefaction under repeated loading (see, *e.g.*, [Woo82]) requires to take them into proper account.

The kinematic hardening models discussed in the previous section – mostly developed during the early ‘80, in response to the problems posed by the design of structures such

as offshore platforms, or by the quantitative prediction of soil response during earthquakes – are certainly capable to deal successfully with this particular issue. However, a number of alternative strategies have also been proposed for the same purpose, which represent genuine generalizations of the classical framework. Among them, definitely worth of mention are the so–called *Bounding Surface models*, originally developed by Dafalias and coworkers, and the models developed in the framework of *Generalized Plasticity*, as defined by Pastor et al. [PZC90].

The key concept in the formulation of a Bounding Surface model is the fact that, as in kinematic hardening elastoplastic models mentioned before, there exists a surface in stress space – the Bounding Surface (BS), defined by an equation similar to eq. (77) – which separates admissible from impossible states. Such a surface is subjected to hardening processes which may change its size, shape and orientation due to the development of plastic strains, exactly as a standard yield surface in classical plasticity. However, such a surface is *not* a yield surface, as plastic strains can occur for stress states located in its interior. In particular, at each admissible state (inside or on the BS), a flow rule identical to eq. $(65)_1$ is assumed, in which the plastic multiplier $\dot{\lambda}$ is replaced by:

$$\dot{\lambda} = \frac{1}{\widetilde{K}_p} \, \langle \boldsymbol{n}_L \cdot \boldsymbol{D}^e \dot{\boldsymbol{\epsilon}} \rangle \tag{87}$$

where:

$$\widetilde{K}_p := \boldsymbol{n}_L \cdot \boldsymbol{D}^e \boldsymbol{n}_g + \widetilde{H}_p \tag{88}$$

in which $\boldsymbol{n}_L$ is a unit tensor defining the loading direction, and $\widetilde{H}_p$, by analogy with the standard formulation, plays the role of the plastic modulus. The definition of these last two quantites relies crucially on the possibility of associating to each stress state $\boldsymbol{\sigma}$ inside the BS a corresponding *image state* $\overline{\boldsymbol{\sigma}}$ on the BS, through a non–invertible *mapping rule*.

In the so–called *radial mapping* BS models, see [Daf86], this is accomplished by simply projecting the current stress onto the BS from a given *projection center* $\boldsymbol{\alpha}$, see Fig. 5. Once the image state is found, the loading direction is taken as the gradient of the BS at $\overline{\boldsymbol{\sigma}}$, while the plastic modulus $\widetilde{H}_p$ is assumed to be a monotonically decreasing function of the distance $\delta := \|\overline{\boldsymbol{\sigma}} - \boldsymbol{\sigma}\|$ between the current state and the image state, and of the plastic modulus $\overline{H}_p$ at $\overline{\boldsymbol{\sigma}}$:

$$\widetilde{H}_p = \widetilde{H}\left(\overline{H}_p, \delta\right) \qquad \frac{\partial \widetilde{H}}{\partial \delta} > 0 \qquad \widetilde{H}\left(\overline{H}_p, 0\right) = \overline{H}_p \tag{89}$$

The stress–strain relation in rate form is then given by an equation similar to eq. $(62)_1$, with the tangent stiffness $\boldsymbol{D}^{ep}$ provided by eq. (67), the plastic multiplier $\dot{\lambda}$ provided by eq. (66) and $\widehat{K}_p$ replaced by $\widetilde{K}_p$ of eq. (89). The analogies existing between this procedure for defining the loading direction and the plastic modulus and the one outlined for kinematic hardening models in Sect. 7.4 are apparent. As a matter of fact, Dafalias [Daf86] considered kinematic hardening models as a special class of BS models, characterized by a special form of mapping rule.

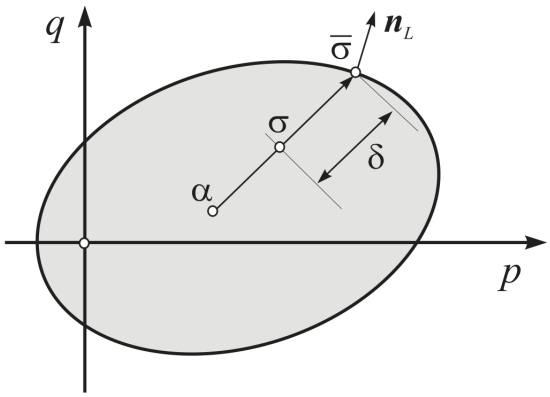

Figure 5: Radial mapping rule in Bounding Surface models.

However, differently than in kinematic hardening plasticity, in radial mapping BS models, no elastic region exists anymore, and the material features an incrementally bi–linear response at *any* state. A comprehensive review of the Bounding Surface concept is provided by Dafalias [Daf86]. Applications of the Bounding Surface Concept to the modelling of clays are reported, *e.g.*, in [ZLP85, DH86, AD86, WK94, LYKT02, DMP06, TDP10], while applications to coarse–grained soils are given, *e.g.*, by [PZL85, Bar86, Cw94, MD97, DM04, TD08].

Starting from the works of Zienkiewicz & Mroz [ZM84], Pastor *et al.* [PZC90] developed the framework of *Generalized Plasticity* as a further generalization of the Bounding Surface concept, where the concepts of plastic potential, yield function and consistency condition are completely abandoned. In the incrementally bi–linear version of the theory, the plastic strain rate is provided by the following equations:

$$\dot{\boldsymbol{\epsilon}}^p = \dot{\lambda}_L \, \boldsymbol{n}_{gL} \qquad \text{if :} \quad \boldsymbol{n}_L \cdot \boldsymbol{D}^e \dot{\boldsymbol{\epsilon}} > 0 \quad \text{(loading)} \tag{90}$$

$$\dot{\boldsymbol{\epsilon}}^p = \dot{\lambda}_U \, \boldsymbol{n}_{gU} \qquad \text{if :} \quad \boldsymbol{n}_L \cdot \boldsymbol{D}^e \dot{\boldsymbol{\epsilon}} < 0 \quad \text{(unloading)} \tag{91}$$

$$\dot{\boldsymbol{\epsilon}}^p = \boldsymbol{0} \qquad \text{if :} \quad \boldsymbol{n}_L \cdot \boldsymbol{D}^e \dot{\boldsymbol{\epsilon}} = 0 \quad \text{(neutral loading)} \tag{92}$$

in which:

$$\dot{\lambda}_L = \frac{1}{\widehat{K}_{p,L}} \, \boldsymbol{n}_L \cdot \boldsymbol{D}^e \dot{\boldsymbol{\epsilon}} \qquad \widehat{K}_{pL} := \boldsymbol{n}_L \cdot \boldsymbol{D}^e \boldsymbol{n}_{gL} + \widehat{H}_{p,L} \tag{93}$$

$$\dot{\lambda}_U = \frac{1}{\widehat{K}_{p,U}} \, \boldsymbol{n}_L \cdot \boldsymbol{D}^e \dot{\boldsymbol{\epsilon}} \qquad \widehat{K}_{pU} := \boldsymbol{n}_L \cdot \boldsymbol{D}^e \boldsymbol{n}_{gU} + \widehat{H}_{p,U} \tag{94}$$

In eqs. (90)–(94), $\boldsymbol{n}_L$, $\boldsymbol{n}_{gL}$ and $\boldsymbol{n}_{gU}$ are three second–order unit tensors representing the loading direction, the plastic flow direction for plastic loading and the plastic flow direction for plastic unloading (*reverse loading*), respectively, while the scalars $\widehat{H}_{p,L}$ and $\widehat{H}_{p,U}$ are the corresponding plastic moduli for (plastic) loading and unloading. All

these quantities are considered as prescribed functions of the state variables $(\boldsymbol{\sigma}, \boldsymbol{q})$, and, in general, their definition do not require any yield function, plastic potential or consistency condition to be assumed.

The corresponding expressions for the elastoplastic tangent stiffness tensor are given by:

$$\boldsymbol{D}^{ep} = \begin{cases} \boldsymbol{D}^e - (1/\widehat{K}_{p,L})\ (\boldsymbol{D}^e\,\boldsymbol{n}_{gL}) \otimes (\boldsymbol{n}_L\,\boldsymbol{D}^e) & \text{(plastic loading)} \\ \boldsymbol{D}^e - (1/\widehat{K}_{p,U})\ (\boldsymbol{D}^e\,\boldsymbol{n}_{gU}) \otimes (\boldsymbol{n}_L\,\boldsymbol{D}^e) & \text{(plastic unloading)} \end{cases} \tag{95}$$

It is worth noting that both classical plasticity and Bounding Surface plasticity are recovered from generalized plasticity as special cases, with suitable choices for the constitutive functions $\boldsymbol{n}_L$, $\boldsymbol{n}_{gL}$, $\boldsymbol{n}_{gU}$, $\widehat{H}_{p,L}$ and $\widehat{H}_{p,U}$, see [PZC90] for further details.

9 Plasticity with generalized hardening

A last, notable case of incrementally bilinear formulations is provided by the theory of plasticity with generalized hardening – as defined by Tamagnini and Ciantia [TC16] – proposed in the geomechanics context to describe a number of practically relevant aspects of the mechanical behavior of geomaterials. A common, distinctive feature of those constitutive theories is that the size and shape of the yield locus, as well as its evolution with the loading process are assumed to depend, in addition to accumulated plastic strains, on some other non–mechanical state variables, usually of scalar nature. Among them, we recall:

- the thermoplastic models proposed by Nova [Nov86] or Laloui and Cekerevac [LC08] to describe the influence of temperature on the brittle–ductile transition of rocks in geophysical applications, in which the preconsolidation pressure depend on the temperature T;
- the elastoplastic models for unsaturated soil (formulated in terms of Bishop effective stresses) in which an explicit dependence of the size of the yield surface on the degree of saturation is assumed to simulate the phenomenon of collapse upon wetting for partially saturated soil, see, *e.g.*, [Jom00];
- the extension of classical elastoplasticity advocated by [Nov00] to describe the effects of weathering on cemented soils or weak rocks, in which some bonding–related internal variables are subject to both mechanical and chemical degradation, described through a normalized, scalar weathering function X_d, see [TCN02, NCT03].

These approaches share also some similarities with a number of viscoplastic models based on the concept of a non–stationary yield locus, see *e.g.*, [FN90, Bor92], and to chemoplastic models proposed for early–age concrete [UC96] or clays subject to environmental loading [Hue92, Hue97].

The main features of the theory, as detailed in [TC16] are summarized in the following. Let ϑ denote the additional (scalar) variable affecting the mechanical response of the material, *i.e.*, temperature, suction or chemical degradation. A first modification of the classical theory to account for the changes in ϑ is introduced in the elastic constitutive equations, which now reads, in rate–form:

$$\dot{\boldsymbol{\sigma}} = \boldsymbol{D}^e\left(\boldsymbol{\sigma},\vartheta\right)\left(\dot{\boldsymbol{\epsilon}} - \dot{\boldsymbol{\epsilon}}^p\right) + \boldsymbol{m}\left(\boldsymbol{\sigma},\vartheta\right)\dot{\vartheta} \tag{96}$$

In eq. (96), $\boldsymbol{m}(\boldsymbol{\sigma},\vartheta)$ is a coupling coefficient (*e.g.*, thermal stress coefficient for $\vartheta \equiv T$). While the definitions of elastic domain, flow rule and loading/unloading conditions are identical to those of the classical theory – eqs. (57), (58) and (55) – the evolution equation for the internal variables now assumes the following generalized form:

$$\dot{\boldsymbol{q}} = \dot{\gamma}\boldsymbol{h}(\boldsymbol{\sigma},\boldsymbol{q},\vartheta) + \dot{\vartheta}\boldsymbol{\eta}(\boldsymbol{\sigma},\boldsymbol{q},\vartheta) \tag{97}$$

where: $\boldsymbol{h}(\boldsymbol{\sigma},\boldsymbol{q},\vartheta)$ and $\boldsymbol{\eta}(\boldsymbol{\sigma},\boldsymbol{q},\vartheta)$ are suitable hardening functions. The first term on the RHS of eq. (97) quantifies the changes in the internal variables due to plastic deformations, while the second term accounts for all non–mechanical hardening/softening processes induced by a change of ϑ.

From the consistency condition $\dot{\gamma}\dot{f}(\boldsymbol{\sigma},\boldsymbol{q}) = 0$, the elastic constitutive equation (96) and the flow rule (58), the following generalized expression for the plastic multiplier is obtained:

$$\dot{\gamma} = \frac{1}{K_p}\left\langle \frac{\partial f}{\partial \boldsymbol{\sigma}} \cdot \boldsymbol{D}^e\dot{\boldsymbol{\epsilon}} + \left(\frac{\partial f}{\partial \boldsymbol{q}} \cdot \boldsymbol{\eta} + \frac{\partial f}{\partial \boldsymbol{\sigma}} \cdot \boldsymbol{m}\right)\dot{\vartheta} \right\rangle \tag{98}$$

with K_p given by eq. (61). This in turns provides the following constitutive equations in rate form:

$$\dot{\boldsymbol{\sigma}} = \boldsymbol{D}^{ep}\,\dot{\boldsymbol{\epsilon}} + \boldsymbol{m}^{ep}\,\dot{\vartheta} \tag{99}$$

$$\dot{\boldsymbol{q}} = \boldsymbol{G}\,\dot{\boldsymbol{\epsilon}} + \boldsymbol{G}_\vartheta\,\dot{\vartheta} \tag{100}$$

in which:

$$\boldsymbol{D}^{ep} := \boldsymbol{D}^e - \frac{\mathcal{H}(\dot{\gamma})}{K_p}\left(\boldsymbol{D}^e\frac{\partial g}{\partial \boldsymbol{\sigma}}\right) \otimes \left(\frac{\partial f}{\partial \boldsymbol{\sigma}}\boldsymbol{D}^e\right) \tag{101}$$

$$\boldsymbol{m}^{ep} := \boldsymbol{m} - \frac{\mathcal{H}(\dot{\gamma})}{K_p}\left(\frac{\partial f}{\partial \boldsymbol{q}} \cdot \boldsymbol{\eta} + \frac{\partial f}{\partial \boldsymbol{\sigma}} \cdot \boldsymbol{m}\right)\boldsymbol{D}^e\frac{\partial g}{\partial \boldsymbol{\sigma}} \tag{102}$$

$$\boldsymbol{G} := \frac{\mathcal{H}(\dot{\gamma})}{K_p}\,\boldsymbol{h} \otimes \left(\frac{\partial f}{\partial \boldsymbol{\sigma}}\boldsymbol{D}^e\right) \tag{103}$$

$$\boldsymbol{G}_\vartheta := \frac{\mathcal{H}(\dot{\gamma})}{K_p}\left(\frac{\partial f}{\partial \boldsymbol{q}} \cdot \boldsymbol{\eta} + \frac{\partial f}{\partial \boldsymbol{\sigma}} \cdot \boldsymbol{m}\right)\boldsymbol{h} + \boldsymbol{\eta} \tag{104}$$

According to eq. (98), the plastic multiplier $\dot{\gamma}$ can be considered the sum of the following two terms:

$$\dot{\gamma}_m := \frac{1}{K_p}\frac{\partial f}{\partial \boldsymbol{\sigma}} \cdot \boldsymbol{D}^e\dot{\boldsymbol{\epsilon}} \qquad \dot{\gamma}_\vartheta := \frac{1}{K_p}\left(\frac{\partial f}{\partial \boldsymbol{q}} \cdot \boldsymbol{\eta} + \frac{\partial f}{\partial \boldsymbol{\sigma}} \cdot \boldsymbol{m}\right)\dot{\vartheta} \tag{105}$$

The first, $\dot{\gamma}_m$, coincides with the plastic multiplier of classical elastoplasticity – see eq. (60) – while the second, $\dot{\gamma}_\vartheta$, accounts for the effect of non–mechanical hardening/softening processes. Note that, for plastic loading to occur, only the sum of $\dot{\gamma}_m$ and $\dot{\gamma}_\vartheta$ needs to be positive. In particular, plastic strains may occur even for a trial stress rate $\dot{\boldsymbol{\sigma}}^{\mathrm{tr}} := \boldsymbol{D}^e \dot{\boldsymbol{\epsilon}}$ pointing *inwards* the current yield locus ($\dot{\gamma}_m < 0$), provided that the change in ϑ gives rise to a reduction in size of the elastic domain sufficiently large to keep the plastic multiplier positive, as, for example, in the case of chemical degradation.

Examples of application of this general framework to the modelling of mechanical and chemical degradation processes in weak rocks or bonded soils are provided in, *e.g.*, [NC01, TCN02, NCT03, CdP16, TC16].

10 Concluding remarks

In this chapter, the basic principles of the theory of plasticity have been presented, starting from the basic thermodynamic foundations of the theory of hyperplasticity and moving to classical (perfect, isotropic and anisotropic hardening) phenomenological plasticity, in which the main ingredients of the theory are selected ad–hoc, based on the available experimental evidence. Some of the most relevant extensions of the classical theory – such as Bounding Surface plasticity, generalized plasticity and plasticity with generalized hardening laws, developed to improve its predictive capabilities for complex loading conditions including cyclic loading and environmental loading – have also been discussed to provide an overview of the capabilities of advanced plasticity formulations as applied to particular geotechnical problems.

One important aspect of mathematical modeling of soil behavior which has been thoroughly discussed is the need to distinguish between the non–linearity of the stress–strain response *for finite stress or strain increments* and the concept of *incremental non–linearity*. While a non–linear soil model can be obtained with a simple hypoelastic constitutive equation, the modeling of irreversible and history–dependent behavior requires the constitutive equation to be formulated in rate–form and the use of *incrementally non–linear* relations between the stress and the strain rates.

The theory of plasticity represents the earliest and perhaps simplest approach to incremental non–linearity, achieved through the introduction of the loading/unloading conditions in the incremental response. Its appeal throughout the decades since its early applications to geotechnical problems stems from the ease with which some of its basic concepts (the elastic response, the yield surface, the plastic potential) could find a physical interpretation in the examination of classical laboratory test results.

While classical perfect plasticity is still widely used in the analysis of failure problems in geotechnical engineering, the more advanced versions of the theory have been mostly developed in the attempt of making more accurate numerical predictions in terms of performance of the geotechnical structures under complex loading conditions – *i.e.*, relevant displacement and deformations.

It is worth noting that, as the models increase in their predictive capabilities, they also necessarily require the introduction of more material constants as well as of a larger pool of history–dependent internal variables. This creates two different order of problems whenever the use of these advanced tools is required:

a) A large pool of experimental data, gathered from tests exploring different loading paths, is required to calibrate models with a large set of material constants.

b) In presence of one or more internal variables, some of which could be second–order tensors, the definition of their initial values at the beginning of the loading process is necessary, in the same way as the definition of the initial stress state is required in order to start the evolution process governed by the constitutive equations in rate–form.

As for point (a), a desirable feature of the model would be that the calibration does not require complex testing procedures to be performed with non–standard experimental devices (*e.g.*, true triaxial cell, hollow cylinder apparatus, simple shear devices). The calibration of a relatively large set of material constants has always been considered one of the main drawbacks of advanced plasticity models, and has motivated a number of studies aimed at devising calibration algorithms for the automatic identification of the model constants from a set of experimental data.

However, it is usually point (b) which poses the most challenging task. In fact, it is sufficient to consider how difficult could be to make a reasonable estimate of the coefficient of earth pressure at rest, K_0, for a heavily overconsolidated soil deposit, even in simple geometric conditions (horizontal ground surface, horizontal contacts between soil layers), to have an idea on how hard is to estimate the initial values of a structure tensor when no information is available on the details of the geological history of the site, or the ground surface is not horizontal and simple geostatic conditions do not apply. In some cases, the definition of the initial state in terms of stress and internal variables fields could require the simulation of the entire geological history of the deposit and could represent a significant part of the numerical modeling activities for the design of a geotechnical structure.

References

[ABS77] D. Allirot, J. P. Boehler, and A. Sawczuk. Irreversible deformations of anisotropic rock under hydrostatic pressure. *Int. J. Rock Mech. Min. Sci. & Geomech. Abstr.*, 14:77–83, 1977.

[AD86] A. Anandarajah and Y. F. Dafalias. Bounding surface plasticity. III: Application to anisotropic cohesive soils. *J. Engng. Mech., ASCE*, 112(12):1292–1318, 1986.

[ARS86] J. H. Atkinson, D. Richardson, and S. E. Stallebrass. Effect of recent stress history on the stiffness of overconsolidated clay. *Géotechnique*, 40(4):531–540, 1986.

[ATW89] A. Al-Tabbaa and D. M. Wood. An experimentally based bubble model for clay. In S. Pietrusczczak and G. N. Pande, editors, *NUMOG III*, pages 91–99. Elsevier Applied Science, 1989.

[Bar86] J. P. Bardet. Modelling of sand behaviour with bounding surface plasticity. In G. N. Pande and W. F. van Impe, editors, *Numerical Models in Geomechanics*, pages 131–150. Jackson and Sons., 1986.

[BD84] R. Baker and C. S. Desai. Induced anisotropy during plastic straining. *Int. J. Num. Anal. Meth. Geomech.*, 8:167–185, 1984.

[Boe75] J. P. Boehler. Sur les formes invariantes dans les sous–groupe orthotrope de revolution. *Zeits. Angew. Math. Mech.*, 55:609–611, 1975.

[Boe87] J. P. Boehler. *Application of tensor functions in solid mechanics*. CISM Courses and Lectures n. 292. Springer Verlag, New York, 1987.

[Bor92] R. I. Borja. Generalized creep and stress–relaxation model for clays. *J. Geotech. Engng., ASCE*, 118(11):1765–1786, 1992.

[Bor13] R. I. Borja. *Plasticity: modeling & computation*. Springer Science & Business Media, 2013.

[BTA97] R. I. Borja, C. Tamagnini, and A. Amorosi. Coupling plasticity and energy-conserving elasticity models for clays. *J. Geotech. Geoenv. Engng., ASCE*, 123(10):948–957, 1997.

[BY86] P. K. Banerjee and N. B. Yousif. A plasticity model for the mechanical behavior of anisotropically consolidated clay. *Int. J. Num. Anal. Meth. Geomech.*, 10:521–541, 1986.

[CC44] A. Casagrande and N. Carillo. Shear failure of anisotropic materials. *Proc. Boston Soc. Civil Engrs.*, 31:74–87, 1944.

[CdP16] M. O. Ciantia and C. di Prisco. Extension of plasticity theory to debonding, grain dissolution, and chemical damage of calcarenites. *Int. J. Num. Anal. Meth. Geomech.*, 40(3):315–343, 2016.

[CH97] I.F. Collins and G. T. Houlsby. Application of thermomechanical principles to the modeling of geotechnical materials. *Proceedings of the Royal Society of London. Series A: Mathematical, Physical and Engineering Sciences*, 453:1975–2000, 1997.

[CH02] I. F. Collins and T. Hilder. A theoretical framework for constructing elastic/plastic constitutive models of triaxial tests. *Int. J. Num. Anal. Meth. Geomech.*, 26(13):1313–1347, 2002.

[Che76] W. F. Chen. *Limit Analysis and Soil Plasticity*. Elsevier, 1976.

[CJR13] B. Cambou, M. Jean, and F. Radjaï. *Micromechanics of granular materials*. John Wiley & Sons, 2013.

[CK02] I. F. Collins and P. A. Kelly. A thermomechanical analysis of a family of soil models. *Géotechnique*, 52(7):507–518, 2002.

[CM03] I. F. Collins and B. Muhunthan. On the relationship between stress–dilatancy, anisotropy, and plastic dissipation for granular materials. *Geotechnique*, 53(7):611–618, 2003.

[Cw94] R. S. Crouch and J. P. wolf. Unified 3d critical state bounding–surface plasticity model for soils incorporating continuous plastic loading under cyclic paths. Part I: constitutive relations. *Int. J. Num. Anal. Meth. Geomech.*, 18:735–758, 1994.

[Daf86] Y. F. Dafalias. Bounding surface plasticity. I: Mathematical foundation and hypoplasticity. *J. Engng. Mech., ASCE*, 112(9):966–987, 1986.

[Dar78] F. Darve. *Une formulation incrémentale non–lineaire des lois rhéologiques; application aux sols*. Thèse d'Etat, Grenoble, 1978.

[Dar90] F. Darve. The expression of rheological laws in incremental form and the main classes of constitutive equations. In F. Darve, editor, *Geomaterials: Constitutive Equations and Modelling*, pages 123–148. Elsevier, 1990.

[DC70] J. M. Duncan and C. Y. Chang. Nonlinear analysis of stress and strain in soils. *J. Soil Mech. Found. Div., ASCE*, 96(SM5):1629–1653, 1970.

[DH86] Y. F. Dafalias and L. R. Herrmann. Bounding surface plasticity. II: Application to isotropic cohesive soils. *J. Engng. Mech., ASCE*, 112(12):1263–1291, 1986.

[DM04] Y. F. Dafalias and M. T. Manzari. Simple plasticity sand model accounting for fabric change effects. *J. Engng. Mech., ASCE*, 130(6):622–634, 2004.

[DMP06] Y. F. Dafalias, M. T. Manzari, and A. G. Papadimitriou. SANICLAY: simple anisotropic clay plasticity model. *Int. J. Num. Anal. Meth. Geomech.*, 30(12):1231–1257, 2006.

[DMS71] F. L. Di Maggio and I. S. Sandler. Material model for granular soil. *J. Engng. Mech. Div., ASCE*, 97:935–950, 1971.

[DP75] Y. F. Dafalias and E. V. Popov. A model of non–linearly hardening materials for complex loading. *Arch. Mech.*, 21:173–192, 1975.

[dPNL93] C. di Prisco, R. Nova, and J. Lanier. A mixed isotropic–kinematic hardening constitutive law for sand. In D. Kolymbas, editor, *Modern Approaches to Plasticity*, pages 83–124. Elsevier, 1993.

[DS66] J. M. Duncan and H. B. Seed. Anisotropy and stress reorientation of clays. *J. Soil Mech. Found. Div., ASCE*, 92(SM5):21–50, 1966.

[DS84] C. S. Desai and H. J. Siriwardane. *Constitutive Laws for Engineering Materials, with Emphasis on Geologic Materials*. Prentice–Hall, 1984.

[DS02] R. O. Davis and A. P. S. Selvadurai. *Plasticity and geomechanics*. Cambridge university press, 2002.

[DT05] A. DeSimone and C. Tamagnini. Stress–dilatancy based modelling of granular materials and extensions to soils with crushable grains. *Int. J. Num. Anal. Meth. Geomech.*, 29(1):73–101, 2005.

[DT13] Y. F. Dafalias and M. Taiebat. Anatomy of rotational hardening in clay plasticity. *Géotechnique*, 63(16):1406–1418, 2013.

[EHN07] I. Einav, G. T. Houlsby, and G. D. Nguyen. Coupled damage and plasticity models derived from energy and dissipation potentials. *Int. Journal of Solids and Structures*, 44(7-8):2487–2508, 2007.

[EP04] I. Einav and A. M. Puzrin. Continuous hyperplastic critical state (chcs) model: derivation. *Int. Journal of Solids and Structures*, 41(1):199–226, 2004.

[FN90] E. Flavigny and R. Nova. Viscous properties of geomaterials. In F. Darve, editor, *Geomaterials: Constitutive Equations and Modelling*, pages 27–54. Elsevier, 1990.

[GDV84] G. Gudehus, F. Darve, and I. Vardoulakis. *Constitutive Relations for Soils*. Balkema, Rotterdam, 1984.

[GH83] J. Graham and G. T. Houlsby. Anisotropic elasticity of a natural clay. *Géotechnique*, 33(2):165–180, 1983.

[GM82] J. Ghaboussi and H. Momen. Modelling and analysis of cyclic behavior of sands. In G. N. Pande and O. C. Zienkiewicz, editors, *Soil Mechanics: Transient and Cyclic Loads*, pages 313–342. Wiley, New York, 1982.

[GNL83] J. Graham, M. L. Noonan, and K. V. Lew. Yield states and stress–strain relationship in a natural plastic clay. *Can. Geotech. J.*, 20:502–516, 1983.

[GNS83] P. Germain, Q. S. Nguyen, and P. Suquet. Continuum thermodynamics. *J. Appl. Mechanics, ASME*, 50:1010–1020, 1983.

[Gre56] A. E. Green. Hypoelasticity and plasticity. *Archive for Rational Mechanics and Analysis*, 5:725–734, 1956.

[Gud79] G. Gudehus. A comparison of some constitutive laws for soils under radially symmetric loading and unloading. In Wittke, editor, *3rd Int. Conf. Num. Meth. Geomech.,* Aachen, pages 1309–1324. Balkema, Rotterdam, 1979.

[GW99] A. Gajo and D. M. Wood. A kinematic hardening constitutive model for sands: the multiaxial formulation. *Int. J. Num. Anal. Meth. Geomech.*, 23:925–965, 1999.

[Has79] K. Hashiguchi. Constitutive equations of granular media with an anisotropic hardening. In *III Int. Conf. Num. Meth. in Geomechanics*, pages 435–439, Aachen, Germany, 1979. Balkema, Rotterdam.

[Has85] K. Hashiguchi. Two– and three–surface models of plasticity. In *V Int. Conf. Num. Meth. in Geomechanics*, pages 285–292, Nagoya, Japan, 1985. Balkema, Rotterdam.

[Has88] K. Hashiguchi. Mathematically consistent formulation of elastoplastic constitutive equations. In *VI Int. Conf. Num. Meth. in Geomechanics*, pages 467–472, Innsbruck, Austria, 1988. Balkema, Rotterdam.

[Has17] K. Hashiguchi. *Foundations of elastoplasticity: subloading surface model*. Springer, 2017.

[Hil50] R. Hill. *The Mathematical Theory of Plasticity*. Oxford University Press, Oxford, 1950.

[HN75] B. Halphen and Q. S. Nguyen. Sur les matériaux standards généralisés. *Journal de Mécanique*, 14:39–63, 1975.

[Hou81] G. T. Houlsby. *A study of plasticity theories and their applicability to soils*. PhD thesis, Cambridge University, 1981.

[Hou85] G. T. Houlsby. The use of a variable shear modulus in elastic–plastic models for clays. *Comp. & Geotechnics*, 1:3–13, 1985.

[HP00] G. T. Houlsby and A. M. Puzrin. A thermomechanical framework for constitutive models for rate-independent dissipative materials. *Intl. J. of Plasticity*, 16(9):1017–1047, 2000.

[HP07] G. T. Houlsby and A. M. Puzrin. *Principles of hyperplasticity: an approach to plasticity theory based on thermodynamic principles*. Springer Science & Business Media, 2007.

[HR99] W. Han and B. D. Reddy. *Plasticity: Mathematical Theory and Numerical Analysis*. Springer Verlag, New York, 1999.

[Hue92] T. Hueckel. Water mineral interactions in hygromechanics of clay exposed to environmental load: a mixture theory approach. *Can. Geotech. J.*, 29:1071–1086, 1992.

[Hue97] T. Hueckel. Chemo–plasticity of clays subjected to stress and flow of a single contaminant. *Int. J. Num. Anal. Meth. Geomech.*, 21:43–72, 1997.

[HWW84] G. T. Houlsby, C. P. Wroth, and D. M. Wood. Prediction of the results of laboratory tests on a clay using a critical state model. In G. Gudehus, F. Darve, and I. Vardoulakis, editors, *Constitutive Relations for Soils*. Balkema, Rotterdam, 1984.

[Iwa67] W. D. Iwan. On a class of models for the yield behaviour of continuous and composite systems. *J. Appl. Mechanics, ASME*, 34:612–617, 1967.

[JB02] M. Jirasek and Z. P. Bazant. *Inelastic Analysis of Structures*. Wiley, Chichester, 2002.

[Jom00] C. Jommi. Remarks on the constitutive modelling of unsaturated soils. In *Experimental evidence and theoretical approaches in unsaturated soils*, pages 139–153. Balkema, Rotterdam, 2000.

[Jom21] C. Jommi. General overview on modelling the coupled behaviour of unsaturated soils. In C. Tamagnini and D. Mašín, editors, *Constitutive modelling of soils*. ALERT Geomaterials, 2021. This volume.

[JP88] R. J. Jardine and D. M. Potts. Hutton tension leg platform foundations: an approach to the prediction of driven pile behaviour. *Géotechnique*, 38(2):231–252, 1988.

[JPFB86] R. J. Jardine, D. M. Potts, A. B. Fourie, and J. B. Burland. Studies of the influence of non-linear stress-strain characteristics in soil-structure interaction. *Géotechnique*, 36(3):377–396, 1986.

[JPSJH91] R. J. Jardine, D. M. Potts, H. D. St. John, and D. W. Hight. Some practical applications of a non–linear ground model. In AGI, editor, *X ECSMFE,* Firenze, volume 1, pages 223–228. Balkema, Rotterdam, 1991.

[KL88] M. K. Kim and P. V. Lade. Single hardening constitutive model for frictional materials. I: Plastic potential function. *Comp. & Geotechnics*, 5:307–324, 1988.

[Kol91] D. Kolymbas. An outline of hypoplasticity. *Archive of Applied Mechanics*, 61:143–151, 1991.

[Kol93] D. Kolymbas. *Modern Approaches to Plasticity*. Elsevier, 1993.

[KZ63] R. L. Kondner and J. S. Zelasko. A hyperbolic stress–strain formulation for sands. In *II Pan.–Am. Conf. SMFE*, volume 1, pages 289–324, 1963.

[LC08] L. Laloui and C. Cekerevac. Non-isothermal plasticity model for cyclic behaviour of soils. *Int. J. Num. Anal. Meth. Geomech.*, 32(5):437–460, 2008.

[LK88] P. V. Lade and M. K. Kim. Single hardening constitutive model for frictional materials. II: Yield criterion and plastic work contours. *Comp. & Geotechnics*, 6:13–29, 1988.

[LS02] A. V. Lyamin and S. W. Sloan. Upper bound limit analysis using linear finite elements and nonlinear programming. *Int. J. Num. Anal. Meth. Geomech.*, 26:181–216, 2002.

[Lub90] J. Lubliner. *Plasticity Theory*. Mac Millan, London, 1990.

[LYKT02] H. I. Ling, D. Yue, V. N. Kaliakin, and N. J. Themelis. Anisotropic elastoplastic bounding surface model for cohesive soils. *J. Engng. Mech., ASCE*, 128(7):748–758, 2002.

[Mas21] D. Masin. Hypoplasticity and other incrementally non–linear modelling approaches. In C. Tamagnini and D. Mašín, editors, *Constitutive modelling of soils*. ALERT Geomaterials, 2021. This volume.

[Mau92] G. A. Maugin. *Thermomechanics of plasticity and fracture*. Cambridge University Press, 1992.

[MD97] M. T. Manzari and Y. F. Dafalias. A critical state two–surface plasticity model for sands. *Géotechnique*, 47(2):255–272, 1997.

[Mit70] R. J. Mitchell. On the yielding and mechanical strength of leda clays. *Can. Geotech. J.*, 7:297–312, 1970.

[MLA94] L. Modaressi, L. Laloui, and D. Aubry. Thermodynamical approach for camclay–family models with roscoe–type dilatancy rules. *Int. J. Num. Anal. Meth. Geomech.*, 18:133–138, 1994.

[MNZ78] Z. Mroz, V. A. Norris, and O. C. Zienkiewicz. An anisotropic hardening model for soils and its application to cyclic loading. *Int. J. Num. Anal. Meth. Geomech.*, 2:203–221, 1978.

[MNZ81] Z. Mroz, V. A. Norris, and O. C. Zienkiewicz. An anisotropical critical state model for soils subject to cyclic loading. *Géotechnique*, 31(4):451–469, 1981.

[Mor70] J. J. Moreau. Sur les lois de frottement, de viscosité et de plasticité. *C. R. Acad. Sci.*, 271:608–611, 1970.

[Mro67] Z. Mroz. On the description of anisotropic work–hardening. *Journal of the Mechanics and Physics of Solids*, 15:163–175, 1967.

[Mur85] S. Murayama. *Constitutive laws of soils*. Japanese Society of Soil Mechanics and Foundation Engineering, 1985.

[NC01] R. Nova and R. Castellanza. Modelling weathering effects on the mechanical on the mechanical behaviour of soft rocks. In *Int. Conf. on Civil Engineering*, pages 157–167, Bangalore, India, 2001. Interline Publishing.

[NCT03] R. Nova, R. Castellanza, and C. Tamagnini. A constitutive model for bonded geomaterials subject to mechanical and/or chemical degradation. *Int. J. Num. Anal. Meth. Geomech.*, 27(9):705–732, 2003.

[Nov77] R. Nova. On the hardening of soils. *Archiwum Mechaniki Stosowanej*, 29:445–458, 1977.

[Nov86] R. Nova. Soil models as a basis for modelling the behaviour of geophysical materials. *Arch. Mech.*, 64:31–44, 1986.

[Nov88] R. Nova. Sinfonietta classica: an exercise on classical soil modelling. In Saada and Bianchini, editors, *Constitutive Equations for Granular Non–Cohesive Soils*, Cleveland, 1988. Balkema, Rotterdam.

[Nov96] R. Nova. Modelling: classical elastoplastic models. In R. Chambon, editor, *8th ALERT School on Bifurcation and Localization in Geomaterials*. ALERT Geomaterials, 1996.

[Nov00] R. Nova. Modelling the weathering effects on the mechanical behaviour of granite. In D. Kolymbas, editor, *Constitutive Modelling of Granular Materials*, Horton, Greece, 2000. Springer, Berlin.

[NW79] R. Nova and D. M. Wood. A constitutive model for sand in triaxial compression. *Int. J. Num. Anal. Meth. Geomech.*, 3:255–278, 1979.

[Ogd97] R. W. Ogden. *Non–linear elastic deformations*. Dover, 1997.

[OKH78] M. Oda, I. Koishikawa, and T. Higuchi. Experimental study of anisotropic shear strength of sand by plane strain test. *Soils and Foundations*, 18(1):25–38, 1978.

[OKKA02] F. Oka, S. Kimoto, H. Kobayashi, and T. Adachi. Anisotropic behavior of soft sedimentary rock and a constitutive model. *Soils and foundations*, 42(5):59–70, 2002.

[ONNK85] M. Oda, S. Nemat-Nasser, and J. Konishi. Stress–induced anisotropy in granular masses. *Soils and Foundations*, 25(3):85–97, 1985.

[OT20] K. Oliynyk and C. Tamagnini. Finite deformation hyperplasticity theory for crushable, cemented granular materials. *Open Geomechanics*, 2:1–33, 2020.

[OT21] K. Oliynyk and C. Tamagnini. Finite deformation plasticity. In C. Tamagnini and D. Mašín, editors, *Constitutive modelling of soils*. ALERT Geomaterials, 2021. This volume.

[OW69] D. R. Owen and W. O. Williams. On the time derivatives of equilibrated response functions. *Archive for Rational Mechanics and Analysis*, 33(4):288–306, 1969.

[Pas91] M. Pastor. Modelling of anisotropic sand behaviour. *Comp. & Geotechnics*, 11:173–208, 1991.

[PBZL97] I. D. S. Pontes, L. A. Borges, N. Zouain, and F. R. Lopes. An approach to limit analysis with cone–shaped yield surfaces. *Int. J. Num. Meth. Engng.*, 40:4011–4032, 1997.

[PH01] A. M. Puzrin and G. T. Houlsby. Fundamentals of kinematic hardening hyperplasticity. *International journal of solids and structures*, 38(21):3771–3794, 2001.

[PHS66] H. B. Pooroshasb, I. Holubec, and A. N. Sherbourne. yielding and flow of sand in triaxial compression (part I). *Can. Geotech. J.*, 3:179–190, 1966.

[PHS67] H. B. Pooroshasb, I. Holubec, and A. N. Sherbourne. yielding and flow of sand in triaxial compression (part II). *Can. Geotech. J.*, 4:376–397, 1967.

[PLS02] S. Pietruszczak, D. Lydzba, and J.-F. Shao. Modelling of inherent anisotropy in sedimentary rocks. *Int. Journal of Solids and Structures*, 39(3):637–648, 2002.

[PM00] S. Pietruszczak and Z. Mroz. Formulation of anisotropic failure criteria incorporating a microstructure tensor. *Computers and Geotechnics*, 26(2):105–112, 2000.

[PP85] H. B. Pooroshasb and S. Pietruszczak. On the yielding and flow of sand: a generalized two–surface model. *Comp. & Geotechnics*, 1:33–58, 1985.

[Pre77] J. H. Prevost. Mathematical modelling of monotonic and cyclic undrained clay behaviour. *Int. J. Num. Anal. Meth. Geomech.*, 1:195–216, 1977.

[Pre86] J. H. Prevost. Constitutive equations for pressure–sensitive soils: theory, numerical implementation, and examples. In R. Dungar and J. A. Studer, editors, *Geomechanical Modelling in Engineering Practice*, pages 331–350. Balkema, Rotterdam, 1986.

[PW99] A. Pestana and A. J. Whittle. Formulation of a unified constitutive model for clays and sands. *Int. J. Num. Anal. Meth. Geomech.*, 23:1215–1243, 1999.

[PZC90] M. Pastor, O. C. Zienkiewicz, and A. H. C. Chan. Generalized plasticity and the modelling of soil behaviour. *Int. J. Num. Anal. Meth. Geomech.*, 14:151–190, 1990.

[PZL85] M. Pastor, O. C. Zienkiewicz, and K. H. Leung. Simple model for transient soil loading in earthquake analysis. II: non–associative model for sands. *Int. J. Num. Anal. Meth. Geomech.*, 9:477–498, 1985.

[RB68] K. H. Roscoe and J. B. Burland. On the generalised stress–strain behaviour of 'wet' clay. In J. Heyman and F. A. Leckie, editors, *Engineering Plasticity*, pages 535–609. Cambridge Univ. Press, Cambridge, 1968.

[RK83] R. K. Rowe and G. J. Kack. A theoretical examination of the settlements induced by tunnelling: four case histories. *Can. Geotech. J.*, 20:299–314, 1983.

[RM93] B.D. Reddy and J.B. Martin. Internal variable formulations of problems in elastoplasticity: constitutive and algorithmic aspects. *Applied Mech. Review*, 47:429–456, 1993.

[RW00] M. Rouainia and D. M. Wood. A kinematic hardening constitutive model for natural clays with loss of structure. *Géotechnique*, 50(2):153–164, 2000.

[SB89] A. S. Saada and G. F. Bianchini. *Constitutive equations for granular non–cohesive soils*. Balkema, Rotterdam, 1989.

[SD83] H. J. Siriwardane and C. S. Desai. Computational procedures for non-linear three–dimensional analysis with some advanced constitutive laws. *Int. J. Num. Anal. Meth. Geomech.*, 7:143–171, 1983.

[SDMB76] I. S. Sandler, F. L. Di Maggio, and G. Y. Baladi. Generalised cap model for geologic materials. *J. Soil Mech. Found. Div., ASCE*, 102:683–697, 1976.

[SGvW95] I. Sharour, S. Ghorbanbeigi, and P. A. von Wolffersdordff. Three–dimensional finite element analysis of diaphragm wall construction. *Revue Francaise de Géotechnique*, 71:39–47, 1995.

[SH92] I. M. Smith and D. K. H. Ho. Influence of construction technique on the performance of a braced excavation in marine clay. *Int. J. Num. Anal. Meth. Geomech.*, 16:845–867, 1992.

[SH97] J. C. Simo and T. J. R. Hughes. *Computational Inelasticity*. Springer, 1997.

[SJH92] P. R. Smith, R. J. Jardine, and D. W. Hight. The yielding of Bothkennar clay. *Géotechnique*, 42(2):257–274, 1992.

[SK95] S. W. Sloan and P. W. Kleeman. Upper bound limit analysis with discontinuous velocity fields. *Comp. Meth. Appl. Mech. Engng.*, 127:293–314, 1995.

[SO77] H. Sekiguchi and H. Ohta. Induced anisotropy and time dependency in clays. In *IX ICSMFE, Specialty Session 9*, pages 229–238. Balkema, Rotterdam, 1977.

[Sok65] V. V. Sokolowski. *Statics of Granular Media*. Pergamon, Oxford, 1965.

[ST97] S. E. Stallebrass and R. N. Taylor. The development and evaluation of a constitutive model for the prediction of ground movements in over-consolidated clay. *Géotechnique*, 47(2):235–253, 1997.

[Sta90] S. E. Stallebrass. *Modelling the effect of recent stress history on the behaviour of overconsolidated soils*. PhD thesis, The City University, London, 1990.

[SW68] A. N. Schofield and C. P. Wroth. *Critical State Soil Mechanics*. McGraw–Hill, London, 1968.

[SWB16] S. J. Semnani, J. A. White, and R. I. Borja. Thermoplasticity and strain localization in transversely isotropic materials based on anisotropic crit-

ical state plasticity. *Int. J. Num. Anal. Meth. Geomech.*, 40(18):2423–2449, 2016.

[TC16] C. Tamagnini and M. O. Ciantia. Plasticity with generalized hardening: constitutive modeling and computational aspects. *Acta Geotechnica*, 11(3):595–623, 2016.

[TCN02] C. Tamagnini, R. Castellanza, and R. Nova. A generalized backward euler algorithm for the numerical integration of an isotropic hardening elastoplastic model for mechanical and chemical degradation of bonded geomaterials. *Int. J. Num. Anal. Meth. Geomech.*, page submitted for publication., 2002.

[TD08] M. Taiebat and Y. F. Dafalias. SANISAND: Simple anisotropic sand plasticity model. *Int. J. Num. Anal. Meth. Geomech.*, 32(8):915–948, 2008.

[TDP10] M. Taiebat, Y. F. Dafalias, and R. Peek. A destructuration theory and its application to SANICLAY model. *Int. J. Num. Anal. Meth. Geomech.*, 34(10):1009–1040, 2010.

[Ter48] K. Terzaghi. *Theoretical Soil Mechanics*. John Wiley, New York, 1948.

[TL77] F. Tavenas and S. Leroueil. Effects of stresses and time on on yielding of clays. In *IX ICSMFE*, volume 1, pages 319–326. Balkema, Rotterdam, 1977.

[TN65] C. A. Truesdell and W. Noll. The non–linear field theories of mechanics. In S. Flügge, editor, *Encyclopedia of Physics*, volume III/3. Springer, Berlin, 1965.

[TP48] K. Terzaghi and R. B. Peck. *Soil Mechanics in Engineering Practice*. John Wiley, New York, 1948.

[TVC00] C. Tamagnini, G. Viggiani, and R. Chambon. A review of two different approaches to hypoplasticity. In D. Kolymbas, editor, *Constitutive Modelling of Granular Materials*, pages 107–145. Springer, Berlin, 2000.

[UC96] F. J. Ulm and O. Coussy. Strength growth as chemo–plastic hardening in early age concrete. *J. Engng. Mech., ASCE*, 122(12):1123–1132, 1996.

[Var19] I. Vardoulakis. *Cosserat continuum mechanics*. Springer, 2019.

[VS95] I. Vardoulakis and J. Sulem. *Bifurcation Analysis in Geomechanics*. Blackie Acad. & Professional, New York, 1995.

[WA85] R. K. S. Wong and J. R. F. Arthur. Induced and inherent anisotropy in sand. *Géotechnique*, 35(4):471–481, 1985.

[Wil77] P. Wilde. Two invariants depending models of granular media. *Arch. Mech. Stos.*, 29:799–809, 1977.

[WK91] R. C. K. Wong and P. K. Kaiser. Performance assessment of tunnels in cohesionless soils. *J. Geotech. Engng., ASCE*, 117(12):1880–1901, 1991.

[WK94] A. J. Whittle and M. J. Kavvadas. Formulation of MIT–E3 constitutive model for overconsolidated clays. *J. Geotech. Engng., ASCE*, 120(1):173–198, 1994.

[WNKL03] S. J. Wheeler, A. Näätänen, M. Karstunen, and M. Lojander. An anisotropic elastoplastic model for soft clays. *Can. Geotech. J.*, 40(2):403–418, 2003.

[Woo82] D. M. Wood. Laboratory investigations of the behaviour of soils under cyclic loading: a review. In G. N. Pande and O. C. Zienkiewicz, editors, *Soil Mechanics – Cyclic and Transient Loads*, pages 513–582. Wiley, Chichester, 1982.

[Woo04] D. M. Wood. *Geotechnical modelling*, volume 1. Spon press, 2004.

[YIV98] M. Yoshimine, K. Ishihara, and W. Vargas. Effects of principal stress direction and intermediate principal stress on undrained shear behavior of sand. *Soils and Foundations*, 38(3):179–188, 1998.

[YMH91] N. Yasufuku, H. Murata, and M. Hyodo. Yield characteristics of anisotropically consolidated sand under low and high stresses. *Soils and Foundations*, 31(1):95–109, 1991.

[Yu06] H.-S. Yu. *Plasticity and geotechnics*, volume 13. Springer Science & Business Media, 2006.

[ZH77] O. C. Zienkiewicz and C. Humpheson. Viscoplasticity: a generalized model for soil behaviour. In C. A. Desai and J. T. Christian, editors, *Numerical Models in Geotechnical Engineering*. McGraw–Hill, New York, 1977.

[ZHL75] O. C. Zienkiewicz, C. Humpheson, and R. W. Lewis. Associated and non–associated visco–plasticity and plasticity in soil mechanics. *Géotechnique*, 25(4):671–689, 1975.

[Zie83] H. Ziegler. *An introduction to thermomechanics*. North Holland, 1983.

[ZLP85] O. C. Zienkiewicz, K. H. Leung, and M. Pastor. Simple model for transient soil loading in earthquake analysis. I: basic model and its application. *Int. J. Num. Anal. Meth. Geomech.*, 9:453–476, 1985.

[ZM84] O. C. Zienkiewicz and Z. Mroz. Generalized plasticity formulation and applications to geomechanics. In C. S. Desai and R. H. Gallagher, editors, *Mechanics of Engineering Materials*. Wiley, 1984.

[ZN71] O. C. Zienkiewicz and D. J. Naylor. An adaptation of critical state soil mechanics theory for use in finite elements. In R. H. G. Parry, editor,

Stress–Strain Behaviour of Soils (Roscoe Mem. Symp.). Foulis, Henley–on–Thames, 1971.

[ZN73] O. C. Zienkiewicz and D. J. Naylor. Finite element studies of soils and porous media. In J. T. Oden and E. R. de Arantes, editors, *Lect. Finite Elements in Continuum Mechanics*. UAH Press, 1973.

[ZRNW78] M. Zytynski, M. F. Randolph, R. Nova, and C. P. Wroth. On modelling the unloading-reloading behaviour of soils. *Int. J. Num. Anal. Meth. Geomech.*, 2(1):87–93, 1978.

[ZW87] H. Ziegler and C. Wehrli. The derivation of constitutive relations from the free energy and the dissipation function. *Advances in applied mechanics*, page 183, 1987.

Hypoplasticity and other incrementally non-linear modelling approaches

David Mašín[1]

[1] *Charles University, Prague, Czech Republic*

In this lecture, incrementally non-linear approaches to constitutive model formulation will be introduced. Unlike elasto-plasticity, incrementally non-linear models are charaterised by a stiffness matrix continuously dependent on strain rate direction with explicit analytical form of stiffness matrix is often neither available nor needed for the model formulation. The incorporation of irreversible behaviour of granular materials is in most cases not utilised through sub-dividing the strain rate into elastic and plastic part, but through incrementally non-linear character of the primary constitutive equation itself. The concepts are demonstrated by describing three different classes of incrementally non-linear models: hypoplasticity, barodesy and incrementally non-linear bounding surface plasticity.

1 Introduction

In this chapter, we will leave aside rate-dependency of soil behaviour and consider constitutive models which can be, at least in principle, written in the form:

$$\mathring{\mathbf{T}} = \mathcal{M}(\mathbf{T}, \mathbf{q}, \vec{\mathbf{D}}) : \mathbf{D} \tag{1}$$

where $\mathcal{M}$ is the tangent stiffness tensor, $\mathbf{T}$ is Cauchy stress, $\mathring{\mathbf{T}}$ is its objective (Jaumann-Zaremba) stress rate, $\mathbf{q}$ is a vector of state variables, $\mathbf{D}$ is the Euler stretching tensor and $\vec{\mathbf{D}}$ is its normalised value defined as $\vec{\mathbf{D}} = \vec{\mathbf{D}}/\|\mathbf{D}\|$, where $\|\mathbf{D}\|$ represents Euclidean norm of $\mathbf{D}$.

In a constitutive model, the tensor $\mathcal{M}$ may or may not depend on $\vec{\mathbf{D}}$. Those models, where $\mathcal{M}$ is independent of $\vec{\mathbf{D}}$ are denoted as incrementally linear or elastic. The elasto-plastic models are characterised by two tensorial zones of $\vec{\mathbf{D}}$ (elastic and elasto-plastic) and, as such, the models can be denoted as incrementally bi-linear. Further discrete increase of the number of tensorial zones to form inceremently multi-linear models is feasible [DL82], but not very practical from the model complexity point of view. Instead, researchers focused on development of models where $\mathcal{M}$ represented

a continuous non-linear function of $\vec{\mathbf{D}}$. These models are denoted as incrementally non-linear and they are the main topic of this chapter.

The reader could pose a question why developing an incrementally non-linear model is preferable with respect to multi-linearity. The main reason is that other constitutive modelling frameworks exist than those based on Eq. (1). Using these frameworks it is possible to design simple and elegant models which, if expressed using (1), would be characterised by a continuous dependency of $\mathcal{M}$ on $\vec{\mathbf{D}}$. Analytical expression of $\mathcal{M}$ is, however, often neither available nor needed for the proper functionality of these models. In this chapter we will focus on three selected approaches to replace Eq. (1) leading to incrementally non-linears models[1]: *hypoplasticity*, *barodesy* and *incrementally non-linear bounding surface plasticity*.

2 Hypoplasticity

Hypoplasticity is a special class of incrementally non-linear constitutive models whose general rate equation reads:

$$\mathring{\mathbf{T}} = \mathcal{L} : \mathbf{D} + \mathbf{N}\|\mathbf{D}\| \tag{2}$$

Central in the model are two constitutive tensors $\mathcal{L}$ and $\mathbf{N}$; $\mathcal{L}$ is a fourth-order tensor and $\mathbf{N}$ is a second-order tensor. For more details on model structure and particular versions, the reader is referred to [Kol00, Nie03, KM16, Maš19].

2.1 Hypoplasticity explained using response envelopes

The first part of the hypoplastic equation $\mathcal{L} : \mathbf{D}$ is, in fact, equivalent to the elastic model with $\vec{\mathbf{D}}$-independent $\mathcal{M}$. Therefore, identically to the elastic model, it yields an elliptic response envelope centred about the reference stress state. In addition to this, however, the hypoplastic model contains additively the second-order tensor part $\mathbf{N}\|\mathbf{D}\|$, which is independent of $\vec{\mathbf{D}}$ (for the given $\|\mathbf{D}\|$). As $\mathbf{N}\|\mathbf{D}\|$ is independent of $\vec{\mathbf{D}}$, its net effect on the response envelope is its *translation* in the stress space (Figure 1). Consequently, the response envelope of the hypoplastic model is a single ellipse (as in elasticity); however, unlike in elasticity, this ellipse is not centred with respect to the stress state. Therefore, unlike elasticity and similar to elasto-plasticity, the hypoplastic model predicts different stiffness in different loading directions.

2.2 Hypoplasticity explained using simplistic 1D version

A 1D hypoplastic model is introduced in this section to demonstrate the main principle of hypoplasticity. 1D equivalent of Eq. (2) for shear deformation reads

$$d\tau = L d\gamma + N|d\gamma| \tag{3}$$

[1] For convenience, this terminology has been chosen to distinguish different approaches to construct the model primary rate equation (the equation replacing (1)). It is pointed out that some authors prefer to use the term hypoplasticity as interchangeable with incremental non-linearity, thus considering also barodesy [Kol12] and incrementally non-linear bounding surface plasticity [Daf86] as sub-classes of hypoplasticity.

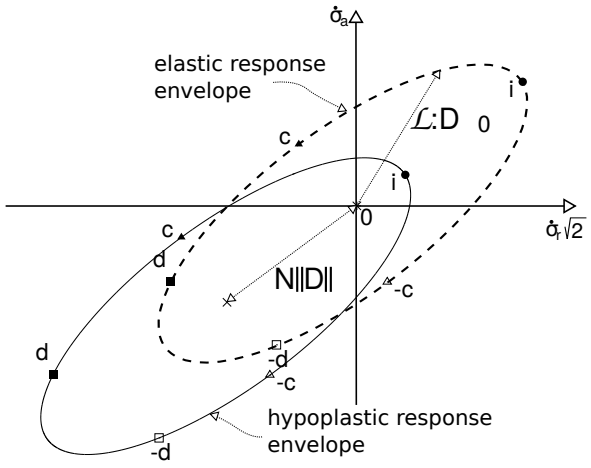

Figure 1: Response envelope of elastic and hypoplastic models. The hypoplastic response envelope is formed from the elastic response envelope $\mathcal{L}$: **D** by translation, which is specified by $\mathbf{N}\|\mathbf{D}\|$ (from [Maš19]).

where the stress state is defined by the shear stress τ, strain by shear strain γ and constitutive response through two moduli L and N. dX represents infinitesimal increment of a variable X. In hypoplasticity, the switch function distinguishing between loading and unloading and the strain decomposition into elastic and plastic parts are not adopted. A scalar "modulus" N may be defined as

$$N = LY \tag{4}$$

where Y is calculated using

$$Y = \frac{\tau}{\tau_{yield}} \tag{5}$$

where τ_{yield} is a limit (yield) shear stress. The modulus L is specified using parameter E_n such that $L = E_n$. The hypoplastic model requires two parameters τ_{yield} and E_n. Eq. (3) leads to predictions of the loading-unloading cycle shown in Fig. 2 (for $E_n = 2000$ kPa and $\tau_{yield} = -100$ kPa), where predictions are compared with equivalent elastic perfectly plastic model.

The following two cases are important for clarifying performance of the hypoplastic model:

1. When $\tau = 0$, Y, calculated using Eq. (5), is also equal to zero. Therefore, $N = 0$ and thus
$$d\tau = Ld\gamma \tag{6}$$
L thus specifies the initial modulus for loading from the state $\tau = 0$.

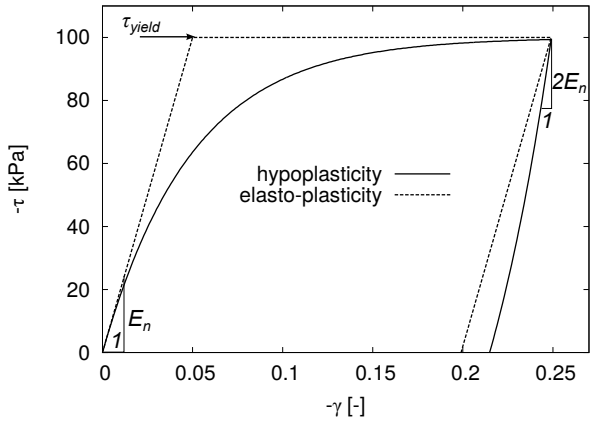

Figure 2: Comparison of predictions of simple scalar hypoplastic and elasto-plastic models for shear (from [Maš19]).

2. When $\tau = \tau_{yield}$, Y is equal to one. Therefore, $N = L$ and the hypoplastic equation reads

$$d\tau = L(d\gamma + |d\gamma|) \tag{7}$$

During loading, $d\gamma < 0$ and therefore $d\tau = 0$. During unloading, $d\gamma > 0$ and hypoplasticity predicts

$$d\tau = 2Ld\gamma \tag{8}$$

It follows from the above that for the special cases of $\tau = 0$ and $\tau = \tau_{yield}$ the hypoplastic model predicts responses identical to the elastic perfectly plastic model (apart from the unloading modulus at $\tau = \tau_{yield}$, which is twice as high as the loading modulus at $\tau = 0$). The two models thus predict the same asymptotic states (see Sect. 2.4). The most important difference in predictions of the two models is in the intermediate states $\tau_{yield} < \tau < 0$. While elastic perfectly plastic model predicts constant stiffness E_n, hypoplasticity predicts a gradual decrease of stiffness, starting from the initial modulus E_n and ending with the fully plastic state with stiffness equal to zero. The stiffness decrease is caused by the definition of Y, whose value gradually increases from 0 to 1 and thus forces the modulus N to vary between zero and L. Hypoplastic model thus inherently predicts non-linearity without having to introduce complex hardening laws of advanced elasto-plastic models.

2.3 Historical overview of hypoplasticity development

The first hypoplastic equations, developed at the end of the 1980's and in the 1990's at the University of Karlsruhe, considered Cauchy stress as the only state variable. The general form of a constitutive equation then reads

$$\mathring{\mathbf{T}} = G(\mathbf{T}, \mathbf{D}) \tag{9}$$

Kolymbas [Kol85, Kol91a, Kol91b] adopted a rational mechanics approach and expressed properties that a constitutive equation of the general form (9) should obey to predict the behaviour of sand. The following requirements and constitutive equation properties have been emphasized:

1. According to the third postulate by Truesdell and Noll [TN65], denoted as the principle of material frame-indifference (principle of material objectivity), constitutive equations must be invariant under changes of frame of reference. That is, two observers, even in a relative motion, must observe the same stress in a body. Objectivity requires $G()$ from Eq. (9) to be an isotropic function of both arguments $\mathbf{T}$ and $\mathbf{D}$. That means

$$\mathbf{Q} \cdot G(\mathbf{T}, \mathbf{D}) \cdot \mathbf{Q}^T = G(\mathbf{Q} \cdot \mathbf{T} \cdot \mathbf{Q}^T, \mathbf{Q} \cdot \mathbf{D} \cdot \mathbf{Q}^T) \qquad \text{for } \forall\, \mathbf{Q} \tag{10}$$

   where $\mathbf{Q}$ is an arbitrary orthogonal tensor, which quantifies rotation.

2. To represent *asymptotic behaviour* (see Sec. 2.4), function $G()$ from Eq. (9) should be positively homogeneous with respect to stress

$$G(\lambda\mathbf{T}, \mathbf{D}) = \lambda^m G(\mathbf{T}, \mathbf{D}) \qquad \text{for} \qquad \forall\lambda > 0 \tag{11}$$

   Note that later on, Niemunis [Nie03] demonstrated that (11) is not necessary to predict asymptotic behaviour (so-called directional homogeneity is sufficient).

3. Rate-independence requires Eq. (9) to be positively homogeneous of degree one in $\mathbf{D}$, that is

$$G(\mathbf{T}, \lambda\mathbf{D}) = \lambda G(\mathbf{T}, \mathbf{D}) \qquad \text{for} \qquad \forall\lambda > 0 \tag{12}$$

The above three properties pose restrictions on $G()$. The general representation theorem of isotropic tensor-valued functions of two symmetric tensorial arguments has been proposed by Wang [Wan70]. He has shown that $G()$ can be, under full generality, written as

$$\begin{aligned} G(\mathbf{T}, \mathbf{D}) = \phi_1\mathbf{1} + \phi_2\mathbf{T} + \phi_3\mathbf{D} + \phi_4\mathbf{T}^2 + \phi_5\mathbf{D}^2 + \phi_6(\mathbf{T}\cdot\mathbf{D} + \mathbf{D}\cdot\mathbf{T}) + \\ \phi_7(\mathbf{T}\cdot\mathbf{D}^2 + \mathbf{D}^2\cdot\mathbf{T}) + \phi_8(\mathbf{T}^2\cdot\mathbf{D} + \mathbf{D}\cdot\mathbf{T}^2) + \phi_9(\mathbf{T}^2\cdot\mathbf{D}^2 + \mathbf{D}^2\cdot\mathbf{T}^2) \end{aligned} \tag{13}$$

where the operation $\mathbf{X}^2$ is defined as $\mathbf{X}^2 = \mathbf{X}\cdot\mathbf{X}$, where the scalars ϕ_1, $\phi_2 \ldots \phi_9$ are joint invariants of $\mathbf{T}$ and $\mathbf{D}$. Considering the other two restrictions on $G()$, Kolymbas [Kol91a] expressed the first hypoplastic model (by that time denoted as the "generalised hypoelastic equation") as

$$\begin{aligned} G(\mathbf{T}, \mathbf{D}) = C_1\mathbf{T}\,\mathrm{tr}\,\mathbf{D} + C_2\,\mathrm{tr}(\mathbf{T})\,\mathrm{tr}(\mathbf{D})\mathbf{1} + C_3\mathbf{T}\frac{\mathbf{D}^2}{\sqrt{\mathrm{tr}\,\mathbf{D}^2}} + \\ C_4(\mathbf{T}\cdot\mathbf{D} + \mathbf{D}\cdot\mathbf{T}) + C_5\mathbf{T}\sqrt{\mathrm{tr}\,\mathbf{D}^2} + \ldots \end{aligned} \tag{14}$$

The summands on the right-hand side of Equation (14) have been termed "generators" and their series is infinite. C_i in (14) are material constants. Kolymbas [Kol91a]

pointed out that this infinite sum is not endowed with a hierarchy, as is the case with, for example, a Taylor series. Instead, any generator can be equally important or unimportant in contributing to the description of the material behaviour. Kolymbas [Kol91a] developed a computer code, which tested different combinations of the generators and, by a trial-and-error procedure, selected a minimal set of generators that best represented the known behaviour of granular materials. For each version of the model, he tested the following predictive capabilities:

1. Response envelopes.
2. Stress paths predicted for proportional strain paths (paths with constant **D**).
3. Predictions of typical laboratory tests on soils (drained triaxial test, oedometric test, simple shear test).
4. Limit surface (equivalent of yield surface in elasto-plasticity).

Illustrative examples of the selection process are given in Figures 3 (response envelopes).

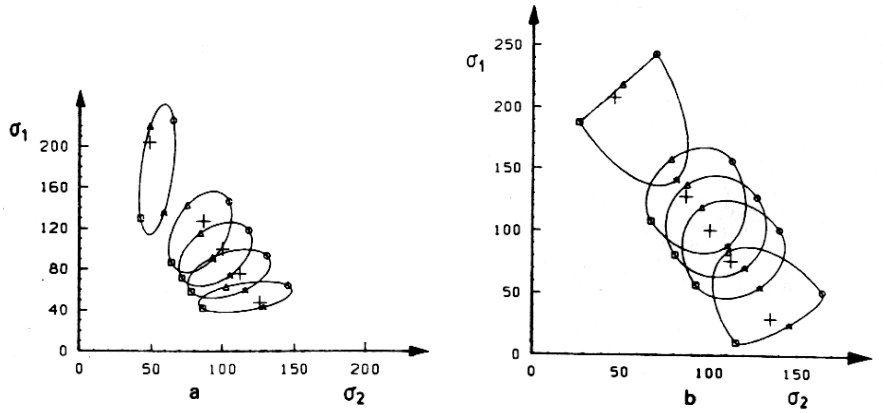

(a) (b)

Figure 3: Response envelopes predicted by two choices of generators in the first hypoplastic equation development by Kolymbas [Kol91a]. (a) accepted, (b) rejected.

The following hypoplastic version has been selected as the most suitable [Kol91a]:

$$\mathring{\mathbf{T}} = C_1 \left(\mathbf{T}\cdot\mathbf{D} + \mathbf{D}\cdot\mathbf{T}\right) + \mathbf{1}C_2\mathbf{T}:\mathbf{D} + \left(C_3\mathbf{T} + C_4\frac{\mathbf{T}\cdot\mathbf{T}}{\operatorname{tr}\mathbf{T}}\right)\sqrt{\mathbf{D}:\mathbf{D}} \qquad (15)$$

with material parameters C_1 to C_4. These can be related to the more familiar soil characteristics like friction angle, dilatancy angle and Young's modulus [Kol85].

Equation (15) was taken over by [Wu92, Wu99], who proposed an alternative version based on the quantitative analysis of the model performance:

$$\mathring{\mathbf{T}} = C_1 \mathbf{D} \operatorname{tr} \mathbf{T} + C_2 \frac{\mathbf{T} \operatorname{tr}(\mathbf{T} \cdot \mathbf{D})}{\operatorname{tr} \mathbf{T}} + \left(C_3 \frac{\mathbf{T} \cdot \mathbf{T}}{\operatorname{tr} \mathbf{T}} + C_4 \frac{\mathbf{T}^* \cdot \mathbf{T}^*}{\operatorname{tr} \mathbf{T}} \right) \sqrt{\mathbf{D} : \mathbf{D}} \tag{16}$$

where $\mathbf{T}^* = \mathbf{T} - (\operatorname{tr} \mathbf{T})\mathbf{1}/3$ is the deviatoric stress tensor. Wu [Wu92] also pointed out that Eq. (16) can be recast in the following more convenient form of Eq. (2):

$$\mathring{\mathbf{T}} = \mathcal{L} : \mathbf{D} + \mathbf{N} \|\mathbf{D}\| \tag{17}$$

with the fourth- and second-order moduli $\mathcal{L}$ and $\mathbf{N}$ defined as

$$\mathcal{L} = \operatorname{tr} \mathbf{T} \left(C_1 \mathcal{I} + C_2 \hat{\mathbf{T}} \otimes \hat{\mathbf{T}} \right) \tag{18}$$

$$\mathbf{N} = \operatorname{tr} \mathbf{T} \left(C_3 \hat{\mathbf{T}} \cdot \hat{\mathbf{T}} + C_4 \hat{\mathbf{T}}^* \cdot \hat{\mathbf{T}}^* \right) \tag{19}$$

where $\hat{\mathbf{T}} = \mathbf{T} / \operatorname{tr} \mathbf{T}$. Later on, Lanier et al. [LCC$^+$04] proved that any other hypoplastic equation based on (13) and combined with the other requirements stated above can be expressed in the form of Eq. (17).

Eq. (17) formed the basis for subsequent development of hypoplastic models. Gudehus [Gud96] introduced critical state concept using so-called *pyknotropy factor* through the incorporation of the pressure-dependent limiting void ratio curves by Bauer [Bau96]. Subsequently, von Wolffersdorff [vW96] included Matsuoka and Nakai [MN74] limit stress condition, creating a model which is nowadays considered as a reference hypoplastic model for sand. Its parameters will be described in more detail in Sec. 2.5.

2.4 Explicit Incorporation of Asymptotic States

Though the procedure for model formulation described in Sec. 2.3 led to the first hypoplastic models, it has later been found that it is possible to directly manipulate Eq. (2) without a need to identify individual generators of the [Wan70] theorem. Such an approach has been put forward by [Nie03] for explicit incorporation of failure surface and later by [Maš12] for explicit introduction of asymptotic states, similarly to what is being done in elasto-plastic critical state-based models and in barodesy (Sec. 3).

The general rate formulation of the model is the same as that proposed by Gudehus [Gud96], that is

$$\mathring{\mathbf{T}} = f_s (\mathcal{L} : \mathbf{D} + f_d \mathbf{N} \|\mathbf{D}\|) \tag{20}$$

where additional scalar *barotropy* f_s and *pyknotropy* f_d factors have been introduced, when compared with the basic hypoplastic equation (2). To incorporate the asymptotic state boundary surface (ASBS), it is assumed that it changes its size with variable void ratio, but not its shape. As the size of the asymptotic state boundary surface is measured by the Hvorslev's equivalent pressure p_e, the following formulation of the isotropic normal compression line was assumed:

$$\ln(1 + e) = N - \lambda^* \ln(p / p_r) \tag{21}$$

where N and λ^* are parameters and $p_r = 1$ kPa is a reference stress. p_e can thus be calculated from

$$p_e = p_r \exp\left[\frac{N - \ln(1+e)}{\lambda^*}\right] \tag{22}$$

As the asymptotic state boundary surface does not change its shape during proportional asymptotic loading, the stress normalised by the Hvorslev's equivalent pressure $\mathbf{T}_n = \mathbf{T}/p_e$ remains constant. Therefore,

$$\mathring{\mathbf{T}}_n = \frac{\mathring{\mathbf{T}}}{p_e} - \frac{\mathbf{T}}{p_e^2}\dot{p}_e = \mathbf{0} \tag{23}$$

$\dot{p}_e$ follows from (22)

$$\dot{p}_e = -\frac{p_e}{\lambda^*}\left(\frac{\dot{e}}{1+e}\right) = -\frac{p_e}{\lambda^*}\operatorname{tr}\mathbf{D} \tag{24}$$

Combining of (24), (23) and (20) implies that

$$\mathring{\mathbf{T}}_n = \frac{f_s}{p_e}\left(\mathcal{L} : \mathbf{D} + f_d\mathbf{N}\|\mathbf{D}\|\right) + \frac{\mathbf{T}}{p_e\lambda^*}\operatorname{tr}\mathbf{D} = \mathbf{0} \tag{25}$$

and thus

$$-\frac{\mathbf{T}}{\lambda^*}\operatorname{tr}\mathbf{D}^A = f_s\left(\mathcal{L} : \mathbf{D}^A + f_d^A\mathbf{N}\|\mathbf{D}^A\|\right) \tag{26}$$

where f_d^A is the value of f_d at the asymptotic state boundary surface and $\mathbf{D}^A$ is the asymptotic strain rate corresponding to the given stress state. Equation (26) can be manipulated in the following way:

$$-\left(\frac{\mathbf{T}}{\lambda^*}\operatorname{tr}\mathbf{D}^A + f_s\mathcal{L} : \mathbf{D}^A\right) = f_s f_d^A\mathbf{N}\|\mathbf{D}^A\| \tag{27}$$

$$-\mathcal{A} : \mathbf{D}^A = f_s f_d^A\mathbf{N}\|\mathbf{D}^A\| \tag{28}$$

$$-\mathcal{A} : \mathbf{d} = f_s f_d^A\mathbf{N} \tag{29}$$

where

$$\mathcal{A} = f_s\mathcal{L} + \frac{\mathbf{T}}{\lambda^*}\otimes\mathbf{1} \tag{30}$$

$$\mathbf{d} = \frac{\mathbf{D}^A}{\|\mathbf{D}^A\|} \tag{31}$$

Eq. (29) implies that

$$\mathbf{N} = -\frac{\mathcal{A} : \mathbf{d}}{f_s f_d^A} \tag{32}$$

Combining (32) with (20) yields an alternative expression for the hypoplastic model:

$$\mathring{\mathbf{T}} = f_s\mathcal{L} : \mathbf{D} - \frac{f_d}{f_d^A}\mathcal{A} : \mathbf{d}\|\mathbf{D}\| \tag{33}$$

An arbitrary shape of the asymptotic state boundary surface can be incorporated into hypoplasticity with the aid of Eq. (33), by appropriate specification of the dependence of f_d^A on the void ratio and stress ratio (Figure 4). The corresponding asymptotic direction of the strain rate is then specified by $\mathbf{d}$. The approach presented in this section has been adopted by Mašín [Maš13] in the development of a rate independent model for clays. Parameters of this model are detailed in Sec. 2.6.

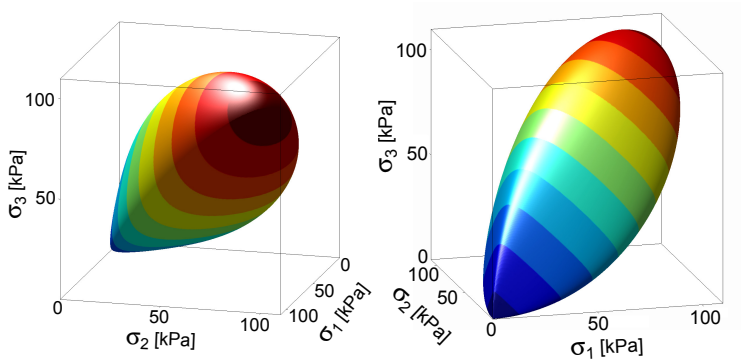

Figure 4: Asymptotic state boundary surface of clay hypoplastic model (from [Maš13])

2.5 Sand hypoplastic model

In this section, the hypoplastic model developed by von Wolffersdorff [vW96] is introduced. This model is often considered as the reference hypoplastic model for predicting the behaviour of granular materials. We will leave aside details of its mathematical formulation, which the interested readers can find elsewhere [Nie03, Maš19]. Instead, we will summarise its material parameters which the students will search for during the calibration excercise. The model is defined using eight parameters φ_c, h_s, n, e_{c0}, e_{d0}, e_{i0}, α and β and void ratio as a state variable additional to Cauchy stress. Its calibration procedure has been described in detail in [HG99, Maš19].

φ_c is a critical state friction angle in a classical critical state soil mechanics sense. The simplest way of calibrating φ_c is to measure the angle of repose. Other means of its determination are triaxial shear tests, preferably on samples in a loose state to reduce shear-banding.

Parameters h_s and n control the shape of the limiting void ratio curves. They are sketched in Fig. 5, and they are described by

$$\frac{e_i}{e_{i0}} = \frac{e_c}{e_{c0}} = \frac{e_d}{e_{d0}} = \exp\left[-\left(\frac{-\operatorname{tr}\mathbf{T}}{h_s}\right)^n\right] \tag{34}$$

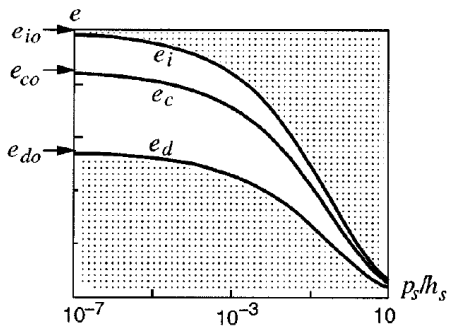

Figure 5: Limiting pressure-dependent void ratio lines by Gudehus [Gud96]; Figure from Herle and Gudehus [HG99].

The parameters h_s and n specify not only the limiting void ratio curves, but also any other normal compression line followed in asymptotic compression, such that

$$e_p = e_{p0} \exp\left[-\left(\frac{3p}{h_s}\right)^n\right] \tag{35}$$

e_{p0} controls the position of the normal compression lines for different strain rate directions, and it is bound by the following inequality: $e_{c0} < e_{p0} < e_{i0}$. Of the possible proportional strain path tests, the oedometric test is the most accessible and easy to perform. This test is thus preferable for h_s and n calibration, where h_s controls its slope and n its curvature.

The parameter e_{c0} specifies the position of the critical state line in the p vs. e plane through Eq. (34). The most appropriate way for its determination is thus based on shear test results; undrained triaxial shear tests are best for the purpose as the samples are less susceptible to shear banding than in drained tests. A simplified way of e_{c0} calibration is based on the following logic. The soil in a heap formed during the angle of repose test is in the loosest possible state, which corresponds to the critical state. Its stress state is close to zero thanks to the small amount of soil used. The void ratio of a soil in this loose heap thus approximates e_{c0}.

Parameter e_{i0} specifies the position of the theoretical isotropic normal compression line. In clays, this line may easily be determined experimentally using isotropic compression experiments. In granular soils, however, its direct experimental investigation is difficult, as the initial void ratio is typically below e_{c0} and the state converges towards e_i-line very slowly during isotropic compression. In fact, e_i-line is a theoretical limit of the maximum void ratio corresponding to the loosest assembly of grains in the gravity-free space. An empirical equation for e_{i0} was investigated by Herle and Gudehus [HG99], who studied idealised packing of spherical particles at a state of minimum density. They proposed the following empirical relationship for e_{i0}, which

is recommended for e_{i0} calibration:

$$e_{i0} = 1.2 e_{c0} \tag{36}$$

e_{d0} specifies the position of the minimum void ratio line. The best densification of a granular material can generally be reached by means of cyclic shearing of small amplitude under constant pressure (Fig. 6). e_{d0} can then be obtained by extrapolation using h_s and n evaluated from the procedure described above.

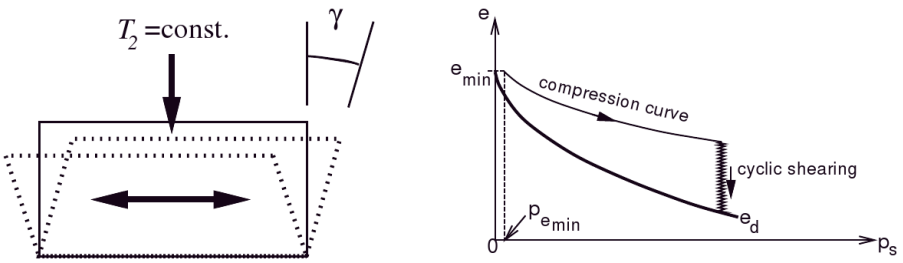

Figure 6: Experimental identification of e_d [HG99].

The peak friction angle φ_p predicted by the hypoplastic model is implied from the value of the relative void ratio r_e. For the given r_e, the actual value of φ_p is controlled by the parameter α. It can, in general, be calibrated using drained triaxial tests on densely compacted soil samples. If available, however, experiments with the relative void ratio present in the soil deposit to be simulated are more suitable (the same recommendation holds true for calibration of the parameter β). Calibration of the parameter α using drained triaxial test on Komorany sand is demonstrated in Fig. 7a. The experiment was performed at a cell pressure of 100 kPa. Figure 7a demonstrates that an increase of the α value increases the predicted peak friction angle. This parameter is typically calibrated by fitting the experimental data using a trial-and-error procedure.

Parameter β enters in the model the formulation of the barotopy factor f_s and controls both the bulk and shear stiffness. The most relevant way to determine β is adopting the results of drained triaxial tests on densely compacted soil samples; the same tests as those used to calculate the parameter α can be adopted. Calibration of β using a drained triaxial test is demonstrated in Fig. 7b. It is clear that an increase of β increases the soil stiffness. Similar to α, parameter β is typically calibrated using a trial-and-error procedure by fitting the experimental data to the model.

2.6 Clay hypoplasticity

Clay hypoplastic model, formulated by [Maš13], has been developed using approach from Sec. 2.4. Its parameters coincide with parameters of the Modified Cam-clay

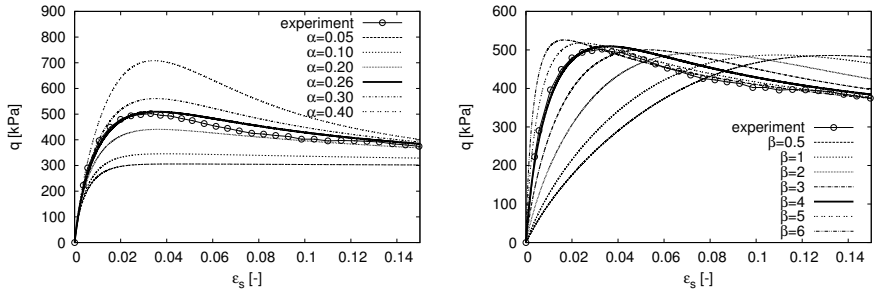

(a) (b)

Figure 7: Calibration of the parameter α (a) and β (b) using the stress-strain curve from a drained triaxial test on dense Komorany sand (from [Maš19]).

model [RB68], namely φ_c, N, λ^*, κ^* and ν. They will be summarised here for student's calibration excercise.

Critical state friction angle φ_c has the same physical meaning as this parameter of sand hypoplastic model and it is typically calibrated using triaxial shear test, preferably undrained triaxial shear test (CIUP) on normally consolidated (soft) reconstituted clay to reduce shear-banding.

Parameter N defines the position of the isotropic normal compression line, whereas the parameter λ^* defines its slope in the $\ln p$ vs $\ln(1+e)$ plane, as shown in Figure 8. Parameters N and λ^* are best calibrated using an isotropic compression test, but the

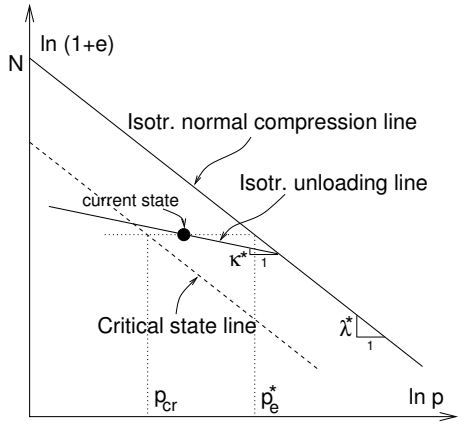

Figure 8: Definition of parameters N and λ^* [Maš05].

oedometric compression test may also be used for this purpose, as λ^* also represents

a slope of the K_0 normal compression line in the $\ln \sigma_a$ vs $\ln(1+e)$ plane (where σ_a is vertical stress) and N can be calibrated from its position.

In the Modified Cam-clay model, the parameter κ specifies the slope of the isotropic unloading line. The hypoplastic parameter κ^* also controls this slope; due to the non-linear model formulation, however, the slope of the unloading line is not constant in the $\ln p$ vs $\ln(1+e)$ plane and it varies with the overconsolidation ratio. It is thus preferable to calibrate the parameter κ^* by direct simulation of the unloading test or by simulation of the compression test starting from the overconsolidated state. Both isotropic (preferable) and oedometric tests can be adopted for this purpose. Calibration of the parameter κ^* using an isotropic unloading test on Weald clay is shown in Fig. 9a (data from Henkel [Hen56]). Another example in Fig. 9b shows the case when an oedometric compression experiment starting from the overconsolidated state is adopted to calibrate κ^* (data from Svoboda et al. [SMB10]).

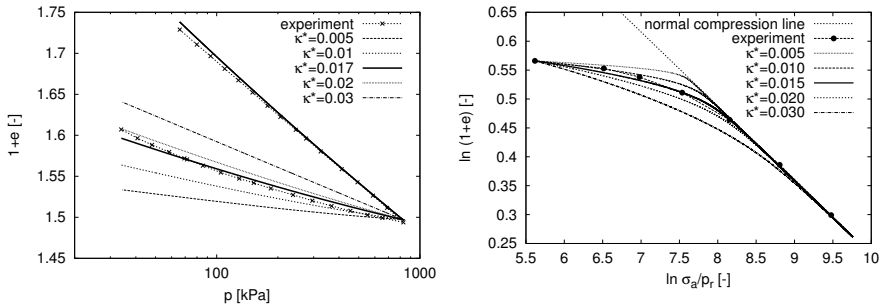

(a) (b)

Figure 9: (a) Calibration of the parameter κ^* using an isotropic unloading test on Weald clay. Experimental data by Henkel [Hen56], (b) Calibration of the parameter κ^* using the oedometric compression test on Brno clay. Experimental data from Svoboda et al. [SMB10] (figures from [Maš19]).

Parameter ν has the standard meaning of the Poisson's ratio within the isotropic elastic tensor $\mathcal{L}$. However, its influence on model predictions is different compared to elasto-plastic models, because in hypoplasticity the radial strains are also always influenced by the non-linear part of the model involving the $\mathbf{N}$ tensor. As in the Cam-clay model, however, ν regulates the shear stiffness. Similarly to the parameter κ^*, ν should be calibrated by means of simulation of triaxial shear tests. An example of such a calibration is shown in Fig. 10, where results of an undrained triaxial test on Dortmund clay (experimental data from [HMK$^+$11]) are compared with the model predictions obtained using different values of ν. An increase of ν decreases the predicted shear modulus (Fig. 10a). The parameter ν also affects the evolution of excess pore water pressures in the undrained test and thus the undrained effective stress paths (Fig. 10b).

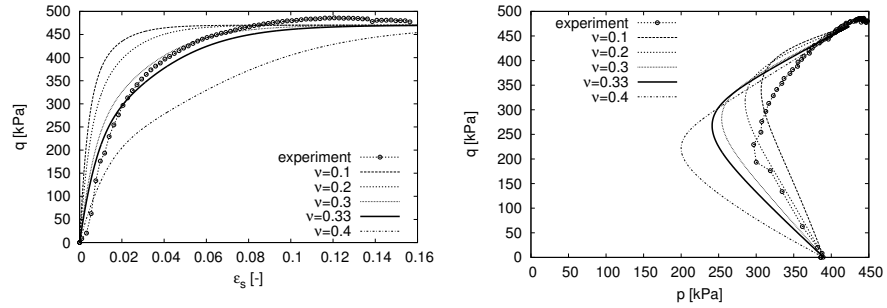

(a) (b)

Figure 10: Calibration of the parameter ν using undrained triaxial test on Dortmund clay. (a) stress-strain curves, (b) stress paths. Experimental data by Herle et al. [HMK$^+$11] (figures from [Maš19]).

3 Barodesy

Barodesy [Kol12, Kol15, MKF16, KM16, MF17] is another class of incrementally non-linear constitutive equations which cannot be expressed analytically using $\mathcal{M}$ from Eq. (1). Barodesy has been build around Goldscheider's rules [Gol82] of soil asymptotic behaviour, telling that [KM16]:

1. Starting from stress-free state, proportional strain paths lead to proportional stress paths.
2. Starting from a non-vanishing stress state and applying a proportional strain path leads asymptotically to the proportional stress path that would be obtained starting from the stress-free state.

Proportional path is a path deviating from origin, such that $\vec{\mathbf{T}} = \vec{\mathbf{T}}$, see Figure 11.

Central to the barodetic model is a function $\mathbf{R}(\mathbf{D})$, which specifies the asymptotic direction of stress depending on the given stretching direction $\mathbf{D}$, such that

$$\mathbf{T} = \mu \mathbf{R}(\mathbf{D}) \tag{37}$$

where $0 < \mu < \infty$. The constitutive model rate form of barodesy reads

$$\dot{\mathbf{T}} = h \left(f \vec{\mathbf{R}} + g \vec{\mathbf{T}} \right) \|\mathbf{D}\| \tag{38}$$

where h, f and g are scalar factors. The term $f\vec{\mathbf{R}}$ represents the target asymptotic stress ratio and the term $g\vec{\mathbf{T}}$ ensures that for other than asymptotic stress ratios the stress ratio converges towards the asymptotic one in proportional loading. Scalar h, which is stress-dependent, controls stress-dependency of soil stiffness and scalars f

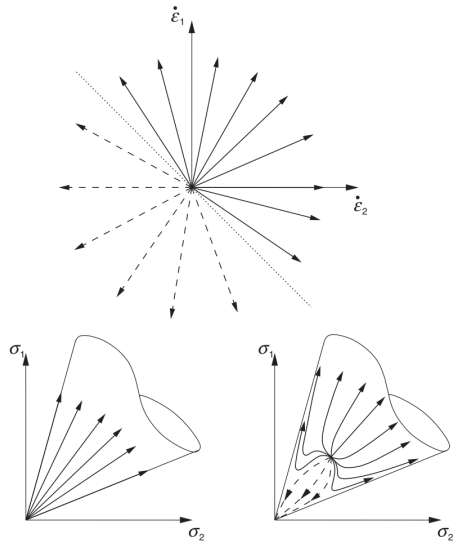

Figure 11: Proportional strain paths (top) and demonstration of the first (bottom left) and second (bottom right) Goldscheider's rules (from [Kol12]).

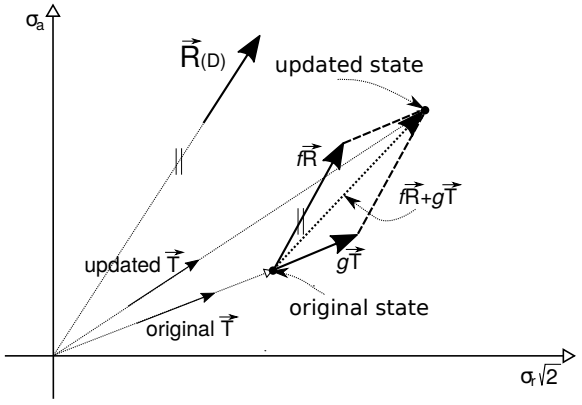

Figure 12: Demonstration of asymptotic properties of barodesy (from [Maš19]), assuming $h\|\mathbf{D}\|\Delta t = 1$ for graphics simplicity.

and g introduce the effect of density. The principle of barodesy is demonstrated in Figure 12.

The function $\vec{\mathbf{R}}$, specifying which proportional stress path associates with particular

stretching direction **D**, is in the more recent versions of barodesy expressed as:

$$\mathbf{R} = -\exp\left(\alpha\vec{\mathbf{D}}\right) \tag{39}$$

where α is a function of $\mathrm{tr}(\vec{\mathbf{D}})$ and exponential of a tensor is defined via its eigenvalues A_1, A_2 and A_3 as

$$\exp\mathbf{A} = \begin{pmatrix} \exp A_1 & 0 & 0 \\ 0 & \exp A_2 & 0 \\ 0 & 0 & \exp A_3 \end{pmatrix} \tag{40}$$

The expression for $\mathbf{R}$ defines proportional stress ratios and, in combination with expressions for f and g it defines a shape of asymptotic state boundary surface predicted by barodesy (and thus also peak and critical states). Properties of Eq. (39) have been studied in [FO13], who observed that the expression for $\mathbf{R}$ practically coincides with yield condition of Matsuoka and Nakai [MN74] (see Figure 13 from [MKF16]).

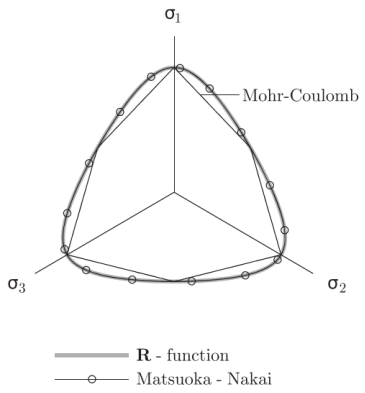

Figure 13: Limit state condition (stress corresponding to zero $\mathrm{tr}\,\mathbf{D}$) of barodesy expressed in deviatoric plane along with failure condition of Matsuoka and Nakai [MN74] and Mohr-Coulomb (from [MKF16]).

Stemming from its very basic formulation (38), barodetic equation is inelastic. As pointed out by [Kol15], the second term in Eq. (38) (that is, $g\vec{\mathbf{T}}$) may be independent of **D** (in that case it does not change if **D** is switched to $-$**D**, similarly to **N** in hypoplasticity), whereas the term $f\vec{\mathbf{R}}$ depends on **D** (note that in some more recent versions, such as [MF17], even the $g\vec{\mathbf{T}}$ term depends on **D**). The directional response of the model is in any case less straightforward to interpret than in hypoplasticity, as the term $f\vec{\mathbf{R}}$ cannot be reconciled in a simple form $\mathcal{L} : \mathbf{D}$, which would yield elliptic response envelopes if $f\vec{\mathbf{R}}$ would be independent of **D**. Actually, barodesy is characterised by response envelopes with rather complex shapes (see Fig. 14), which makes it more difficult to combine it with a model for small-strain elastic behaviour [BFM$^+$19].

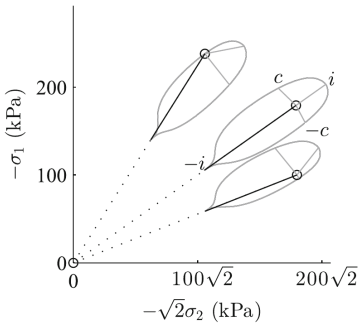

Figure 14: Response envelopes predicted by barodesy (from [MF17]).

Similarly to the initial versions of hypoplasticity, barodesy has first been defined to represent the behaviour of sand [Kol12, Kol15], but the models have soon be extended for the behaviour of clay [MF17], their properties were studied in detail [MKF16] and specific features of the model formulation were further updated [Fel13]. Recently, the model has been incorporated into an approach to predict small strain stiffness and cyclic loading effects [BFM$^+$19].

4 Incrementally non-linear bounding surface plasticity

Most advanced elasto-plastic models with kinematic hardening rules [Mróz67, ATMW89, ST97, TD08, GMW99] and even the generalized plasticity models with different plastic mechanisms for loading and unloading [PZC90], which are highly non-linear in stress-strain response, are inceremental bi-linear. Nevertheless, models exist which are based on elasto-plasticicty concepts and fall within the incrementally non-linear category. The most notable examples are bounding surface models with stress-rate direction dependent flow rule [Daf86, WDS90, DT16]. Note that these models have been denoted by their authors as hypoplastic due to their incrementally non-linear character (the term hypoplasticity has actually been first used for these type of models, before the term was taken over for the group of models described by Eq. (2)). These models will be described in this chapter. Another example of incrementally-nonlinear model is so-called overlay enhancement of existing elasto-plastic model proposed by Benz et al. [BVS09] and applied to the hardening soil model by Benz [Ben07]. In their model, the elastic stiffness matrix depends on the loading direction with respect to the previous loading history and the model is thus incrementally non-linear. Its principle is similar to the intergranular strain extension of hypoplastic models.

An interesting property of incrementally non-linear bounding surface plasticity models is that they become intrinsically implicit - the stress rate $\mathbf{T}$ is calculated by Eq. (1)

using stiffness matrix $\mathcal{M}$, where $\mathcal{M}$ itself depends on the stress rate $\dot{\mathbf{T}}$. This property makes the models more complex from the numerical integration standpoint, implicit integration algorithm can however still be defined [PD19] and models used within numerical computations of boundary value problems.

A notable recent example of these models is a zero elastic range plasticity model for sands denoted as SANISAND-Z [DT16, TD17], which will be described in this section. Most of the components of SANISAND-Z model actually follow from the family of rotational and isotropic hardening elasto-plastic models (such as [MD97, GMW99]), with a version of SANISAND model enhanced by fabric changes effects [DM04] as a direct predecessor. These models consider a rotational hardening yield surface to be represented by a thin cone (either closed for isotropic hardening, or not for simplicity) in the stress space (Figure 15), with hardening modulus controlling the model response calculated by means of distance of current stress from so-called image point on bounding surface and possibly other helper surfaces (critical state surface and dilatancy surface for SANISAND model), see Figure 15.

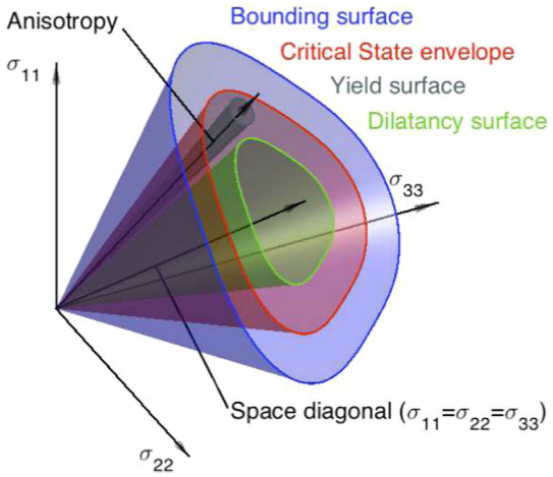

Figure 15: Yield, bounding and other surfaces of SANISAND model [YST19].

Central to the model are then so-called mapping rules, defining how an image point is found on bounding surface from the known stress-state and current position of the yield surface. This mapping rule is for the case of SANISAND model (for simplicity for bounding surface F^b only) demonstrated in Figure 16a.

The hardening law is defined in deviatoric plane. The key is to find an image point $\boldsymbol{r}^b$ on the bounding surface F^b for current stress deviator $\boldsymbol{r}$. For this, normal $\boldsymbol{n}$ to the yield surface is constructed first and $\boldsymbol{r}^b$ is found by projecting the deviatoric plane origin onto bounding surface in the direction $\boldsymbol{n}$. Hardening rules are then assembled such that the deviatoric stress rate direction $\vec{\boldsymbol{r}}$ coincides with the direction of the tensor

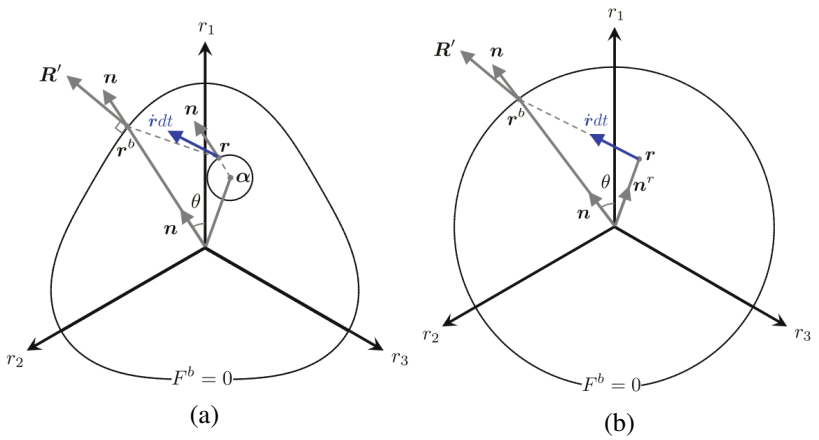

Figure 16: Mapping rule of SANISAND model (a) and equivalent mapping rule of SANISAND-Z model (b) (from [TD17]).

$\boldsymbol{r} - \boldsymbol{r}^b$. Plastic deviatoric strain rate direction is then defined by normal $\boldsymbol{R'}$ to the bounding surface at the image point $\boldsymbol{r}^b$.

The idea of zero elastic range model is founded in experimental observations indicating that the "true" elastic range of soils is very small, if not vanishing, such that the yield surface of properly calibrated SANISAND model is very narrow, still adding-up significantly to the model complexity. In addition, it has been observed that from the standpoint of cyclic loading simulations, which is the primary target of these models, vanishing elastic range does not lead to much different results. In SANISAND-Z, the procedure of defining the image point is very much reversed, with $\vec{\dot{\boldsymbol{r}}}$ being input into the derivation of image point instead of being output of the model elasto-plastic structure (in [DM04] model, the direction of $\dot{\boldsymbol{r}}$ is implied by the translation of the yield surface centre $\boldsymbol{\alpha}$ in the deviatoric plane in the direction $\boldsymbol{r} - \boldsymbol{r}^b$). In the incrementally non-linear version of the model, current deviatoric stress $\boldsymbol{r}$ is simply projected onto the bounding surface F_b in the direction $\vec{\dot{\boldsymbol{r}}}$ (Figure 16b). Plastic deviatoric strain rate direction is then defined as before to be a normal $\boldsymbol{R'}$ to the Lode angle dependent bounding surface at the image point $\boldsymbol{r}^b$. The Lode-angle dependency of the bounding surface shape has been neglected, while it has been preserved in the calculation of plastic strain increment direction $\boldsymbol{R'}$. Omitting Lode-angle dependency of bounding surface allowed the authors to find a closed-form solution of the image point $\boldsymbol{r}^b$, it would have to be calculated numerically otherwise [Tai21].

From Figure 16b it is clear that plastic strain increment direction $\boldsymbol{R'}$ depends on the stress increment direction $\vec{\dot{\boldsymbol{r}}}$ which renders the model incrementally non-linear. The remaining model features are taken-over from the original model [DM04], preserving thus the primary model predictive capabilities, while simplifying its mathematical formulation, but increasing complexity of its numerical integration through the implicit

formulation as a trade-off.

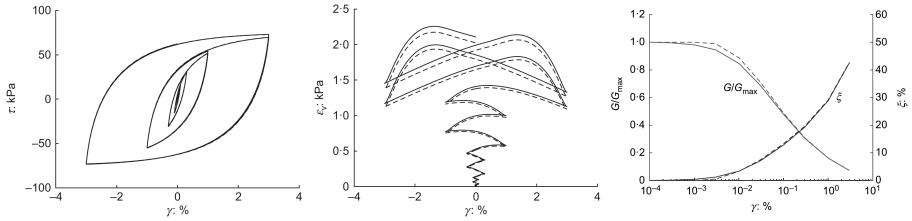

(a) (b)

Figure 17: Drained cyclic simple shear test simulated with [DM04] (dashed lines) and SANISAND-Z (solid lines) models (figure from [DT16]).

For demonstration, see Figure 17 where results of drained cyclic simple shear test are simulated with the incrementally bi-linear model from [DM04] (dashed lines) and with SANISAND-Z model (solid lines). The cyclic response is indeed practically indentical. As expected, the shear modulus degradation curve (Figure 17c) shows a small-strain "plateau" for the [DM04] governed by its non-zero purely elastic range and a gradual decrease for SANISAND-Z. Still, even for the SANISAND-Z model, the "S-shape" of the curve is preserved, which is critical for correct predictions of boundary value problems at continuous loading [DRB96, FPB05, GZP02, YMY06, Mašˇ09].

5 Conclusions

This lecture introduced a particular class of constitutive models for soils, which are characterised by their stiffness matrix $\mathcal{M}$ contiuously dependent on loading direction $\vec{\mathbf{D}}$ (with analytical expression for $\mathcal{M}$ often unavailable). The concepts have been introduced using three particular model classes, namely hypoplasticity, barodesy and incrementally non-linear bounding surface plasticity. Regardless the fact that their formulation often deviates from the well-established concepts of elasto-plasticity, the goal in correctly predicting soil non-linear behaviour is the same and thus also the response of the models is often comparable to advanced elasto-plastic models (see Figure 17). An advantage of incremental non-linear models over advanced models elasto-plastic is arguably simpler mathematical formulation, with some advanced properties such as possibility of explicitly treating the bifurcation and instability phenomena [CD89, Wu00]. This, however, comes at a price of less straightforward modification for various intricate features of soil mechanical behaviour (for hypoplasticity and barodesy) or implicit mathematical structure rendering its numerical implementation a demanding task (for incrementally non-linear bounding surface plasticity).

In any case, incrementally non-linear models, not long ago considered an academic excersise (even in 2002, [TV02] concluded that "the theory of hypoplasticity remains mainly confined to research applications") now have a firm position within the field

of soil constitutive modelling, being available in commercial finite element codes (not only through the SoilModels project [GAG$^+$08]) and adopted in various advanced applications by both academia and practitioners.

6 Acknowledgement

The author is grateful to Mahdi Taiebat, Gertraud Medicus and Jose Duque for their valuable comments on the manuscript.

References

[ATMW89] A. Al-Tabbaa and D. Muir Wood. An experimentally based "bubble" model for clay. In *Proc. 3^{th} Int. Conf. on Numerical Models in Geomechanics*. Niagara Falls, 1989.

[Bau96] E. Bauer. Calibration of a comprehensive constitutive equation for granular materials. *Soils and Foundations*, 36(1):13–26, 1996.

[Ben07] T. Benz. *Small-strain stiffness of soils and its numerical consequences*. PhD thesis, University of Stuttgart, 2007.

[BFM$^+$19] M. Bode, W. Fellin, D. Mašín, G. Medicus, and A. Ostermann. An intergranular strain concept for material models formulated as rate equations. *International Journal for Numerical and Analytical Methods in Geomechanics*, 44:1003–1018, 2019.

[BVS09] T. Benz, P. A. Vermeer, and R. Schwab. A small-strain overlay model. *International Journal for Numerical and Analytical Methods in Geomechanics*, 33:25–44, 2009.

[CD89] R. Chambon and J. Desrues. Shear band analysis for granular materials: The question of incremental non-linearity. *Ingenieur-Archiv*, 59:187–196, 1989.

[Daf86] Y. F. Dafalias. Bounding surface plasticity. I: Mathematical foundation and hypoplasticity. *Journal of Engineering Mechanics ASCE*, 112(9):966–987, 1986.

[DL82] F. Darve and S. Labanieh. Incremental constitutive law for sands and clays: simulation of monotonic and cyclic tests. *International Journal for Numerical and Analytical Methods in Geomechanics*, 6:243–275, 1982.

[DM04] Y. F. Dafalias and M. T. Manzari. Simple plasticity sand model accounting for fabric change effects. *Journal of Engineering Mechanics*, 130(6):622–634, 2004.

[DRB96] G. R. Dasari, C. G. Rawlings, and M. D. Bolton. Numerical modelling of a NATM tunnel construction in London Clay. In R. J. Mair and R. N.

Taylor, editors, *Geotechnical Aspects of Underground Construction in Soft Ground*, pages 491–496. A.A.Balkema, Rotterdam, 1996.

[DT16] Y. F. Dafalias and M. Taiebat. SANISAND-Z: Zero elastic range sand plasticity model. *Géotechnique*, 12:999–1013, 2016.

[Fel13] W. Fellin. Extension to barodesy to model void ratio and stress dependency of the k_0 value. *Acta Geotechnica*, 8:561–565, 2013.

[FO13] W. Fellin and A. Ostermann. The critical state behaviour of barodesy compared with the Matsuoka–Nakai failure criterion. *International Journal for Numerical and Analytical Methods in Geomechanics*, 37(3):299–308, 2013.

[FPB05] J. N. Franzius, D. M. Potts, and J. B. Burland. The influence of soil anisotropy and K_0 on ground surface movements resulting from tunnel excavation. *Géotechnique*, 55(3):189–199, 2005.

[GAG+08] G. Gudehus, A. Amorosi, A. Gens, I. Herle, D. Kolymbas, D Mašín, D. Muir Wood, R. Nova, A. Niemunis, M. Pastor, C. Tamagnini, and G. Viggiani. The soilmodels.info project. *International Journal for Numerical and Analytical Methods in Geomechanics*, 32(12):1571–1572, 2008.

[GMW99] A. Gajo and D. Muir Wood. Severn-Trent sand: a kinematic hardening constitutive model: the q-p formulation. *Géotechnique*, 49(5):595–614, 1999.

[Gol82] M. Goldscheider. True triaxial tests on dense sand. In G. Gudehus, editor, *Constitutive relations for soils*, pages 11–54. Workshop Grenoble, Balkema, 1982.

[Gud96] G. Gudehus. A comprehensive constitutive equation for granular materials. *Soils and Foundations*, 36(1):1–12, 1996.

[GZP02] A. Grammatikopoulou, L. Zdravković, and D. M. Potts. The behaviour of 'bubble' models in tunneling problems. In *Proc. 2^{nd} Int. Conference on Soil Structure Interaction in Urban Civil Engineering, Zürich*, 2002.

[Hen56] D. J. Henkel. The effect of overconsolidation on the behaviour of clays during shear. *Géotechnique*, 6:139–150, 1956.

[HG99] I. Herle and G. Gudehus. Determination of parameters of a hypoplastic constitutive model from properties of grain assemblies. *Mechanics of Cohesive-Frictional Materials*, 4:461–486, 1999.

[HMK+11] I. Herle, D. Mašín, V. Kostkanová, C. Karcher, and D. Dahmen. Experimental investigation and theoretical modelling of soft soils from mining deposits. In C.-K. Chung, Y.-H. Jung, H.-K. Kim, J.-S. Lee, and D.-S. Kim, editors, *Proc. 5^{th} International Symposium on Deformation*

Characteristics of Geomaterials, Seoul, Korea, volume 2, pages 858–864, 2011.

[KM16] D. Kolymbas and G. Medicus. Genealogy of hypoplasticity and barodesy. *International Journal for Numerical and Analytical Methods in Geomechanics*, 40:2532–2550, 2016.

[Kol85] D. Kolymbas. A generalised hypoelastic constitutive law. In *Proc.* 11^{th} *Int. Conf. Soil Mechanics and Foundation Engineering, San Francisco*, page 2626, 1985.

[Kol91a] D. Kolymbas. Computer-aided design of constitutive laws. *International Journal for Numerical and Analytical Methods in Geomechanics*, 15:593–604, 1991.

[Kol91b] D. Kolymbas. An outline of hypoplasticity. *Archive of Applied Mechanics*, 61:143–151, 1991.

[Kol00] D. Kolymbas. *Introduction to hypoplasticity*. A.A.Balkema, 2000.

[Kol12] D. Kolymbas. Barodesy: a new hypoplastic approach. *International Journal for Numerical and Analytical Methods in Geomechanics*, 36:1220–1240, 2012.

[Kol15] D. Kolymbas. Introduction to barodesy. *Géotechnique*, 65(1):52–65, 2015.

[LCC+04] J. Lanier, D. Caillerie, R. Chambon, G. Viggiani, P. Bésuelle, and J. Desrues. A general formulation of hypoplasticity. *International Journal for Numerical and Analytical Methods in Geomechanics*, 28:1461–1478, 2004.

[Mašín05] D. Mašín. A hypoplastic constitutive model for clays. *International Journal for Numerical and Analytical Methods in Geomechanics*, 29(4):311–336, 2005.

[Mašín09] D. Mašín. 3D modelling of a NATM tunnel in high K_0 clay using two different constitutive models. *Journal of Geotechnical and Geoenvironmental Engineering ASCE*, 135(9):1326–1335, 2009.

[Mašín12] D. Mašín. Hypoplastic Cam-clay model. *Géotechnique*, 62(6):549–553, 2012.

[Mašín13] D. Mašín. Clay hypoplasticity with explicitly defined asymptotic states. *Acta Geotechnica*, 8(5):481–496, 2013.

[Mašín19] D. Mašín. *Modelling of Soil Behaviour with Hypoplasticity - Another Approach to Soil Constitutive Modelling*. Springer International Publishing, 2019.

[MD97] M. T. Manzari and Y. F. Dafalias. A critical state two-surface plasticity model for sands. *International Journal for Numerical and Analytical Methods in Geomechanics*, 47(2):255–272, 1997.

[MF17] G. Medicus and W. Fellin. An improved version of barodesy for clay. *Acta Geotechnica*, 12:365–376, 2017.

[MKF16] G. Medicus, D. Kolymbas, and W. Fellin. Proportional stress and strain paths in barodesy. *International Journal for Numerical and Analytical Methods in Geomechanics*, 40:509–522, 2016.

[MN74] H. Matsuoka and T. Nakai. Stress–deformation and strength characteristics of soil under three different principal stresses. In *Proc. Japanese Soc. of Civil Engineers*, volume 232, pages 59–70, 1974.

[Mróz67] Z. Mróz. On the description of anisotropic work-hardening. *Journal of the Mechanics and Physics of Solids*, 15:163–175, 1967.

[Nie03] A. Niemunis. *Extended Hypoplastic Models for Soils*. Habilitation thesis, Ruhr-University, Bochum, 2003.

[PD19] Alexandros L. Petalas and Yannis F. Dafalias. Implicit integration of incrementally non-linear, zero- elastic range, bounding surface plasticity. *Computers and Geotechnics*, 112:386–402, 2019.

[PZC90] M. Pastor, O. C. Zienkiewicz, and A. H. C. Chan. Generalized plasticity and the modelling of soil behaviour. *International Journal for Numerical and Analytical Methods in Geomechanics*, 14:151–190, 1990.

[RB68] K. H. Roscoe and J. B. Burland. On the generalized stress-strain behaviour of wet clay. In J. Heyman and F. A. Leckie, editors, *Engineering Plasticity*, pages 535–609. Cambridge University Press, Cambridge, 1968.

[SMB10] T. Svoboda, D. Mašín, and J. Boháč. Class A predictions of a NATM tunnel in stiff clay. *Computers and Geotechnics*, 37(6):817–825, 2010.

[ST97] S. E. Stallebrass and R. N. Taylor. Prediction of ground movements in overconsolidated clay. *Géotechnique*, 47(2):235–253, 1997.

[Tai21] Mahdi Taiebat. *Personal communication*. University of British Columbia, 2021.

[TD08] M. Taiebat and Y. F. Dafalias. SANISAND: Simple anisotropic sand plasticity model. *International Journal for Numerical and Analytical Methods in Geomechanics*, 32:915–948, 2008.

[TD17] Mahdi Taiebat and Yannis F. Dafalias. *A Zero Elastic Range Hypoplasticity Model for Sand*, pages 237–256. Springer International Publishing, Cham, 2017.

[TN65] C. Truesdell and W. Noll. *The Non-Linear Field Theories of Mechanics*. Springer, 1965.

[TV02] C. Tamagnini and G. Viggiani. Constitutive modelling for rate-independent soils: a review. *Revue Française de Génie Civil*, 6(6):933–974, 2002.

[vW96] P. A. von Wolffersdorff. A hypoplastic relation for granular materials with a predefined limit state surface. *Mechanics of Cohesive-Frictional Materials*, 1(3):251–271, 1996.

[Wan70] C. C. Wang. A new representation theorem for isotropic tensor functions. *Archive for Rational Mechanics and Analysis*, 36:166–223, 1970.

[WDS90] Z.-L. Wang, Y. F. Dafalias, and C.-K. Shen. Bounding surface hypoplasticity model for sand. *Journal of Engineering Mechanics ASCE*, 116(5):983–1001, 1990.

[Wu92] W. Wu. *Hypoplastizität als mathematisches Modell zum mechanischen Verhalten granularer Stoffe*. Publication Series of the Institute of Soil Mechanics and Rock Mechanics, No. 129, Karlsruhe University, 1992.

[Wu99] W. Wu. On a simple critical state model for sand. In Pande and Pietruszczak, editors, *Proc. of the 7^{th} International Symposium Numerical Models in Geomechanics, NUMOG VII*, pages 47–52. Balkema, Rotterdam, 1999.

[Wu00] W. Wu. Non-linear analysis of shear band formation in sand. *International Journal for Numerical and Analytical Methods in Geomechanics*, 24:245–263, 2000.

[YMY06] M. Yazdchi, S. R. Macklin, and H.-C. Yeow. 3D modelling of sprayed-concrete-lined tunnels in clay. *Geotechnical Engineering, Proc. Inst. Civil. Eng., London*, 159(GE4):243–250, 2006.

[YST19] Ming Yang, Gaziz Seidalinov, and Mahdi Taiebat. Multidirectional cyclic shearing of clays and sands: Evaluation of two bounding surface plasticity models. *Soil Dynamics and Earthquake Engineering*, 124:230–258, 2019.

Modelling non-linearity, small-strain stiffness and cyclic loading

David Mašín[1]

[1] *Charles University, Prague, Czech Republic*

Non-linear stress-strain behaviour is possibly one of the most strinking behavioural patterns of soils (and granular materials in general) distinguishing it from other engineering materials. In this chapter, we first summarise the approaches developed for modelling non-linear state- and history- dependent soil response. In subsequent sections, approaches to modelling the effects of strain and stress accumulation in cyclic loading are described. Both "implicit" approaches, which adopt standard non-linear constitutive models to predict cyclic response, as well as the explicit accumulation models, which aim for tracking the final "accumulated" state only are covered.

1 Introduction

The source of soil non-linear behaviour is its granular structure, where irreversible strains develop from the very beginning of the loading process due to relative movement of soil grains and redistribution of contact forces. For this reason, granular materials differ from other engineering materials, which often exhibit non-negligible elastic regions before they start developing irreversible strains. To capture this complex behaviour using a continuum constitutive model, standard approaches used for example for modelling the behaviour of metals must be extended significantly, allowing for tiny (or zero) elastic ranges and introducing state variables tracking recent history of deformation. These approaches are described in this chapter.

In principle, predicting non-linear response is also key for predictions of the effects of cyclic loading. As a matter of fact, however, models developed using the information on stiffness degradation during monotonic loading often do not deliver sufficient accuracy when predicting soil subject to loading cycles and additional enhancements of these models are needed. Predictive capabilities and deficiencies of some of the most advanced models for cyclic loading are presented here. Finally, an alternative approach is covered, which does not aim to follow the individual loading cycles, but which rather aims to track explicitly the overall average response as cycling proceeds.

2 Modelling soil non-linearity and small strain stiffness

This section on small strain stiffness follows from [Maš19].

The history of modelling soil stiffness non-linearity is directly related to the history of understanding soil non-linearity stimulated by advances in experimental techniques. Early soil constitutive models considered linear elastic behaviour before failure. Such predictions seemed reasonable before the development of local strain transducer methods for small strain stiffness measurements (see Fig. 1a).

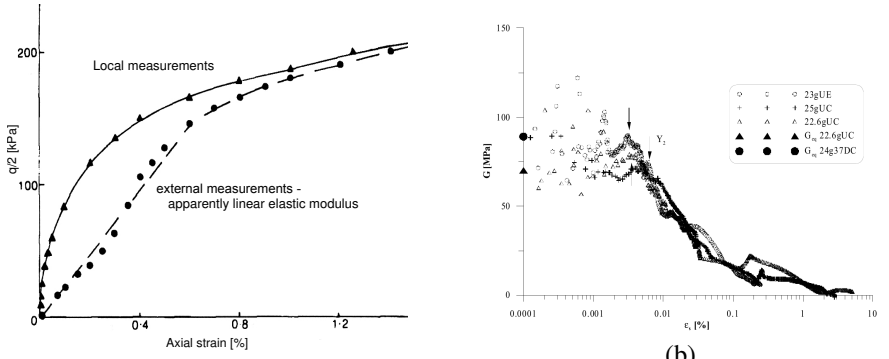

Figure 1: (a) Comparison of stress-strain curves obtained from external and local deformation measurement (from Jardine et al. [JSB84], modified). (b) Shear stiffness vs. shear strain (log-scale) curve measured on London clay using local transducers (from Gasparre et al. [Gas05, GNM+07])

The following aspects of predictive capabilities of constitutive models will be discussed in more detail in this lecture:

1. Predictions of small strain stiffness non-linearity; i.e., a decrease of soil stiffness measured by local strain transducers (approx. 0.001% to 0.1%).
2. Predictions of unloading non-linearity; i.e., the soil non-linear response predicted not only in loading, but also in unloading.
3. Predictions of very small strain stiffness; i.e., the initial stiffness measured by dynamic methods (below 0.001%).
4. Predictions of recent history effects; i.e., the dependency of soil stiffness on the general loading history (including directions other than loading and unloading).

A straightforward modification of a linear elastic perfectly plastic model to include stiffness non-linearity is based on replacement of linear elasticity by *non-linear elasticity* with the stiffness depending on strain level. Such a model has been proposed,

for example, by Jardine et al. [JPFB86]. This model has been set up to closely represent the stiffness degradation curve (see Figure 2 [APP97]). Thanks to the inherent properties of the non-linear elastic formulation, this model is incapable of predicting stiffness dependency on loading direction (recent history effects) and, in fact, it leads to incorrect predictions for any non-monotonous path (for example, it predicts an unrealistic increase of soil stiffness in unloading). Also, the predictions are unreliable for stress paths different to those used for model calibration. In specific cases, however, the model provides reasonable predictions of geotechnical problems. These models were used in particular for predictions of ground deformation due to tunnelling [APP97, FPB05]. The non-linear elastic model described in this paragraph predicts in monotonous loading not only small strain stiffness non-linearity, but also very small strain stiffness as measured by dynamic methods.

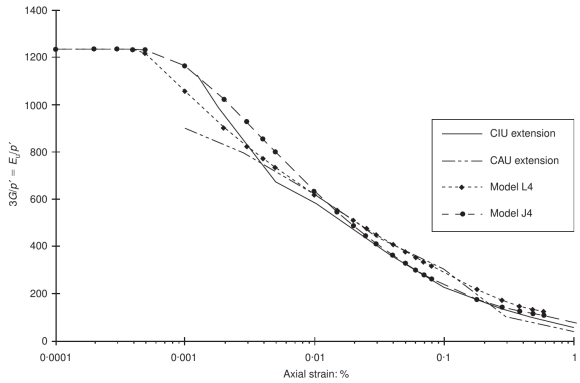

Figure 2: Prediction of stiffness degradation curve by non-linear elastic model (figure from [APP97]).

Most of the other approaches to modelling soil non-linearity activate plastic strains within the state boundary surface to predict the non-linear and irreversible response. The first class of such models, which will be outlined in this summary chapter, predicts plasticity and non-linearity in continuous loading, while still predicting the elastic response in unloading. Notable examples of this class of models are radial-mapping *bounding surface plasticity* models [Daf86]. These models are typically based on the critical state soil mechanics Cam-clay type models, which will be denoted as single-surface models here. The yield surface of the single-surface model is contained also in the bounding surface plasticity model, and predictions at this surface coincide with predictions of the single-surface models. In bounding surface models, however, this surface is not a yield surface in the elasto-plastic sense, because plastic strains can be generated even within this surface. This surface is denoted as a bounding surface instead.

The principle of bounding surface models can be explained with the aid of Fig. 3 (from Russel and Khalili [RK06]). The current state ($\boldsymbol{\sigma}$ in Fig. 3) is at the loading sur-

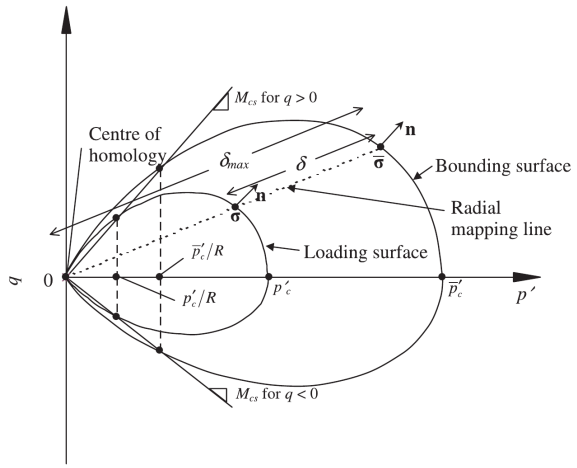

Figure 3: Schematic representation of loading surface, bounding surface and radial mapping rule of the bounding surface plasticity model (figure from Russel and Khalili [RK06]).

face. A so-called mapping rule is adopted to find a corresponding conjugated position at the bounding surface ($\bar{\boldsymbol{\sigma}}$ in Fig. 3). The elasto-plastic hardening modulus and plastic strain increment direction is found as if the soil state was at the bounding surface. The hardening modulus used in the model is then composed of two parts: the hardening modulus at the bounding surface, plus an additional contribution calculated from the distance between the current state and conjugated state at the bounding surface (denoted as δ in Fig. 3). In unloading, model predictions are elastic. Radial-mapping bounding surface plasticity models are capable of predicting stiffness non-linearity in the small strain range. However, the lack of the "elastic nucleus" does not allow the prediction of high elastic stiffness in the very-small-strain range. Elasticity in unloading means the model is incapable of predictions of recent history effects and stiffness variation in unloading. This shortcoming of the bounding surface plasticity models has been eliminated in [KHV05], this model will be introduced in Sec. 3.

Different in notation but similar in principle and in predictive capabilities to the bounding surface plasticity models are the so-called *subloading surface plasticity* models by Hashiguchi et al. [Has89, HSOT02], the MIT-E3 model by Whittle and Kavvadas [Whi93, WK94] and subsequent models evolved from the MIT-E3 concept [PW99]. Similar in principle (non-linear response in loading and elastic response in unloading) is also the hardening soil model of Schanz et al. [SVB00]. Also these models need to be further enhanced to predict small strain stiffness effects [Ben07].

An important addition to the radial mapping bounding surface plasticity models is the consideration of a non-linear response in unloading. A concept that enabled these predictions is the so-called *generalized plasticity* by Pastor et al. [PZC90]. These

models predict plastic strains in both loading and unloading. In these models, the plastic hardening modulus H and plastic strain increment direction $\mathbf{m}$ are defined for both loading (H_L, $\mathbf{m}_L$) and unloading (H_U, $\mathbf{m}_U$). Loading and unloading is distinguished by means of a tensor $\mathbf{n}$, which, in classical elasto-plasticity, is calculated as a normal to the yield surface f as $\mathbf{n} = \partial f / \partial \boldsymbol{\sigma}$. In generalized plasticity, the notion of the yield surface is abandoned, and it is sufficient to define an explicit expression for $\mathbf{n}$. Similarly, generalized plasticity models abandon the notion of the plastic potential, and it is sufficient to provide an explicit expression for $\mathbf{m}$ (that is, for $\mathbf{m}_L$ and $\mathbf{m}_U$). Classical elasto-plasticity, as well as bounding surface plasticity, may then be seen as special cases of generalized plasticity with $H_U \to \infty$.

While generalized plasticity models predict small strain stiffness non-linearity in both loading and unloading, they do not predict the very small strain range of elastic behaviour (so-called "elastic nucleus"). This range is tiny – as discussed above (Figs. 1b and 2), its size is of the order of 0.001% in the strain space, but it turns out to be important for correctly predicting the displacement field in boundary value problems. One of the concepts for predicting the elastic nucleus and non-linear response in loading as well as in unloading is denoted as *kinematic hardening plasticity*.

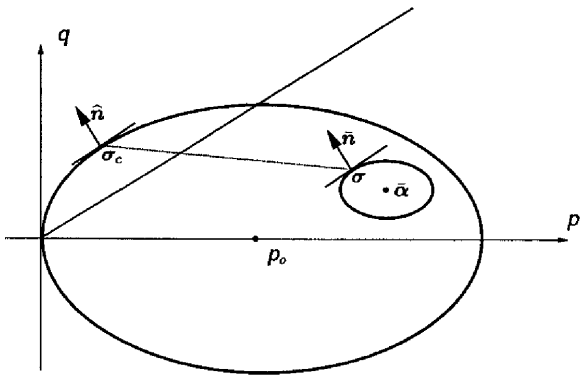

Figure 4: Principle of the kinematic hardening "bubble" model (figure from Rouainia and Muir Wood [RMW01], modified).

Kinematic hardening plasticity for modelling of soils was introduced by Mróz et al. [Mróz67, MNZ78, MNZ79]. A typical model was proposed by Al-Tabbaa and Muir Wood [ATMW89]. This model is based on the critical state soil mechanics Modified Cam-clay model and it is known as the *"bubble" model* in the soil mechanics community. The concept will be explained with the aid of Fig. 4. Kinematic hardening bubble models consider the outer (bounding) surface, similar to the radial mapping bounding surface of plasticity models. As in bounding surface plasticity models, predictions at the bounding surface coincide with predictions by the single-surface critical state model. Unlike generalized plasticity, but the same as bounding surface plasticity,

bubble models predict the elastic behaviour in unloading. Unlike bounding surface models, however, the elastic range is limited in the stress space to a small elastic nucleus (Fig. 4). Once the stress state in unloading reaches the opposite side of the elastic nucleus, plastic strains are generated again, and the surface moves within the stress space following the current stress point (thus "kinematic hardening").

The plastic modulus is a sum of two components as seen in bounding surface models. The first part is a modulus at the conjugated point at the bounding surface (denoted as $\boldsymbol{\sigma}_c$ in Fig. 4). It is not found using a mapping rule as in bounding surface models, but is instead defined as a point having the same normal to the bounding surface as is the normal to the elastic nucleus constructed at the current stress $\boldsymbol{\sigma}$ (Fig. 4). To facilitate this geometrical construction, the elastic nucleus is assumed to have the same shape (and different size) as the bounding surface. The second component of the hardening modulus is a function of the distance between the current stress $\boldsymbol{\sigma}$ and conjugated stress $\boldsymbol{\sigma}_c$, similar to the bounding surface models. The plastic strain increment direction is calculated from a normal to the plastic potential surface, which moves together with the elastic nucleus (most often, associated plasticity is assumed). Finally, the kinematic hardening law controlling the elastic nucleus movement is introduced into the model such that the yield surface and bounding surface never intersect each other. Kinematic hardening bubble models represent a successful concept of soil constitutive modelling, and many variants of them have been proposed in the literature [RMW00, GMW01, KA00]. Similar concepts to the kinematic hardening bubble models have been incorporated into the bounding surface model of Khalili et al. [KHV05]. To predict cyclic loading phenomena of sands, they proposed a kinematic loading surface moving within the main bounding surface, similar to bubble models. Instead of calculating the hardening modulus based on conjugated points with the same normals to the loading and bounding surfaces, they proposed a new mapping rule with a moving projection centre.

Kinematic hardening models other than the bubble models have been proposed for modelling granular materials (such as sands or gravels). They focus on predictions in shear and instead of considering closed "bubbles" within the stress space, they consider the yield surface as a narrow region radiating from the origin of the stress space (Fig. 5). The yield surface is subject to rotational hardening (it does not move freely within the stress space, but rotates about the origin of the stress space). While these models cannot represent the behaviour of sand in compression, they are successful in predicting the response in shear. This choice is facilitated by the fact that, in sands, plastic straining is predominantly associated with shearing. Typical examples of this class of models are the SANISAND model by Manzari and Dafalias [MD97] and the Severn-Trent sand model by Gajo and Muir Wood [GMW99]. A more recent version of the SANISAND model eliminates its shortcoming by closing the yield surface in the compression direction [TD08].

The kinematic hardening single-bubble models described above predict small strain stiffness non-linearity in loading and unloading, as well as very small strain stiffness. They, however, do not predict the effects of recent history. To this aim, Stalle-

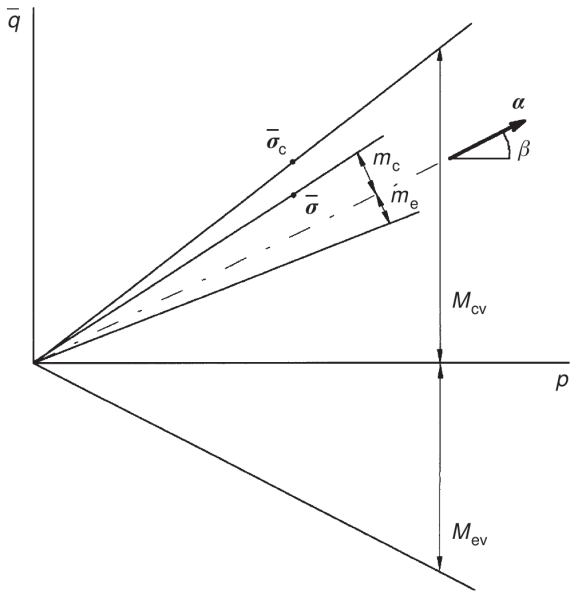

Figure 5: Kinematic hardening model for sand (figure from Gajo and Muir Wood [GMW99]).

brass and Taylor [ST97] enhanced the bubble model [ATMW89] from Fig. 4 by an additional kinematic "history" surface, which encloses a much smaller elastic locus (yield surface) and sets a boundary around the current stress state where the soil behaviour is influenced by recent history effects. Subsequently, several modifications of this model have been developed by different authors [BS04, GZP06, MH03]. A similar concept has also been proposed by Puzrin and Burland [PB98, PB00]. Einav et al. [EPH03, EP04, EP03] demonstrated that kinematic hardening models may be constructed in a way consistent with thermodynamics theory, and that the number of kinematic surfaces can, in principle, be unlimited (Fig. 6).

Apart from the above models based on elasto-plasticity, models exist for predicting non-linearity based on different concepts. One approach specifically developed to predict the effects of recent history (and consequently also soil non-linearity in the small strain range both in loading in unloading), is a *brick model* concept by Simpson [Sim92]. In the brick model the elastic locus and soil history is defined in the *strain space*, instead of the stress space as in typical elasto-plastic models. The modelling concept has a geometrical interpretation of a man pulling bricks (Fig. 7); loose strings do not contribute to soil stiffness, whereas each taut string decreases soil stiffness in a pre-defined way. While the main concept of the brick model is defined in the strain space, it incorporates a stress-space based critical state failure condition. Advantage is taken of the fact that the area below the shear strain vs. normalised shear stiffness

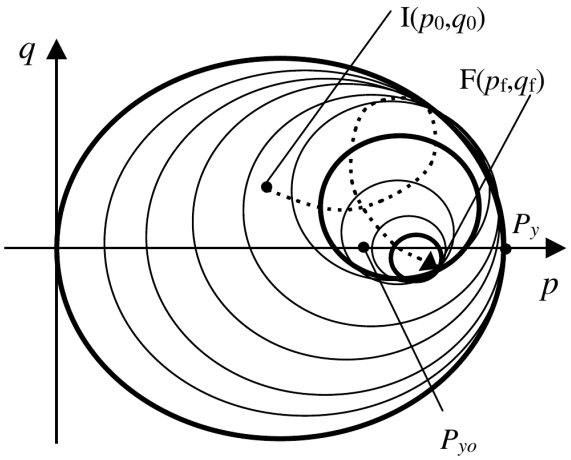

Figure 6: Multiple kinematic surfaces of a continuous hyperplastic critical state model (figure from Einav and Puzrin [EP04]).

curve determines the critical state friction angle [Sim92]. More recent models based on the brick concept can be found in [VLJ05, ESS12, CT20].

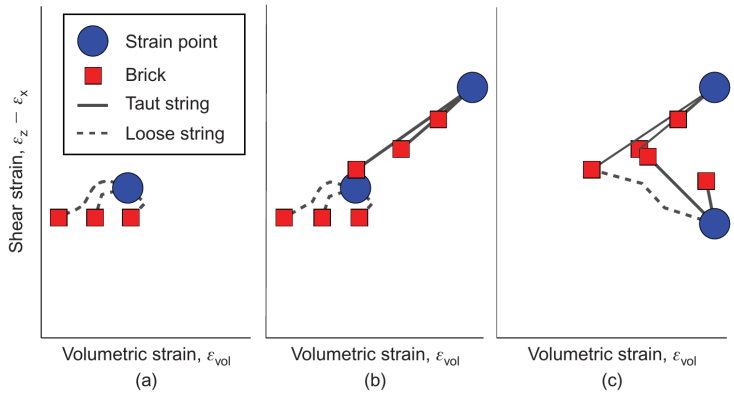

Figure 7: Geometrical interpretation of the brick model (figure from Ellison et al. [ESS12]).

Another approach to modelling soil non-linearity is the so-called multi-laminate framework [PS83, PP87, CV04]. The multi-laminate model is based on the elasto-plastic theory; calculation of the plastic strain increment is, however, different from standard elasto-plastic models. In the multi-laminate framework, soil is assumed to be a solid block behaving elastically, intersected by a number of randomly oriented planes where

plastic straining may occur. The actual macro stress tensor is projected onto the micro stress vectors on every plane where the possible plastic strain increments are calculated. The plastic contribution from all planes is then spatially summed up to obtain the macro plastic strain [CV04] (Fig. 8). The basic multi-laminate framework has been enhanced by Scharinger et al. [SSP09] to predict very small strain stiffness.

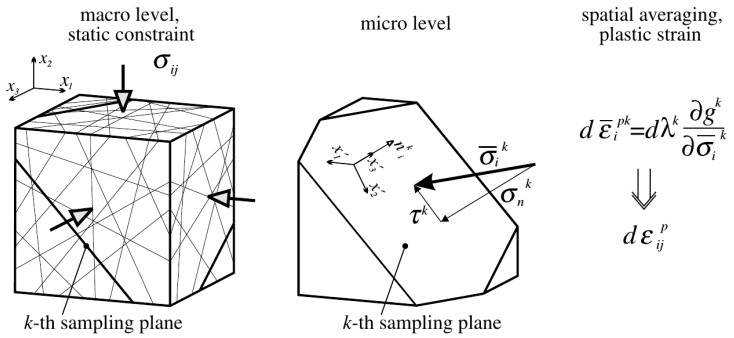

Figure 8: Schematic representation of the multi-laminate model (figure from Cudny and Vermeer [CV04]).

An approach for incorporating small strain stiffness effects into elasto-plastic models that do not consider soil non-linearity has been proposed by Benz et al. [BVS09] and applied to the hardening soil model by Benz [Ben07]. In their model, plastic strains are not considered. The elastic stiffness matrix depends on the loading direction with respect to the previous loading history and the model is thus incrementally non-linear. In cyclic loading, the model predicts a hysteretic response, but the original stress is recovered in a strain cycle; such a class of models is often denoted as paraelastic [HN79]. Another paraelastic model capable of improving the small strain stiffness predictions of other models is due to Niemunis et al. [NPSGT11b].

One of the approaches inherently capable of modelling soil non-linearity is hypoplasticity. When compared to other modelling approaches discussed in this section, the basic hypoplastic models are capable of predicting non-linear soil behaviour in both loading and unloading. These models are incapable of predicting very small strain stiffness and the effects of recent history. To include these two effects, the hypoplastic models can be enhanced. The most commonly adopted way of hypoplastic model enhancement is the intergranular strain concept [NH97], but other approaches are also possible. For example, Niemunis et al. [NPSGT11b, NPSGT11a] proposed hypoplastic model enhancement by paraelasticity and Fuentes and Triantafyllidis [FT15] developed so-called ISA extension of hypoplasticity, which is an extension of intergranular strain concept and specifically targets cyclic loading effects. Simplified version of this approach, denoted as ISI, has been proposed by [DMF20]. [WH14] updated the intergranular strain model such that it reasonably predicts the effects of cyclic accumulation if calibrated using monotonic experiments.

The idea behind the intergranular strain concept is as follows: it is assumed that at the beginning of the loading process the grain skeleton does not rearrange, and all the measured deformation of the soil is attributed to reversible deformation of the so-called intergranular strain layer, combined with the elastic deformation of the grains themselves. After a certain amount of strain, the grains start to rearrange. The reversible deformation is described by an additional component of the model, which will be described below. The deformation associated with the grain rearrangement is irreversible and is predicted by the base model, which is typically hypoplasticity but the concept can be combined with other modelling approaches [BFM$^+$19].

In the intergranular strain-enhanced hypoplasticity model, it is assumed that during loading the intergranular layer deforms first, before rearrangement of the soil skeleton. The deformation of the intergranular layer is thought to be associated with the reversible response. The skeleton starts to fully rearrange without the intergranular layer contribution once the intergranular strain reaches its maximum value. The intergranular strain is a strain-like quantity, and it is an additional state variable denoted as $\boldsymbol{\delta}$. The intergranular strain is, in general, a second-order tensor (as is the strain rate). However, the concept will be described here in 1D for simplicity, in which case the intergranular strain is a scalar (δ).

Fig. 9 shows the evolution of δ in an unloading-reloading cycle prescribed by the strain rate D. As the model is rate independent, the actual strain rate is arbitrary, and it has been selected as $|D| = 1$. Figure 9a shows the initial state with zero δ and zero strain rate. Figure 9b shows the intergranular strain, which reaches its maximum value $|\delta| = R$ in unloading, and Figs. 9c to 9e show its development in reloading.

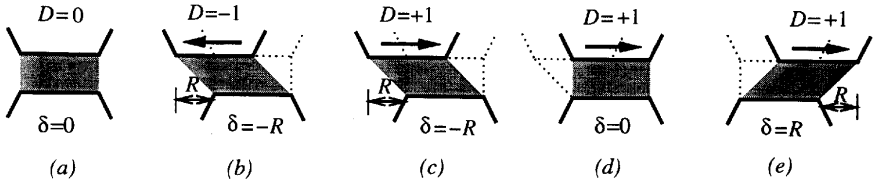

Figure 9: Intergranular strain limit values in 1D (figure from [NH97]).

The evolution of the intergranular strain in 1D is described by

$$\dot{\delta} = \begin{cases} \left(1 - \frac{|\delta|}{R}\right) D & \text{for } \delta D > 0 \\ D & \text{for } \delta D \leq 0 \end{cases} \tag{1}$$

where the maximum value of the intergranular strain is denoted as R and it is a parameter. Equation (1) is graphically represented in Fig. 10, which shows the dependency of the intergranular strain rate $\dot{\delta}$ on the value of δ for a strain cycle of $D = \pm 1$. Initially, the intergranular strain δ, intergranular strain rate $\dot{\delta}$ as well as strain rate D are zero (state "0"). Once the sample starts to be deformed at $D = -1$, the intergranular

strain rate becomes equal to $\dot{\delta} = -1$ (state "1"), but after that, as $\delta D > 0$, the intergranular strain rate decreases with its normalised value $|\delta|/R$ down to zero (state "2"). Any further deformation in the same direction does not change the maximum value $\delta = -R$. Once the strain rate is reversed to $D = 1$, the intergranular strain rate is equal to $\dot{\delta} = 1$ (state "3"), and it remains so as long as $\delta D \leq 0$. When $\delta = 0$ (state "4") the intergranular strain rate starts to decrease again and it vanishes when $\delta = R$ (state "5"). Another strain reversal then activates the intergranular strain rate in the opposite direction $\dot{\delta} = -1$ (state "6").

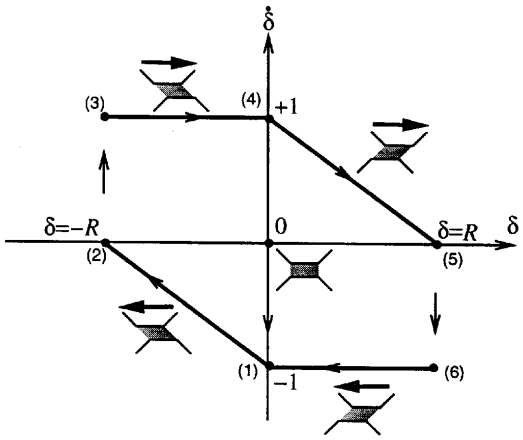

Figure 10: Graphical representation of the evolution equation (1) of the intergranular strain (figure from [NH97]).

In the model, the value of the intergranular strain controls the response so the behaviour is interpolated between reversible elastic with high stiffness (when $\delta D \leq 0$) and hypoplastic (when $|\delta| = R$ and $\delta D > 0$).

$$\dot{\sigma} = \begin{cases} mLD & \text{for } \delta D \leq 0 \\ (1-\rho)mLD + \rho(LD + N|D|) & \text{for } \delta D > 0 \end{cases} \tag{2}$$

where ρ is the normalised length of the intergranular strain tensor $\rho = |\delta|/R$. The reversible elastic response in the small strain range is governed by the stiffness mL, where L is the stiffness tensor of the linear part of the hypoplastic equation and m is a model parameter controlling the stiffness magnitude. When $|\delta| = R$ and $\delta D > 0$, the model response is hypoplastic ($\dot{\sigma} = LD + N|D|$). Linear interpolation between these two cases that are controlled by the value of ρ which governs the response otherwise. In the full 3D version of the model, the parameter m is actually represented by two parameters m_R (for 180° strain path direction change) and m_T (for 90° strain path direction change), one parameter is included to control the interpolation process (χ) and one other parameter is included to control the intergranular strain evolution (β_r).

3 ”Implicit” modelling of cyclic loading

Modelling of soil cyclic behaviour can be accomplished in two ways. Firstly, stress-strain constitutive models capable of simulating the effects of cyclic loading (in particular, strain and pore water pressure accumulation) can be used. This approach is fully general but has several shortcomings. In particular:

- Regardless remarkable development in past decades, constitutive models are still not accurate for predicting cyclic accumulation for more than hundreds or few thousands of cycles.
- Simulations are extremely CPU-intensive for large number of cycles, making them practically impossible for tens of thousands of cycles or more.
- Constitutive model integration error, which can be relatively well controlled in monotonic loading, amplifies significantly when cyclic accumulation is a simulation target. This again increases simulation times, as the relative integration error tolerances must be kept at very tight values to guarantee acceptable accuracy of model integration.
- Even the most advanced models do not provide reliable extrapolation of predictions outside the range of loading conditions used for model calibration.

Some of these shortcomings can be resolved through the use of explicit accumulation models, described later in Sec. 4. In this section, we will focus on predicting the effects of soil cyclic loading through standard constitutive models. This approach is sometimes denoted as ”implicit” modelling of the effects of cyclic loading (as opposed to the explicit modelling through the accumulation models).

As a matter of fact, predicting the effects of cyclic loading requires the models to accurately predict soil non-linear behaviour, from the very small to large strain range. Therefore, models used for cyclic loading predictions often coincide with models predicting non-linear behaviour, which have been described thoroughly in Sec. 2. For this reason, we will not describe additional modelling approaches in this section. Instead, we will focus on some examples of model predictions along with demonstration of model shortcomings.

3.1 Cyclic modelling of sands

Out of many approaches available, we will demonstrate here predictions of two advanced modelling methods: based on kinematic hardening plasticity (SANISAND model family [DM04, YTD21]) and based on hypoplasticity [vW96] with intergranular strain [NH97] (denoted as hypoplasticity IS model hereafter). The models performance under cyclic loading has been studies in detail in [WFT19] and some of their limitations demonstrated in [DFM$^+$21] using experimental data by [WT16a, WT16b]. Some observations of these authors are summarised in this section.

Let us first analyse the monotonic response of the models as a background informa-

tion. Figure 11a,b shows predictions of drained monotonic triaxial tests on sand samples with different initial densities for hypoplastic IS model (a) and for SANISAND model (b). Predictive trends are reasonable for these tests, although discrepancies exist in stiffness evolution (for SANISAND model, in particular). Predictions of monotonic oedometric loading-unloading tests are presented in Fig. 11c,d, where hypoplasticity delivers reasonable predictions, while SANISAND model does not properly capture the position of normal compression line, which is a typical consequence of kinematic hardening structure of the model where yield surface is represented by a rotating cone in the stress space without specific mechanism to tackle compressive behaviour. This shortcoming is not corrected even in recent advanced versions of the model [DFM$^+$21], though SANISAND family models with capped yield cone have also been developed [TD08]. Additionally, hypoplasticity may not properly capture normal compression behaviour for small oedometric unloading cycles [DFM$^+$21].

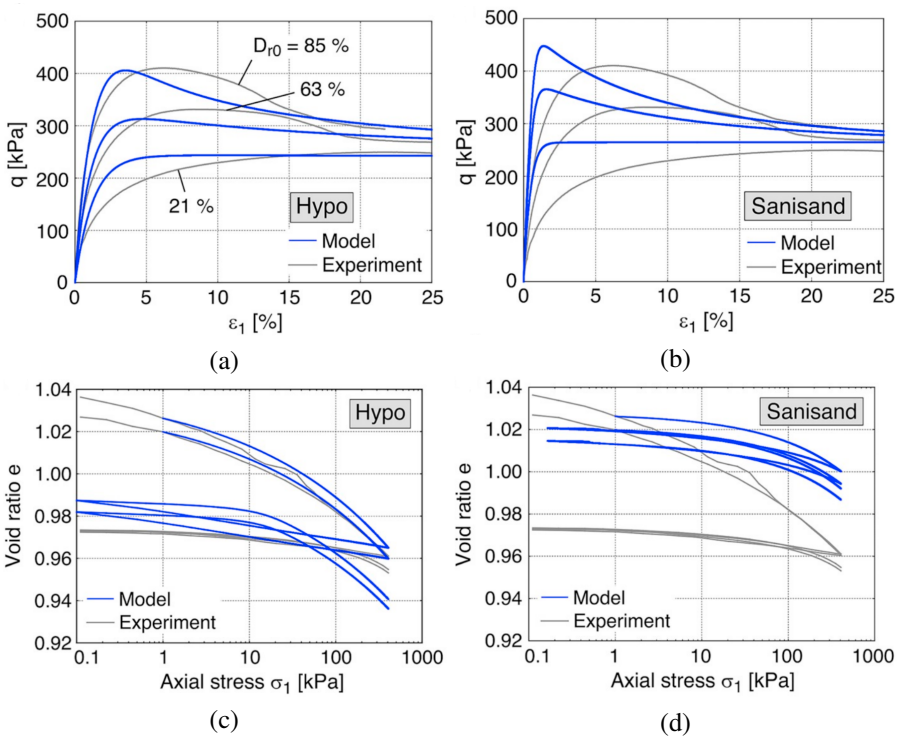

Figure 11: Prediction of drained monotonic triaxial tests (a, b) and oedometric tests (c, d) by hypoplastic IS model (a, c) and SANISAND model (b, d). Figure from [WFT19], data from [WT16a, WT16b].

Let us now focus on the effects of cyclic loading. We will study cyclic loading effects under undrained conditions, as they are relevant for the most critical applications

(such as soil liquefaction during earthquake loading or cyclic effects of thunderstorm loading of offshore structures). Figure 12 shows predictions by SANISAND and hypoplastic IS model for undrained cyclic triaxial tests with deviatoric stress magnitude for each cycle being symmetric about p-axis. Both models predict the response qualitatively correctly in that they reproduce accumulation of pore water pressure leading to a decrease in mean effective stress, which is dragging the state towards the liquefaction point of zero mean effective stress and is accompanied with specimen failure.

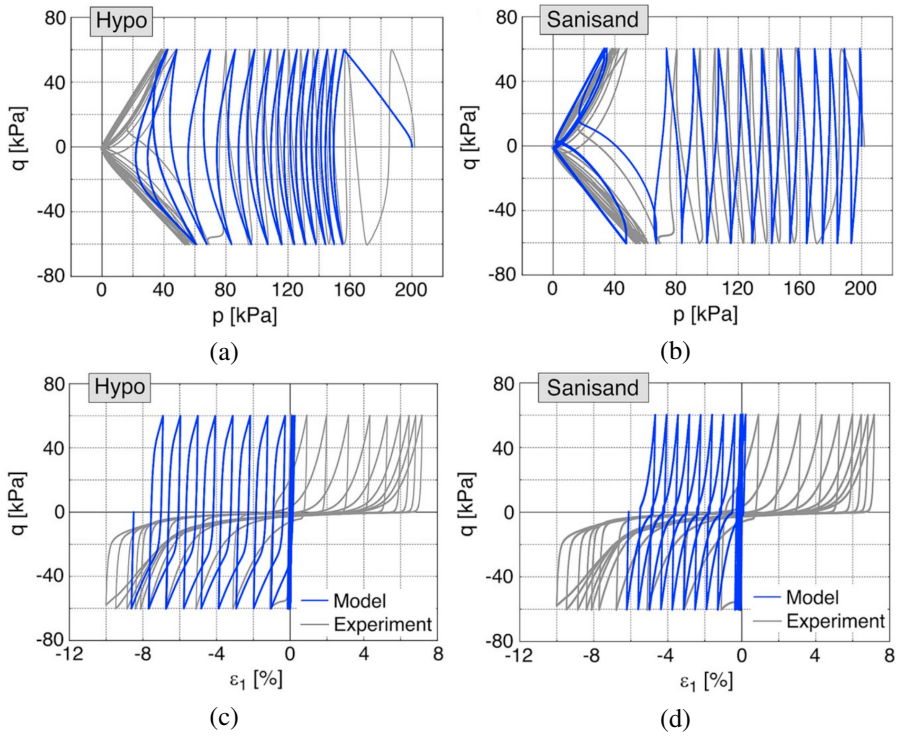

Figure 12: Prediction of undrained cyclic triaxial tests with deviatoric stress magnitude for each cycle being symmetric about p-axis by hypoplastic IS model (a, c) and SANISAND model (b, d). Figure from [WFT19], data from [WT16a, WT16b].

Even this ”standard” experiment from the model development point of view reveals, however, three typical shortcomings of the models:

1. Unlike SANISAND, hypoplastic model does not really reach the liquefaction point of zero mean effective stress with ”butterfly-shaped” cyclic stress paths. Cyclic loops finally stabilise at a non-negligible minimal value of mean effective stress. This shortcoming is corrected by hypoplasticity with evolving fabric by [LY21] (Fig. 13a).

2. As in the experiments, cyclic loading imposes accumulation of axial strain, which is, however, biased towards extension for both hypoplastic IS and SANISAND models. This shortcoming is also corrected by hypoplasticity with evolving fabric by [LY21] (Fig. 13b). Even better improvement is delivered by SANISAND-MSf [YTD21] extension of SANISAND model (Fig. 14 from [DFM$^+$21]).

3. Irrespectively of the fact that the cyclic accumulation is reasonable for one particular cyclic q amplitude for which the models have been calibrated, all the models fail to a significant extent in extrapolating the pore water pressure accumulation for different cyclic loading amplitudes than used for model calibration. This is demonstrated through CSR-N curves in Figure 15a, where cyclic stress ratio ($q^{ampl}/(2p_0)$) is plotted with respect to number of cycles needed to reach liquefaction-induced failure (defined by a deliberately chosen threshold value of vertical strain). For completeness, Figure 15b shows cyclic stress paths predicted by SANISAND model calibrated to tests from Fig. 12, exhibiting significant overprediction of the rate of cyclic pore water pressure accumulation. This is possibly the most significant issue of models for cyclic loading, somewhat improved by more advanced versions of the models (such as SANISAND-MSf), but still relatively far from correct [DFM$^+$21].

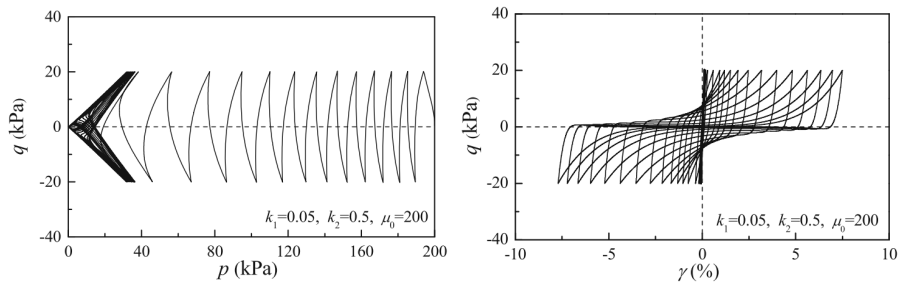

Figure 13: Improvement of predictions of hypoplastic IS model from Figure 12 through fabric evolution by [LY21].

Other typical experimental pattern, captured by some but not all models for cyclic loading, are results of undrained triaxial tests interrupted by unloading to $q = 0$ kPa after a constant axial strain increment for each cycle. Such results are shown in Fig. 16. It is clear that hypoplasticity IS fails in predicting gradual deterioration of shear stiffness during loading, and, similarly to item No. 1 discussed above, soil does not really reach liquefaction point of zero mean effective stress. This state is reached by SANISAND, however, in that case the rate of reaching cyclic mobility is exaggerated, a consequence of inaccurate extrapolation outside the cyclic conditions used for model calibration (item No. 3 discussed above). In addition, SANISAND model overpredicts q, which is a consequence of wrongly predicted evolution of shear stiffness during monotonic loading, discussed above when describing predictions of monotonic

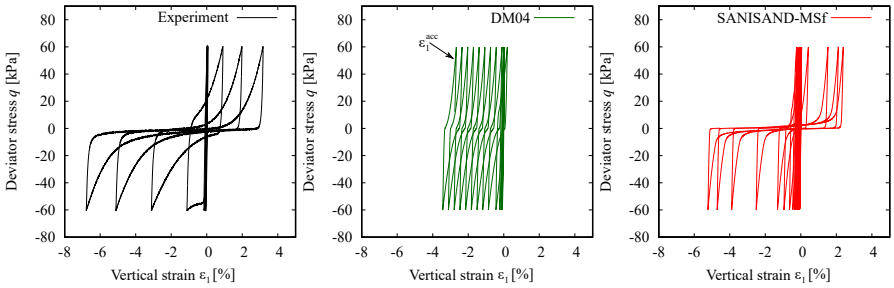

Figure 14: Improvement of predictions of SANISAND model from Figure 12 (labelled as DM04 in this figure) through the MSf extension. Figure from [DFM+21], data from [WT16a].

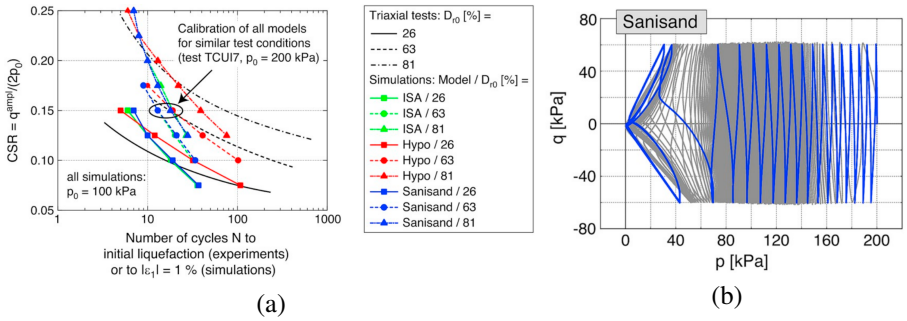

Figure 15: Inability of the models to extrapolate predictions outside the narrow range of cyclic conditions used for their calibration. Figure from [WFT19], data from [WT16a].

triaxial tests (reference to Fig. 11).

Apart of the model features and limitations discussed above, many other predictive issues obviously exist, such as ”overshooting” effect after minor unloading or improper model predictions after drained preloading (see [DFM+21]). Another example of model formulation problem has been discussed by [WH14], who demonstrated that if the hypoplastic IS model was calibrated using stiffness degradation curve in monotonic loading, it did not properly capture the effects of cyclic loading and vice versa. They have developed an improvement of the hypoplastic IS model targeting this problem.

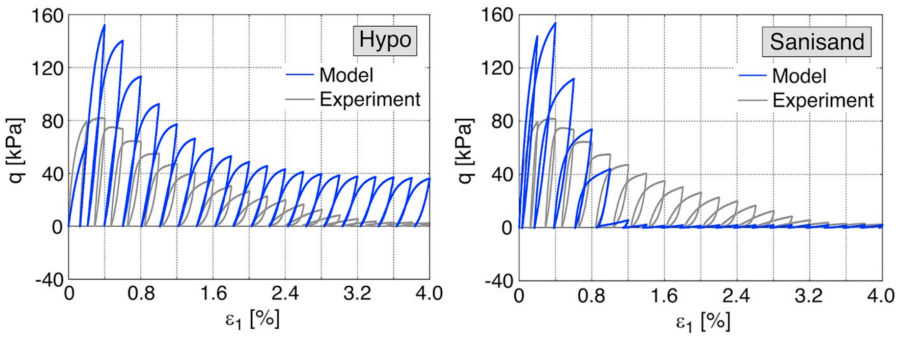

Figure 16: Predictions of undrained triaxial tests interrupted by unloading to $q = 0$ kPa after a constant axial strain increment for each cycle by Hypoplastic IS (a) and SANISAND (b) models. Figure from [WFT19].

3.2 Cyclic modelling of clays

In demonstrating predictive capabilities of cylic models for clays, we will adopt the following three advanced models: the ISA [FT15] extension of intergranular strain concept in combination with clay hypoplastic model by [Maš14]. This combination has been proposed and evaluated in [FMD20], while ISA was also combined with the sand hypoplastic model in [FWGL20]. The second model tested will be a kinematic hardening model from the "SANI" family, denoted as SANICLAY-B [ST14]. The third modelling approach will be the three surface kinematic hardening "bubble" model by [ST97] extended by the transversally isotropic elastic behaviour by [GH83] inside the yield surface (A3-SKH). Comparison of the model predictive capabilities has been presented in [DTS$^+$21] using experimental data on kaolin clay from [WT18].

As in the case of sands, we again start with predictions of monotonic tests as a background information. Predictions of undrained monotonic triaxial tests and oedometric loading-unloading tests are compared with experiments on kaolin in Fig. 17. It is worth pointing out that, as in the case of sands, models do not capture perfectly shear stiffness evolution and thus the shape of stress-strain curves in triaxial tests, SANICLAY-B performing worst (consistently with predictions of SANISAND for sand). Apart of hypoplasticity, in this case also the two elasto-plastic models (SANICLAY-B and A3-SKH) predict normal compression line in oedometric loading, contrary to predictions of SANISAND for sand. This is because advanced clay models adopt closed state boundary surface shape of elliptic or quasi-elliptic shape to predict both compression and shear behaviour. Contrary, in sands, the shear-induced mechanism is considered as the most critical and thus the authors often adopt "cone" rotational hardening models, which do not capture compression behaviour properly.

Continuing to cyclic loading, let us again start with undrained cyclic triaxial tests

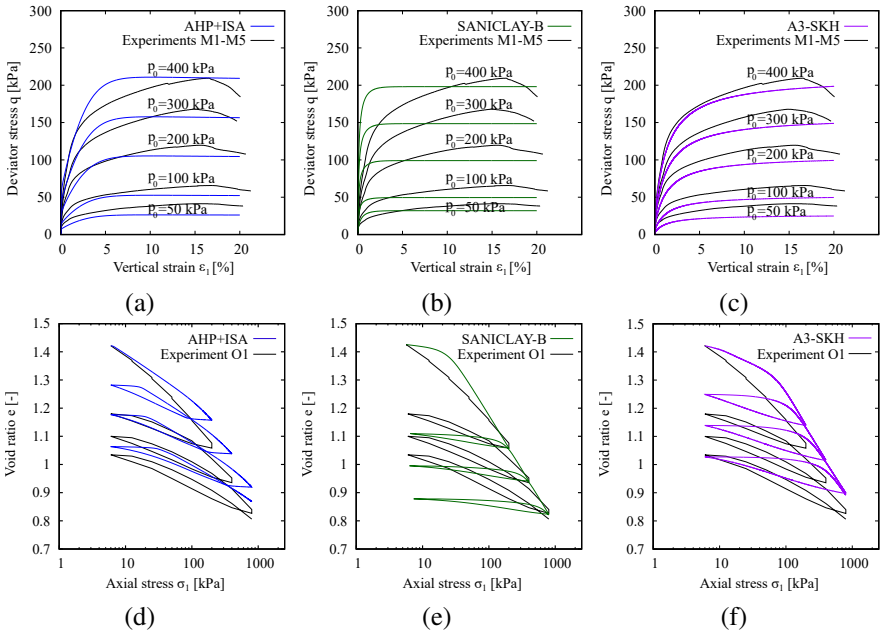

Figure 17: Predictions of undrained monotonic triaxial tests (a, b, c) and oedometric tests (d, e, f) on kaolin clay. ISA clay hypoplasticity (a, d), SANICLAY-B (b, e) and A3-SKH (c, f). Figure from [DTS$^+$21], data from [WT18].

with deviatoric stress magnitude for each cycle being symmetric about p-axis (Fig. 18). In this case, the two elasto-plastic models fail in predicting pore water pressure accumulation, as the accumulation stops when critical state mean effective stress is reached. This fact is also clear from the accumulated pore water pressure vs. cycle number curves, shown in Fig. 20 for tests from Fig. 18 (C4) and also for tests at other cyclic deviatoric stress amplitudes (see [DTS$^+$21] for detailed explanation). The hypoplastic ISA model delivers much more reasonable predictions here than the tested elasto-plastic models, although it fails in predicting the final "butterfly" shape of stress paths at cyclic mobility. The SANICLAY-B model is, however, better representing strain accumulation, at least for specific loading amplitude of 45 kPa (C4 test) from (Fig. 18). Here, both hypoplastic ISA model and A3-SKH model fail to a large extent (hypoplasticity is exaggerating strain accumulation into compression side and A3-SKH is underpredicting strain acumulation). As in the case of sands, no model is capable of extrapolating the predictions for different cyclic amplitudes for single parameter set, however. As a typical demonstration of this fact, equivalent of Fig. 18 is shown for cyclic deviatoric stress amplitude of 70 kPa in Fig. 19. For example, while SANICLAY-B model performed very well in predicting cyclic strain accumulation for deviator stress amplitude of 45 kPa (Fig. 18g), it underpredicts significantly strain accumulation for the amplitude of 70 kPa (Fig. 19g). For further comparisons

regarding the effect of the initial overconsolidation ratio and stress ratio, the reader is pointed to [DTS$^+$21].

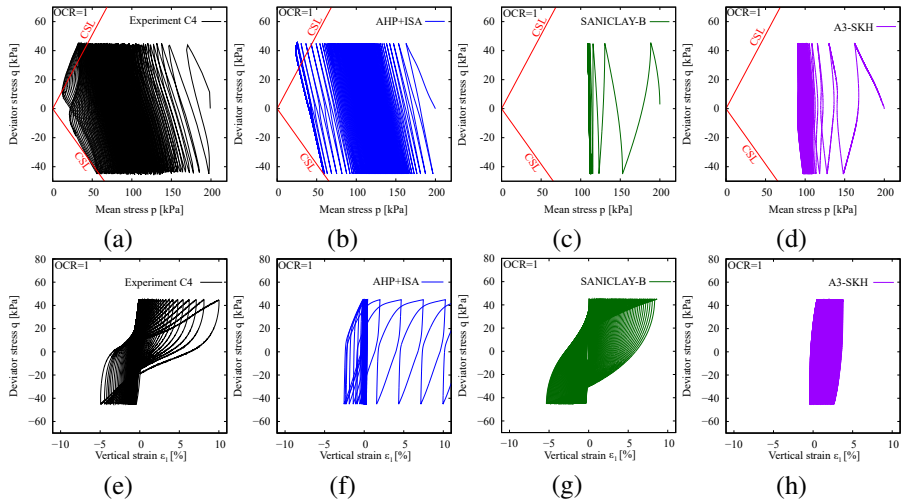

Figure 18: Predictions of undrained cyclic triaxial tests on kaolin with deviatoric stress magnitude of 45 kPa, for each cycle being symmetric about p-axis. ISA clay hypoplasticity (b, f), SANICLAY-B (c, g) and A3-SKH (d, h). Figure from [DTS$^+$21], data from [WT18].

Consistent with these results are predictions of cyclic tests controlled not by the fixed deviatoric stress cyclic amplitude, but by the fixed axial strain cyclic amplitude (Figure 21). Also in this case, the two elasto-plastic (SANICLAY-B and A3-SKH) models fail in predicting pore water pressure accumulation behind the critical state mean stress. Here, the hypoplastic ISA model works reasonably well. Similarly to cyclic tests with constant q^{ampl}, SANICLAY-B predicts best the vertical strain vs. deviatoric stress profile, with hypoplastic ISA model showing too low stiffness for the final cycles. This is a consequence of the fact that, unlike experiment, the model reaches almost in full the state of zero mean stress. While stiffness is considered as proportional to mean stress, it becomes underpredicted.

4 Explicit cyclic accumulation models

The examples of "implicit" cyclic model predictions and their limitations presented in previous section showed that regardless remarkable development of models in past years, implicit modelling of cyclic loading still poses a challenge for model developers. For some specific applications, it may thus be beneficial to use explicit modelling strategies, which are described in this section. In these models, average accumulated values of the tracked variables (such as pore water pressure and strain) are being pre-

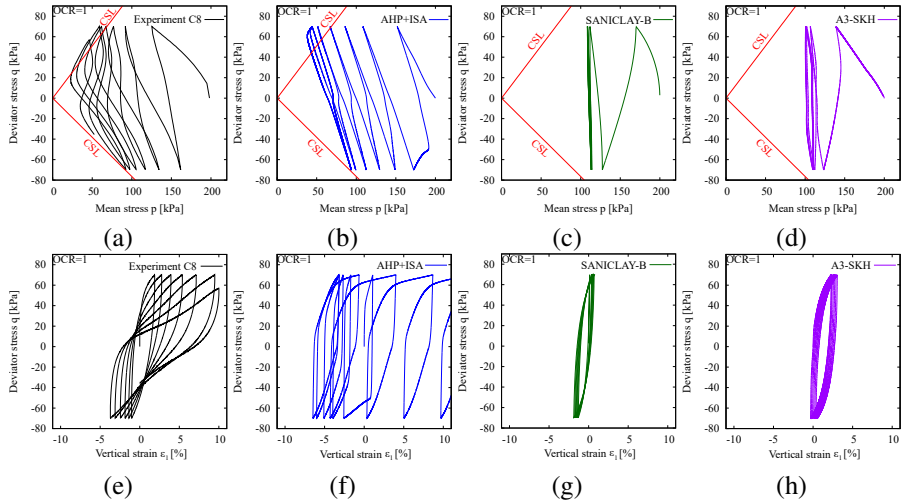

Figure 19: Predictions of undrained cyclic triaxial tests on kaolin with deviatoric stress magnitude of 70 kPa, for each cycle being symmetric about p-axis. ISA clay hypoplasticity (b, f), SANICLAY-B (c, g) and A3-SKH (d, h). Figure from [DTS$^+$21], data from [WT18].

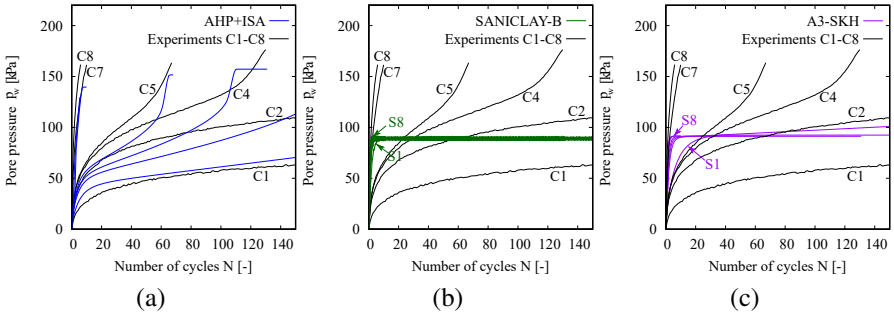

Figure 20: Accumulated pore water pressure of experiments from Figure 18 (C4) and experiments at other deviatoric stress magnitudes (C1, C2, C5, C7 and C8) plotted with respect to cycle number. ISA clay hypoplasticity (a), SANICLAY-B (b) and A3-SKH (c). Figure from [DTS$^+$21], data from [WT18].

dicted, instead of detailed evolution of these variables in each of the cycles. Details of the model formulation are presented later on. As with the case of "implicit" modelling, we will first start with summarising the main properties of this approach:

- The explicit approach does not suffer the main drawbacks of the implicit methods. Most importantly, accumulation curves can be fit to very high number of cycles (of the order of magnitude of 10000 and higher), where implicit solution

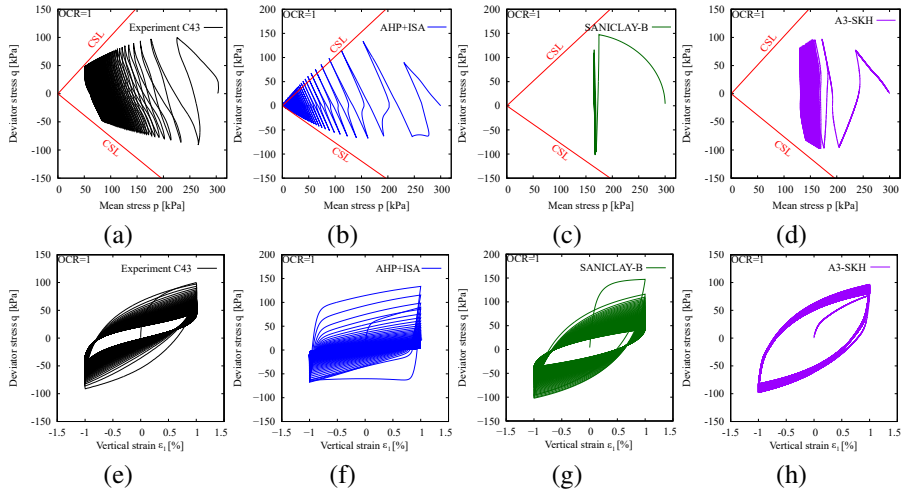

Figure 21: Predictions of undrained cyclic triaxial tests on kaolin with constant axial strain amplitude of 1%. Figure from [DTS+21], data from [WT18].

is no-more feasible, namely due to inaccurate constitutive model itself, due to magnified errors of the model integration and due to extremely high CPU-cost.

- The main drawback of the explicit accumulation models is the fact that the accumulation curves are constructed for specific cyclic states (such as magnitudes of cycles in terms of strain or stress, current stress ratios, cyclic loop shapes, etc.). It thus becomes tricky to use these methods for irregular cyclic loading (such as loading occurring during earthquakes).
- Explicit accumulation models are best suited to cyclic loading of small to moderate total strain amplitudes ($< 10^{-3}$). For larger amplitudes, accumulation becomes rapid due to state approaching failure and accumulation response to symmetric cycles of controlled variables (for example, strain) becomes progressively asymmetric. In this case, implicit calculation often becomes more beneficial than the explicit approach.

In this chapter, we will cover an explicit modelling approach proposed by [NWT05, Wic16].

Principle of explicit accumulation models is presented in Fig. 22. Fig. 22a demonstrate the standard "implicit" calculation strategy, where each cycle is calculated using a nonlinear "implicit" constitutive model. Explicit strategy is sketched in Fig. 22b. As indicated there, the explicit accumulation models allow us to follow the average accumulation curve (instead of simulating each cycle independently) with all the benefits of explicit calculation (speed, low CPU cost, eliminated integration errors). Still, explicit simulation cannot be used on its own. This is because a cyclic strain magnitude and tensorial strain loop shape is a key input into the explicit constitutive model and,

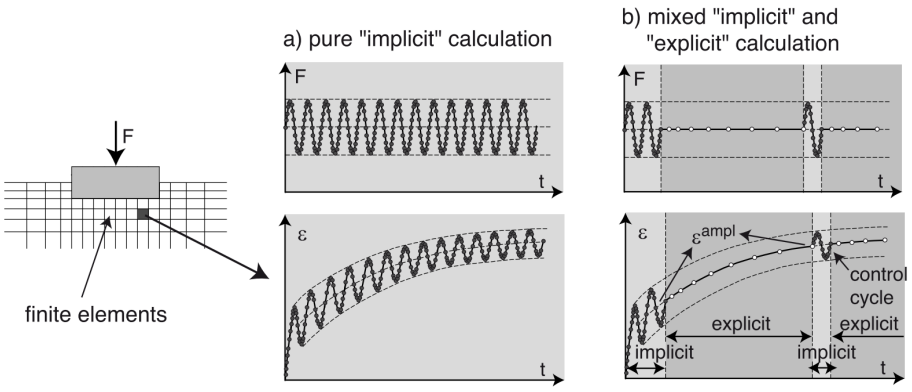

Figure 22: Principle of explicit accumulation models (figure from [Wic16]).

for general boundary value problems, these quantities cannot be found without running the implicit simulation. The procedure of running the explicit simulation is as follows [NWT05, Wic16]:

1. The finite element model is setup as standard using an implicit constitutive model and first few cycles are calculated. More cycles than one are needed so that the internal state variables of the constitutive model evolve towards steady cyclic conditions.
2. Strain path is recorded for each integration point during the last implicit cycle and the tensorial strain amplitude is calculated.
3. Based on the input from item No. 2 and based on current state, accumulation strain rate $\mathbf{D}^{\mathrm{acc}}$ is calculated using the explicit accumulation model equations (see later).
4. Stress rate $\mathring{\mathbf{T}}$ is calculated from $\mathbf{D}^{\mathrm{acc}}$ using the model equations (see later) and stress increment for the given integration step is found using $\Delta\mathbf{T} = \mathring{\mathbf{T}}\Delta t$, where Δt represents pseudo-time increment in current integration step. In the model implementation, cycle number N is often mapped to pseudo-time (for example, simply by setting $N = t/[\mathrm{time\ unit}]$), simulations thus from the standpoint of the finite element code resemble simulations with time-dependent constitutive models, which consider time as a state variable. Note that, as the accumulation curves are not highly non-linear in N, ΔN significantly higher than 1 can often be used in one calculation step (for higher cycle numbers in particular), which makes for an enormous CPU efficiency when compared with standard implicit modelling.
5. As the stress state may gradually change during the explicit phase and this change affects cyclic tensorial strain amplitudes, additional implicit steps ("control cycle" in Fig. 22b) are included within the explicit phase to update the

information on tensorial strain amplitudes to increase accuracy of subsequent explicit solution.

Central to the accumulation model are equations for $\mathring{\mathbf{T}}$ and $\mathbf{D}^{\mathrm{acc}}$. $\mathring{\mathbf{T}}$ is calculated using the simple equation resembling visco-plastic formulation:

$$\mathring{\mathbf{T}} = \mathcal{E} : \left(\mathbf{D} - \mathbf{D}^{\mathrm{acc}} - \mathbf{D}^{\mathrm{pl}}\right) \tag{3}$$

where $\mathbf{D}^{\mathrm{acc}}$ is the cyclic accumulation strain rate, $\mathcal{E}$ is an elastic stiffness matrix (preferably stress-dependent for consistency with stress-dependent soil behaviour). $\mathbf{D}^{\mathrm{pl}}$ is a plastic strain rate, which is needed in the case that the cyclic loading is accompanied with monotonic loading to make sure the state does not surpass failure surface.

Equation $\mathbf{D}^{\mathrm{acc}}$ is in the model from [NWT05] considered as a product of accumulation strain direction $\mathbf{m}$ and a number of factors, each representing a physical quantity affecting the accumulation rate:

$$\mathbf{D}^{\mathrm{acc}} = \mathbf{m} f_{\mathrm{ampl}} \dot{f}_N f_p f_Y f_e f_\pi \tag{4}$$

The direction of accumulation found experimentally is shown in Fig. 23. [NWT05] actually proposed that the accumulation direction closely follows associated flow rule used in Modified Cam-clay model [RB68] and adopted thus its equation without further modifications. The other scalar factors in Eq. 4 represent the effects of the following quantities. A simple description is provided here, the reader is directed to [NWT05] for details of the formulation:

- f_{ampl} represents the effect of tensorial strain amplitude A_ϵ Note that an elaborate procedure is needed to quantify A_ϵ for complicated cycle shapes.
- $\dot{f}_N$ represents the effects of cyclic history, that is, change of the accumulation rate with increasing number of cycles. Actually, product $\dot{g} = f_{\mathrm{ampl}} \dot{f}_N$ must be defined as a single equation to make sure the model obeys so-called Miner's rule (it implies that the sequence of application of constant-amplitude blocks of cycles is of no importantce).
- f_Y quantifies the effect of stress ratio, f_p the effect of mean stress and f_e the effect of void ratio.
- Finally, f_π quantifies the effect of *cycle polarisation* (for details of its elaborate formulation, see [NWT05]).

Note that the use of Eq. (3) does not necessarily imply that $\mathbf{D}^{\mathrm{acc}}$ must be a controlling variable and $\mathring{\mathbf{T}}$ the controlled one. Depending on the boundary conditions, the Equations (3) and (4) imply either change of permanent deformation, or the change of stress, or both [Wic16]. As a special case, accumulation strain rate can be restricted by a zero volume change condition $\mathrm{tr}\,\mathbf{D}^{\mathrm{acc}} = 0$, which implies undrained conditions. Eq. (3) then predicts the pore water pressure accumulation rate. The model can thus be used to predict both drained and undrained conditions. This makes it, at least in

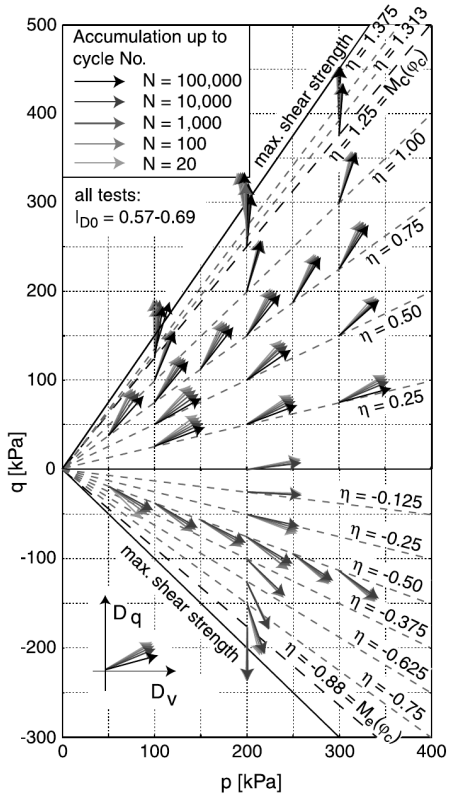

Figure 23: Experimental data showing directions $\mathbf{m}$ of strain accumulation (figure from [NWT05]).

principle, also suitable for predicting cyclic response of clays. Such a model has been tested by [Wic16], who included two further scalar factors, namely the factor controlling the effects of overconsolidation ratio f_{OCR} and the factor controlling the effect of loading frequency f_f to allow for rate-dependency of clay behaviour. Different procedure to calculate the effects of cyclic phenomena in clays has been proposed by [JGA$^+$14].

5 Conclusions

Predicting soil non-linearity and the effects of cyclic loading gives rise to possibly the most complex modelling approaches adopted for predicting the behaviour of "simple" soils, where the effects of additional variables such as temperature, partial saturation and chemical composition of pore fluid do not play a role. Various approaches exist with the same target, which is predicting the non-linear state- and history-dependent

stress-strain response. Some of them were covered in this lecture, showing how the same physical phenomenon may be approached using quite different mathematical frameworks. As the next step, evaluation of the models for predicting the effects of cyclic loading was presented. It was quite clear, that regardless the development in past decades, modelling of stress- and strain-accumulation during cyclic loading has their limits which are very difficult to surpass. An alternative approach is represented by explicit accumulation models, where the average accumulated state is followed, instead of soil response within each cycle. While valuable for conditions of low-amplitude regular cyclic loading, these models present less accurate predictive capabilities for irregular large loading cycles.

It is the author's opinion that modelling the effects of cyclic loading is one of the directions of soil constitutive modelling research which are far from being solved and many interesting approaches have yet to come.

6 Acknowledgement

The author is grateful to Jose Duque for his valuable comments on the manuscript.

References

[APP97] T.I. Addenbrooke, D.M. Potts, and A.M. Puzrin. The influence of prefailure soil stiffness on the numerical analysis of tunnel construction. *Géotechnique*, 47(3):693–712, 1997.

[ATMW89] A. Al-Tabbaa and D. Muir Wood. An experimentally based "bubble" model for clay. In *Proc. 3^{th} Int. Conf. on Numerical Models in Geomechanics*. Niagara Falls, 1989.

[Ben07] T. Benz. *Small-strain stiffness of soils and its numerical consequences*. PhD thesis, University of Stuttgart, 2007.

[BFM+19] M. Bode, W. Fellin, D. Mašín, G. Medicus, and A. Ostermann. An intergranular strain concept for material models formulated as rate equations. *International Journal for Numerical and Analytical Methods in Geomechanics*, 44:1003–1018, 2019.

[BS04] B. A. Baudet and S. E. Stallebrass. A constitutive model for structured clays. *Géotechnique*, 54(4):269–278, 2004.

[BVS09] T. Benz, P. A. Vermeer, and R. Schwab. A small-strain overlay model. *International Journal for Numerical and Analytical Methods in Geomechanics*, 33:25–44, 2009.

[CT20] M. Cudny and A. Truty. Refinement of the hardening soil model within the small strain range. *Acta Geotechnica*, 15(8):2031–2051, 2020.

[CV04] M. Cudny and P. A. Vermeer. On the modelling of anisotropy and destruction of soft clays within the multi-laminate framework. *Computers and Geotechnics*, 31(1):1–22, 2004.

[Daf86] Y. F. Dafalias. Bounding surface plasticity. I: Mathematical foundation and hypoplasticity. *Journal of Engineering Mechanics ASCE*, 112(9):966–987, 1986.

[DFM+21] J. Duque, W. Fuentes, Yang. M., D. Mašín, and M. Taiebat. Characteristic limitations of advanced plasticity and hypoplasticity models for cyclic loading of sands. *Acta Geotechnica (submitted)*, 2021.

[DM04] Y. F. Dafalias and M. T. Manzari. Simple plasticity sand model accounting for fabric change effects. *Journal of Engineering Mechanics*, 130(6):622–634, 2004.

[DMF20] J. Duque, D. Mašín, and W. Fuentes. Improvement to the intergranular strain model for larger numbers of repetitive cycles. *Acta Geotechnica*, 15:3593–3604, 2020.

[DTS+21] J. Duque, M. Tafili, G. Seidalinov, D. Mašín, and W. Fuentes. Inspection of four advanced constitutive models for fine-grained soils under monotonic and cyclic loading. *Acta Geotechnica (submitted)*, 2021.

[EP03] I. Einav and A. M. Puzrin. Evaluation of continuous hyperplastic critical state (CHCS) model. *Géotechnique*, 53(10):901–913, 2003.

[EP04] I. Einav and A. M. Puzrin. Continuous hyperplastic critical state (CHCS) model derivation. *International Journal of Solids and Structures*, 41:199–226, 2004.

[EPH03] I. Einav, A. M. Puzrin, and G. T. Houlsby. Numerical studies of hyperplasticity with single, multiple and a continuous field of yield surfaces. *International Journal for Numerical and Analytical Methods in Geomechanics*, 27:837–858, 2003.

[ESS12] K. C. Ellison, K. Soga, and B. Simpson. A strain space soil model with evolving stiffness anisotropy. *Géotechnique*, 62(7):627–641, 2012.

[FMD20] William Fuentes, David Mašín, and Jose Duque. Constitutive model for monotonic and cyclic loading on anisotropic clays. *Géotechnique (in print)*, 2020.

[FPB05] J. N. Franzius, D. M. Potts, and J. B. Burland. The influence of soil anisotropy and K_0 on ground surface movements resulting from tunnel excavation. *Géotechnique*, 55(3):189–199, 2005.

[FT15] W. Fuentes and T. Triantafyllidis. ISA: a constitutive model for deposited sand. In Tom Schanz and Achim Hettler, editors, *Aktuelle Forschung in der Bodenmechanik 2015*, pages 169–187, Berlin, Heidelberg, 2015. Springer Berlin Heidelberg.

[FWGL20] W. Fuentes, T. Wichtmann, M. Gil, and C. Lascarro. ISA-Hypoplasticity accounting for cyclic mobility effects for liquefaction analysis. *Acta Geotechnica*, 15(6):1513–1531, 2020.

[Gas05] A. Gasparre. *Advanced laboratory characterisation of London Clay*. PhD thesis, University of London, Imperial College of Science, Technology and Medicine, 2005.

[GH83] J. Graham and G. T. Houlsby. Anisotropic elasticity of a natural clay. *Géotechnique*, 33(2):165–180, 1983.

[GMW99] A. Gajo and D. Muir Wood. Severn-Trent sand: a kinematic hardening constitutive model: the *q-p* formulation. *Géotechnique*, 49(5):595–614, 1999.

[GMW01] A. Gajo and D. Muir Wood. A new approach to anisotropic, bounding surface plasticity: general formulation and simulations of natural and reconstituted clay behaviour. *International Journal for Numerical and Analytical Methods in Geomechanics*, 25:207–241, 2001.

[GNM+07] A. Gasparre, S. Nishimura, N. A. Minh, M. R. Coop, and R. J. Jardine. The stiffness of natural London Clay. *Géotechnique*, 57(1):33–47, 2007.

[GZP06] A. Grammatikopoulou, L. Zdravković, and D. M. Potts. General formulation of two kinematic hardening constitutive models with a smooth elastoplastic transition. *International Journal of Geomechanics*, 6(5):291–302, 2006.

[Has89] K. Hashiguchi. Subloading surface model in unconventional plasticity. *Int. J. Solids Struct.*, 25(8):917–945, 1989.

[HN79] T. Hueckel and R. Nova. Some hysteresis effects of the behaviour of geological media. *International Journal of Solids and Structures*, 15(8):625–642, 1979.

[HSOT02] K. Hashiguchi, K. Saitoh, T. Okayasu, and S. Tsutsumi. Evaluation of typical conventional and unconventional plasticity models in prediction of softening behaviour of soils. *Géotechnique*, 52(8):561–578, 2002.

[JGA+14] H. P. Jostad, G. Grimstad, H. H. Andersen, M. Saue, Y. Shin, and D. You. A FE procedure for foundation design of offshore structures – applied to study a potential owt monopile foundation in the Korean Western sea. *Geotechnical Engineering Journal of the SEAGS & AGSSEA*, 45(4):63–72, 2014.

[JPFB86] R. J. Jardine, D. M. Potts, D. M. Fourie, and J. B. Burland. Studies of the influence of non-linear stress-strain characteristics in soil-structure interaction. *Géotechnique*, 36(3):377–396, 1986.

[JSB84] R. J. Jardine, M. J. Symes, and J. B. Burland. The measurement of soil stiffness in the triaxial apparatus. *Géotechnique*, 34(3):323–340, 1984.

[KA00] M. Kavvadas and A. Amorosi. A constitutive models for structured soils. *Géotechnique*, 50(3):263–273, 2000.

[KHV05] N. Khalili, M. A. Habte, and S. Valliapan. A bounding surface plasticity model for cyclic loading of granular soils. *International Journal for Numerical Methods in Engineering*, 63:1939–1960, 2005.

[LY21] D. Liao and Z. Yang. Hypoplastic modeling of anisotropic sand behavior accounting for fabric evolution under monotonic and cyclic loading. *Acta Geotechnica*, 16(7):2003–2029, 2021.

[Maš14] D. Mašín. Clay hypoplasticity model including stiffness anisotropy. *Géotechnique*, 64(3):232–238, 2014.

[Maš19] D. Mašín. *Modelling of Soil Behaviour with Hypoplasticity - Another Approach to Soil Constitutive Modelling*. Springer International Publishing, 2019.

[MD97] M. T. Manzari and Y. F. Dafalias. A critical state two-surface plasticity model for sands. *International Journal for Numerical and Analytical Methods in Geomechanics*, 47(2):255–272, 1997.

[MH03] G. R. McDowell and K. W. Hau. A simple non-associated three surface kinematic hardening model. *Géotechnique*, 53(4):433–437, 2003.

[MNZ78] Z. Mroz, V. A. Norris, and O. C. Zienkiewicz. An anisotropic hardening model for soils and its application to cyclic loading. *International Journal for Numerical and Analytical Methods in Geomechanics*, 2:203–221, 1978.

[MNZ79] Z. Mróz, V. A. Norris, and O. C. Zienkiewicz. Application of an anisotropic hardening model in the analysis of elasto-plastic deformation of soil. *Géotechnique*, 29(1):1–34, 1979.

[Mróz67] Z. Mróz. On the description of anisotropic work-hardening. *Journal of the Mechanics and Physics of Solids*, 15:163–175, 1967.

[NH97] A. Niemunis and I. Herle. Hypoplastic model for cohesionless soils with elastic strain range. *Mechanics of Cohesive-Frictional Materials*, 2(4):279–299, 1997.

[NPSGT11a] A. Niemunis, L. F. Prada Sarmiento, and C. E. Grandas Tavera. Extended paraelasticity and its application to a boundary value problem. *Acta Geotechnica*, 6:91–92, 2011.

[NPSGT11b] A. Niemunis, L. F. Prada Sarmiento, and C. E. Grandas Tavera. Paraelasticity. *Acta Geotechnica*, 6:67–80, 2011.

[NWT05] A. Niemunis, T. Wichtmann, and T. Triantafyllidis. A high-cycle accumulation model for sand. *Computers and Geotechnics*, 32:245–263, 2005.

[PB98] A. M. Puzrin and J. B. Burland. Non-linear model of small-strain behaviour of soils. *Géotechnique*, 48(2):217–233, 1998.

[PB00] A. M. Puzrin and J. B. Burland. Kinematic hardening plasticity formulation of small strain behaviour of soils. *International Journal for Numerical and Analytical Methods in Geomechanics*, 24:753–781, 2000.

[PP87] S. Pietruszczak and G. N. Pande. Multi-laminate framework of soil models – plasticity formulation. *International Journal for Numerical and Analytical Methods in Geomechanics*, 11(6):651–658, 1987.

[PS83] G. N. Pande and K. G. Sharma. Multi-laminate model for clays – a numerical evaluation of the influence of rotation of principal axes. *International Journal for Numerical and Analytical Methods in Geomechanics*, 7(4):397–418, 1983.

[PW99] J. M. Pestana and A. J. Whittle. Formulation of a unified constitutive model for clays and sands. *International Journal for Numerical and Analytical Methods in Geomechanics*, 23:1215–1243, 1999.

[PZC90] M. Pastor, O. C. Zienkiewicz, and A. H. C. Chan. Generalized plasticity and the modelling of soil behaviour. *International Journal for Numerical and Analytical Methods in Geomechanics*, 14:151–190, 1990.

[RB68] K. H. Roscoe and J. B. Burland. On the generalized stress-strain behaviour of wet clay. In J. Heyman and F. A. Leckie, editors, *Engineering Plasticity*, pages 535–609. Cambridge University Press, Cambridge, 1968.

[RK06] A. R. Russell and N. Khalili. A unified bounding surface plasticity model for unsaturated soils. *International Journal for Numerical and Analytical Methods in Geomechanics*, 30(3):181–212, 2006.

[RMW00] M. Rouainia and D. Muir Wood. A kinematic hardening constitutive model for natural clays with loss of structure. *Géotechnique*, 50(2):153–164, 2000.

[RMW01] M. Rouainia and D. Muir Wood. Implicit numerical integration for a kinematic hardening soil plasticity model. *International Journal for Numerical and Analytical Methods in Geomechanics*, 25:1305–1325, 2001.

[Sim92] B. Simpson. Retaining structures: displacement and design. *Géotechnique*, 42(4):539–576, 1992.

[SSP09] F. Scharinger, H. F. Schweiger, and G. N. Pande. On a multilaminate model for soil incorporating small strain stiffness. *International Jour-*

nal for Numerical and Analytical Methods in Geomechanics, 33:215–243, 2009.

[ST97] S. E. Stallebrass and R. N. Taylor. Prediction of ground movements in overconsolidated clay. *Géotechnique*, 47(2):235–253, 1997.

[ST14] G. Seidalinov and M. Taiebat. Bounding surface SANICLAY plasticity model for cyclic clay behavior. *International Journal for Numerical and Analytical Methods in Geomechanics*, 38(7):702–724, 2014.

[SVB00] T. Schanz, P. A. Vermeer, and P. G. Bonnier. The hardening soil model: Formulation and verification. In *Beyond 2000 in Computational Geotechnics - 10 Years of PLAXIS*, pages 281–296. Balkema, Rotterdam, 2000.

[TD08] M. Taiebat and Y. F. Dafalias. SANISAND: Simple anisotropic sand plasticity model. *International Journal for Numerical and Analytical Methods in Geomechanics*, 32:915–948, 2008.

[VLJ05] V. Vukadin, J. Likar, and V. Jovičić. Development of a conceptual material model for structured materials - S_BRICK. *Acta Geotechnica Slovenica*, 2005(1):33–43, 2005.

[vW96] P. A. von Wolffersdorff. A hypoplastic relation for granular materials with a predefined limit state surface. *Mechanics of Cohesive-Frictional Materials*, 1(3):251–271, 1996.

[WFT19] T. Wichtmann, W. Fuentes, and T. Triantafyllidis. Inspection of three sophisticated constitutive models based on monotonic and cyclic tests on fine sand: Hypoplasticity vs. sanisand vs. isa. *Soil Dynamics and Earthquake Engineering*, 124:172–183, 2019.

[WH14] D. Wegener and I. Herle. Prediction of permanent soil deformations due to cyclic shearing with a hypoplastic constitutive model. *Geotechnik*, 37(2):113–122, 2014.

[Whi93] A. J. Whittle. Evaluation of a constitutive model for overconsolidated clays. *Géotechnique*, 43(2):289–313, 1993.

[Wic16] T. Wichtmann. *Soil behaviour under cyclic loading - experimental observations, constitutive description and applications*. Habilitation thesis, 2016.

[WK94] A. J. Whittle and M. J. Kavvadas. Formulation of MIT-E3 constitutive model for overconsolidated clays. *Journal of Geotechnical Engineering ASCE*, 120(1):173–198, 1994.

[WT16a] T. Wichtmann and T. Triantafyllidis. An experimental data base for the development, calibration and verification of constitutive models for sand with focus to cyclic loading. Part I - tests with monotonic loading and stress cycles. *Acta Geotechnica*, 11(4):739–761, 2016.

[WT16b] T. Wichtmann and T. Triantafyllidis. An experimental data base for the development, calibration and verification of constitutive models for sand with focus to cyclic loading. Part II: tests with strain cycles and combined loading. *Acta Geotechnica*, 11(4):763–774, 2016.

[WT18] T. Wichtmann and T. Triantafyllidis. Monotonic and cyclic tests on kaolin: a database for the development, calibration and verification of constitutive models for cohesive soils with focus to cyclic loading. *Acta Geotechnica*, 13(5):1103–1128, 2018.

[YTD21] M. Yang, M. Taiebat, and Y. F. Dafalias. SANISAND-MSf: a sand plasticity model with memory surface and semifluidised state. *Géotechnique (in print)*, 71, 2021.

Meta-stable structure, breakage and thermal effects

David Mašín[1]

[1] *Charles University, Prague, Czech Republic*

In this lecture, we will focus on the effect of various phenomena affecting soil behaviour, such as meta-stable structure caused by clay fabric and bonding or by inter-particle cementation in coarse-grained soils. Also, the effects of particle breakage and the effects of temperature on soil behaviour will be explored. In all cases, we first start with experimental evidence on the particular effect, followed by micromechanical interpretation of the processes involved. Finally, a procedure for modelling these phenomena will be discussed. It will be shown that, however independent these effects may seem, they can all be well represented using a simple concept of additional hardening laws controlling the size of the yield surface (or bounding surface, state boundary surface, asymptotic state boundary surface, whatever modelling concept is adopted for definition of reference model). Obviously, additional effects can take place depending on the process of interest (such as thermally-induced strains due to thermal expansion of grains) and these effects must also be included in the model formulation to obtain correct overall prediction of the process of interest.

1 Introduction

The effects of meta-stable structure, inter-particle cementation, breakage and thermal effects, along with the effects of partial saturation discussed in a separate lecture, may appear quite independent from the perspective of physical processes involved, leading to very similar modelling approaches. In this lecture, we will show how to include these advanced phenomena into models. Thanks to the hierarchical model structure, the concepts presented here can equally be adopted in combination with different modelling theories (being it single-surface elasto-plasticity, bounding plasticity, generalised plasticity or hypoplasticity), provided the reference models are based on the critical state soil mechanics principles.

2 Clay Structure

This section on the effects of soil structure follows from [Maš19].

2.1 Mechanical Behaviour of Structured Clays

The influence of structure on the behaviour of fine-grained soils has been thoroughly studied in the past; see, in particular, Burland [Bur90], Cotecchia and Chandler [CC00] and Leroueil and Vaughan [LV90].

The notion of soil structure is considered to be a combination of 'fabric' (the arrangement of soil particles) and 'bonding' (cementation of particles) [CC00]. By this definition, any clay has a structure. To eliminate ambiguity in the description of the effects of structure, standardised way for fabrication of a reference material has been adopted in soil mechanics. The widely accepted method is the so-called reconstitution method. As defined by Burland [Bur90], reconstituted soil is prepared by thorough mixing of natural soil at a water content of 1 to 1.5 times higher than its liquid limit w_L. The soil is mixed with water to form a slurry without drying prior to mixing. After reconstitution, the samples are prepared by one-dimensional consolidation in a high oedometer ('consolidometer'). A reconstituted soil prepared in this way does not show any effects of bonding and has a 'standardised' fabric.

The effects of fabric and bonding are best illustrated using their influence on soil normal compression behaviour and shear strength. As illustrated in Fig. 1, structured soil has the normal compression line (NCL) shifted higher in the graph of $\ln p$ vs. $\ln(1+e)$. The normal compression line represents the highest possible void ratio the soil can exhibit for the given mean stress p. Structure thus allows the soil to exist at a higher porosity than the corresponding reconstituted material. In other words (see Fig. 1), structured soil has (for the given void ratio) a higher Hvorslev's equivalent pressure p_e than the reconstituted soil. The ratio of the Hvorslev's equivalent pressures of structured and reconstituted soils can be denoted as 'stress sensitivity' s_σ [CC00][1].

Structure also influences undrained shear strength of the soil. While the critical state friction angle appears to be unaffected by the effects of structure, structured soil has a higher undrained shear strength than the reconstituted soil at the same void ratio. The ratio of these undrained shear strengths has been denoted as the strength sensitivity s_{us} by Cotecchia and Chandler [CC00]. By investigation of a number of different structured soils, Cotecchia and Chandler [CC00] observed that it is reasonable to assume that the strength sensitivity is equal to the stress sensitivity and to define a single variable s_t (denoted simply as "sensitivity"), such that $s_t = s_{us} = s_\sigma$. Sensitivity thus represents a primary variable adopted in the description of the behaviour of structured soils.

[1] Note that Cotecchia and Chandler [CC00] define stress sensitivity as a ratio of the preconsolidation stresses p_c of structured and reconstituted soils, but it can be formulated using equivalent pressure p_e alternatively.

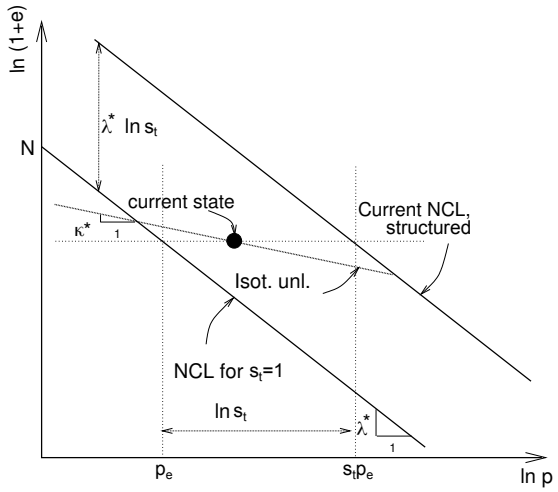

Figure 1: Definition of stress sensitivity, the primary variable adopted in the description of the structured soil behaviour (graph from Mašín [Maš07]).

The position of the isotropic normal compression line determines the size of the state boundary surface in the isotropic direction, whereas the undrained shear strength controls its apex in the p vs. q space. Cotecchia and Chandler [CC00] also studied the complete shape of the state boundary surface and found that, within reason, the shape of the state boundary surface (that is, the shape of its constant void ratio cross-section) is similar for reconstituted and structured soils. The state boundary surfaces thus differ in size only, determined by s_t. The principle is clear from the sketch in Fig. 2.

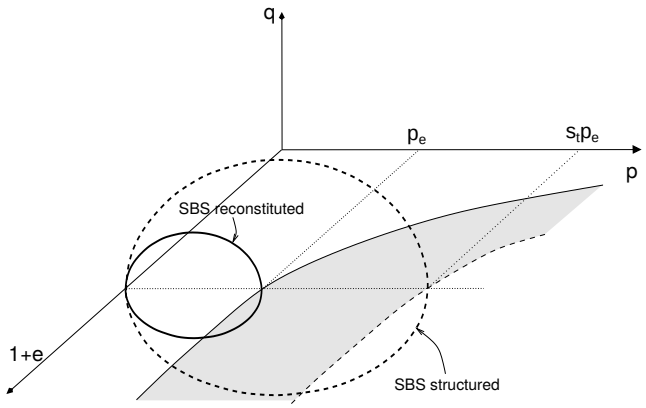

Figure 2: Sketch of state boundary surfaces (SBS) of reconstituted and structured soils (figure from [Maš19]).

Earlier in this chapter, it was mentioned that the soil structure is composed of the combination of fabric and bonding. These two types of structure influence the soil behaviour in different ways. Fabric cannot be easily disturbed by loading within the strain range applicable to most geoengineering problems. Thus, when structure is caused by fabric only, s_t may be assumed to be a constant [BS04]. The normal compression line of structured soil then has in the plane $\ln p$ vs. $\ln(1+e)$ the same slope as the normal compression line of reconstituted soil (measured by the parameter λ^*). Its position is controlled by the parameter N_{str}, related to N and s_t by $N_{str} = N + \lambda^* \ln s_t$. The undrained shear strength of the structured soil is s_t-times higher than the undrained shear strength of the reconstituted soil at the same void ratio. Stiff sedimentary clays typically behave in this way.

Contrary to fabric, inter-particle bonding in natural soils is typically not high enough to sustain loading relevant to geotechnical applications. Due to the bonding degradation, s_t of bonded clays decreases during compression and shearing. The normal compression line of a structured soil thus has a higher slope than the normal compression line of a reconstituted soil, until the bonds degrade completely. The normal compression line of a bonded material is sketched in Figure 3. It demonstrates that it is possible to represent this behaviour by assuming a constant slope of the normal compression line λ^* combined with variable sensitivity s_t. Figure 4 shows two experimental examples of such a behaviour. Soft sedimentary clays typically behave in this way.

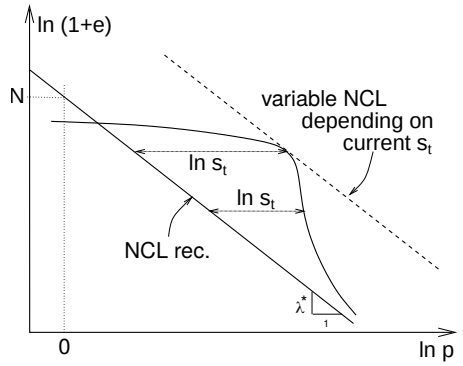

Figure 3: Normal compression behaviour of bonded soils.

2.2 Constitutive Modelling of Structured Clays

In this section, we will demonstrate incorporation of the effects of structure into existing critical state soil mechanics-based constitutive models. While many models exist using similar concept [LC02, WNKL03, MNZ79, BS04, RMW00, KA00, GMW01, CV04, RFDP03, Asa05], we will demonstrate the procedure here through its incorporation into hypoplasticity. The procedure described has been adopted by [Mašˇ07] to

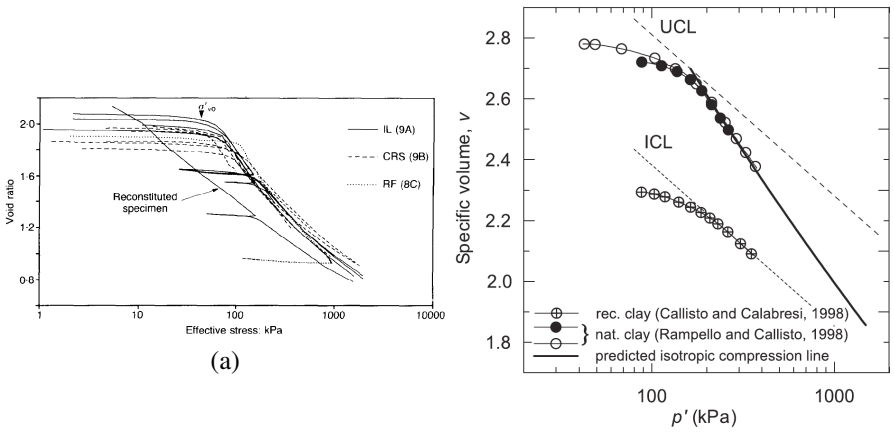

Figure 4: Examples of normal compression behaviour of bonded soils. (a) Bothkennar clay from [NSD92], (b) Pisa clay from [CR04].

modify the existing hypoplastic model for clays by [Maš05].

When the effects of structure are to be implemented into existing constitutive from, the following changes need to be done. First of all, sensitivity s_t must be considered as a state variable in the enhanced model. The Hvorslev's equivalent pressure is expressed as in the enhanced model by

$$p_e = s_t p_r \exp\left[\frac{N - \ln(1+e)}{\lambda^*}\right] \tag{1}$$

where N and λ^* are parameters representing the reconstituted soil behaviour.

Next, it is necessary to specify the rate equation for sensitivity s_t. Since the degradation of inter-particle bonding is caused by soil deformation, the rate of s_t depends on the stretching tensor $\mathbf{D}$. Both the volume strains and shear strains can cause degradation of bonding. In the model, a separate parameter is introduced to distinguish the effect of the shear and volumetric strain components on structure degradation. The rate equation for s_t reads

$$\dot{s}_t = -\frac{k}{\lambda^*}(s_t - s_f)\dot{\epsilon}^d \tag{2}$$

where k is a model parameter controlling the rate of structure degradation and s_f is the final sensitivity. As suggested by Baudet and Stallebrass [BS04], s_f is not necessarily equal to one. The value $s_f > 1$ represents stable elements of the structure caused purely by the soil fabric. $\dot{\epsilon}^d$ is the damage strain rate, defined as

$$\dot{\epsilon}^d = \sqrt{(\dot{\epsilon}_v)^2 + \frac{A}{1-A}(\dot{\epsilon}_s)^2} \tag{3}$$

where $\dot{\epsilon}_v = -\operatorname{tr}\mathbf{D}$ is the volume strain rate, $\dot{\epsilon}_s = \sqrt{2/3}\|\mathbf{D}^*\|$ is the shear strain rate and A is a parameter controlling their relative influence on the structure degradation.

Further, it is necessary to modify the formulation so that the model properly predicts the softer response in normal compression. It is clear from Fig. 3 that while p_e is calculated using the theoretical normal compression line of the slope λ^* corresponding to the current void ratio (i.e., Eq. (1)), the model predicts a softer response in normal compression thanks to the decrease of sensitivity. Let us denote the actual slope of the normal compression line of a structured soil as λ^*_{str}. It can be evaluated using the following procedure: the normal compression line of the structured soil can be expressed as (see Fig. 1)

$$\ln(1+e) = N + \lambda^* \ln s_t - \lambda^* \ln\left(\frac{p}{p_r}\right) \tag{4}$$

Its time differentiation results in

$$\frac{\dot{e}}{1+e} = \lambda^* \left(\frac{\dot{s}_t}{s_t} - \frac{\dot{p}}{p}\right) \tag{5}$$

The rate equation (5) can alternatively be written using the actual slope λ^*_{str} as

$$\frac{\dot{e}}{1+e} = -\lambda^*_{str}\frac{\dot{p}}{p} \tag{6}$$

To evaluate λ^*_{str}, the isotropic form of the structure degradation law is needed. It reads (from (2))

$$\dot{s}_t = \frac{k}{\lambda^*}(s_t - s_f)\frac{\dot{e}}{1+e} \tag{7}$$

A combination of (4), (5) and (7) leads to the following expression for λ^*_{str}:

$$\lambda^*_{str} = \frac{\lambda^* s}{s - k(s - s_f)} \tag{8}$$

In the structured model, λ^*_{str} enters the expression of the tensor $\mathcal{A}$:

$$\mathcal{A} = f_s\mathcal{L} + \frac{\mathbf{T}}{\lambda^*_{str}} \otimes \mathbf{1} \tag{9}$$

and factor f_s

$$f_s = \frac{3p}{2}\left(\frac{1}{\lambda^*_{str}} + \frac{1}{\kappa^*}\right)\frac{1-2\nu}{1+\nu} \tag{10}$$

The slope of the unloading line is controlled by κ^* and it is assumed to be independent of the value of s_t.

The above approach is needed to predict the behaviour of bonded clays. In the case where the sensitivity s_t is constant during loading (most stiff clays), N of the original model may be simply replaced by $N + \lambda^* \ln s_t$ and the original model can be used without any modification.

2.3 Calibration of Material Parameters – Clays with a Stable Structure

Calibration of the new parameters k, A and s_f, together with parameters controlling normal compression behaviour N and λ^*, will be discussed here. Calibration of parameters will be discussed separately for clays with a stable structure (constant s_t caused primarily by fabric) and a meta-stable structure (variable s_t caused by fabric and bonding).

As explained in Sect. 2.2, calibration of the model for clays with a stable structure is simpler. In principle, we may adopt the basic hypoplastic model for the modelling. The following two identical alternatives are available:

- Evaluate the parameters N and λ^* based on tests on reconstituted soils. Then adopt the basic model with the parameter N replaced by $N_{str} = N + \lambda^* \ln s_t$.
- Evaluate the parameters N and λ^* based on tests on reconstituted soils. Then adopt the model for structured clays with the calibrated value of sensitivity s_t, while assuming $k = 0$ and any $A \neq 1$.

In both cases, isotropic (or oedometric) tests on reconstituted soil should be performed. This is because clays with a stable structure (typically stiff clays) often have very high preconsolidation pressures. Calibration of the true slope of the normal compression line λ^* is complicated in this case, as it is often not clear whether the normal compression line has already been reached; see Figure 5. Once the parameter λ^* is known from the test results on a reconstituted soil, the value of N_{str} or s_t can be evaluated using the compression tests on the structured clay.

The sensitivity value can be evaluated as the ratio of the Hvorslev's equivalent pressures of structured and reconstituted soils (see Figure 1). Alternatively, it can also be evaluated as a ratio of the undrained shear strengths of structured and reconstituted soils. Note, however, that the reconstituted soil must be consolidated to the same void ratio as the equivalent structured soil prior to undrained shear strength testing in this case.

2.4 Calibration of Material Parameters – Clays with a Meta-Stable Structure

To calibrate the model for clays with a meta-stable structure, the initial value of sensitivity s_t needs to be evaluated using the same procedure as described in Sect. 2.3. Also, similarly to the stiff clay behaviour, the parameters N and λ^* need to be calibrated using tests on reconstituted soils.

The parameter k represents the rate of structure degradation and it controls the actual slope of the normal compression line λ^*_{str} predicted by the model (Eq. (8)). For calibration of k, the isotropic compression test is more suitable than the oedometric test, as in the latter case structure degradation is also influenced by the parameter A. The influence of the parameter k on the normal compression line is demonstrated in Figure

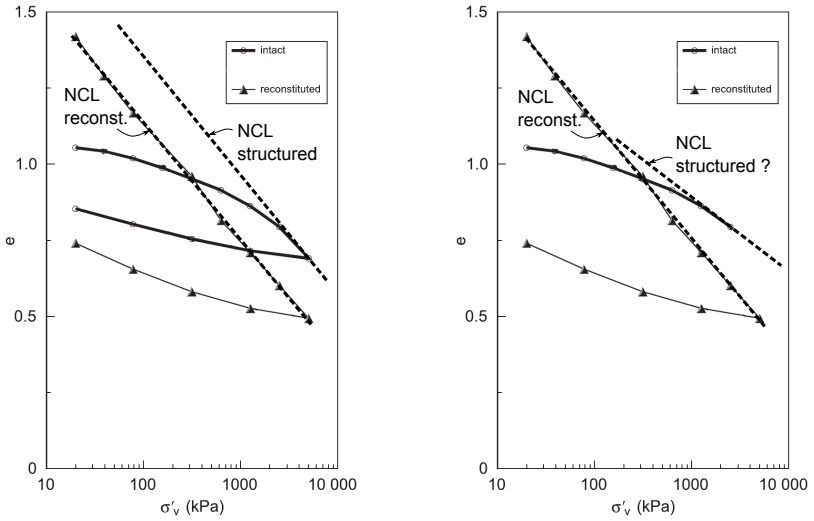

Figure 5: Typical problem in calibration of the parameter λ^* using compression test on undisturbed stiff clay samples. (a) correct calibration leading to the same value value of λ^* for reconstituted and undisturbed samples. (b) possible incorrect calibration using tests on an undisturbed sample which would have been stopped at $\sigma_v = 2500$ kPa. Experimental data on Calabria clay and the background graph (retouched) from [GMM06]. Figure used in [Maš19].

6. The value of $k = 0$ implies a model with constant s_t (stable structure). Increasing the value of k increases the rate of structure degradation. The parameter k can be calibrated by means of simulation of the soft clay normal compression behaviour using element test software. Alternatively, in the case of the isotropic compression test, Eq. (2) may be integrated analytically giving a finite expression for the dependency of s_t on the volume strain ϵ_v and other model parameters:

$$s_t = s_f + (s_{t0} - s_f) \exp\left[-\frac{k}{\lambda^*}\epsilon_v\right] \tag{11}$$

where s_{t0} is the initial value of sensitivity.

The parameter A controls the influence of shear strains on structure degradation. A should preferably be calibrated using undrained shear test results after the parameter k has been calibrated using isotropic (or oedometric) compression tests. The parameter A influences the stress path of the undrained shear test (see Figure 7). It should be calibrated by means of element test simulations of shear tests.

The model also requires specification of the final sensitivity s_f. Following Baudet and Stallebrass [BS04], this parameter quantifies stable elements of structure solely

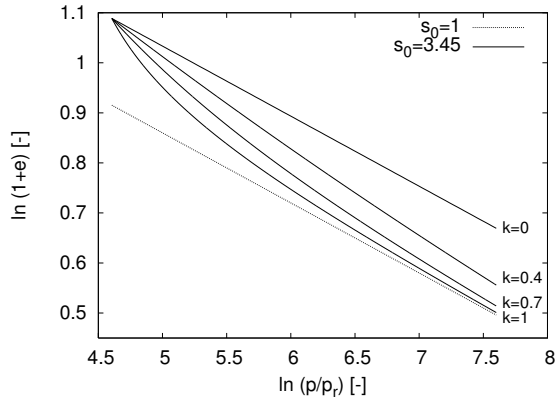

Figure 6: The influence of the parameter k on the isotropic normal compression line of clay with a meta-stable structure (figure from [Maš19]).

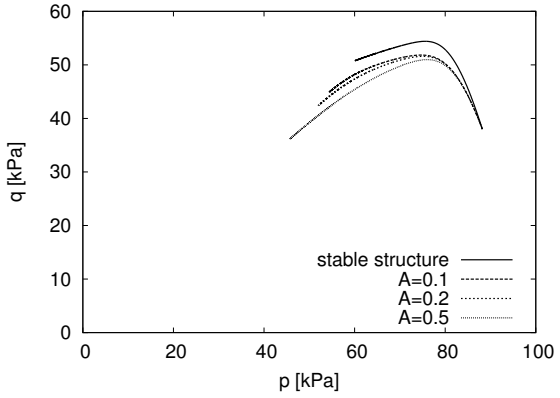

Figure 7: The influence of the parameter A on the undrained stress path of clay with a meta-stable structure (figure from [Maš19]).

due to the soil fabric. While s_f may be higher than one, many natural soft clays can reasonably be represented by $s_f = 1$. The influence of s_f on the isotropic normal compression behaviour of natural structured clay with both bonding and fabric is demonstrated in Fig. 8.

2.5 Examples of Model Predictions

The model for structured clays has been evaluated by [Maš07] using experimental data on Pisa clay by Callisto and Calabresi [CC98] and Bothkennar clay by Smith et

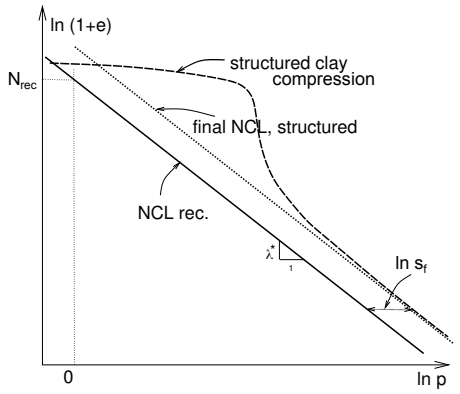

Figure 8: The influence of the parameter s_f characterising stable elements of structure due to soil fabric (figure from [Maš19]).

al [SJH92]. Here, we presented predictions of an updated model from [Maš19].

Figure 9 shows predictions of oedometric tests on undisturbed and reconstituted Bothkennar clay (data on samples extracted using two sampling methods). It is clear from Figure 9 that it is reasonable to assume the value of $s_f = 1$ in the case of Bothkennar clay.

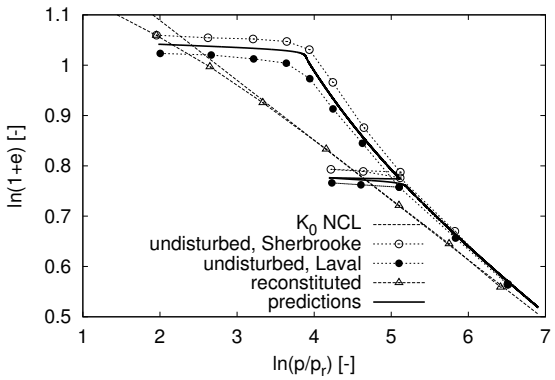

Figure 9: Predictions of oedometric test on undisturbed and reconstituted Bothkennar clay. Experimental data from [SJH92], simulations from [Maš07].

Structure degradation in shear is best represented using stress paths plotted in the space of stress normalised by the Hvorslev's equivalent pressure of reconstituted soil. Figure 10a shows results of two experimental data sets on Pisa clay from [CC98]. The tests

labeled as Ri were performed on reconstituted soil, whereas the tests labeled as Ai were performed on undisturbed soil. The tests were performed from the anisotropic stress state (estimated *in situ* stress state) with a controlled stress path direction. This direction (in degrees, measured anti-clockwise in the p vs. q space) is indicated as a number i in the experiment label. Structure degradation in the experiment is manifested by bending of the normalised stress paths when the state approaches the state boundary surface. Figure 10b shows predictions of these tests using the hypoplastic model, together with the shape of the asymptotic state boundary surface predicted by the model. The model properly predicts these structure degradation characteristics.

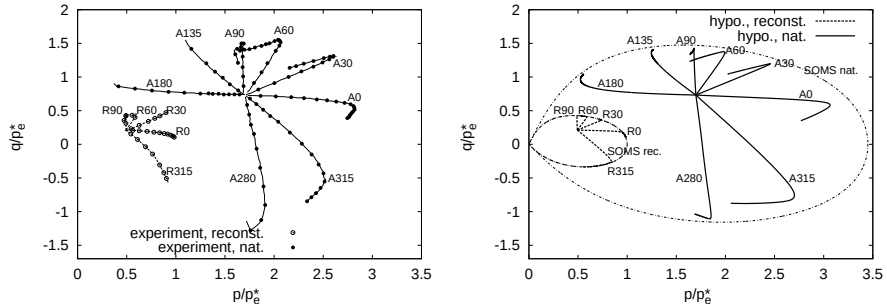

Figure 10: Predictions of stress probing tests on reconstituted and undisturbed Pisa clay. Experimental data from [CC98], simulations from [Maš07].

To demonstrate the effects of structure degradation, Figure 11 shows the same predictions for experiments on undisturbed samples as in Fig. 10b, together with predictions using the original hypoplastic model (that is, using the model with the parameter k set to 0). This model is incapable of predicting the structure degradation and thus the normalised stress paths are not predicted properly.

3 Cementation of coarse-grained soils

3.1 Experimental and micromechanical evidence of the effect of cementation in coarse-grained soils

In coarse-grained soils, an important feature affecting soil behaviour is cementation. Similar to structured clays, discussed in the previous section, cementation increases soil peak shear strength. [WL08] studied mechanical behaviour of cemented sands and observed a significant effect of cementation on peak shear strength (Figure 12a). They also concluded that if cementation is not extreme, its influence on critical strength is much less significant due to almost complete bond degradation in shearing. Some influence was still observed, however, due to remaining clusters of bonded particles.

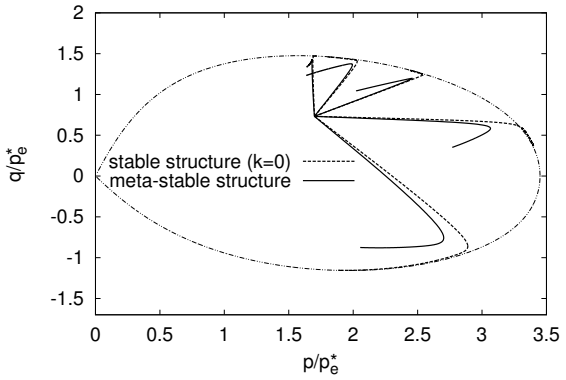

Figure 11: Predictions of stress probing tests on undisturbed Pisa clay. Comparison of predictions from Fig. 10b with predictions by the same model without structure degradation ($k = 0$).

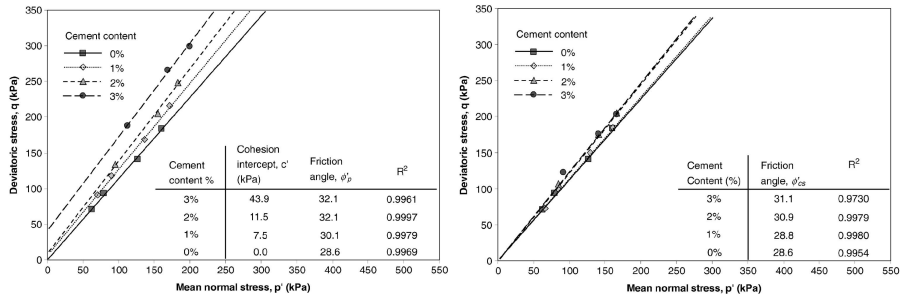

(a) (b)

Figure 12: The effect of cementation on peak (a) and critical state (b) strength of cemented sands (figures from [WL08]).

Similar effect of cementation structure in sands to the effects of structure in clays has also been observed in compression. Soil exhibits stiff response up to the yield point, when the bonds start to break and softer response follows. Finally, soil behaves as an uncemented sand, which is a consequence of complete bond breakage. This behaviour is demonstrated in Figure 13 from [LN95] showing compression behaviour of calcarenite.

Cementation in sands may be quite realistically modelled using discrete element method (DEM), which gives an insight into the soil behaviour from micromechanical point of view. Such models have been presented by [JYZU11], adopting contact model representing bonds shown in Figure 14. Consistently with the experimental results pre-

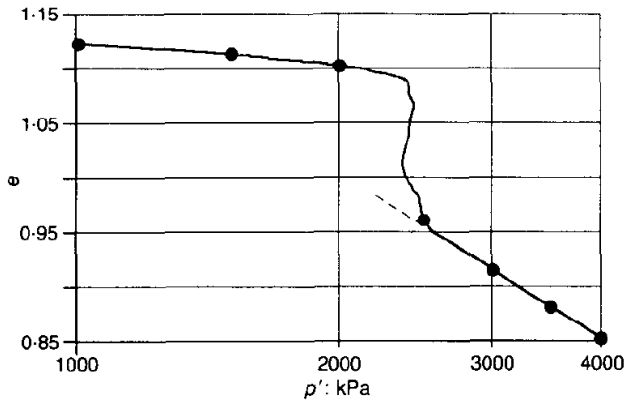

Figure 13: Compression behaviour of calcarenite (figure from [LN95]).

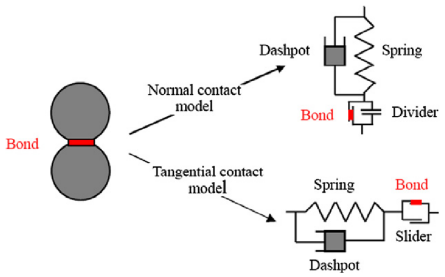

Figure 14: Contact model used in DEM analysis by [JYZU11] to represent inter-particle cementation.

sented above, [JYZU11] observed a significant effect of cementation on peak shear strength at low confining pressures (Figure 15a). At higher confining pressures, the effect is much less pronounced, as the inter-particle bonds had already been broken during the pre-shear compression stage (Figure 15b). Discrete element method allows us to investigate micromechanics of the process shown in Figure 15. Figure 16 shows bond breakage rate shown together with stress-strain curve from Figure 15. A clear peak in bond breakage rate can be observed, associated with the peak in stress-strain curve.

3.2 Modelling the effect of cementation in coarse-grained soils

Modelling of the effects of cementation is, similarly to modelling the behaviour of structured clays, based on variable size of the state boundary surface. A typical example is represented by the model by [LN95]. The yield surfaces of the fully cemented

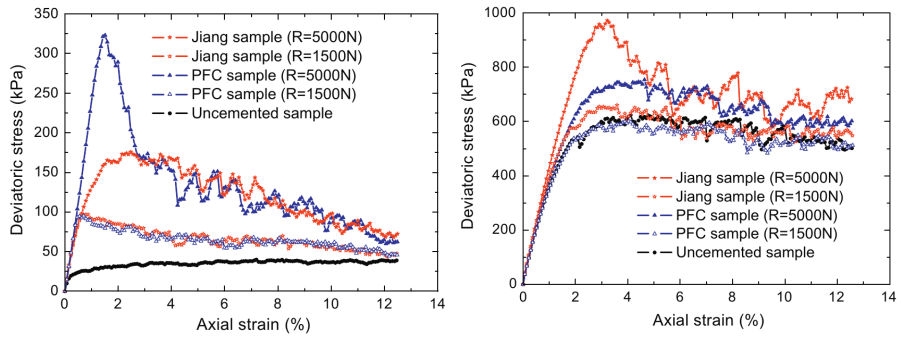

Figure 15: The effect of cementation on biaxial test results investigated using DEM method by [JYZU11]. (a) low confining pressure, (b) high confining pressure.

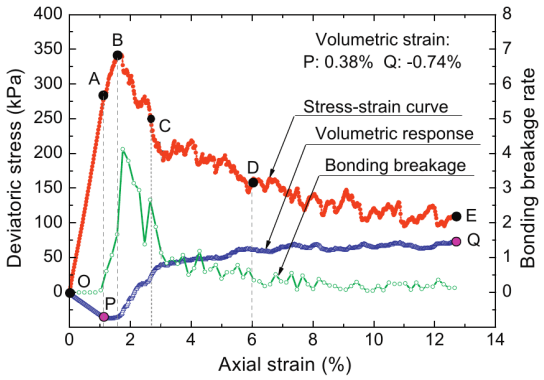

Figure 16: Bond breakage rate plotted together with stress-strain curve of biaxial test on cemented DEM sample (figure from [JYZU11]).

and uncemented soil are shown in Figure 17. Note that, unlike in clays, the yield surface of cemented material spans quite significantly into the tensile stress region thanks to tensile strength of the bonds.

Key to the model is, again similarly to modelling of structured clays, specification of the evolution equation for internal variables defining current cementation level and controlling the size of the yield surface. They are defined in terms of damage strain rate $\dot{\epsilon}^d$, calculated as a function of both plastic volumetric and shear strain rate. With properly selected evolution equations, the model predicts the response both in compression and in shear in agreement with experimental data (Figure 18) and in accordance with DEM observations developed later.

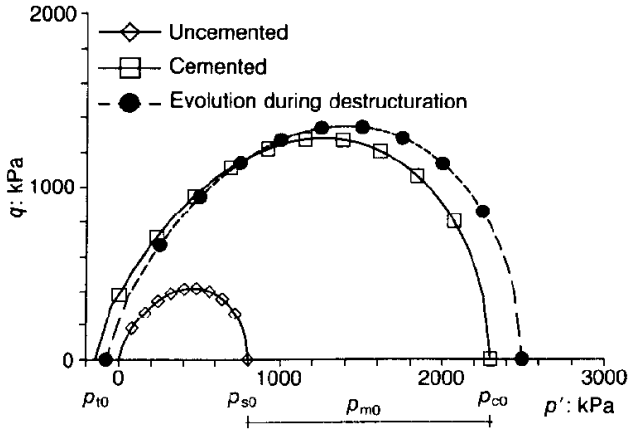

Figure 17: Yield surfaces for bonded and unbonded coarse grained soil model adopted by [LN95].

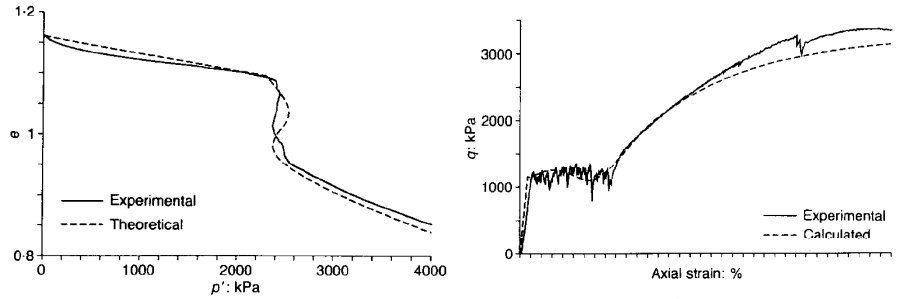

Figure 18: Predictions of the model for cemented soils by [LN95]. (a) behaviour in compression, (b) behaviour in shear.

Note that, similar concepts as used here for modelling of cemented materials can be used for modelling of the other effects. For example, [NCT03] extended the model by [LN95] to include effects of chemical degradation of inter-particle bonds, which can take place independently of mechanical loading.

4 Particle breakage

Particle breakage is an important phenomenon influencing the behaviour of granular materials. In this chapter, we first show that particle breakage commonly takes place, being inevitable part of loading process in granular materials. Subsequently,

its influence on the mechanical behaviour of granular materials will be clarified using experimental data and, finally, approaches to model these effects will be shown.

4.1 Measures of particle breakage

First of all, before studying the effects of particle breakage, we need to define measures quantifying the breakage. They will later play a role of state variables within the continuum constitutive models. Several measures have been proposed in the literature, most notably:

- Marsal [Mar67] breakage index B_g: When measuring the level of particle breakage, soil grain size distribution is determined before and after the experiment using standard set of sieves. B_g represents the sum of increases of material weight on the sieves when compared to the original state.
- Hardin [Har85] relative breakage B_r, which represents weight increase of particles below 0.74 mm normalised by the initial weight of particles above 0.74 mm.
- Einav [Ein07a, Ein07b] modified relative breakage B_r^E: Follows on Hardin's definition, but considers that breakage is not unlimited and, finally, an ultimate grain size distribution is reached which is not modified any further, see Figure 19.

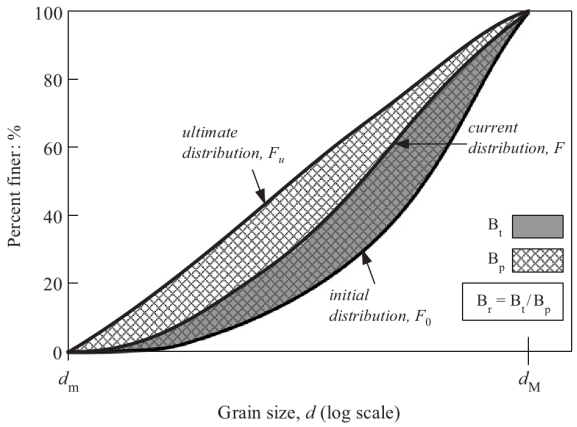

Figure 19: On the definition of Einav modified relative breakage index B_r^E (figure from [Ein07a])

4.2 Experimental evidence on particle breakage – shear experiments

Let us now show experimental evidence on particle breakage. First, we start with breakage induced by shear experiments. Figure 20 from [IS02] shows variation of Marsal breakage index B_g of railway ballast measured in large-scale triaxial apparatus during shear test. Clearly, the level of particle breakage increases with both effective confining pressure and axial strain. Similar conclusions have been obtained by [ASR10] - Figure 21 shows the dependency of breakage index B_g on confining stress in large-scale triaxial testing of rockfill materials of various grain shapes. Soils with rounded grain shapes ("Alluvium" trend line and soils with code starting "A") show somewhat lower degree of breakage than materials with angular grain shapes ("Blasting" trend line and soils with code starting "B"). Evolution of B_r in ring shear testing of carbonate sand has been studied by [CSBFG04]. They investigated the level of particle breakage for different sampling positions within the ring shear sample, demonstrating clearly that material in the shear zone is much more prone to particle breakage when compared to materials from zones above and below the shear zone (22).

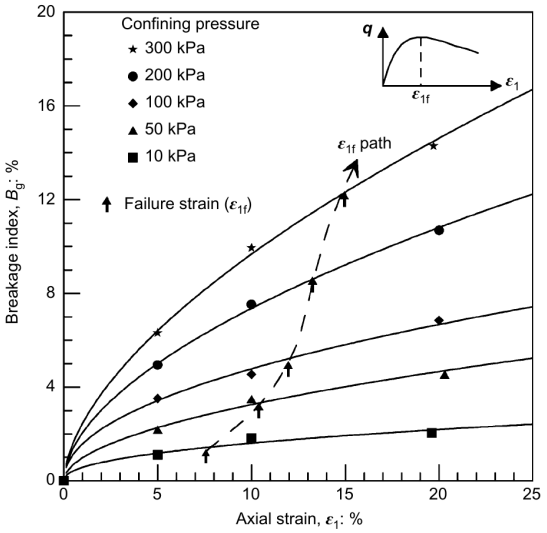

Figure 20: Variation of B_g of railway ballast in large-scale triaxial apparatus during shear test (figure from [IS02]).

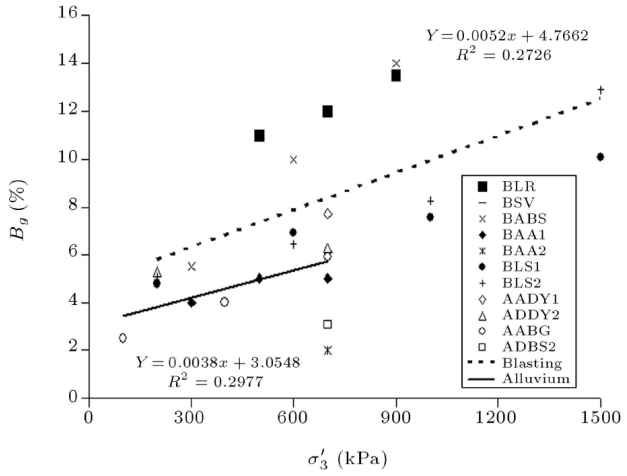

Figure 21: Dependency of B_g on confining stress in large-scale triaxial testing of various rockfill materials (angular and rounded) (figure from [ASR10]).

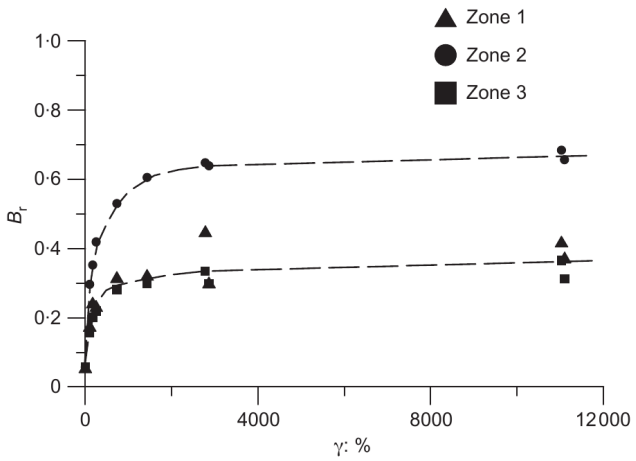

Figure 22: Evolution of B_r in ring shear testing of carbonate sand for different sampling positions within the ring shear sample. Zone 2 is the shear zone, zones 1 and 3 are above and below the shear zone respectively (figure from [CSBFG04]).

4.3 Experimental evidence on particle breakage – compression experiments

Particle breakage during soil loading is not restricted to tests in shear, though this deformation mode appears to be the most efficient for breaking the grains. Evolution

of particle breakage during experiments in compression (high-pressure oedometric tests) of Leighton Buzzard silica sand has been studied by [McD02], results are shown in Figure 23. Particle breakage is evident with the major breakage event taking place at the stress levels corresponding to the yield stress (Fig. 23b), which is rather well defined (Fig. 23a).

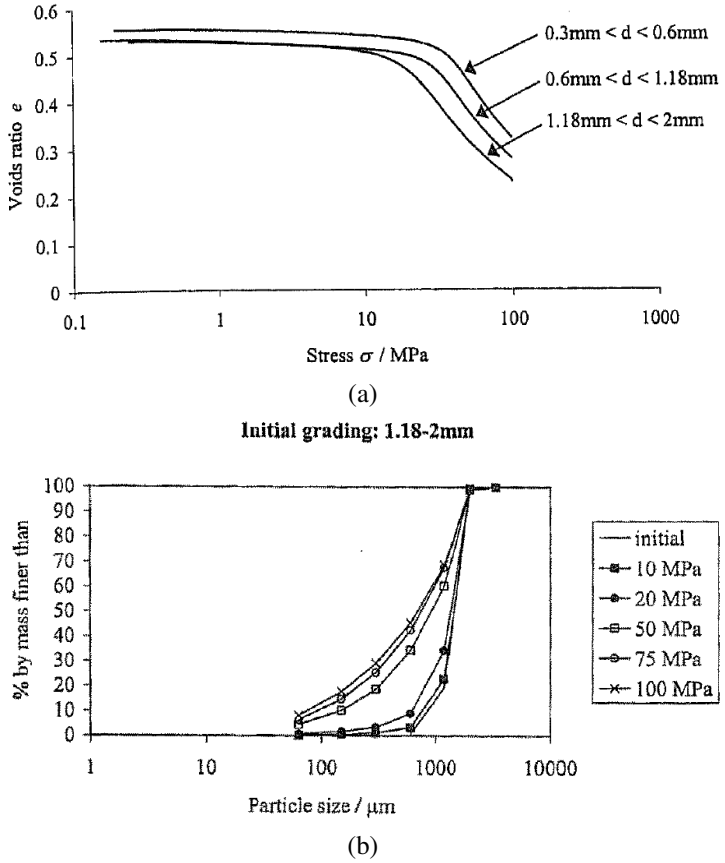

Figure 23: Particle breakage of Leighton Buzzard silica sand in high-pressure oedometric tests. (a) Evolution of void ratio with stress, (b) particle size evolution (figure from [McD02]).

4.4 Influence of particle breakage on soil mechanical behaviour

The soil mechanical properties are determined by particle size and shape, mineralogy and soils structure. Breakage, which causes changes of granulometry and of particle shape thus, indeed, affects the soil mechanical behaviour. Quantification of the effect is, however, not straightforward. As grains crush inevitably, a suitable reference

material (ideally unbreakable material) is not available. This makes quantification of the effects of particle breakage less straightforward than, for example, quantification of the effects of structure (Sec. 2), where reference "unstructured" material can be formed easily by reconstitution. Still, the influence of particle breakage can be judged using indirect methods or using DEM modelling.

First of all, let us inspect indirect methods. Here, we focus on the effect of grain size on soil properties in experiments, which were repeated on soils artificially prepared at various grain size distributions mimicking change of grain size distribution due to breakage. Sure, the experimental results are further effected by the particle breakage during the tests themselves, but this breakage will occur in all the cases, so the tests with different initial granulometry may be considered as indicative of the effect of evolving grain size distribution due to breakage, at least from a qualitative point of view.

Simply speaking, soil granulometry affects practically all soil properties. The only case where the effect would be reduced is for self-similar grain size distribution curves (translated horisontally in grain size distribution chart plotting fraction percentage vs. logarithm of grain size), but even in that case the size effects affect properties of grains and thus the overall soil behaviour. Here, we will discuss the most important/relevant effect of grain size from the constitutive modelling point of view: critical state friction angle, normal compression line and stress/dilatancy relationship.

Experiments studying the effect of particle breakage on critical state have been presented by [YS16, Yu17] and [BC11]. Both authors imposed artificially particle breakage by shearing the original soil in triaxial apparatus under high confining pressures. The same soil was subsequently shared again under low confining stress conditions (not imposing significant further breakage) to test the effect of breakage on critical state line. It turned out that particle breakage did not affect critical state friction angle significantly, but it changed position and inclination of the critical state line in $\ln p$ vs e plane, affected stress-dilatancy relationship and thus also peak friction angle (see Figure 24). The effect of particle breakage on peak friction angle has also been studied by [SMR11] for coarse grained (grains up to 50 mm) alluvial gravel, who clearly observed a decrease of peak friction angle with increasing particle breakage (Figure 25). Downward parallel shift of normal compression line in $\ln p$ vs e plane was observed by [GSD14].

Stress-dilatancy relationship was a focus of the work by [CDTV02] who studied shear behaviour of pyroclastic soil with crushable particles. They observed that the stress-dilatancy relationship progressively deviates from the linear dependency between dilatancy d and stress ratio η expected by classical soil mechanics theories (e.g., [Row62, Bol86]). They suggest this is because soil particles progressively crush during the shear process thus affecting the stress-dilatancy relationship continuously. These authors also assume the effect of grain crushing on critical state friction angle, which is not consistent with observations by [YS16, Yu17, BC11] discussed above; it is however to be noted that soil they tested has significantly more crushable particles that the soils investigated in [YS16, Yu17, BC11].

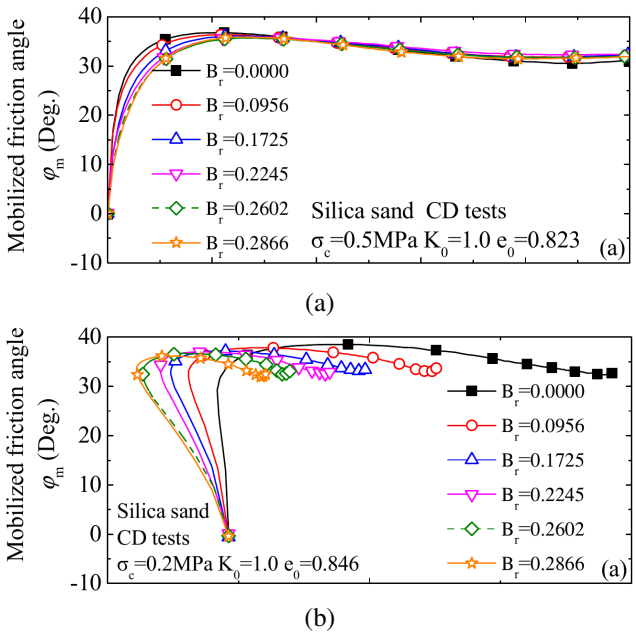

Figure 24: The effect of particle breakage on critical state friction angle (a) and dilatancy (b) on breakage during drained triaxial tests (figure from [McD02]).

The influence of particle breakage on compression behaviour can be also studied using discrete element method which (unlike soils) has an advantage of being able to simulate behaviour of ideally unbreakable soils for comparison. Breakable grains are typically created by agglomerating unbreakable spheres and proper setting of contact parameters [CBN04] (Figure 27a). Numerous works show that particle breakage is the major source of normal compression line shape for granular materials. For example, see Figure 27b by [BNC08], demonstrating downward shift of normal compression line due to breakage: effect similar to the loss of structure in structured soils.

4.5 Constitutive modelling of particle breakage

A number of models exist to predict the effects of particle breakage. It is to be pointed out that various authors focus on different soils with different breakage characteristics of grains so they may consider different features of soil behaviour to be of a different importance from the constitutive modelling point of view.

One of the models has been proposed by [CDTV02], which will be discussed here. These authors introduced a state variable $b \geq 1$ varying with breakage (measured here through damage strain), such that $b = 1$ for fully broken grains. This approach allowed them to model downward shift of NCL with particle breakage through the concept of

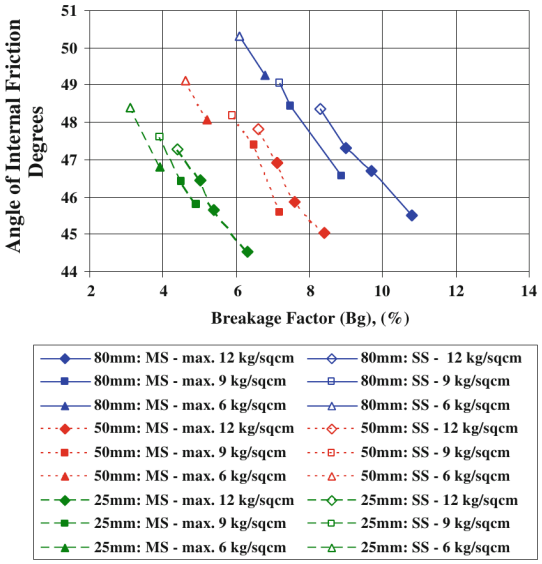

Figure 25: The effect of particle breakage on peak friction angle of alluvial gravel (figure from [YS16]).

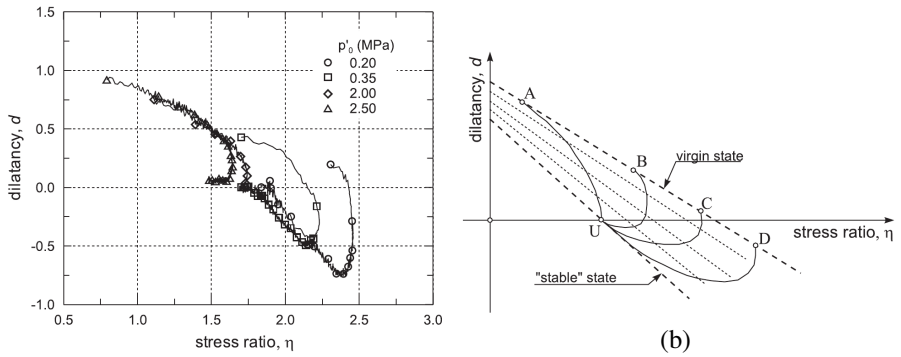

Figure 26: The effect of particle breakage on stress-dilatancy relationship. Experimental data (a) and interpretation (b) by [CDTV02]

breakage dependent size of the yield surface (Figure 28), similar to the concept of debonding in cemented soils. They also considered the effect of breakage on critical state friction angle. Different ways of obtaining similar shape of normal compression line has been proposed by [RK04], which specified multi-linear NCL equation directly without introducing additional breakage-related state variables (Figure 29a) and by

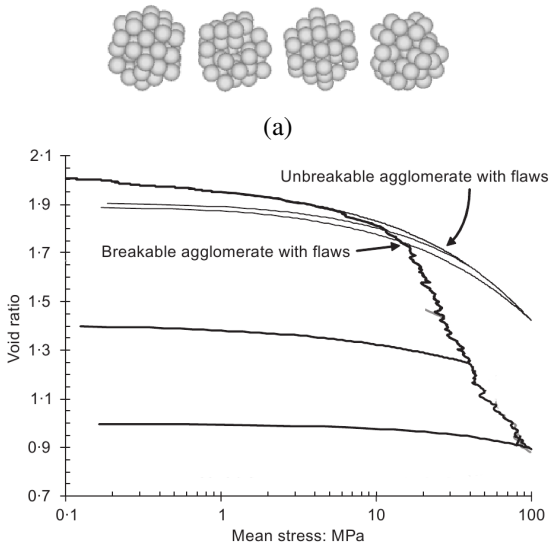

Figure 27: The effect of particle breakage investigated through DEM modelling. (a) breakable "particles" constructed by agglomeration of elementary spheres (figure from [CBN04]), (b) the effect of breakage on the isotropic normal compression line (figure from [BNC08]).

[Ein07b], who obtained the expression through thermodynamically-based continuum breakage mechanics (Figure 29b).

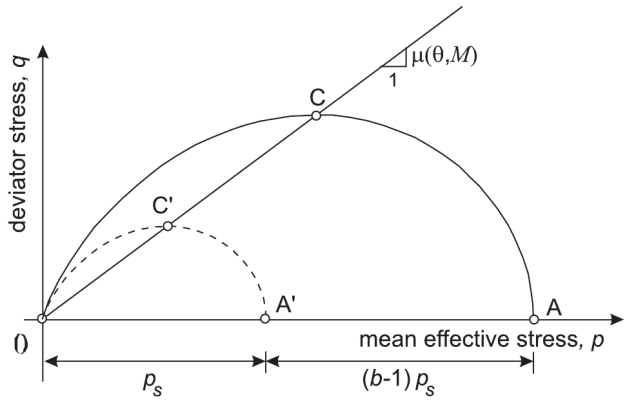

Figure 28: Yield surface dependency on particle breakage quantified through state variable b (figure from [CDTV02]).

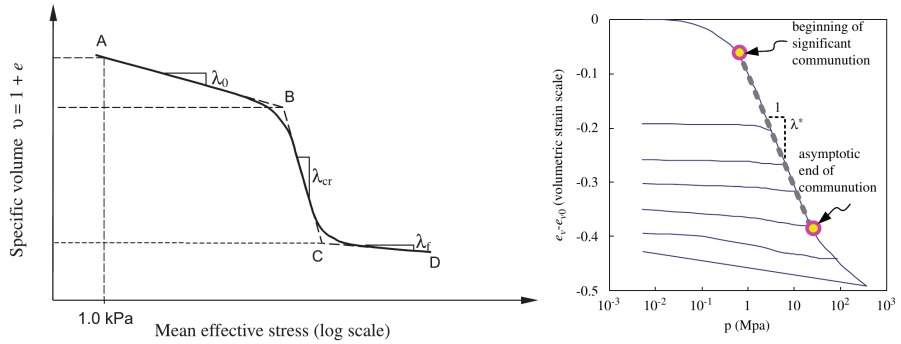

Figure 29: The effect of particle breakage on normal compression line predicted by models by [RK04] (a) and [Ein07b] (b)

Interesting to point out is the modelling procedure adopted by [CDTV02] to predict stress-dilatancy relationship introduced in Figure 26. They considered decreasing φ_c with particle breakage. This dependency also implies variable shape of the yield surface with breakage. When combined with the associative flow rule, this means also variable stress-dilatancy relationship, which is however still not representing well the experimental stress-dilatancy data. As a remedy, [CDTV02] chose associative flow rule and included additional parameter controlling yield surface shape such that the implied stress-dilatancy relationship during breakage matched the experiments.

5 Thermal Effects

This section on the effects of temperature follow from [Maš19].

Soil behaviour is influenced by temperature. Samples tested at different temperatures exhibit different stiffness and strength. Temperature variation even at a constant stress level causes the soil to deform. In most cases in geotechnical practice, temperature variations are not substantial and temperature effects do not need to be considered in simulations. However, temperature effects become important in a number of special applications, such as nuclear waste disposal facilities, buried high-voltage cables, pavements and geothermal energy. A model to predict temperature effects on soi behaviour is presented in this section.

5.1 Influence of Temperature on Soil Mechanical Behaviour

The influence of temperature on soil behaviour is discussed by Mašín and Khalili [MK12], who summarised the experimental evidence along with modelling approaches suggested by various authors. The following aspects of soil thermal behaviour appear to be the most important.

5.1.1 Compression behaviour under constant temperature

Temperature influences the soil normal compression lines. A majority of the experimental data show that in the stress range relevant to engineering applications, the normal compression lines at different temperatures may be considered parallel to each other, while as the temperature increases the void ratio at the normal compression line for the given effective mean stress p decreases [UK09, CM68, CL04, BDM00]. Although a number of research studies show a constant slope for the normal compression line with temperature, exceptions have also been reported [TGC97, RGL03]. In all the cases, however, an increase in temperature leads to a decrease in the apparent preconsolidation stress.

5.1.2 Behaviour in shear under constant temperature

The experimental evidence of the influence of temperature on the soil peak strength is contradictory, as is discussed below. However, most results show that the critical state friction angle is independent of temperature [UK09, HPDO98, HB90, LGY$^+$96, TGC97, CL04, ANBBP09]. Variation of the peak strength with temperature appears to be dependent on the soil being tested. Some authors report a decrease in the peak strength of an overconsolidated soil with increasing temperature [UK09, HPDO98, HB90, LGY$^+$96, DBT96]; Contradictory to this behaviour, however, some authors have reported an increase in the peak shear strength and a decrease of the apparent preconsolidation pressure with temperature [TGC97, HHW85, ANBBP09, CL04, KTOS95].

5.1.3 Soil response due to variation in temperature at high overconsolidation ratios

It is generally agreed that the soil response to heating-cooling cycles is strongly dependent on the apparent overconsolidation ratio. At high overconsolidation ratios, the soil response is essentially reversible, thus, there are no permanent changes in the soil structure. As discussed in detail by Khalili et al. [KUJ10], this type of response is controlled solely by the thermal expansion coefficient of the solid particles and it is independent of the soil porosity. The available experimental data also demonstrates that the thermal expansion coefficient of the soil skeleton α_s may essentially be considered as independent of the effective stress and temperature [UK09, DOFG$^+$96, SDC02, AE93].

5.1.4 Soil response due to variation in temperature at low overconsolidation ratios

As indicated in the previous paragraph, the response of a soil at high overconsolidation ratios is generally reversible. At low overconsolidation ratios, however, the mechanisms controlling the heating and cooling responses are substantially different. Upon cooling, the state boundary surface increases in size and the soil structure is

thus stable. Consequently, the volumetric response is the result of the thermal contraction of the soil particles, which does not depend on the overconsolidation ratio [UK09, DOFG$^+$96, SDC02]. In contrast, a reduction in the size of the state boundary surface due to heating imposes irreversible changes to the open structure of a soil at low overconsolidation ratios, leading to the so-called heating-induced compaction. In general, the compaction strains due to heating of a soil at low overconsolidation ratios are significantly larger than the straining imposed by the expansion of soil particles, and they are controlled by the relative position of the normal compression lines at different temperatures. The compaction due to heating is not an abrupt process that activates once the soil state reaches the state boundary surface; instead, its influence gradually increases with decreasing overconsolidation ratios [DOFG$^+$96, HB90, BHP88, SDC02, DC82].

5.2 Thermomechanical Constitutive Modelling of Saturated Soils

In this section, a thermomechanical model proposed by [MK12] is described as an example of enhancing constitutive models for the effect of structure. First, reversible strains due to thermal expansion and cooling contraction of soil particles are incorporated. These thermally-induced strains are independent of the effective stress. The enhanced hypoplastic equation is written as

$$\mathring{\mathbf{T}} = f_s \left[\mathcal{L} : (\mathbf{D} - \mathbf{D}^{TE}) + f_d \mathbf{N} \| \mathbf{D} - \mathbf{D}^{TE} \| \right] \tag{12}$$

where $\mathbf{D}^{TE}$ is the strain rate due to thermal volume changes of the solid particles. In agreement with the experimental evidence cited above, $\mathbf{D}^{TE}$ may be calculated using an elastic volumetric model as

$$\mathbf{D}^{TE} = \frac{\mathbf{1}}{3} \alpha_s \dot{T} \tag{13}$$

In Eq. (13), T represents temperature and α_s is the thermal expansion coefficient of solid particles. Khalili et al. [KUJ10] demonstrated that the thermal expansion/cooling contraction of solid particles alone does not lead to rearrangement of the soil skeleton. Consequently, it does not impose any change in the void ratio. In the thermal model the void ratio rate is calculated as

$$\dot{e} = (1 + e) \operatorname{tr} (\mathbf{D} - \mathbf{D}^{TE}) \tag{14}$$

The dependency of the normal compression line on temperature is calculated similarly to the dependency of the normal compression line on suction in the model for partially saturated soils. Parameters N and λ^* of the basic model become functions of temperature. The temperature dependent normal compression line reads:

$$\ln(1 + e) = N(T) - \lambda^*(T) \ln \frac{p}{p_r} \tag{15}$$

with

$$N(T) = N + n_T \ln \left(\frac{T}{T_0} \right) \qquad \lambda^*(T) = \lambda^* + l_T \ln \left(\frac{T}{T_0} \right) \tag{16}$$

where N, λ^*, n_T and l_T are parameters and T_0 is an (arbitrary) reference temperature.

To incorporate compaction of the soil structure due to wetting, the hypoplastic model is enhanced by the thermal-induced collapse factor $\mathbf{H}_T$ calculated to ensure consistency of the model with the asymptotic state boundary surface (see [MK12] for derivations).

5.3 Demonstration of the Model Predictions

The thermomechanical model for partially saturated soils has been developed and evaluated in [MK12]. The model has been evaluated using comprehensive experimental data on partially saturated compacted silt by Uchaipchat and Khalili [UK09]. Figure 30 shows experimental data and simulations of isotropic compression tests at different suctions and temperatures. The model correctly predicts the increase of the apparent preconsolidation stress with increasing suction and decreasing temperature, as well as the non-linear stiffness decrease as the state approaches the normal compression line. Figure 31 shows the volumetric strains generated by heating-cooling cycles at different effective stresses under saturated conditions. At a low effective stress, the model predicts a practically reversible behaviour solely controlled by the thermal expansion coefficient α_s which is in agreement with experimental results. As the stress level increases, the material compacts upon heating due to structural rearrangements and shrinks upon cooling due to cooling-induced particle shrinkage. The effects of suction and temperature on the behaviour in shear are shown in Fig. 32. An increase in temperature and decrease of suction decreases the predicted peak strength and dilatancy of the soil.

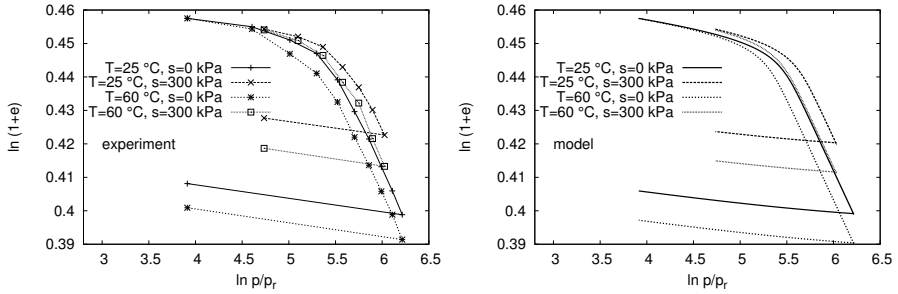

(a) (b)

Figure 30: Constant suction and constant temperature isotropic compression and unloading tests. Experimental data (a) by Uchaipchat and Khalili [UK09], predictions (b) by [MK12].

Finally, Figure 33 shows pore water pressures generated by pure heating of a saturated soil under undrained conditions and at an isotropic stress state. Unlike in the case of constant temperature undrained tests, heating under undrained conditions causes

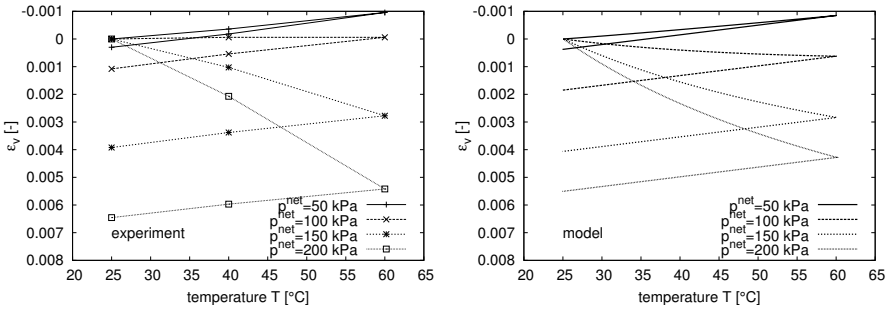

(a) (b)

Figure 31: Volume changes generated by drained heating experiments of saturated soil. Experimental data (a) by Uchaipchat and Khalili [UK09], predictions (b) by [MK12].

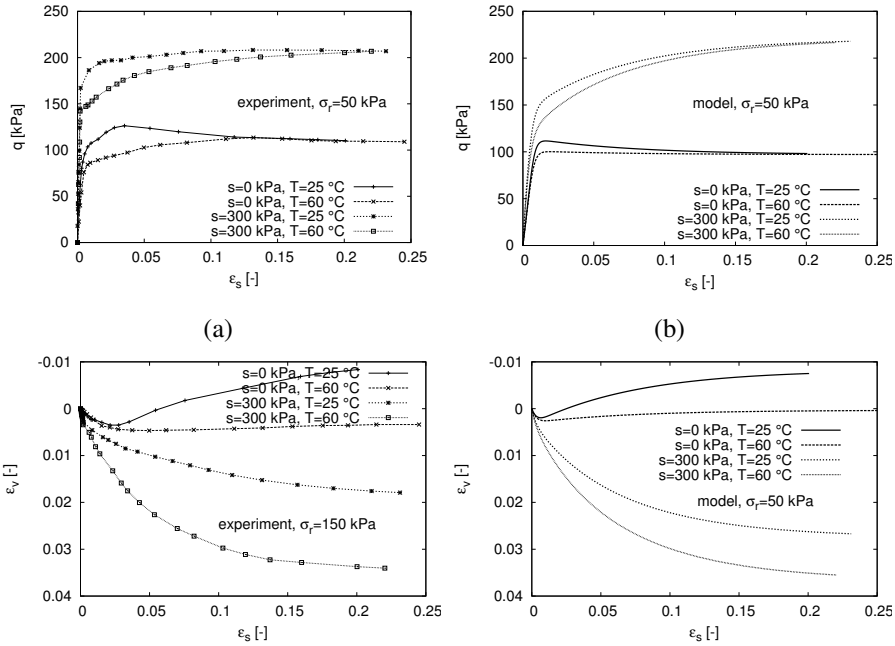

(a) (b)

(c) (d)

Figure 32: Drained triaxial shear tests at different temperatures and suctions. Experimental data (a,c) by Uchaipchat and Khalili [UK09], predictions (b,d) by [MK12]

changes in the soil volume. This can be calculated using the thermal expansion coef-

ficients of the solid particles α_s and water α_w:

$$\operatorname{tr} \mathbf{D} = [\alpha_w n + \alpha_s (1 - n)] \, \dot{T} \tag{17}$$

where n is the porosity $n = e/(1+e)$. The development of pore water pressures is then controlled by the hypoplastic model. The coefficient α_w depends on both temperature and pressure. An empirical expression by Baldi et al. [BHP88] was adopted in the simulations:

$$\alpha_w = \alpha_0 + (\alpha_1 + \beta_1 T) \ln m u_w + (\alpha_2 + \beta_2 T)(\ln m u_w)^2 \tag{18}$$

where u_w is the pore water pressure in kPa and the constants have the following values: $\alpha_0 = 4.505 \times 10^{-4}\ ^\circ C^{-1}$, $\alpha_1 = 9.156 \times 10^{-5}\ ^\circ C^{-1}$, $\beta_1 = -1.2 \times 10^{-6}\ ^\circ C^{-2}$, $\alpha_2 = 6.381 \times 10^{-6}\ ^\circ C^{-1}$, $\beta_2 = -5.766 \times 10^{-8}\ ^\circ C^{-2}$ and $m = 1.5 \times 10^{-6}$ kPa^{-1}. The model properly predicts the pore water pressure development and its dependency on the initial effective stress.

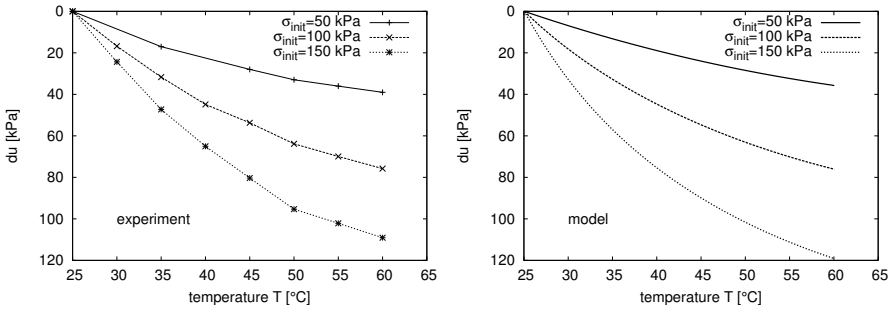

(a) (b)

Figure 33: Pore water pressures generated during undrained heating of saturated soils. Experimental data (a) by Uchaipchat and Khalili [UK09], predictions (b) by Mašín and Khalili [MK12].

6 Conclusions

Meta-stable structure, inter-particle cementation, breakage and thermal effects, along with the effects of partial saturation discussed in a separate lecture, are all phenomena which can be covered using similar constitutive modelling concept based on critical state soil mechanics combined with additional hardening laws specific for the process of interest. This simplifies constitutive model development, as existing modelling procedures for specific problems may be easily combined with newly developed reference constitutive models.

7 Acknowledgement

The author is grateful to Jose Duque for his valuable comments on the manuscript.

References

[AE93] S. Aversa and A. Evangelista. Thermal expansion of Neapolitan yellow tuff. *Rock Mech. Rock Engng.*, 26(4):281–306, 1993.

[ANBBP09] H. M. Abuel-Naga, D. T. Bergado, A. Bouazza, and M. Pender. Thermomechanical model for saturated clays. *Géotechnique*, 59(3):273–278, 2009.

[Asa05] A. Asaoka. Compaction of sand and consolidation of clay: a super/subloading yield surface approach. In *Proc.* 11^{th} *Int. Conference IACMAG*, volume 4, pages 121–140. Turin, Italy, 2005.

[ASR10] A. A. Araei, A. Soroush, and M. T. Rayhani. Large-scale triaxial testing and numerical modeling of rounded and angular rockfill materials. *Scientia Iranica, Transaction A: Civil Engineering*, 17(3):169–183, 2010.

[BC11] V. Bandini and M. Coop. The influence of particle breakage on the location of the critical state line of sands. *Soils and Foundations*, 51(4):591–600, 2011.

[BDM00] A. Burghignoli, A. Desideri, and S. Miliziano. A laboratory study on the thermomechanical behaviour of clayey soils. *Canadian Geotechnical Journal*, 37:764–780, 2000.

[BHP88] G. Baldi, T. Hueckel, and R. Pellegrini. Thermal volume changes of the mineral - water system in low-porosity clay soils. *Canadian Geotechnical Journal*, 25:807–825, 1988.

[BNC08] M. D. Bolton, Y. Nakata, and Y. P. Cheng. Micro- and macro-mechanical behaviour of dem crushable materials. *Géotechnique*, 58(6):471–480, 2008.

[Bol86] M. Bolton. The strength and dilatancy of sands. *Géotechnique*, 36(1):65–78, 1986.

[BS04] B. A. Baudet and S. E. Stallebrass. A constitutive model for structured clays. *Géotechnique*, 54(4):269–278, 2004.

[Bur90] J. B. Burland. On the compressibility and shear strength of natural clays. *Géotechnique*, 40(3):329–378, 1990.

[CBN04] Y. P. Cheng, M. D. Bolton, and Y. Nakata. Crushing and plastic deformation of soils simulated using DEM. *Géotechnique*, 54(2):131–141, 2004.

[CC98] L. Callisto and G. Calabresi. Mechanical behaviour of a natural soft clay. *Géotechnique*, 48(4):495–513, 1998.

[CC00] F. Cotecchia and J. Chandler. A general framework for the mechanical behaviour of clays. *Géotechnique*, 50(4):431–447, 2000.

[CDTV02] M. Cecconi, A. DeSimone, C. Tamagnini, and G. M. B. Viggiani. A constitutive model for granular materials with grain crushing and its application to a pyroclastic soil. *International Journal for Numerical and Analytical Methods in Geomechanics*, 26:1531–1560, 2002.

[CL04] C. Cekerevac and L. Laloui. Experimental study of thermal effects on the mechanical behaviour of a clay. *International Journal for Numerical and Analytical Methods in Geomechanics*, 28:209–228, 2004.

[CM68] R. G. Campanella and J. K. Mitchell. Influence of temperature variations on soil behaviour. *Journal of the Soil Mechanics and Foundations Division ASCE*, 94(3):709–734, 1968.

[CR04] L. Callisto and S. Rampello. An interpretation of structural degradation for three natural clays. *Canadian Geotechnical Journal*, 41:392–407, 2004.

[CSBFG04] M. R. Coop, K. K. Sorensen, T. Bodas Freitas, and G. Georgoutsos. Particle breakage during shearing of a carbonate sand. *Géotechnique*, 54(3):157–163, 2004.

[CV04] M. Cudny and P. A. Vermeer. On the modelling of anisotropy and destruction of soft clays within the multi-laminate framework. *Computers and Geotechnics*, 31(1):1–22, 2004.

[DBT96] D. De Bruyn and J.-F. Thimus. The influence of temperature on mechanical characteristics of Boom clay: The results of an initial laboratory programme. *Engineering Geology*, 41:117–126, 1996.

[DC82] K. R. Demars and R. D. Charles. Soil volume changes induced by temperature cycling. *Canadian Geotechnical Journal*, 19:188–194, 1982.

[DOFG+96] C. Del Olmo, V. Fioravante, F. Gera, T. Hueckel, J. C. Mayor, and R. Pellegrini. Thermomechanical properties of deep argillaceous formations. *Engineering Geology*, 41:87–101, 1996.

[Ein07a] Itai Einav. Breakage mechanics - Part I: Theory. *Journal of the Mechanics and Physics of Solids*, 55(6):1274–1297, 2007.

[Ein07b] Itai Einav. Breakage mechanics - Part II: Modelling granular materials. *Journal of the Mechanics and Physics of Solids*, 55(6):1298–1320, 2007.

[GMM06] G. Gullà, M. C. Mandaglio, and N. Moraci. Effect of weathering on the compressibility and shear strength of a natural clay. *Canadian Geotechnical Journal*, 43:618–625, 2006.

[GMW01] A. Gajo and D. Muir Wood. A new approach to anisotropic, bounding surface plasticity: general formulation and simulations of natural and reconstituted clay behaviour. *International Journal for Numerical and Analytical Methods in Geomechanics*, 25:207–241, 2001.

[GSD14] M. Ghafghazi, D.A. Shuttle, and J.T. DeJong. Particle breakage and the critical state of sand. *Soils and Foundations*, 54(3):451–461, 2014.

[Har85] B. O. Hardin. Crushing of soil particles. *Journal of Geotechnical Engineering, ASCE*, 111(10):1177–1192, 1985.

[HB90] T. Hueckel and G. Baldi. Thermoplasticity of saturated clays: Experimental constitutive study. *Journal of Geotechnical Engineering ASCE*, 116(12):1778–1796, 1990.

[HHW85] S. L. Houston, W. N. Houston, and N. D. Williams. Thermo-mechanical behaviour of seafloor sediments. *Journal of Geotechnical Engineering ASCE*, 111(11):1249–1263, 1985.

[HPDO98] T. Hueckel, R. Pellegrini, and C. Del Olmo. A constitutive study of thermo-elasto-plasticity of deep carbonatic clays. *International Journal for Numerical and Analytical Methods in Geomechanics*, 22:549–574, 1998.

[IS02] B. Indraratna and W. Salim. Modelling of particle breakage of coarse aggregates incorporating strength and dilatancy. *Proceedings of the Institution of Civil Engineers, Geotechnical Engineering*, 155(4):243–252, 2002.

[JYZU11] M.J. Jiang, H.B. Yan, H.H. Zhu, and S. Utili. Modeling shear behavior and strain localization in cemented sands by two-dimensional distinct element method analyses. *Computers and Geotechnics*, 38(1):14–29, 2011.

[KA00] M. Kavvadas and A. Amorosi. A constitutive model for structured soils. *Géotechnique*, 50(3):263–273, 2000.

[KTOS95] P. Kuntiwattanakul, I. Towhata, K. Ohishi, and I. Seko. Temperature effects on undrained shear characteristics of clay. *Soils and Foundations*, 35(1):147–162, 1995.

[KUJ10] N. Khalili, A. Uchaipichat, and A. A. Javadi. Skeletal thermal expansion coefficient and thermo-hydro-mechanical constitutive relations for saturated porous media. *Mechanics of Materials*, 42:593–598, 2010.

[LC02] M. D. Liu and J. P. Carter. A structured Cam Clay model. *Canadian Geotechnical Journal*, 39:1313–1332, 2002.

[LGY+96] B. E. Lingau, J. Graham, D. Yarechewski, N. Tanaka, and M. N. Gray. Effects of temperature on strength and compressibility of sand-bentonite buffer. *Engineering Geology*, 41:103–115, 1996.

[LN95] R. Lagioia and R. Nova. An experimental and theoretical study of the behaviour of a calcarenite in triaxial compression. *Géotechnique*, 45(4):633–648, 1995.

[LV90] S. Leroueil and P. R. Vaughan. The important and congruent effects of structure in natural soils and weak rocks. *Géotechnique*, 40(3):467–488, 1990.

[Mar67] R. J. Marsal. Large scale testing of rockfill materials. *Journal of the Soil Mechanics and Foundations Division*, 93(2):27–43, 1967.

[Mašín] D. Mašín. A hypoplastic constitutive model for clays. *International Journal for Numerical and Analytical Methods in Geomechanics*, 29(4):311–336, 2005.

[Mašín] D. Mašín. A hypoplastic constitutive model for clays with meta-stable structure. *Canadian Geotechnical Journal*, 44(3):363–375, 2007.

[Mašín] D. Mašín. *Modelling of Soil Behaviour with Hypoplasticity - Another Approach to Soil Constitutive Modelling*. Springer International Publishing, 2019.

[McD02] G. R. McDowell. On the yielding and plastic compression of sand. *Soils and Foundations*, 42(1):139–145, 2002.

[MK12] D. Mašín and N. Khalili. A thermo-mechanical model for variably saturated soils based on hypoplasticity. *International Journal for Numerical and Analytical Methods in Geomechanics*, 36(12):1461–1485, 2012.

[MNZ79] Z. Mróz, V. A. Norris, and O. C. Zienkiewicz. Application of an anisotropic hardening model in the analysis of elasto-plastic deformation of soil. *Géotechnique*, 29(1):1–34, 1979.

[NCT03] R. Nova, R. Castellanza, and C. Tamagnini. A constitutive model for bonded geomaterials subject to mechanical and/or chemical degradation. *International Journal for Numerical and Analytical Methods in Geomechanics*, 27:705–732, 2003.

[NSD92] D. F. T. Nash, G. C. Sills, and L. R. Davison. One-dimensional consolidation testing of soft clay from Bothkennar. *Géotechnique*, 42(2):241–256, 1992.

[RFDP03] G. Rocchi, M. Fontana, and M. Da Prat. Modelling of natural soft clay destruction processes using viscoplasticity theory. *Géotechnique*, 53(8):729–745, 2003.

[RGL03] E. Romero, A. Gens, and A. Lloret. Suction effects on a compacted clay under non-isothermal conditions. *Géotechnique*, 53(1):65–81, 2003.

[RK04] A. R. Russell and N. Khalili. A bounding surface plasticity model for sands exhibiting particle crushing. *Canadian Geotechnical Journal*, 41(6):1179–1192, 2004.

[RMW00] M. Rouainia and D. Muir Wood. A kinematic hardening constitutive model for natural clays with loss of structure. *Géotechnique*, 50(2):153–164, 2000.

[Row62] P. W. Rowe. The stress-dilatancy relation for static equilibrium of an assembly of particles in contact. *Proc. of the Royal Society of London, Series A*, 269:500–527, 1962.

[SDC02] N. Sultan, P. Delage, and Y. J. Cui. Temperature effects on the volume change behaviour of Boom clay. *Engineering Geology*, 64:135–145, 2002.

[SJH92] P. R. Smith, R. J. Jardine, and D. W. Hight. The yielding of Bothkennar clay. *Géotechnique*, 42(2):257–274, 1992.

[SMR11] P. Sharma, N. Mahure, and M. Ratnam. Influence of different stress conditions on behavior of rockfill materials. *Geotechnical and Geological Engineering*, 29(6):1035–1048, 2011.

[TGC97] N. Tanaka, J. Graham, and T. Crilly. Stress-strain behaviour of reconstituted illitic clay at different temperatures. *Engineering Geology*, 47:339–350, 1997.

[UK09] A. Uchaipchat and N. Khalili. Experimental investigation of thermo-hydro-mechanical behaviour of an unsaturated silt. *Géotechnique*, 59(4):339–353, 2009.

[WL08] Y. H. Wang and S. C. Leung. Characterization of cemented sand by experimental and numerical investigations. *Journal of Geotechnical and Geoenvironmental Engineering ASCE*, 134(7):992–1004, 2008.

[WNKL03] S. J. Wheeler, A. Näätänen, M. Karstunen, and M. Lojander. An anisotropic elastoplastic model for soft clays. *Canadian Geotechnical Journal*, 40:403–418, 2003.

[YS16] F. Yu and L. Su. Particle breakage and the mobilized drained shear strengths of sand. *Journal of Mountain Science*, 13(8):1481–1488, 2016.

[Yu17] F. Yu. Particle breakage and the critical state of sands. *Géotechnique*, 67(8):713–719, 2017.

Time and rate dependence

Claudio di Prisco, Luca Flessati

Politecnico di Milano

The time dependence of the mechanical behaviour of geomaterials is testified by numerous experimental test results. According to the material taken into consideration, the time dependency is associated with different phenomena, some of them purely mechanical, other thermo/hydro/chemo/mechanically coupled. In this chapter, a synthetic description of the most popular constitutive modelling approaches, conceived in the last decades to account for the time variable in the light of rate dependent elastic-plasticity, is provided.

1 Introduction

The mechanical response of geomaterials is severely affected by both time and application rate of perturbations and this governs the response of numerous geostructures. Typical examples are (i) creeping landslides, (ii) delayed static liquefaction in artificial berms, (iii) ageing in clayey materials, (iv) squeezing in deep tunnels, (v) solid to fluid and viceversa phase transition in granular materials.

According to the type of natural materials taken into consideration, the rate dependency of the mechanical response is characterized by different time scales (material characteristic time) and due to a large variety of thermo/hydro/chemo/mechanical processes.

As far as pure mechanical processes are concerned, in §2 “micro-inertial effects”, associated with the micro-structural fabric rearrangement, are discussed, whereas in §3 material progressive failure, associated with the propagation with time of microcracks present in either the grains themselves or in the intergranular bonds (in case of cemented/structured materials), is considered. Even if these two mechanical phenomena are completely different from a micro-mechanical point of view, the macroscopic (at the representative elementary volume scale) response can fruitfully be simulated by employing a unique constitutive framework: the delayed plasticity (or viscoplasticity) theory originally proposed in [P63] (§2).

Since elastic-viscoplasticity is a trivial extension of standard elastic-plasticity and its numerical implementation is very simple, its popularity is very large. Under suitable simplifying hypotheses, for very slow perturbations (or for sufficiently small material characteristic times) the visco-plastic solution converges to the corresponding rate independent elastic-plastic one and the same can be stated for the conditions for mechanical instability (§4).

When the delayed/rate dependent material response is due to coupled thermo/hydro/chemo/mechanical processes (§5), the material characteristic time is governed by the necessarily coupled processes taking place at the micro-scale. As far as chemo/mechanical coupling is concerned, elastic-plastic constitutive relationships are usually modified, by making yield function/plastic potential to be dependent, by means of the definition of suitable state/hardening variables, on both accumulated irreversible strains and chemical reactions.

Strain rate dependency is also observed when granular materials are subject to very large strain rates or when effective stresses are negligible (§6), that is when the so called inertial number ([JFP06], [MiD04]) is sufficiently large. In this case, according to the strain rate time history, the material may experience a phase transition from a solid-like to a fluid-like behaviour ("fluidization") or viceversa ("reconsolidation").

2 Micro-inertial effects

When granular materials, even under dry conditions, are perturbed by the application of external loads (creep tests), if micro-structural irreversible fabric rearrangements take place, the material response is delayed and macroscopic irreversible strains progressively increase with time. According to [dPI96] such a time dependency is due to particle micro-inertia ([SV95]) and to a probabilistic evolution of the microstructure from an initial stable configuration to the final one, passing through a large number of intermediate fabric configurations.

To reproduce this material behaviour, the delayed plasticity theory proposed in [P63], can be employed. According to this theory, strain rate tensor is decomposed into an instantaneous/reversible and a delayed/irreversible part ($\dot{\varepsilon}_{ij}^{irr}$). With respect to standard plasticity theory, the consistency condition is abolished (implying that the effective stress state can be either inside or outside the yield locus f (Figure 1)) and the flow rule is expressed as it follows:

$$\dot{\varepsilon}_{ij}^{irr} = \gamma \Phi \frac{\partial g}{\partial \sigma'_{ij}}, \tag{1}$$

being g the plastic potential, σ'_{ij} the effective stress tensor, γ a positive constitutive fluidity parameter and Φ the viscous nucleus. Φ can be defined as the distance (measured through a suitably defined mapping rule) between the state of stress and

the yield locus position, but, in most of the cases, Φ is a non-negative and increasing function of f. Under this assumption, f may be interpreted as a scalar measure of the probability of occurrence with time of fabric rearrangements and, consequently, of the irreversible strain accumulation. In most of the cases Φ is assumed to be nil when f<0, implying the existence of an elastic domain, but, in general, irreversible strains may also be assumed to develop within the yield locus ([dPSZ07]). The dimensional fluidity (inverse of a viscosity) parameter γ (generally coinciding with t_c^{-1}, being t_c the material characteristic time) governs the strain rate: when $\gamma \to \infty$ the irreversible strain rate becomes infinite and the material response becomes instantaneous. If the previously mentioned hypothesis of Φ definition is assumed, when $\gamma \to \infty$ standard elastic-plasticity is recovered. As in standard elastic-plasticity, the yield locus may evolve with the accumulated irreversible strains according to the hardening law, taking into account the influence of microstructural rearrangement on the REV response. In case of creep tests, the hardening (Figure 1) of the yield function is associated with a reduction in strain rates (primary creep), whereas the softening (Figure 1) with an increase (tertiary creep).

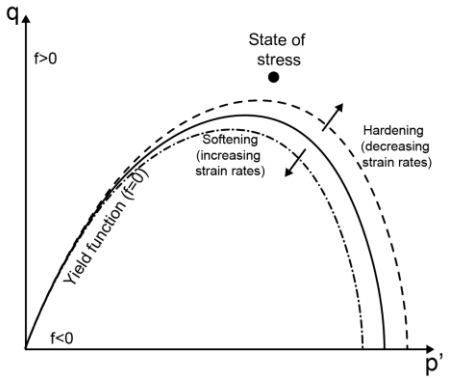

Figure 1: Evolution of the yield function

3 Material progressive failure

In granular materials rate dependency is also observed when experimental tests at large confining pressures are performed. In this case, in addition to the previously cited micro-inertia effects, grain crushing may also take place ([YL93]). This is associated with the evolution with time of microcracks naturally present in the grains. Rate dependency associated with grain crushing may be described by employing models based on breakage mechanics ([E07a], [E07b]), coinciding, as was shown by [ZB17], with elastic-viscoplastic models, whose viscous nucleus is the results of a suitable upscaling procedure.

An analogous process, named “subcritical crack growth” ([WFT80, A84, OA01, OA07]), may also occur in cemented/structured materials, where a dominant role is

played by the crack evolution with time in the intergranular bonds. From '90s ([GN93], [LN95], [NCT03]) the mechanical behaviour of bonded geomaterials is simulated by employing elastic-plastic constitutive relationships, in which yield function and plastic potential are assumed to depend on additional hardening variables, related to the strength of intergranular bonds. Under the hypothesis of material isotropy, these reduce to two (p_m and p_t of Figure 2), that in general are assumed to be independent of p_s, describing the size of the yield locus for the equivalent unbonded material. According to this approach, during either diagenesis or natural cementation, both p_m and p_t increase with time, result of chemo/mechanical processes. In case of mechanical perturbations, both local damages and spatial propagation of microcracks in intergranular bonds may cause a progressive reduction in p_m and p_t. This process takes place with time and an alternative ([N82]) approach to simulate such a time dependency is based on the introduction of a prescribed time evolution of p_m and p_t.

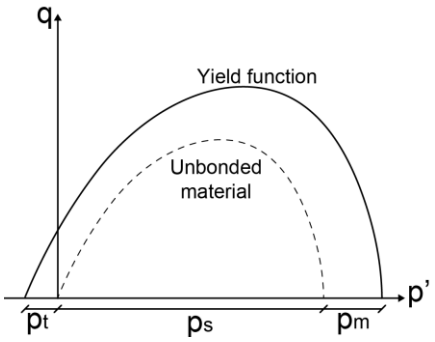

Figure 2: Yield function for cemented/bonded geomaterials \

4 Stability analysis for elastic-viscoplastic materials

As is well-known, when geomaterials are tested under constant effective loads (for instance standard triaxial creep tests), strain rate may evolve with time (Figure 3): after the load increment, if the applied load is sufficiently high, an initial strain deceleration (primary creep) may be followed by a constant strain rate branch (secondary creep) and by a severe strain acceleration (tertiary creep). This transition cannot be simulated by employing incremental constitutive relationships and the condition associated with the onset of instability, cannot be obtained neither by means of bifurcation ([SV95]) nor controllability ([N94]) theories.

For elastic-viscoplastic materials, the onset of instability can be defined by employing the approach proposed in [PdP16], combining Lyapunov theory of stability [L92] and the controllability theory [N94]. According to this approach, under quasi-static (inertia contributions are neglected) mixed stress-strain control conditions, the constitutive relationship can be written as it follows:

$$\dot{\mathbf{X}} = \mathbf{A}\mathbf{X} + \mathbf{F} \tag{2}$$

being **X** a vector containing the rate of the response variables (changing according to the test control), **F** a forcing term related with the controlled variables and their first and second time derivative, whereas matrix **A** depends on both constitutive relationship and controlled variable rates. In case of "generalized creep tests" (i.e. when both rate and acceleration of controlled variables are nil), **F=0** and **A** only depends on the constitutive relationship. The eigenvalues of **A** can be employed to analyse the stability: a stable response is obtained when all the eigenvalues are negative. Instability takes place when at least one eigenvalue becomes non-negative, corresponding to the condition $H \leq H_\chi$, being H the hardening modulus and H_χ the controllability modulus ([BDdP11]). This condition is coincident with the one of elastic-plastic materials ([BDdP11]).

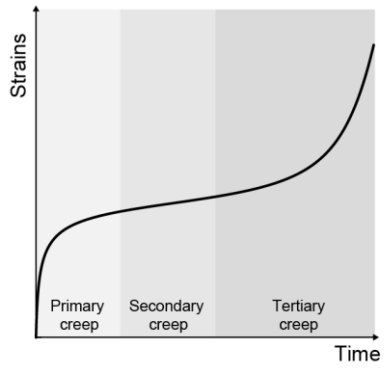

Figure 3: Transition from primary to tertiary creep.

5 Thermo/hydro/chemo/mechanical processes

Time dependency in geomaterials may also be due to thermo/hydro/chemo mechanical processes, evident in case of clays, peats and naturally/artificially cemented soils. Common in the literature is the use of constitutive modelling approaches, in which the viscoplastic parameters, taking the hydro/chemo mechanical coupling into account, are phenomenologically calibrated ([ZC74], [AO82], [BK85], [DZ87], [KS92]). The secondary compression of clays can also be interpreted as a hydro/chemo/mechanical process [NA01], consisting in the migration toward macropores of water present the micropores (the adsorbed water and the water present within the clay aggregates).

In case of cemented/bonded materials, by following the strategy already mentioned in §3, the time factor may be conveniently introduced in the (generalized) hardening functions, that become dependent not only on the accumulated irreversible strains

but also on non-mechanical processes, such as hydro-chemical reactions taking place at the microscopic scale. Since the yield function may evolve even without mechanical perturbations (i.e. at a constant effective stress) and the evolution with time of the yield locus is not necessarily associated with the development of irreversible strains, until yield locus shrinkage is not sufficiently severe any macroscopic evidence of material degradation is absent. On the contrary, when hydro/chemical damage is sufficiently severe, the yield function nullifies and a variation in effective stresses and an accumulation of irreversible strains occur, governed by the fulfilment of the consistency rule and by the time dependent hydro/chemo process ([GCH15], [CdP16]).

An example of the use of this type of approach is in [CdP16], where the weathering of calcarenites induced by the material saturation is studied. In this model, p_m and p_t are assumed to be correlated via a non-dimensional constant and to be related, by employing a simplified upscaling procedure, to the intact material tensile strength $\bar{\sigma}$, to the mean diameter of intergranular bonds $\bar{Y}$, evolving with time due to dissolution of calcium carbonate into water inducing a change in a (normalized with respect to the initial mass) calcite mass ξ, throughout a suitably defined non-dimensional micro to macro upscaling parameter X:

$$p_t = \bar{\sigma} X \bar{Y}(\xi). \tag{3}$$

In case of calcarenite, the intergranular bonds are made of calcite, and therefore the evolution rule for ξ is derived from the rate of dissolution of calcium carbonate into water solutions ([CH13]):

$$\dot{\xi} = K_b \left(C - [Ca^{2+}]^{\frac{1}{2}} [CO_3^{2-}]^{\frac{1}{2}} \right) (1 + \phi \varepsilon_v^{pl}) \tag{4}$$

being K_b a dissolution parameter, C an equilibrium constant, ε_v^{pl} the volumetric plastic strains, $[Ca^{2+}]$ and $[CO_3^{2-}]$ are the ionic concentration values and ϕ a chemo-mechanical coupling parameter, taking into consideration the increase in wet surface due to micro cracks development within the intergranular bonds.

6 Response under large strain rates

Under quasi static conditions, the soil is able to sustain external loads by means of a network of permanent contacts (“force chains”) developing among grains. In this case the soil is characterized by a solid-like behaviour. On the contrary, when the soil is subjected to fast deformations or the effective pressure is very low, this force chains network becomes unstable and grains start colliding to each other (“collisional regime”). In this second case the soil behaves like a fluid and any change in strain rate may induce a change in both stress level and void ratio.

To reproduce the steady state response of granular materials under both small and large strain rates, is very common the employment of a simplified constitutive relationship known in literature as $\mu - e - I$ rheology ([JFP06], [MiD04]), being μ the stress ratio, e the void index and I the inertial number, defined as: $I = d\dot{\varepsilon}_d\sqrt{\rho/p'}$, being d and ρ the soil particle (average) size and density, $\dot{\varepsilon}_d$ the second invariant of the deviatoric strain rate tensor and p' the effective pressure. According to this constitutive law, at steady state, a unique relationship among I, μ and e exists. This constitutive relationship cannot capture some basic characteristic of granular material behaviour, such as the dependency of the μ value on the Lode angle (θ, Figure 4a, [RdP19]) and the dependence of e on both $\dot{\varepsilon}_d$ and p'. In fact, in Figure 4b where DEM results ([RdP19]) are reported, a reduction in I due to a decreasing $\dot{\varepsilon}_d$ is associated, for sufficiently small values of I with a constant e value, whereas a reduction in I due to a decreasing p' is related to a marked reduction in e.

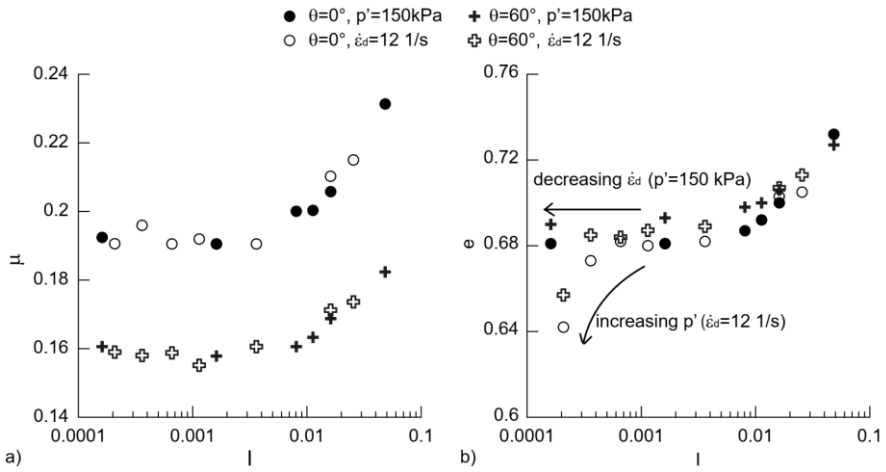

Figure 4: DEM numerical results: a) μ vs I and b) e vs I for triaxial compression ($\theta = 0°$) and extension ($\theta = 60°$)

To overcome the limitations of the $\mu - e - I$ rheology, recently visco-elastoplastic constitutive relationships, assuming an in parallel scheme (Figure 5, [RdPV16], [RdP19], [VMdP20], [RMdP21], [MRdP21]) for the stress contributions associated with the force chains (σ_{ij}^{qs}) and the one associated with the collisional regime (σ_{ij}^{c}), were proposed. σ_{ij}^{qs} is therefore calculated by using elastic plastic constitutive relationships for granular materials, including the critical state theory. In the perspective of the in parallel scheme, the critical state is a particular steady state, occurring when the collisional contribution is negligible (quasi static conditions). σ_{ij}^{c} is calculated by using kinetic theories for granular gases ([GD99], [BJ15]), according to which collisional stresses depend on both $\dot{\varepsilon}_d$ and on a scalar state variable, measuring the degree of agitation of grains (the ensemble average grain velocity fluctuation about their mean velocity), usually named granular temperature (T). For

small $\dot{\varepsilon}_d$ values both T and σ_{ij}^c are negligible. The stress is almost entirely carried by force chains and the material behaves like a solid. On the contrary, for large $\dot{\varepsilon}_d$ values both T and σ_{ij}^c become dominant, while σ_{ij}^{qs} is negligible and the material has a behaves like a fluid. In case of progressively increasing $\dot{\varepsilon}_d$ ("heating"), σ_{ij}^{qs} progressively decreases and a solid to fluid transition (fluidization) takes place, whereas for progressively decreasing $\dot{\varepsilon}_d$ ("cooling"), σ_{ij}^{qs} progressively increases and a fluid to solid transition (resolidification) takes place.

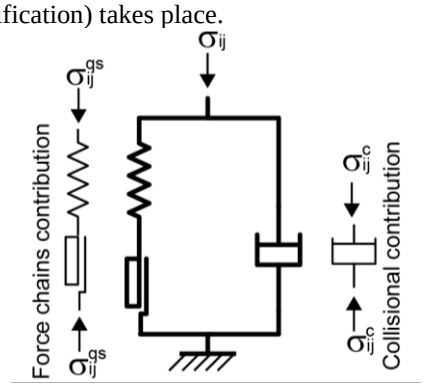

Figure 5: In parallel scheme

7 Concluding remarks

Time and rate dependency of geomaterials is associated with different hydro/chemo/mechanical processes taking place at the microscopic level. According to the process governing the material response, different constitutive modelling approaches can be adopted. In this chapter the authors have presented different strategies, each one interpretable as an extension of elastoplasticity, for theoretically capturing and numerically simulating material time dependence. From the pioneering works of the last century, nowadays the researchers are focused on the attempt of justifying time dependent material mechanical response on the basis of suitable upscaling approaches, capable not only of justifying the constitutive assumptions but also of conceiving them.

References

[AO82] Adachi, T., & Oka, F. (1982). Constitutive equations for normally consolidated clay based on elasto-viscoplasticity. Soils and foundations, 22(4), 57-70.

[A84] Atkinson, B. K. (1984). Subcritical crack growth in geological materials. J. Geophys. Res.: Solid Earth 89, No. B6, 4077–4114.

[BJ15] Berzi, D., Jenkins, J.: Steady shearing flows of deformable, inelastic spheres. Soft Matter 11(24), 4799–4808 (2015)

[BK85] Borja, R. I., & Kavazanjian, E. (1985). A constitutive model for the stress–strain–time behaviour of 'wet'clays. Geotechnique, 35(3), 283-298.

[BDdP11] Buscarnera, G., Dattola, G., & di Prisco, C. (2011). Controllability, uniqueness and existence of the incremental response: A mathematical criterion for elastoplastic constitutive laws. International Journal of Solids and Structures, 48(13), 1867–1878

[CdP16] Ciantia, M. O., & di Prisco, C. (2016). Extension of plasticity theory to debonding, grain dissolution, and chemical damage of calcarenites. International Journal for Numerical and Analytical Methods in Geomechanics, 40(3), 315-343.

[CH13] Ciantia, M. O., & Hueckel, T. (2013). Weathering of submerged stressed calcarenites: chemo-mechanical coupling mechanisms. Géotechnique, 63(9), 768-785.

[DZ87] Desai, C. S., & Zhang, D. (1987). Viscoplastic model for geologic materials with generalized flow rule. International Journal for Numerical and Analytical Methods in Geomechanics, 11(6), 603-620.

[dPI96] di Prisco, C., & Imposimato, S. (1996). Time dependent mechanical behaviour of loose sands. Mechanics of Cohesive-frictional Materials: An International Journal on Experiments, Modelling and Computation of Materials and Structures, 1(1), 45-73.

[dPSZ07] di Prisco, C., Stupazzini, M., & Zambelli, C. (2007). Nonlinear SEM numerical analyses of dry dense sand specimens under rapid and dynamic loading. International Journal for Numerical and Analytical Methods in Geomechanics, 31(6), 757-788.

[E07a] Einav, I. (2007). Breakage mechanics—part I: theory. Journal of the Mechanics and Physics of Solids, 55(6), 1274-1297.

[E07b] Einav, I. (2007). Breakage mechanics—Part II: Modelling granular materials. Journal of the Mechanics and Physics of Solids, 55(6), 1298-1320.

[GD99] Garzó, V., Dufty, J.W.: Dense fluid transport for inelastic hard spheres. Phys. Rev. E 59(5), 895–5911 (1999)

[GCH15] Gajo, A., Cecinato, F., & Hueckel, T. (2015). A micro-scale inspired chemo-mechanical model of bonded geomaterials. International Journal of Rock Mechanics and Mining Sciences, 80, 425-438.

[GN93] Gens, A., & Nova, R. (1993). Conceptual bases for a constitutive model for bonded soils and weak rocks. Geotechnical engineering of hard soils-soft rocks, 1(1), 485–494

[JFP06] Jop, P., Forterre, Y., Pouliquen, O.: A constitutive law for dense granular flows. Nature 441 (7094), 727 (2006)

[KS92] Kutter, B.L., and Sathialingam, N. 1992. Elastic–viscoplastic modelling of the rate-dependent behaviour of clays. Géotechnique,42(3): 427–441.

[LN95] Lagioia, R. & Nova, R. (1995). An experimental and theoretical study of the behaviour of a calcarenite in triaxial compression. Géotechnique 45, No. 4, 633–648

[L92] Lyapunov, A. M. (1892). The general problem of the stability of Q13 motion. Kharkovskoye Matematicheskoe Obshchestvo

[MRdP21] Marveggio, P., Redaelli, I., & di Prisco, C. (2021). A New Constitutive Approach for Simulating Solid-to Fluid-like Phase Transition in Dry and Saturated Granular Media. Lecture Notes in Civil Engineering Volume 125, Pages 491 - 497

[MiD04] MiDi, G.D.R.: On dense granular flows. Eur. Phys. J. E 14(4), 341–365 (2004)

[NA01] Navarro, V., & Alonso, E. E. (2001). Secondary compression of clays as a local dehydration process. Géotechnique, 51(10), 859-869.

[N82] Nova, R. (1982) A viscoplastic constitutive model for normally consolidated clay. In proceedings IUTAM conf. Deformation and Failure of Grnaular Materials 287-295

[N94] Nova, R. (1994). Controllability of the incremental response of soil specimens subjected to arbitrary loading programmes. J. Mech. Behav. Mater. 5, No. 2, 193–202.

[NCT03] Nova, R., Castellanza, R., & Tamagnini, C. (2003). A constitutive model for bonded geomaterials subject to mechanical and/or chemical degradation. International Journal for Numerical and Analytical Methods in Geomechanics, 27(9), 705–732

[OA01] Oldecop, L. A. & Alonso, E. E. (2001). A model for rockfill compressibility. Géotechnique 51, No. 2, 127–139

[OA07] Oldecop, L. A. & Alonso, E. E. (2007). Theoretical investigation of the time-dependent behaviour of rockfill. Géotechnique 57, No. 3, 289–301

[P63] Perzyna, P. (1963). The constitutive equations for rate sensitive plastic materials. Quarterly of applied mathematics, 20(4), 321-332.

[PdP16] Pisanò, F., & di Prisco, C., (2016). A stability criterion for elasto-viscoplastic constitutive relationships. International Journal for Numericaland Analytical Methods in Geomechanics, 40(1), 141–156.

[RdP19] Redaelli, I., di Prisco, C.: Three dimensional steady-state locus for dry monodisperse granular materials: DEM numerical results and theoretical modelling. Int. J. Numer. Anal. Meth. Geomech. 43(16), 2525–2550 (2019)

[RdPV16] Redaelli, I., di Prisco, C., Vescovi, D. (2016): A visco-elasto-plastic model for granular materials under simple shear conditions. Int. J. Numer. Anal. Meth. Geomech. 40(1), 80–104

[RMdP21] Redaelli, I., Marveggio, P., & di Prisco, C. (2021). Three-Dimensional Constitutive Model for Dry Granular Materials Under Different Flow Regimes. Volume 125, Pages 548 - 555

[SV95] Sulem, J., & Vardoulakis, I. G. (1995). Bifurcation analysis in geomechanics. CRC Press.

[VMdP20] Vescovi, D., Marveggio, P., & di Prisco, C. G. (2020). Saturated granular flows: constitutive modelling under steady simple shear conditions. Géotechnique, 70(7), 608-620.

[WFT80] Wiederhorn, S. M., Fuller, E. R. & Thomson, R. (1980). Micromechanisms of crack growth in ceramics and glasses in corrosive environments. Met. Sci. 14, No. 8–9, 450–458.

[YL93] Yamamuro, J. A., & Lade, P. V. (1993). Effects of strain rate on instability of granular soils. Geotechnical Testing Journal, 16(3), 304-313.

[ZC74] Zienkiewicz, O.C., and Cormeau, I.C. 1974. Visco-plasticity, plasticity and creep in elastic solids: a unified numerical solution approach. International Journal for Numerical and Analytical Methods in Geomechanics, 8(2): 821–845

Finite deformation plasticity

Kateryna Oliynyk[a,b], **Claudio Tamagnini**[b]

[a] *University of Dundee, UK*
[b] *University of Perugia, Italy*

In recent times, much attention has been given in the computational geomechanics community to those geotechnical problems in which geometric non–linearity plays an important role. Notable examples are provided by the evaluation of pile bearing capacity, the modeling of subsidence phenomena associated to hydrocarbon extraction, sinkhole formation, the evaluation of the effects of pile driving, the interpretation of cone penetration tests and the modeling of slow slope deformations in presence of significant modifications of the slope geometry. The need for robust and accurate numerical modeling tools for analyzing this type of problems has led to the development of innovative material point–based *numerical methods, such as SPH, MPM and PFEM, as an alternative to the classical FEM. In both FEM and material point–based approaches, a fundamental issue to be addressed is the extension of existing inelastic constitutive theories to the finite deformation regime. This chapter provides a review of two different and widely used approaches to finite deformation plasticity. The first approach is based on an* ad–hoc *additive split of the rate of deformation tensor into an elastic and a plastic part. In this case, objective stress rates are employed to address the issue of objectivity of the material response. The second approach is based on the assumptions of: i) multiplicative decomposition of the deformation gradient into an elastic and a plastic part, and ii) characterization of the elastic response of the material by postulating the existence of a suitable free energy function.*

1 Introduction

Non–linearity is a very important feature of the behavior of most geotechnical systems and a particular challenging one when the numerical modeling of the performance of such systems under the design loads is required by the design demands.

Historically, the research activities in the characterization of non–linearity in geotechnical engineering have been focused on the modeling of *material non–linearity*, emerging from the non–linear, inelastic and history–dependent behavior of soils and rocks.

Significant development in the constitutive modeling of soils within the framework of the theory of plasticity or of other incrementally non–linear theories such as the theory of hypoplasticity have been achieved in the last decades. An overview of these developments is provided by the chapters by Tamagnini and Oliynyk [TO21] and Mašín [Mas21] in this volume.

In recent years, however, the attention of researchers working in the field of computational geomechanics has been shifted from material to *geometric non–linearity*, which may play a major role in all those situations in which the deformed configuration of the soil body differs significantly from initial (reference) configuration. This may occur due to either large deformations or to large rotations, even in presence of relatively small strains.

Early interest in geometric non–linearity has been motivated by the study of one–dimensional consolidation problems in very soft soils or slurries. One–dimensional finite deformation theories of consolidation have been proposed since the early '60, see, *e.g.*, [GEH67, GSC81] and references therein. However, it is only with the parallel developments of the Finite Element method that the multidimensional analysis of non–linear geotechnical problems addressing the issue of geometric non–linearity from the general principles of continuum mechanics became possible, see *e.g.*, [CBS79, BA95, BTA98].

Besides the prediction of time–dependent deformations and displacements of soft, saturated soils subjected to time–dependent loading conditions, geometric non–linearity may play an important role in other geotechnical engineering applications. Notable examples are provided by the evaluation of pile bearing capacity in offshore platforms design [McL88, KL88]; the modeling of subsidence phenomena associated to hydrocarbon extraction [PJB88] and sinkhole formation [MCG20]; the study of the effects of pile driving [JBK$^+$18]; the interpretation of cone penetration tests under undrained or partially drained conditions [CS17, MACG18, MG21, OCT21]; the modeling of slow slope deformations in presence of significant modifications of the slope geometry [SAY$^+$16, CPT19, BN21].

Most of these applications motivated the development of a new class of numerical methods – broadly classifiable as *material point–based methods* – to circumvent the problems experienced with the classical or ALE FE methods in presence of severe mesh distortions. Among these, we recall the *Smoothed Particle Hydrodynamics* (SPH) method, see [BN21] and references therein; the *Material Point Method*, see [SCS94, BWV11], and the *Particle Finite Element Method* (PFEM), see [OCW$^+$07, COS13, MCAG17, MACG17].

In all the aforementioned applications, a fundamental point to be addressed is how to extend existing constitutive theories developed for infinitesimal deformations to the finite strain regime. The scope of this chapter is to illustrate the different approaches proposed in the literature to address this point, focusing on the mathematical theory of plasticity. After a short summary of the scheme of notation adopted (Sect. 2), to make the exposition sufficiently self–contained, some basic concepts of non–linear contin-

uum mechanics – including the fundamental issue of objectivity with respect to superposed rigid body motions – are briefly recalled in Sect. 3. The approaches to finite deformation plasticity based on an *ad–hoc* decomposition of the rate of deformation tensors – still widely used in practice – are discussed in Sect. 4. The fundamentals of the finite deformation plasticity theories based on the multiplicative split of the deformation gradient and on the existence of a free energy function for the characterization of the elastic response of the material are presented in detail in Sect. 5. Finally, Sect. 6 provides some concluding remarks concerning the relative merits and drawbacks of the two approaches.

2 Notation

In the following, all stresses and stress–related quantities are effective, unless otherwise stated. The sign convention of continuum mechanics (traction and extension positive) is adopted throughout. Both direct and index notations will be used to represent vector and tensor quantities according to convenience. In direct notation, vectors and second–order tensors will be represented by boldface italic characters; upper– and lowercase blackboard bold fonts – as for example $\mathbb{C}^e$ and $\mathfrak{c}^e$ – will be used for fourth–order tensors. Following standard practice, for any two vectors $\boldsymbol{v}, \boldsymbol{w} \in \mathbb{R}^3$, the dot product is defined as: $\boldsymbol{v} \cdot \boldsymbol{w} := v_i w_i$, and the dyadic product as: $[\boldsymbol{v} \otimes \boldsymbol{w}]_{ij} := v_i w_j$. Accordingly, for any two second–order tensors $\boldsymbol{X}, \boldsymbol{Y}$, $\boldsymbol{X} \cdot \boldsymbol{Y} := X_{ij} Y_{ij}$ and $[\boldsymbol{X} \otimes \boldsymbol{Y}]_{ijkl} := X_{ij} Y_{kl}$. The quantity $\|\boldsymbol{X}\| := \sqrt{\boldsymbol{X} \cdot \boldsymbol{X}}$ denotes the Euclidean norm of the second order tensor $\boldsymbol{X}$.

3 Preliminaries: basic kinematic concepts

3.1 Deformation

Let $\mathcal{B} \in \mathbb{R}^3$ be the *reference configuration* of the continuous body, and let $\boldsymbol{X}$ denote the position of a macroscopic material point in $\mathcal{B}$. A smooth *deformation* is a one–to–one mapping $\boldsymbol{\varphi} : \mathcal{B} \mapsto \mathcal{S} \in \mathbb{R}^3$ providing the position $\boldsymbol{x}$ of the material point $\boldsymbol{X}$ in the *current configuration* $\mathcal{S}$:

$$\boldsymbol{x} = \boldsymbol{\varphi}(\boldsymbol{X}) \tag{1}$$

see Fig. 1.

The *deformation gradient* is the gradient of the deformation $\boldsymbol{\varphi}$:

$$\boldsymbol{F}(\boldsymbol{X}) = \frac{\partial \boldsymbol{\varphi}}{\partial \boldsymbol{X}} = \nabla_{\boldsymbol{X}} \boldsymbol{\varphi}(\boldsymbol{X}) \tag{2}$$

The local condition of impenetrability of matter requires that:

$$J(\boldsymbol{X}) = \det(\boldsymbol{F}) > 0 \tag{3}$$

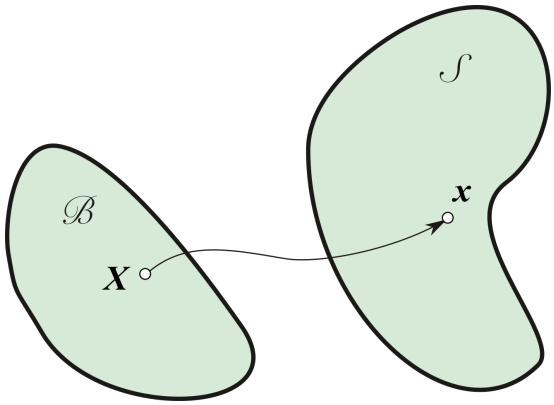

Figure 1: Reference configuration, current configuration and deformation mapping.

The scalar J is known as *Jacobian determinant*. According to the polar decomposition theorem, the deformation gradient can be decomposed as:

$$\boldsymbol{F} = \boldsymbol{R}\boldsymbol{U} = \boldsymbol{V}\boldsymbol{R} \tag{4}$$

in which $\boldsymbol{R}$ is a proper orthogonal tensor, called *rotation tensor*, while $\boldsymbol{U}$ and $\boldsymbol{V}$ are symmetric, positive–definite tensors called *right* and *left stretch tensors*, respectively. These two tensors measure locally the changes in volume and shape of the body. Frequently, in place of $\boldsymbol{U}$ and $\boldsymbol{V}$, the following alternative deformation tensors are adopted:

$$\boldsymbol{C} := \boldsymbol{F}^T\boldsymbol{F} \qquad\qquad \boldsymbol{b} := \boldsymbol{F}\boldsymbol{F}^T \tag{5a}$$

$$\boldsymbol{E} := \frac{1}{2}\left(\boldsymbol{C} - \boldsymbol{1}\right) \qquad\qquad \boldsymbol{e} := \frac{1}{2}\left(\boldsymbol{1} - \boldsymbol{b}^{-1}\right) \tag{5b}$$

The tensors $\boldsymbol{C}$ and $\boldsymbol{b}$ are called *right* and *left Cauchy–Green deformation tensors*, while $\boldsymbol{E}$ and $\boldsymbol{e}$ are known as the *Green* and *Almansi strain tensors*.

3.2 Motion

A *motion* of a continuum body is a one–parameter family of configurations, indexed by time. If we indicate with $\mathbb{I} := [0, T]$ the time interval of interest, for each $t \in \mathbb{I}$ the mapping:

$$\boldsymbol{\varphi}_t : \mathcal{B} \mapsto \mathcal{S}_t \in \mathbb{R}^3 \tag{6}$$

is a deformation which maps the reference configuration $\mathcal{B}$ onto the configuration $\mathcal{S}_t$ at time t. Consequently, we can write:

$$\boldsymbol{x} = \boldsymbol{\varphi}_t(\boldsymbol{X}) = \boldsymbol{\varphi}(\boldsymbol{X}, t) \tag{7}$$

for the position of the material point $\boldsymbol{X} \in \mathcal{B}$ at time t. We define *trajectory* of the material point $\boldsymbol{X}$ the mapping:

$$t \in \mathbb{I} \mapsto \boldsymbol{\varphi}_t(\boldsymbol{X})\Big|_{\boldsymbol{X}=\text{fixed}}$$

i.e., the set of all points $\boldsymbol{x}$ occupied by the material point $\boldsymbol{X}$ as t varies within the interval $\mathbb{I}$.

The *material velocity*, denoted by $\boldsymbol{V}(\boldsymbol{X}, t)$[1], is the time derivative of the motion:

$$\boldsymbol{V}(\boldsymbol{X}, t) = \frac{\partial \boldsymbol{\varphi}(\boldsymbol{X}, t)}{\partial t} \tag{8}$$

The material velocity is tangent to the trajectory of the material point $\boldsymbol{X}$ at all times t. Similarly, the *material acceleration*, $\boldsymbol{A}(\boldsymbol{X}, t)$, is defined as the time derivative of the material velocity:

$$\boldsymbol{A}(\boldsymbol{X}, t) = \frac{\partial \boldsymbol{V}(\boldsymbol{X}, t)}{\partial t} = \frac{\partial^2 \boldsymbol{\varphi}(\boldsymbol{X}, t)}{\partial t^2} \tag{9}$$

The material velocity and acceleration are vector fields defined on $\mathcal{B}$. Since $\boldsymbol{X}$ appears explicitly as an independent variable, $\boldsymbol{V}$ and $\boldsymbol{A}$ provide the so–called *Lagrangian description* of the motion.

The *spatial* or *Eulerian description* of the motion is obtained from the material description by changing the independent variable $\boldsymbol{X}$ (material coordinates) to the position vector $\boldsymbol{x}$ in the Euclidean space. Accordingly, we define the *spatial velocity* and *acceleration* as:

$$\boldsymbol{v} := \boldsymbol{V} \circ \boldsymbol{\varphi}_t^{-1} \qquad\qquad \boldsymbol{a} := \boldsymbol{A} \circ \boldsymbol{\varphi}_t^{-1} \tag{10}$$

where the symbol ($\circ$) denotes the function composition, and $\boldsymbol{X} = \boldsymbol{\varphi}^{-1}(\boldsymbol{x}, t)$ is the inverse deformation mapping. The fact that $\boldsymbol{\varphi}$ is invertible is guaranteed by the condition (3), applied to $J_t = \det(\nabla_{\boldsymbol{X}} \boldsymbol{\varphi}_t)$.

From eq. (2), the rate of change of the deformation gradient is given by:

$$\frac{\partial \boldsymbol{F}}{\partial t} = \frac{\partial^2 \boldsymbol{\varphi}_t}{\partial \boldsymbol{X} \partial t} = \frac{\partial \boldsymbol{V}}{\partial \boldsymbol{X}} = \nabla_{\boldsymbol{X}} \boldsymbol{V} \tag{11}$$

where $\nabla_{\boldsymbol{X}} \boldsymbol{V}$ is the *material velocity gradient*. By the chain rule,

$$\nabla_{\boldsymbol{X}} \boldsymbol{V} = \frac{\partial}{\partial \boldsymbol{X}} (\boldsymbol{v} \circ \boldsymbol{\varphi}_t) = \nabla \boldsymbol{v} \, \frac{\partial \boldsymbol{\varphi}_t}{\partial \boldsymbol{X}} = \nabla \boldsymbol{v} \, \boldsymbol{F} \tag{12}$$

Combining eqs. (11) and (12), we arrive at the following expression for the *spatial velocity gradient* $\nabla \boldsymbol{v}$:

$$\nabla \boldsymbol{v} = \frac{\partial \boldsymbol{F}}{\partial t} \, \boldsymbol{F}^{-1} \tag{13}$$

[1]Note that, to follow the standard notation of continuum mechanics, the same symbol is used for the material velocity and the left stretch tensor. The context will make clear which of these two object is being considered.

The symmetric part of $\nabla \boldsymbol{v}$, denoted by $\boldsymbol{d}$, is called the *spatial rate of deformation tensor*, and its antisymmetric part, denoted by $\boldsymbol{w}$, is called the *spin tensor*:

$$\boldsymbol{d} := \frac{1}{2}\left(\nabla \boldsymbol{v} + \nabla \boldsymbol{v}^T\right) \qquad \boldsymbol{w} := \frac{1}{2}\left(\nabla \boldsymbol{v} - \nabla \boldsymbol{v}^T\right) \tag{14}$$

Combining eqs. $(5a)_1$, (12) and $(14)_1$, we can obtain the following relation between the time rate of $\boldsymbol{C}$ and $\boldsymbol{d}$:

$$\frac{1}{2}\frac{\partial \boldsymbol{C}}{\partial t} = \frac{1}{2}\left(\frac{\partial \boldsymbol{F}^T}{\partial t}\boldsymbol{F} + \boldsymbol{F}^T\frac{\partial \boldsymbol{F}}{\partial t}\right) = \frac{1}{2}\boldsymbol{F}^T\left(\nabla \boldsymbol{v}^T + \nabla \boldsymbol{v}\right)\boldsymbol{F} = \boldsymbol{F}^T\boldsymbol{d}\,\boldsymbol{F} \tag{15}$$

The quantity:

$$\frac{1}{2}\left(\frac{\partial \boldsymbol{C}}{\partial t}\right)$$

is known as *material rate of deformation tensor*. Eq. (15) indicates that the spatial rate of deformation is the push–forward to the spatial configuration of the material rate of deformation.

By defining *rotated configuration* the *local* configuration obtained by applying the rotation tensor $\boldsymbol{R}$ to the neighborhood $\mathcal{O}_x$ of $\boldsymbol{x} \in \mathcal{S}_t$, we can define the *rotated rate of deformation tensor* $\boldsymbol{D}$ as follows:

$$\boldsymbol{D}(\boldsymbol{X}, t) = \boldsymbol{R}^T\left(\boldsymbol{d} \circ \boldsymbol{\varphi}_t\right)\boldsymbol{R} \tag{16}$$

The tensor $\boldsymbol{D}$ is a material field, and can be considered the pull–back of $\boldsymbol{d}$ to $\mathcal{B}$ by the rotation tensor only.

3.3 Stress measures

The usual measure of stress, the symmetric *Cauchy stress tensor* $\boldsymbol{\sigma}$, is a spatial field defined on the current configuration of the body. Another widely used spatial measure of stress in finite deformations is the *Kirchhoff stress tensor* $\boldsymbol{\tau}$, defined as:

$$\boldsymbol{\tau} := \left(J \circ \boldsymbol{\varphi}_t^{-1}\right)\boldsymbol{\sigma} \tag{17}$$

In writing the balance of momentum in the material setting, a different material measure of stress – the *first Piola–Kirchhoff* stress tensor $\boldsymbol{P}$ – emerges naturally to quantify the effect of contact forces. The first Piola–Kirchhoff stress tensor is related to $\boldsymbol{\sigma}$ and $\boldsymbol{\tau}$ by the relations:

$$\boldsymbol{P} = (\boldsymbol{\tau} \circ \boldsymbol{\varphi}_t)\boldsymbol{F}^{-T} = J(\boldsymbol{\sigma} \circ \boldsymbol{\varphi}_t)\boldsymbol{F}^{-T} \tag{18}$$

The first Piola–Kirchhoff stress tensor is a two–point tensor, and for this reason, its symmetry properties are given by:

$$\boldsymbol{P}\boldsymbol{F}^T = \boldsymbol{F}\boldsymbol{P}^T \tag{19}$$

The *second Piola–Kirchhoff* stress tensor, defined as:

$$\boldsymbol{S} = \boldsymbol{F}^{-1}\boldsymbol{P} = \boldsymbol{F}^{-1}(\boldsymbol{\tau} \circ \boldsymbol{\varphi}_t)\boldsymbol{F}^{-T} = J\boldsymbol{F}^{-1}(\boldsymbol{\sigma} \circ \boldsymbol{\varphi}_t)\boldsymbol{F}^{-T} \tag{20}$$

is a material stress measure whose symmetry is inherited from the symmetry of the Cauchy stress tensor. It is worth noting that, in geometrical terms, the second Piola–Kirchhoff stress tensor can be considered the pull–back of the spatial Kirchhoff stress tensor to the reference configuration, see eq. $(20)_2$.

Finally, another useful symmetric material stress measure is provided by the *rotated stress tensor* $\boldsymbol{\Sigma}$, defined as:

$$\boldsymbol{\Sigma} = \boldsymbol{R}^T(\boldsymbol{\tau} \circ \boldsymbol{\varphi}_t)\boldsymbol{R} \tag{21}$$

All the stress measures introduced in this section are power–conjugated to the different rate of deformation measures introduced in Sect. 3.2. Indicating with $\mathcal{P}$ the stress power per unit reference volume, we have:

$$\mathcal{P} = J\boldsymbol{\sigma} \cdot \boldsymbol{d} = \boldsymbol{\tau} \cdot \boldsymbol{d} = \boldsymbol{P} \cdot \dot{\boldsymbol{F}} = \boldsymbol{S} \cdot \left(\frac{1}{2}\dot{\boldsymbol{C}}\right) = \boldsymbol{\Sigma} \cdot \boldsymbol{D} \tag{22}$$

where the superposed dot denotes the derivation with respect to time following the motion of the material point (*material time derivative*).

3.4 Objectivity and objective stress rates

The notion of objectivity is one of the fundamental principle of mechanics and plays a major role in the definition of constitutive equations in rate–form in the finite deformation setting.

Let $\boldsymbol{\varphi} : \mathcal{B} \times \mathbb{I} \mapsto \mathcal{S}$ be a given motion, with $\boldsymbol{x} = \boldsymbol{\varphi}(\boldsymbol{X}, t)$ be the position in $\mathcal{S}$ of the material point $\boldsymbol{X}$ at time t. Consider a superposed *rigid body motion* which carries $\boldsymbol{x}$ into $\boldsymbol{x}^+$ by the map:

$$\boldsymbol{x} \in \mathcal{S}_t \mapsto \boldsymbol{x}^+ = \boldsymbol{c}(t) + \boldsymbol{Q}(t)\boldsymbol{x} \in \mathbb{R}^3 \tag{23}$$

where $\boldsymbol{c}(t)$ is a time–dependent translation and $\boldsymbol{Q}(t)$ is a time–dependent proper orthogonal transformation which defines a rigid rotation. The superposed motion is *rigid* as it preserves the distance between any two points $\boldsymbol{x}_1$ and $\boldsymbol{x}_2$ in $\mathcal{S}_t$.

A spatial tensor field is said to *transform objectively* under the superposed rigid body motion of eq. (23) if *it transforms according to the standard rules of tensor analysis* [SH98].

Applying the superposed rigid body motion (23) to the motion $\boldsymbol{\varphi}(\boldsymbol{X}, t)$ we have:

$$\boldsymbol{x}^+ = \boldsymbol{\varphi}^+(\boldsymbol{X}, t) = \boldsymbol{c}(t) + \boldsymbol{Q}(t)\boldsymbol{\varphi}(\boldsymbol{X}, t) \tag{24}$$

and thus the deformation gradient transforms as:

$$\boldsymbol{F}^+ = \nabla_{\boldsymbol{X}}\boldsymbol{\varphi}^+ = \boldsymbol{Q}(t)\boldsymbol{F}(\boldsymbol{X}, t) \tag{25}$$

This allows to obtain the following transformations for the spatial velocity gradient, rate of deformation tensor and spin tensor:

$$\nabla^+ \boldsymbol{v}^+ = \dot{\boldsymbol{F}}^+ (\boldsymbol{F}^+)^{-1} = \boldsymbol{Q} \nabla \boldsymbol{v} \boldsymbol{Q}^T + \dot{\boldsymbol{Q}} \boldsymbol{Q}^T \tag{26}$$

$$\boldsymbol{d}^+ = \boldsymbol{Q} \boldsymbol{d} \boldsymbol{Q}^T \tag{27}$$

$$\boldsymbol{w}^+ = \boldsymbol{Q} \boldsymbol{w} \boldsymbol{Q}^T + \dot{\boldsymbol{Q}} \boldsymbol{Q}^T \tag{28}$$

Due to the presence of the antisymmetric term $\dot{\boldsymbol{Q}} \boldsymbol{Q}^T$ on the RHS of eqs. (26) and (28), neither $\nabla \boldsymbol{v}$ nor $\boldsymbol{w}$ transforms objectively. On the contrary, the rate of deformation tensor $\boldsymbol{d}$ does transform objectively.

Assuming that the Cauchy stress tensor is objective, and thus transforms as:

$$\boldsymbol{\sigma}^+ = \boldsymbol{Q} \boldsymbol{\sigma} \boldsymbol{Q}^T \tag{29}$$

it is simple to show that its material time derivative $\dot{\boldsymbol{\sigma}}$ does not transform objectively. In fact, taking the material time derivative of both sides of eq. (29), one obtains:

$$\begin{aligned} \dot{\boldsymbol{\sigma}}^+ &= \dot{\boldsymbol{Q}} \boldsymbol{\sigma} \boldsymbol{Q}^T + \boldsymbol{Q} \dot{\boldsymbol{\sigma}} \boldsymbol{Q}^T + \boldsymbol{Q} \boldsymbol{\sigma} \dot{\boldsymbol{Q}}^T \\ &= \boldsymbol{Q} \dot{\boldsymbol{\sigma}} \boldsymbol{Q}^T + \dot{\boldsymbol{Q}} \boldsymbol{Q}^T \boldsymbol{\sigma}^+ + \boldsymbol{\sigma}^+ \boldsymbol{Q} \dot{\boldsymbol{Q}}^T \\ &= \boldsymbol{Q} \dot{\boldsymbol{\sigma}} \boldsymbol{Q}^T + \dot{\boldsymbol{Q}} \boldsymbol{Q}^T \boldsymbol{\sigma}^+ - \boldsymbol{\sigma}^+ \dot{\boldsymbol{Q}} \boldsymbol{Q}^T \end{aligned} \tag{30}$$

which is clearly a non–objective transformation. Following the same lines, it is trivial to show that the material time rate of the Kirchhoff stress tensor $\dot{\boldsymbol{\tau}}$ is also non–objective.

The importance of this result stems from the fact that a superimposed rigid body motion on a body occupying the spatial position $\mathcal{S}_t$ would give rise to a change in $\dot{\boldsymbol{\sigma}}$ or $\dot{\boldsymbol{\tau}}$ which is not associated to any deformation. Therefore, constitutive equations in rate–form suitable for finite deformations must be constructed linking an objective measure of rate of deformation with an objective measure of the stress rate.

Objective stress rates are modified material time derivatives of Cauchy or Kirchhoff stress tensors constructed to restore objectivity. Many such rates have been proposed in the literature but, as pointed out by Simo and Hughes [SH98], all of them are particular cases of a fundamental geometric object referred to as the *Lie derivative*. In particular, the Lie derivative of the Kirchhoff stress tensor is defined as:

$$\begin{aligned} \mathscr{L}_v[\boldsymbol{\tau}] &:= \left\{ \boldsymbol{F} \frac{\partial}{\partial t} \left[\boldsymbol{F}^{-1} (\boldsymbol{\tau} \circ \boldsymbol{\varphi}_t) \boldsymbol{F}^{-T} \right] \boldsymbol{F}^T \right\} \circ \boldsymbol{\varphi}_t^{-1} \\ &= \left\{ \boldsymbol{F} \left(\frac{\partial \boldsymbol{S}}{\partial t} \right) \boldsymbol{F}^T \right\} \circ \boldsymbol{\varphi}_t^{-1} \end{aligned} \tag{31}$$

where the last result is a consequence of eq. (20). The objectivity of the Lie derivative of $\boldsymbol{\tau}$ derives from the fact that its calculation requires the following steps: i) first, the

tensor $\boldsymbol{\tau}$ is pulled back to the reference configuration, where the resulting object – the second Piola–Kirchhoff stress $\boldsymbol{S}$ – is not affected by rigid body motions superimposed on the spatial configuration; ii) then, the time derivative of $\boldsymbol{S}$ is calculated; and, iii) the result is pushed forward to the spatial configuration to transform it in a spatial object.

Taking into account that $\dot{\boldsymbol{F}}^{-1} = -\boldsymbol{F}^{-1}\dot{\boldsymbol{F}}\boldsymbol{F}^{-1}$, it is relatively easy to show that:

$$\mathscr{L}_v[\boldsymbol{\tau}] = \dot{\boldsymbol{\tau}} - (\nabla \boldsymbol{v})\boldsymbol{\tau} - \boldsymbol{\tau}(\nabla \boldsymbol{v})^T \tag{32}$$

Another widely used objective stress rate is the so–called *Jaumann–Zaremba stress rate*, which, for the Kirchhoff stress tensor reads:

$$\overset{\nabla}{\boldsymbol{\tau}} = \dot{\boldsymbol{\tau}} - \boldsymbol{w}\boldsymbol{\tau} + \boldsymbol{\tau}\boldsymbol{w} \tag{33}$$

This is essentially a corotated derivative relative to spatial axes rotating with instantaneous angular velocity equal to $\boldsymbol{w}$.

4 Finite deformation plasticity based on the additive split of the deformation gradient

Early applications of rate–independent plasticity to finite deformations have been developed starting from *ad–hoc* extensions of the fundamental assumptions of infinitesimal plasticity. In particular, models of this class are all based on a additive decomposition of the rate of deformation tensors. Models formulated *in the spatial description* assume that:

$$\boldsymbol{d} = \boldsymbol{d}^e + \boldsymbol{d}^p \tag{34}$$

where $\boldsymbol{d}^e$ and $\boldsymbol{d}^p$ are the elastic and plastic parts of the spatial rate of deformation $\boldsymbol{d}$. Models formulated *in the rotated description* (Sect. 3.2) assume that:

$$\boldsymbol{D} = \boldsymbol{D}^e + \boldsymbol{D}^p \tag{35}$$

in which $\boldsymbol{D}^e$ and $\boldsymbol{D}^p$ are the elastic and plastic parts of the rotated rate of deformation $\boldsymbol{D}$. In the following, the basic assumptions and the resulting constitutive equations for these two classes of finite deformation plasticity model will be briefly reviewed.

4.1 Formulation in the spatial description

In models of this class, the elastic response is characterized by a *hypoelastic* constitutive equation in rate–form of the type:

$$\overset{\nabla}{\boldsymbol{\tau}} = \mathbb{a}^e\, \boldsymbol{d}^e = \mathbb{a}^e\, (\boldsymbol{d} - \boldsymbol{d}^p) \tag{36}$$

Due to the principle of material frame indifference [Tru56], the hypoelastic tangent stiffness tensor $\mathbb{a}^e$ must be an isotropic tensor function of $\boldsymbol{\tau}$. In geomechanics, this is usually accomplished by adopting the following expression for $\mathbb{a}^e$:

$$\mathbb{a}^e = K_t(P)\mathbf{1}\otimes\mathbf{1} + 2G_t(P)\left(\boldsymbol{I}^s - \frac{1}{3}\mathbf{1}\otimes\mathbf{1}\right) \tag{37}$$

where $P = \mathrm{tr}\,\boldsymbol{\tau}/3$ is the mean Kirchhoff stress, $\mathbf{1}$ is the second–order identity tensor and $\boldsymbol{I}^s$ is the symmetric fourth–order identity tensor.

As with the infinitesimal theory, irreversibility is introduced by assuming that the state of the material $(\boldsymbol{\tau}, \boldsymbol{q})$ must belong to the convex set:

$$\mathbb{E} := \Big\{ (\boldsymbol{\tau}, \boldsymbol{q}) \;\Big|\; f\,(\boldsymbol{\tau}, \boldsymbol{q}) \leq 0 \Big\} \tag{38}$$

defined in terms of a yield function $f(\boldsymbol{\tau}, \boldsymbol{q})$, where $\boldsymbol{q}$ is a set of internal (scalar or tensorial) variables which account for the effects of the previous loading history.

The plastic rate of deformation is prescribed, as in infinitesimal plasticity, by the following flow rule:

$$\boldsymbol{d}^p = \dot{\gamma}\, \frac{\partial g}{\partial \boldsymbol{\tau}}(\boldsymbol{\tau}, \boldsymbol{q}) \tag{39}$$

in which $g(\boldsymbol{\sigma}, \boldsymbol{q})$ is a prescribed *plastic potential* function, chosen in order to match available experimental observations, and $\dot{\gamma}$ is the plastic multiplier. The yield function and the plastic multiplier are subjected to the *Kuhn–Tucker complementarity conditions*:

$$\dot{\gamma} \geq 0 \qquad\qquad f(\boldsymbol{\tau}, \boldsymbol{q}) \leq 0 \qquad\qquad \dot{\gamma} f(\boldsymbol{\tau}, \boldsymbol{q}) = 0 \tag{40}$$

stating that plastic flow may occur only for stress states on the yield surface (yield states).

Indicating with the symbol $q_k \in \boldsymbol{q}$ the scalar internal variables and with the symbol $\boldsymbol{\alpha}_m \in \boldsymbol{q}$ the tensorial internal variables, so that $\boldsymbol{q} = \{q_k, \boldsymbol{\alpha}_m\}$, the evolution equations for the components of $\boldsymbol{q}$ are given by:

$$\dot{q}_k = \dot{\gamma}\, h_k(\boldsymbol{\tau}, \boldsymbol{q}) \tag{41}$$

$$\overset{\nabla}{\boldsymbol{\alpha}}_m = \dot{\gamma}\, \boldsymbol{h}_m(\boldsymbol{\tau}, \boldsymbol{q}) \tag{42}$$

where h_k and $\boldsymbol{h}_m$ are suitable hardening functions. Note that, differently from infinitesimal plasticity, the hardening law for the tensorial internal variables must be formulated in terms of their objective rates – the Jaumann rate in the case of eq. (42).

The consistency condition for plastic loading processes ($\dot{f} = 0$) allows to derive the following expression for the plastic multiplier:

$$\dot{\gamma} = \frac{1}{K_p} \left\langle \frac{\partial f}{\partial \boldsymbol{\tau}} \cdot \mathfrak{a}^e \boldsymbol{d} \right\rangle \tag{43}$$

where:

$$K_p := \frac{\partial f}{\partial \boldsymbol{\tau}} \cdot \mathfrak{a}^e \frac{\partial g}{\partial \boldsymbol{\tau}} + H_p > 0 \qquad\qquad H_p := -\frac{\partial f}{\partial q_k} h_k - \frac{\partial f}{\partial \boldsymbol{\alpha}_m} \cdot \boldsymbol{h}_m \tag{44}$$

The principle of material frame indifference poses the following restrictions on the scalar functions f and g. For any proper orthogonal transformation $\boldsymbol{Q}$, we must have:

$$f(\boldsymbol{Q}\boldsymbol{\tau}\boldsymbol{Q}^T, \boldsymbol{Q}\boldsymbol{\alpha}_m\boldsymbol{Q}^T, q_k) = f(\boldsymbol{\tau}, \boldsymbol{\alpha}_m, q_k) \tag{45}$$

$$g(\boldsymbol{Q}\boldsymbol{\tau}\boldsymbol{Q}^T, \boldsymbol{Q}\boldsymbol{\alpha}_m\boldsymbol{Q}^T, q_k) = g(\boldsymbol{\tau}, \boldsymbol{\alpha}_m, q_k) \tag{46}$$

The consequences of eqs. (45) and (46) are discussed in detail in [BD84, Boe87].

Applications of this approach to the formulation of finite deformation plasticity models for metals are reported, *e.g.*, in the works of [ND81, POP83], while applications to geomaterials are provided, *e.g.*, by [Pre80, MSZ95].

The main advantage of this formulation of finite deformation plasticity lies in its simplicity. The main constitutive functions of a specific model can be easily derived with minimal modifications directly from the corresponding infinitesimal plasticity counterpart. The most important limitation lies in the characterization of the elastic response given by eq. (36). Since $\boldsymbol{d}^e$ need not be the rate of deformation of any "elastic" strain measure, the elastic constitutive equation (36) cannot be related to any elastic potential function, and it is therefore hypoelastic. This limits the applicability of this class of models to "small" elastic strains. Moreover, in computational applications, the hypoelastic constitutive equation (36) has to be integrated numerically via *incrementally objective* integration algorithms, whose formulation is by no means trivial.

4.2 Formulation in the rotated description

A possible alternative to the plasticity formulation in the spatial description is obtained by recasting the constitutive functions and the evolution laws in the rotated description of Sect. 3.2. In this case, the structure of the theory is similar to that of the spatial formulation of Sect. 4.1, but the relevant state variables and the total deformation rate are all expressed in the rotated configuration:

$$\boldsymbol{\Sigma} = \boldsymbol{R}^T\boldsymbol{\tau}\boldsymbol{R} \qquad \boldsymbol{A}_m = \boldsymbol{R}^T\boldsymbol{\alpha}_m\boldsymbol{R} \qquad \boldsymbol{D} = \boldsymbol{R}^T\boldsymbol{d}\boldsymbol{R} \tag{47}$$

In the rotated configuration, the scalar internal variables q_k remain unaffected. The additive decomposition of eq. (35) is adopted for the rotated rate of deformation.

The elastic response of the material is characterized by a *hypoelastic* constitutive equation in rate–form of the type:

$$\dot{\boldsymbol{\Sigma}} = \mathbb{A}^e\, \boldsymbol{D}^e = \mathbb{A}^e\, (\boldsymbol{D} - \boldsymbol{D}^p) \tag{48}$$

where the hypoelastic tangent stiffness tensor $\mathbb{A}^e$ is related to the hypoelastic tangent stiffness in the spatial setting, $\mathfrak{a}^e$, by the transformation:

$$\mathfrak{a}^e_{ijkl} = R_{iA}R_{jB}R_{kC}R_{lD}\mathbb{A}^e_{ABCD} \tag{49}$$

Irreversibility of the material response is introduced by assuming that the state of the material $(\boldsymbol{\Sigma}, q_k, \boldsymbol{A}_m)$ must belong to the convex set:

$$\mathbb{E} := \left\{ (\boldsymbol{\Sigma}, q_k, \boldsymbol{A}_m) \;\middle|\; F\left(\boldsymbol{\Sigma}, q_k, \boldsymbol{A}_m\right) \leq 0 \right\} \tag{50}$$

defined in terms of a yield function $F(\boldsymbol{\Sigma}, q_k, \boldsymbol{A}_m)$.

The plastic rate of deformation is prescribed by the following flow rule:

$$\boldsymbol{D}^p = \dot{\gamma}\, \frac{\partial G}{\partial \boldsymbol{\Sigma}}(\boldsymbol{\Sigma}, q_k, \boldsymbol{A}_m) \tag{51}$$

in which $G(\boldsymbol{\Sigma}, q_k, \boldsymbol{A}_m)$ is a prescribed *plastic potential* function. The yield function and the plastic multiplier are subjected to the Kuhn–Tucker complementarity conditions:

$$\dot{\gamma} \geq 0 \qquad F(\boldsymbol{\Sigma}, q_k, \boldsymbol{A}_m) \leq 0 \qquad \dot{\gamma} F(\boldsymbol{\Sigma}, q_k, \boldsymbol{A}_m) = 0 \tag{52}$$

stating that plastic flow may occur only for stress states on the yield surface.

The evolution equations for the (scalar and tensorial) internal variables are given by the following hardening laws:

$$\dot{q}_k = \dot{\gamma}\, H_k(\boldsymbol{\Sigma}, q_k, \boldsymbol{A}_m) \tag{53}$$

$$\dot{\boldsymbol{A}}_m = \dot{\gamma}\, \boldsymbol{H}_m(\boldsymbol{\Sigma}, q_k, \boldsymbol{A}_m) \tag{54}$$

where H_k and $\boldsymbol{H}_m$ are suitable hardening functions for the rotated description. Note that, in this case, the time derivatives appearing on the LHS of eqs. (48) and (54) are standard material time derivatives, as the tensors $\boldsymbol{\Sigma}$ and $\boldsymbol{A}_m$ are material objects.

The consistency condition for plastic loading processes ($\dot{F} = 0$) allows to derive the following expression for the plastic multiplier:

$$\dot{\gamma} = \frac{1}{K_p} \left\langle \frac{\partial F}{\partial \boldsymbol{\Sigma}} \cdot \mathbb{A}^e \boldsymbol{D} \right\rangle \tag{55}$$

where:

$$K_p := \frac{\partial F}{\partial \boldsymbol{\Sigma}} \cdot \mathbb{A}^e \frac{\partial G}{\partial \boldsymbol{\Sigma}} + H_p > 0 \qquad H_p := -\frac{\partial F}{\partial q_k} H_k - \frac{\partial F}{\partial \boldsymbol{A}_m} \cdot \boldsymbol{H}_m \tag{56}$$

The formulation in the rotated description appears to have been favored by a number of researchers in metal plasticity, *e.g.*, [Die79, JB84]. As a matter of fact, it is used in a number of large scale simulation codes, such as, for example ABAQUS Standard [HKS16].

This approach presents the same limitation of the formulation based on the spatial description: since $\boldsymbol{D}^e$ need not be the rate of deformation of any "elastic" strain measure, the elastic constitutive equation (48) cannot be related to any elastic potential function, and it is therefore hypoelastic. In addition, the implementation of the rotated description approach in Finite Element procedures is computationally quite involved and requires repeated use of the polar decomposition theorem, see, *e.g.*, [SH98].

5 Finite deformation multiplicative plasticity

In contrast with the formulations outlined in the previous Sect. 4, the formulation of finite deformation plasticity based on the multiplicative decomposition of the deformation gradient allows for a proper definition of elastic and plastic deformation measures. As such, multiplicative plasticity is amenable to a rigorous thermodynamical treatment, leading to a hyperelastic characterization of the reversible response of the material, as well as to associative evolution laws for the plastic deformation and the internal variables.

In the following Sects. 5.1–5.5, we will present in detail the finite deformation theory of multiplicative hyperplasticity proposed by Oliynyk and Tamagnini [OT20] as an extension of the infinitesimal theory of hyperplasticity as defined by Houlsby and Puzrin [HP07], in order to provide a clear motivation for the associative flow rules and hardening law to be used in finite kinematics. In Sect. 5.6, we will extend the theory to the general non–associative case, which encompasses most of the constitutive models of this class developed for soils. The presentation of the theory will be limited to the particular case of isotropic materials, for which the internal variables are all scalars. This allows to keep the mathematical structure of the constitutive equations to an acceptable level of complexity, while maintaining a sufficient level of generality to encompass most of the relevant constitutive models for geomaterials developed within this theory. The reader is referred to, *e.g.*, [MS03, BRL19] for the extension of multiplicative plasticity to the case of anisotropic materials.

5.1 Kinematics

The key point in finite deformation multiplicative plasticity is the assumption of a *product decomposition* of the deformation gradient $\boldsymbol{F}$ into a reversible (elastic) part, $\boldsymbol{F}^e$, and an irreversible (plastic) part, $\boldsymbol{F}^p$:

$$\boldsymbol{F} = \boldsymbol{F}^e \boldsymbol{F}^p \tag{57}$$

see, *e.g.*, [Lee68, SH98, Bor13].

An essential feature of the product decomposition is the introduction of a *local intermediate configuration*, relative to which the elastic response of the material is defined, see Fig. 2. From a phenomenological point of view, $(\boldsymbol{F}^e)^{-1}$ can be interpreted as the *local* deformation which brings the neighborhood $\mathcal{O}_x$ of $\boldsymbol{x}$ to the neighborhood $\mathcal{O}_\xi$ of $\boldsymbol{\xi}$ when the material is unloaded back to the reference stress state. The local configurations for each material point of $\mathcal{B}$ are, in general, not compatible, in the sense that they generally "do not fit together" to produce an intermediate configuration for the entire body.

The decomposition (57) is not unique, as an arbitrary rigid body rotation can be superposed on the intermediate configuration without altering the total deformation gradient. However, in the particular case of isotropic materials, the orientation of the local intermediate configuration is not relevant.

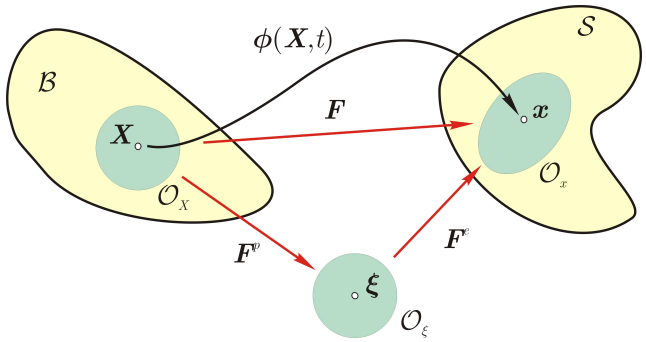

Figure 2: Multiplicative decomposition and intermediate configuration.

The following symmetric strain tensors for elastic and plastic deformations can be defined from $\boldsymbol{F}^e$ and $\boldsymbol{F}^p$:

$$\boldsymbol{b}^e := \boldsymbol{F}^e \boldsymbol{F}^{eT} \qquad\qquad \boldsymbol{C}^p := \boldsymbol{F}^{pT} \boldsymbol{F}^p \tag{58}$$

The first tensor is known as *left elastic Cauchy–Green tensor* and is a spatial measure of the elastic deformation. The second tensor is known as *right plastic Cauchy–Green tensor* and is a material measure of the plastic deformation. They are linked by the following relation:

$$\boldsymbol{b}^e = \boldsymbol{F}\boldsymbol{C}^{p-1}\boldsymbol{F}^T \tag{59}$$

i.e., $\boldsymbol{b}^e$ is the push–forward to the spatial configuration of the inverse of $\boldsymbol{C}^p$.

The time rate of the elastic left Cauchy–Green tensor is provided by:

$$\dot{\boldsymbol{b}}^e = \boldsymbol{l}\boldsymbol{b}^e + \boldsymbol{b}^e\boldsymbol{l}^T + \mathscr{L}_v[\boldsymbol{b}^e] \tag{60}$$

where we have indicated with the symbol $\boldsymbol{l}$ the spatial velocity gradient $\nabla\boldsymbol{v}$, see eq. (13), and

$$\mathscr{L}_v[\boldsymbol{b}^e] = \boldsymbol{F}\left\{\frac{d}{dt}\left(\boldsymbol{C}^{p-1}\right)\right\}\boldsymbol{F}^T$$

is the Lie derivative of the elastic left Cauchy–Green tensor.

Mimicking the relation (13) for the spatial velocity gradient, we define the elastic and plastic velocity gradients as follows:

$$\boldsymbol{l}^e := \dot{\boldsymbol{F}}^e \boldsymbol{F}^{e-1} \qquad\qquad \overline{\boldsymbol{L}}^p := \dot{\boldsymbol{F}}^p \boldsymbol{F}^{p-1} \tag{61}$$

While $\boldsymbol{l}^e$ is a spatial tensor, $\overline{\boldsymbol{L}}^p$ is an object defined in the intermediate configuration. To obtain the spatial counterpart of $\overline{\boldsymbol{L}}^p$ we consider its push–forward to the spatial configuration

$$\boldsymbol{l}^p = \boldsymbol{F}^e \overline{\boldsymbol{L}}^p \boldsymbol{F}^{e-1} \tag{62}$$

and define it *spatial plastic velocity gradient*. It is easy to show that, with the above definitions:

$$\boldsymbol{l} = \boldsymbol{l}^e + \boldsymbol{l}^p \tag{63}$$

i.e., the multiplicative decomposition of the deformation gradient is consistent with an additive split of the rate of deformation tensor, provided that $\boldsymbol{l}^e$ and $\boldsymbol{l}^p$ are defined as in eqs. $(61)_1$ and (62).

It is also possible to show that the following relation holds between $\mathscr{L}_v[\boldsymbol{b}^e]$ and $\boldsymbol{l}^p$:

$$\mathscr{L}_v[\boldsymbol{b}^e] = -2\ \mathrm{sym}\,(\boldsymbol{l}^p \boldsymbol{b}^e) \tag{64}$$

see [Sim98].

From the spatial elastic and plastic velocity gradients, $\boldsymbol{l}^e$ and $\boldsymbol{l}^p$, the *elastic* and *plastic* rates of deformation and spins can be defined:

$$\boldsymbol{d}^e := \mathrm{sym}\,(\boldsymbol{l}^e) \qquad \boldsymbol{w}^e := \mathrm{skw}\,(\boldsymbol{l}^e) \tag{65}$$

$$\boldsymbol{d}^p := \mathrm{sym}\,(\boldsymbol{l}^p) \qquad \boldsymbol{w}^p := \mathrm{skw}\,(\boldsymbol{l}^p) \tag{66}$$

In order to construct a plasticity theory, both components of the plastic velocity gradient need to be specified by suitable flow rules. In the following, we will assume that the plastic spin is always equal to zero, and $\boldsymbol{l}^p = \boldsymbol{d}^p$, as in [Sim98].

5.2 Free energy function

Consistent with the assumption of isotropy, let the set $\mathscr{S}$ of state variables be given by:

$$\mathscr{S} := \{\boldsymbol{b}^e, \boldsymbol{\alpha}\}$$

where $\boldsymbol{\alpha} = \{\alpha_1, \alpha_2, \ldots, \alpha_m\}$ is a vector containing the m scalar, strain–like internal variables accounting for the effects of deformation history. Assuming that the elastic response is not affected by microstructural changes, the following *free energy function* per unit reference volume can be adopted:

$$\psi(\mathscr{S}) = \psi^e(\boldsymbol{b}^e) + \psi^p(\boldsymbol{\alpha}) \tag{67}$$

in which the contributions of the elastic deformation and of the internal variables are fully uncoupled. As a consequence of the principle of material frame indifference, the function ψ^e must depend on $\boldsymbol{b}^e$ only through its invariants (*i.e.*, the principal elastic stretches λ^e_A, eigenvalues of $\boldsymbol{F}^e$).

The material time rate of the free energy function ψ is given by:

$$\dot{\psi} = \frac{\partial \psi^e}{\partial \boldsymbol{b}^e} \cdot \dot{\boldsymbol{b}}^e + \frac{\partial \psi^p}{\partial \boldsymbol{\alpha}} \cdot \dot{\boldsymbol{\alpha}} = \frac{\partial \psi^e}{\partial \boldsymbol{b}^e} \cdot \dot{\boldsymbol{b}}^e + \frac{\partial \psi^p}{\partial \alpha_k} \dot{\alpha}_k \tag{68}$$

Taking into account eqs. (60) and (64), and considering that, due to the symmetry of $\partial\psi/\partial\boldsymbol{b}^e$ and the fact that $\boldsymbol{b}^e$ and $\partial\psi/\partial\boldsymbol{b}^e$ commute:

$$\frac{\partial\psi^e}{\partial\boldsymbol{b}^e}\cdot\mathrm{sym}\left(\boldsymbol{d}^p\boldsymbol{b}^e\right)=\frac{\partial\psi^e}{\partial\boldsymbol{b}^e}\cdot\left(\boldsymbol{d}^p\boldsymbol{b}^e\right)$$
$$\frac{\partial\psi}{\partial\boldsymbol{b}^e}\cdot\left(\boldsymbol{l}\boldsymbol{b}^e\right)+\frac{\partial\psi}{\partial\boldsymbol{b}^e}\cdot\left(\boldsymbol{b}^e\boldsymbol{l}^T\right)=\left(2\,\frac{\partial\psi}{\partial\boldsymbol{b}^e}\boldsymbol{b}^e\right)\cdot\boldsymbol{d}$$

we obtain:

$$\dot{\psi}=\left(2\,\frac{\partial\psi^e}{\partial\boldsymbol{b}^e}\boldsymbol{b}^e\right)\cdot\boldsymbol{d}-\left(2\,\frac{\partial\psi^e}{\partial\boldsymbol{b}^e}\boldsymbol{b}^e\right)\cdot\boldsymbol{d}^p-\overline{\boldsymbol{\chi}}\cdot\dot{\boldsymbol{\alpha}}\tag{69}$$

where:

$$\overline{\boldsymbol{\chi}}:=-\frac{\partial\psi^p}{\partial\boldsymbol{\alpha}}\tag{70}$$

is the so–called *generalized stress*, work–conjugated to $\boldsymbol{\alpha}$.

5.3 Dissipation function

Let:

$$\mathscr{D}:=\boldsymbol{\tau}\cdot\boldsymbol{d}-\dot{\psi}\tag{71}$$

be the *dissipation function* of the material per unit reference volume for isothermal processes. The second principle of thermodynamics requires that $\mathscr{D}$ be non–negative:

$$\boldsymbol{\tau}\cdot\boldsymbol{d}-\dot{\psi}\geq 0$$

Inserting eq. (69) in eq. (71), we have:

$$\mathscr{D}=\left(\boldsymbol{\tau}-2\frac{\partial\psi}{\partial\boldsymbol{b}^e}\boldsymbol{b}^e\right)\cdot\boldsymbol{d}+2\frac{\partial\psi}{\partial\boldsymbol{b}^e}\boldsymbol{b}^e\cdot\boldsymbol{d}^p+\overline{\boldsymbol{\chi}}\cdot\dot{\boldsymbol{\alpha}}\geq 0\tag{72}$$

Since inequality (72) must hold for any non–dissipative process (for which $\boldsymbol{d}^p=\boldsymbol{0}$, $\dot{\boldsymbol{\alpha}}=\boldsymbol{0}$) a standard argument leads to the following hyperelastic constitutive equation:

$$\boldsymbol{\tau}=2\frac{\partial\psi}{\partial\boldsymbol{b}^e}\boldsymbol{b}^e\tag{73}$$

and to the reduced dissipation inequality:

$$\mathscr{D}=\boldsymbol{\tau}\cdot\boldsymbol{d}^p+\overline{\boldsymbol{\chi}}\cdot\dot{\boldsymbol{\alpha}}\geq 0\tag{74}$$

5.4 Yield function and evolution equations

Under the assumption of rate–independence for the material response, the dissipation function $\mathscr{D}$ must be a homogeneous function of degree one in the fluxes $(\boldsymbol{d}^p,\dot{\boldsymbol{\alpha}})$. Euler's theorem for homogeneous functions then requires that:

$$\mathscr{D}=\frac{\partial\mathscr{D}}{\partial\boldsymbol{d}^p}\cdot\boldsymbol{d}^p+\frac{\partial\mathscr{D}}{\partial\dot{\boldsymbol{\alpha}}}\cdot\dot{\boldsymbol{\alpha}}=\boldsymbol{\chi}_\tau\cdot\boldsymbol{d}^p+\boldsymbol{\chi}\cdot\dot{\boldsymbol{\alpha}}\tag{75}$$

where the two quantities:

$$\boldsymbol{\chi}_\tau = \frac{\partial \mathscr{D}}{\partial \boldsymbol{d}^p} \qquad\qquad \boldsymbol{\chi} = \frac{\partial \mathscr{D}}{\partial \dot{\boldsymbol{\alpha}}} \tag{76}$$

are defined *generalized dissipative stresses*. Comparing eqs. (74) and (75) we deduce the following equality:

$$(\boldsymbol{\chi}_\tau - \boldsymbol{\tau}) \cdot \boldsymbol{d}^p + (\boldsymbol{\chi} - \overline{\boldsymbol{\chi}}) \cdot \dot{\boldsymbol{\alpha}} = 0 \tag{77}$$

which is trivially satisfied if Ziegler's orthogonality conditions [Zie83, HP07] are assumed:

$$\boldsymbol{\chi}_\tau = \boldsymbol{\tau} \qquad\qquad \boldsymbol{\chi} = \overline{\boldsymbol{\chi}} \tag{78}$$

Eqs. (78) are sufficient conditions for eq. (77) to hold, but not necessary ones. Ziegler's orthogonality conditions must be considered as a (weak) restrictive constitutive assumption, yet compatible with realistic descriptions of many classes of granular materials, see, *e.g.*, [CH97, HP07]. When eqs. (78) hold, eqs. (76) represent the dual flow rules for the material, linking the conjugates state variables $(\boldsymbol{\tau}, \overline{\boldsymbol{\chi}})$ to the plastic fluxes $(\boldsymbol{d}^p, \dot{\boldsymbol{\alpha}})$ when the material is at yield ($\mathscr{D} > 0$).

The classical associative flow rule can be obtained by observing that the homogeneity of degree one of the dissipation function implies that the (degenerate) Legendre transform of $\mathscr{D}$ provides the *yield function* in stress space:

$$\dot{\gamma} f(\boldsymbol{\chi}_\tau, \boldsymbol{\chi}) = \dot{\gamma} f(\boldsymbol{\tau}, \overline{\boldsymbol{\chi}}) = \boldsymbol{\tau} \cdot \boldsymbol{d}^p + \overline{\boldsymbol{\chi}} \cdot \dot{\boldsymbol{\alpha}} - \mathscr{D} = 0 \tag{79}$$

where the non–negative scalar quantity $\dot{\gamma}$ multiplying f plays the role of the plastic multiplier. The set:

$$\mathbb{E} := \left\{ (\boldsymbol{\tau}, \overline{\boldsymbol{\chi}}) \;\middle|\; f(\boldsymbol{\tau}, \overline{\boldsymbol{\chi}}) < 0 \right\}$$

is the elastic domain of the material, where the plastic multiplier is zero and all the processes are non–dissipative ($\boldsymbol{d}^p = \boldsymbol{0}$, $\dot{\boldsymbol{\alpha}} = \boldsymbol{0}$). The boundary of $\mathbb{E}$:

$$\partial\mathbb{E} := \left\{ (\boldsymbol{\tau}, \overline{\boldsymbol{\chi}}) \;\middle|\; f(\boldsymbol{\tau}, \overline{\boldsymbol{\chi}}) = 0 \right\}$$

is the yield surface, on which $\dot{\gamma}$ may be positive and irreversible processes may occur. Note that the vector $\overline{\boldsymbol{\chi}}$ plays the role of a stress–like internal variable, linked to the vector of the strain–like internal variables $\boldsymbol{\alpha}$ by the constitutive equation (70).

From eq. (79), a standard argument provides the associative flow rule and hardening law for $\boldsymbol{d}^p$ and $\dot{\boldsymbol{\alpha}}$:

$$\boldsymbol{d}^p = \dot{\gamma} \frac{\partial f}{\partial \boldsymbol{\tau}} \tag{80a}$$

$$\dot{\boldsymbol{\alpha}} = \dot{\gamma} \frac{\partial f}{\partial \overline{\boldsymbol{\chi}}} \tag{80b}$$

Eq. (64) and the flow rule (80a) provide the following expression for the Lie derivative of $\boldsymbol{b}^e$ consistent with the assumed yield function:

$$\mathscr{L}_v[\boldsymbol{b}^e] = -2\,\mathrm{sym}\,(\boldsymbol{d}^p\boldsymbol{b}^e) = -2\dot{\gamma}\;\mathrm{sym}\left(\frac{\partial f}{\partial \boldsymbol{\tau}}\boldsymbol{b}^e\right) \tag{81}$$

The corresponding evolution equation for the elastic left Cauchy–Green tensor is then given by:

$$\dot{\boldsymbol{b}}^e = \boldsymbol{l}\boldsymbol{b}^e + \boldsymbol{b}^e\boldsymbol{l}^T - 2\dot{\gamma}\,\frac{\partial f}{\partial \boldsymbol{\tau}}\,\boldsymbol{b}^e \tag{82}$$

In the RHS of eq. (82) the isotropy of the yield function and of the elastic constitutive equation allow to replace the term $\mathrm{sym}\,\{(\partial f/\partial\boldsymbol{\tau})\boldsymbol{b}^e\}$ with $(\partial f/\partial\boldsymbol{\tau})\boldsymbol{b}^e$, since $\partial f/\partial\boldsymbol{\tau}$ and $\boldsymbol{b}^e$ commute.

5.5 Constitutive equations in rate–form

By a pull–back/push–forward operation to the intermediate configuration, the elastic constitutive equation (73) can be recast in the alternative format:

$$\boldsymbol{\tau} = 2\,\boldsymbol{F}^e\frac{\partial\bar{\psi}^e}{\partial\overline{\boldsymbol{C}}^e}\boldsymbol{F}^{eT} \tag{83}$$

where $\overline{\boldsymbol{C}}^e := \boldsymbol{F}^{eT}\boldsymbol{F}^e$ is the elastic right Cauchy–Green tensor, and $\bar{\psi}^e(\overline{\boldsymbol{C}}^e) = \psi^e(\boldsymbol{b}^e) = \hat{\psi}^e(\lambda^e_A)$ due to material isotropy.

Taking the material time derivative of this last expression we obtain, after some algebra, the following constitutive equation in rate–form:

$$\dot{\boldsymbol{\tau}} = \boldsymbol{l}^e\boldsymbol{\tau} + \boldsymbol{\tau}\boldsymbol{l}^{eT} + \mathbb{c}^e\boldsymbol{d}^e \tag{84}$$

where:

$$\mathbb{c}^e_{ijkl} = \mathbb{C}^e_{ABCD}F^e_{iA}F^e_{jB}F^e_{kC}F^e_{lD} \qquad \mathbb{C}^e_{ABCD} = 4\,\frac{\partial^2\bar{\psi}^e}{\partial\overline{C}_{AB}\partial\overline{C}_{CD}} \tag{85}$$

Noting that $\boldsymbol{l}^e = \boldsymbol{d}^e + \boldsymbol{w}^e = \boldsymbol{d}^e + \boldsymbol{w}$ and recalling the definition of the Jaumann objective rate of Kirchhoff stress of eq. (33), eq. (84) transforms into:

$$\overset{\nabla}{\boldsymbol{\tau}} = \mathbb{a}^e\,(\boldsymbol{d} - \boldsymbol{d}^p) = \mathbb{a}^e\left(\boldsymbol{d} - \dot{\gamma}\frac{\partial f}{\partial\boldsymbol{\tau}}\right) \tag{86}$$

where:

$$\mathbb{a}^e_{ijkl} = \mathbb{c}^e_{ijkl} + \tau_{ik}\delta_{jl} + \tau_{il}\delta_{jk} \tag{87}$$

For the stress–like internal variables $\overline{\boldsymbol{\chi}}$, eq. (70) and the associative hardening law (80b) provide the following evolution equation:

$$\dot{\overline{\boldsymbol{\chi}}} = -\dot{\gamma}\mathbb{H}^p\frac{\partial f}{\partial\overline{\boldsymbol{\chi}}} \qquad \text{with} \qquad \mathbb{H}^p := \frac{\partial^2\psi^p}{\partial\boldsymbol{\alpha}\otimes\partial\boldsymbol{\alpha}} \tag{88}$$

Enforcing the consistency condition for plastic processes, we finally obtain the expression for the plastic multiplier:

$$\dot{\gamma} = \frac{1}{K_p} \left\langle \frac{\partial f}{\partial \boldsymbol{\tau}} \cdot \mathbf{a}^e \boldsymbol{d} \right\rangle \tag{89}$$

in which:

$$K_p := \frac{\partial f}{\partial \boldsymbol{\tau}} \cdot \mathbf{a}^e \frac{\partial f}{\partial \boldsymbol{\tau}} + \frac{\partial f}{\partial \overline{\boldsymbol{\chi}}} \cdot \mathbb{H}^p \frac{\partial f}{\partial \overline{\boldsymbol{\chi}}} > 0 \tag{90}$$

The elastoplastic constitutive equation in rate–form then reads

$$\overset{\nabla}{\boldsymbol{\tau}} = \mathbf{a}^{ep} \boldsymbol{d} \qquad \mathbf{a}^{ep} = \mathbf{a}^e - \frac{1}{K_p} \left(\mathbf{a}^e \frac{\partial f}{\partial \boldsymbol{\tau}} \right) \otimes \left(\mathbf{a}^e \frac{\partial f}{\partial \boldsymbol{\tau}} \right) \tag{91}$$

where $\mathbf{a}^{ep}$ is the elastoplastic continuum tangent stiffness of the material. This results coincides with the one provided by [Sim98], Ch. III, Sect. 38, for multiplicative associative plasticity, generalized to multiple plastic mechanisms.

5.6 Generalization to non–associativity

In many circumstances the assumption of associative plastic flow for both the plastic rate of deformation and the stress–like internal variables could be too restrictive and not suitable to reproduce some important aspects of the mechanical response of granular materials. Under such circumstances, a phenomenological extension of the results presented in Sect. 5 can be obtained by introducing ad–hoc, non–associative flow rules for the plastic flow variables. Their evolution equations then take the form:

$$\boldsymbol{d}^p = \dot{\gamma} \, \frac{\partial g}{\partial \boldsymbol{\tau}} \left(\boldsymbol{\tau}, \boldsymbol{q} \right) \tag{92a}$$

$$\dot{\boldsymbol{q}} = \dot{\gamma} \, \boldsymbol{h} \left(\boldsymbol{\tau}, \boldsymbol{q} \right) \tag{92b}$$

where the scalar function g is the *plastic potential* and the function $\boldsymbol{h}$ defines the so–called *hardening law* of the material. In eqs. (92) the symbol $\boldsymbol{q}$ has been used in place of $\overline{\boldsymbol{\chi}}$ for the stress–like internal variables to stress the fact that they are generally not associated to any free energy function.

As in the associative case, the consistency condition yields the following expression for the plastic multiplier:

$$\dot{\gamma} = \frac{1}{\widehat{K}_p} \left\langle \frac{\partial f}{\partial \boldsymbol{\tau}} \cdot \mathbf{a}^e \boldsymbol{d} \right\rangle \tag{93}$$

in which:

$$\widehat{K}_p := \frac{\partial f}{\partial \boldsymbol{\tau}} \cdot \mathbf{a}^e \frac{\partial g}{\partial \boldsymbol{\tau}} - \frac{\partial f}{\partial \boldsymbol{q}} \cdot \boldsymbol{h} > 0 \tag{94}$$

The rate form of the constitutive equation in the spatial setting is still given by eq. (91) but the elastoplastic tangent stiffness now reads:

$$\mathbf{a}^{ep} = \mathbf{a}^e - \frac{1}{\widehat{K}_p} \left(\mathbf{a}^e \frac{\partial g}{\partial \boldsymbol{\tau}} \right) \otimes \left(\mathbf{a}^e \frac{\partial f}{\partial \boldsymbol{\tau}} \right) \tag{95}$$

The formulation of multiplicative plasticity within the framework of the theory of hyperplasticity is relatively recent. It is due to Oliynyk and Tamagnini, [OT20], who adopted this approach to extend to the finite deformation setting a breakage mechanics model for cemented granular materials [Ten15]. The applications of this approach in its non–associative form date back to the pioneering works of Simo and Meschke [SM93] and Borja and Tamagnini [BT98] in the early '90. Since then, a number of finite deformation plasticity models for geomaterials have been proposed within this framework, see, *e.g.*, [CAS98, JRS01, SSS02, RW06, MCAG17, BB18, BRL19, MCC+19, OCT21].

6 Concluding remarks

In this chapter, two widely used alternative approaches to finite deformation plasticity have been presented in detail. The main advantage of the formulation based on the additive split of the rate of deformation tensor is in its simplicity. With this approach, any existing infinitesimal plasticity model can be easily adapted to finite deformations. The main drawback of this approach is in the hypoelastic nature of the elastic constitutive equation, which may give rise to physically unrealistic behavior under repeated loading cycles and actually limits the applicability of this class of models to the case of "small" elastic deformations. This aspect of the formulation has also important computational implications. In fact, in classical elastic predictor–plastic corrector implicit stress–point algorithms, the state update during the "elastic" predictor step is by no means trivial, since incrementally objective algorithms, as defined by Hughes and Winget [HW80], need to be employed to prevent integration errors in presence of finite rotations, see [SH98].

Plasticity models based on the assumption of multiplicative split of the deformation gradient circumvent completely this issue by relying on a hyperelastic characterization of the reversible response of the material which allows for arbitrarily large elastic deformations. In addition, the evolution equations for the plastic rate of deformation and the internal variables can be derived rigorously from the basic principles of hyperplasticity theory [HP07]. Finally the existence of a one–to–one relation between the relevant stress and elastic deformation measures makes it possible to formulate the evolution problem using the elastic deformation as the primary state variable, so that the elastic predictor stage reduces to a trivial kinematic update, see, *e.g.*, [BT98, OT20]. The main disadvantages of the multiplicative plasticity approach in its applications to geomechanics are the mathematical complexity associated to the treatment of anisotropic behavior and the proper choice of a suitable free energy function capable of reproducing the observed elastic behavior of the soil.

References

[BA95] R. I. Borja and E. Alarcón. A mathematical framework for finite strain elastoplastic consolidation part 1: Balance laws, variational formulation,

and linearization. *Comp. Meth. Appl. Mech. Engng.*, 122(1-2):145–171, 1995.

[BB18] K. C. Bennett and R. I. Borja. Hyper–elastoplastic/damage modeling of rock with application to porous limestone. *Int. Journal of Solids and Structures*, 143:218–231, 2018.

[BD84] R. Baker and C. S. Desai. Induced anisotropy during plastic straining. *Int. J. Num. Anal. Meth. Geomech.*, 8:167–185, 1984.

[BN21] H. H. Bui and G. D. Nguyen. Smoothed particle hydrodynamics (sph) and its applications in geomechanics: From solid fracture to granular behaviour and multiphase flows in porous media. *Comp. & Geotechnics*, 138, 2021.

[Boe87] J. P. Boehler. *Application of tensor functions in solid mechanics*. CISM Courses and Lectures n. 292. Springer Verlag, New York, 1987.

[Bor13] R. I. Borja. *Plasticity: Modeling & Computation*. Springer Science & Business, 2013.

[BRL19] K. C. Bennett, R. A. Regueiro, and D. J. Luscher. Anisotropic finite hyper–elastoplasticity of geomaterials with Drucker–Prager/cap type constitutive model formulation. *Int. J. of Plasticity*, 123:224–250, 2019.

[BT98] R. I. Borja and C. Tamagnini. Cam–clay plasticity, part III: Extension of the infinitesimal model to include finite strains. *Comp. Meth. Appl. Mech. Engng.*, 155:73–95, 1998.

[BTA98] R. I. Borja, C. Tamagnini, and E. Alarcón. Elastoplastic consolidation at finite strain part 2: finite element implementation and numerical examples. *Comp. Meth. Appl. Mech. Engng.*, 159(1-2):103–122, 1998.

[BWV11] L. Beuth, Z. Wieckowski, and P. A. Vermeer. Solution of quasi-static large-strain problems by the material point method. *Int. J. Num. Anal. Meth. Geomech.*, 35(13):1451–1465, 2011.

[CAS98] C. Callari, F. Auricchio, and E. Sacco. A finite-strain cam-clay model in the framework of multiplicative elasto-plasticity. *Int. J. of Plasticity*, 14(12):1155–1187, 1998.

[CBS79] J. P. Carter, J. R. Booker, and J. C. Small. The analysis of finite elasto-plastic consolidation. *Int. J. Num. Anal. Meth. Geomech.*, 3(2):107–129, 1979.

[CH97] I.F. Collins and G. T. Houlsby. Application of thermomechanical principles to the modeling of geotechnical materials. *Proc. Royal Soc. London Series A*, 453:1975–2000, 1997.

[COS13] J. M. Carbonell, E. Oñate, and B. Suárez. Modelling of tunnelling processes and rock cutting tool wear with the particle finite element method. *Computational Mechanics*, 52(3):607–629, 2013.

[CPT19] E. Conte, L. Pugliese, and A. Troncone. Post-failure stage simulation of a landslide using the material point method. *Engineering Geology*, 253:149–159, 2019.

[CS17] F. Ceccato and P. Simonini. Numerical study of partially drained penetration and pore pressure dissipation in piezocone test. *Acta Geotechnica*, 12(1):195–209, 2017.

[Die79] J. K. Dienes. On the analysis of rotation and stress rate in deforming bodies. *Acta Mechanica*, 32(4):217–232, 1979.

[GEH67] R. E. Gibson, G. L. England, and M. J. L. Hussey. The theory of one-dimensional consolidation of saturated clays: 1. finite non–linear consolidation of thin homogeneous layers. *Géotechnique*, 17(3):261–273, 1967.

[GSC81] R. E. Gibson, R. L. Schiffman, and K. W. Cargill. The theory of one-dimensional consolidation of saturated clays. II. finite nonlinear consolidation of thick homogeneous layers. *Can. Geotech. J.*, 18(2):280–293, 1981.

[HKS16] H. D. Hibbitt, B. I. Karlsson, and E. P. Sorensen. *ABAQUS Standard theory manual*. ABAQUS Standard documentation. Simulia, 2016.

[HP07] G. T. Houlsby and A. M. Puzrin. *Principles of hyperplasticity: an approach to plasticity theory based on thermodynamic principles*. Springer Science & Business Media, 2007.

[HW80] T. J. R. Hughes and J. Winget. Finite rotation effects in numerical integration of rate constitutive equations arising in large-deformation analysis. *Int. J. Num. Meth. Engng.*, 15(12):1862–1867, 1980.

[JB84] G. C. Johnson and D. J. Bammann. A discussion of stress rates in finite deformation problems. *Int. Journal of Solids and Structures*, 20(8):725–737, 1984.

[JBK+18] R. J. Jardine, R. M. Buckley, S. Kontoe, P. Barbosa, and F. C. Schroeder. Behaviour of piles driven in chalk. *Engineering in chalk*, pages 33–51, 2018.

[JRS01] B. Jeremić, K. Runesson, and S. Sture. Finite deformation analysis of geomaterials. *Int. J. Num. Anal. Meth. Geomech.*, 25(8):809–840, 2001.

[KL88] R. King and M. Lodge. North west shelf development-the foundation engineering challenge. In *International conference on calcareous sediments*, pages 333–341, 1988.

[Lee68] E. H. Lee. Elastic-plastic deformation at finite strains. *J. Appl. Mechanics, ASME*, 36:1–6, 1968.

[MACG17] L. Monforte, M. Arroyo, J. M. Carbonell, and A. Gens. G–PFEM: A particle finite element method platform for geotechnical applications. In *ALERT Geomaterials Workshop*, 2017.

[MACG18] L. Monforte, M. Arroyo, J. M. Carbonell, and A. Gens. Coupled effective stress analysis of insertion problems in geotechnics with the particle finite element method. *Computers & Geotechnics*, 101:114–129, 2018.

[Mas21] D. Masin. Hypoplasticity and other incrementally non–linear modelling approaches. In C. Tamagnini and D. Mašín, editors, *Constitutive modelling of soils*. ALERT Geomaterials, 2021. This volume.

[MCAG17] L. Monforte, J. M. Carbonell, M. Arroyo, and A. Gens. Performance of mixed formulations for the particle finite element method in soil mechanics problems. *Computational Particle Mechanics*, 4(3):269–284, 2017.

[MCC+19] L. Monforte, M. O. Ciantia, J. M. Carbonell, M. Arroyo, and A. Gens. A stable mesh–independent approach for numerical modelling of structured soils at large strains. *Comp. & Geotechnics*, 116:103215, 2019.

[MCG20] M. A. Mánica, M. O. Ciantia, and A. Gens. On the stability of underground caves in calcareous rocks due to long-term weathering. *Rock Mechanics and Rock Engineering*, 53:3885–3901, 2020.

[McL88] B. McLelland. Calcareous sediments: an engineering enigma. In *International conference on calcareous sediments*, pages 777–784, 1988.

[MG21] M. Martinelli and V. Galavi. Investigation of the material point method in the simulation of cone penetration tests in dry sand. *Computers and Geotechnics*, 130, 2021.

[MS03] A. Menzel and P. Steinmann. On the spatial formulation of anisotropic multiplicative elasto-plasticity. *Comp. Meth. Appl. Mech. Engng.*, 192(31-32):3431–3470, 2003.

[MSZ95] E. A. Meroi, B. A. Schrefler, and O. C. Zienkiewicz. Large strain static and dynamic semisaturated soil behaviour. *Int. J. Num. Anal. Meth. Geomech.*, 19(2):81–106, 1995.

[ND81] J. C. Nagtegaal and J. E. De Jong. Some computational aspects of elastic-plastic large strain analysis. *Int. J. Num. Meth. Engng.*, 17(1):15–41, 1981.

[OCT21] K. Oliynyk, M. O. Ciantia, and C. Tamagnini. A finite deformation multiplicative plasticity model with non–local hardening for bonded geomaterials. *Comp. & Geotechnics*, 137, 2021.

[OCW+07] J. Oliver, J. C. Cante, R. Weyler, C. González, and J. Hernández. Particle finite element methods in solid mechanics problems. *Computational Methods in Applied Sciences*, 7:87–103, 2007.

[OT20] K. Oliynyk and C. Tamagnini. Finite deformation hyperplasticity theory for crushable, cemented granular materials. *Open Geomechanics*, 2:1–33, 2020.

[PJB88] DM Potts, ME Jones, and OP Berget. Subsidence above the ekofisk oil reservoirs. In *Proceedings of the International Congress on behaviour of offshore structures*, pages 113–128, Trondheim, Norway, 1988.

[POP83] P. M. Pinsky, M. Ortiz, and K. S. Pister. Numerical integration of rate constitutive equations in finite deformation analysis. *Comp. Meth. Appl. Mech. Engng.*, 40(2):137–158, 1983.

[Pre80] J. H. Prevost. Mechanics of continuous porous media. *Int. Journal of Engineering Science*, 18:787–800, 1980.

[RW06] M. Rouainia and D. M. Wood. Computational aspects in finite strain plasticity analysis of geotechnical materials. *Mechanics Research Communications*, 33(2):123–133, 2006.

[SAY+16] K. Soga, E. Alonso, A. Yerro, K. Kumar, and S. Bandara. Trends in large-deformation analysis of landslide mass movements with particular emphasis on the material point method. *Géotechnique*, 66(3):248–273, 2016.

[SCS94] D. Sulsky, Z. Chen, and H. L. Schreyer. A particle method for history-dependent materials. *Comp. Meth. Appl. Mech. Engng.*, 118(1-2):179–196, 1994.

[SH98] J. C. Simo and T. J. R. Hughes. *Computational inelasticity*, volume 7. Springer Science & Business Media, 1998.

[Sim98] J.C. Simo. Numerical analysis and simulation of plasticity. *Handbook of numerical analysis*, 6:183–499, 1998.

[SM93] J. C. Simo and G. Meschke. A new class of algorithms for classical plasticity extended to finite strains. application to geomaterials. *Computational Mechanics*, 11(4):253–278, 1993.

[SSS02] L. Sanavia, B. A. Schrefler, and P. Steinmann. A formulation for an unsaturated porous medium undergoing large inelastic strains. *Computational Mechanics*, 28(2):137–151, 2002.

[Ten15] A. Tengattini. *A micro-mechanical study of cemented granular materials*. PhD thesis, University of Sydney, 2015.

[TO21] C. Tamagnini and K. Oliynyk. The theory of plasticity in constitutive modeling of rate–independent soils. In C. Tamagnini and D. Mašín, ed-

itors, *Constitutive modelling of soils*. ALERT Geomaterials, 2021. This volume.

[Tru56] C. A. Truesdell. Hypo–elastic shear. *J. Appl. Physics*, 27:441–447, 1956.

[Zie83] H. Ziegler. *An introduction to thermomechanics*. North Holland, 1983.

Numerical implementation of elastoplastic models in the Finite Element Method

Claudio Tamagnini[a], **Kateryna Oliynyk**[a,b]

[a)] *University of Perugia, Italy*
[b)] *University of Dundee, UK*

This chapter presents an overview of some of the most widely used numerical procedures for the implementation of elastoplastic constitutive models in non–linear Finite Element codes. The first part of the chapter is devoted to the formulation of the evolution equations and the discussion of the stress–point algorithms for infinitesimal plasticity. The second part focuses on the evolution equations of finite deformation multiplicative plasticity and the corresponding stress–point algorithms. Both the implicit Backward Euler method – based on a two–stage procedure with an elastic predictor problem and a plastic corrector problem – and explicit adaptive schemes with substepping and error control are covered for both infinitesimal and finite deformation plasticity models.

1 Introduction

In recent years the parallel development of: i) advanced constitutive theories for the mechanical behavior of geomaterials, ii) robust and accurate numerical methods for the solution of partial differential equations, and iii) powerful computer architectures, has led to a radical change in the analysis of geotechnical problems, notably in some areas such as the design of deep excavations or the analysis of complex soil–structure interaction problems where traditional design methods – based on the classical distinction between "failure" and "deformation" problems – are not able to capture the most relevant aspects of the soil–structure system behavior.

A common and almost universal feature of the constitutive models proposed for geomaterials – from those which have now became a standard design tool in geotechnical practice to the ones which were mainly developed for research purposes – is the fact that they are cast in *incremental* form. Rather than providing the state of stress associated to a specific state of strain, they define the *evolution laws* for the state variables. Therefore, the quantitative evaluation of the mechanical effects of a given "load", be

it an imposed stress increment, strain increment or a combination of both, requires the solution of an initial value problem, consisting in the *integration* of the constitutive equation along the assigned loading path, with prescribed *initial conditions*. As this task cannot be performed analytically, except in very special cases, the development of a numerical algorithm for this purpose is a crucial part of any computational procedure for the solution of non–linear problems in geomechanics.

More specifically, in the application of numerical methods – such as the finite Element method – to the solution of a non–linear initial/boundary value problem, the following general strategy is usually adopted, see [SH98]:

1. from the original system of governing partial differential equations (PDEs), a non–linear system of algebraic *balance equations* is obtained by the introduction of appropriate space and time discretizations. Such a system is typically solved by adopting an incremental–iterative approach;
2. for any given *global* iteration, the discretized equilibrium equations generate incremental motions, which, in turn, are used to determine the incremental strain history by purely kinematic relationships;
3. for a given strain increment, updated values of the state variables are obtained by integrating numerically the constitutive equations at the *local* level, with given initial conditions; for their local scope, the procedures employed for this task are typically referred to as *stress–point algorithms*;
4. the discrete balance equations are then checked for convergence, and if the convergence criterion is not met, the iteration process is continued by returning to step (2).

As first pointed out by Hughes [Hug84], the integration of the constitutive equation at the local level – *i.e.*, step (3) – represents the central problem of computational plasticity, since it corresponds to the main role played by the constitutive equation in actual computations. There are of course many other important computational ingredients in the overall procedure, but they are particular to the type of solution strategy employed, and involve the constitutive theory only in a limited way, if at all. Moreover, the precision with which the constitutive equations are integrated has a direct impact on the overall accuracy of the analysis.

Since the early works on metal plasticity, summarized in [Hug84], a number of fundamental treatises have been published on this subject. Among them we cite the books of Simo and Hughes [SH98], de Souza Neto *et al.* [dPO11] and the chapter written by Simo [Sim98] for the Handbook of Numerical Analysis.

In this chapter, we present an overview of some of the most widely used stress–point algorithms for the integration of classical and advanced plasticity models for soils, reflecting our personal experience in this field. After a brief description of the notation (Sect. 2), in Sect. 3 we address the main problem of computational plasticity for the case of infinitesimal deformations, summarizing the evolution equations to be

integrated and the different numerical procedures for their integration, separating explicit adaptive strategies with error control based on Runge–Kutta methods and the implicit Backward–Euler algorithm, which has now become a standard in computational plasticity. The evolution equations for finite deformation multiplicative plasticity and the corresponding explicit, semi–implicit and implicit integration algorithms are presented in Sect. 4. In both Sect. 3 and 4, particular attention is paid to the definition and the computation of the *consistent tangent stiffness matrix*, which guarantees the asymptotic quadratic convergence of the Newton–Raphson method when it is used for the iterative solution of the discrete equilibrium equations.

2 Notation

In the following, all stresses and stress–related quantities are effective, unless otherwise stated. The sign convention of continuum mechanics (traction and extension positive) is adopted throughout. Both direct and index notations will be used to represent vector and tensor quantities according to convenience. In direct notation, vectors and second–order tensors will be represented by boldface italic fonts. Boldface italic fonts and blackboard bold fonts – such as $\mathfrak{c}^e$ and $\mathbb{C}^e$ – are used to represent fourth–order tensors, according to convenience. Following standard practice, for any two vectors $\boldsymbol{v}, \boldsymbol{w} \in \mathbb{R}^3$, the dot product is defined as: $\boldsymbol{v} \cdot \boldsymbol{w} := v_i w_i$, and the dyadic product as: $[\boldsymbol{v} \otimes \boldsymbol{w}]_{ij} := v_i w_j$. Accordingly, for any two second–order tensors $\boldsymbol{X}, \boldsymbol{Y}$, $\boldsymbol{X} \cdot \boldsymbol{Y} := X_{ij} Y_{ij}$ and $[\boldsymbol{X} \otimes \boldsymbol{Y}]_{ijkl} := X_{ij} Y_{kl}$. The quantity $\|\boldsymbol{X}\| := \sqrt{\boldsymbol{X} \cdot \boldsymbol{X}}$ denotes the Euclidean norm of the second order tensor $\boldsymbol{X}$, unless otherwise stated.

3 Stress–point algorithms for infinitesimal plasticity

3.1 Evolution equations

The evolution equations of the theory of infinitesimal plasticity are briefly summarized below. Let $\boldsymbol{\epsilon}$ be the strain tensor and $\boldsymbol{q}$ be the vector (of dimension n_{int}) of the internal state variables accounting for the effects of the previous loading history. Also, let:

$$\mathbb{E} := \left\{ (\boldsymbol{\sigma}, \boldsymbol{q}) \;\middle|\; f(\boldsymbol{\sigma}, \boldsymbol{q}) \leq 0 \right\} \tag{1}$$

be the elastic domain, defined through a suitable yield function $f(\boldsymbol{\sigma}, \boldsymbol{q}) = 0$. Taking into account the usual additive decomposition of the strain rate tensor, $\dot{\boldsymbol{\epsilon}}$, into an elastic ($\dot{\boldsymbol{\epsilon}}^e$) and a plastic ($\dot{\boldsymbol{\epsilon}}^p$) part, we have:

$$\dot{\boldsymbol{\sigma}} = \boldsymbol{D}^e(\boldsymbol{\sigma}) \left[\dot{\boldsymbol{\epsilon}} - \dot{\boldsymbol{\epsilon}}^p \right] \tag{2}$$

$$\dot{\boldsymbol{\epsilon}}^p = \dot{\gamma} \frac{\partial g}{\partial \boldsymbol{\sigma}}(\boldsymbol{\sigma}, \boldsymbol{q}) \tag{3}$$

$$\dot{\boldsymbol{q}} = \dot{\gamma} \boldsymbol{h}(\boldsymbol{\sigma}, \boldsymbol{q}) \tag{4}$$

subject to the following Kuhn–Tucker complementarity conditions:

$$\dot{\gamma} \geq 0 \ , \quad f(\boldsymbol{\sigma}, \boldsymbol{q}) \leq 0 \ , \quad \dot{\gamma} f(\boldsymbol{\sigma}, \boldsymbol{q}) = 0 \tag{5}$$

which state that plastic processes ($\dot{\gamma} > 0$) can occur only for states on the yield surface, and to the consistency condition:

$$\dot{\gamma} \dot{f} = \dot{\gamma} \left(\frac{\partial f}{\partial \boldsymbol{\sigma}} \cdot \dot{\boldsymbol{\sigma}} + \frac{\partial f}{\partial \boldsymbol{q}} \cdot \dot{\boldsymbol{q}} \right) = 0 \tag{6}$$

requiring that the state of the material remains on the yield surface ($f = 0$) whenever plastic loading occurs. Eq. (2) is the elastic constitutive equation of the material in incremental form. The fourth–order tensor $\boldsymbol{D}^e(\boldsymbol{\sigma})$ is the elastic tangent stiffness of the material. Eq. (3) provides the flow rule for the plastic strain rate, defined in terms of the plastic potential function $g = \widehat{g}(\boldsymbol{\sigma}, \boldsymbol{q})$. The non–negative scalar $\dot{\gamma}$ is the plastic multiplier. The evolution of the internal variables $\boldsymbol{q}$ is provided by the hardening law (4), in which $\boldsymbol{h}$ is a prescribed hardening function.

From the consistency condition (6) the following expression for the plastic multiplier is obtained:

$$\dot{\gamma} = \frac{1}{K_p} \left\langle \frac{\partial f}{\partial \boldsymbol{\sigma}} \cdot \boldsymbol{D}^e \dot{\boldsymbol{\epsilon}} \right\rangle \tag{7}$$

in which:

$$K_p := \frac{\partial f}{\partial \boldsymbol{\sigma}} \cdot \boldsymbol{D}^e \frac{\partial g}{\partial \boldsymbol{\sigma}} + H_p > 0 \qquad\qquad H_p := -\frac{\partial f}{\partial \boldsymbol{q}} \cdot \boldsymbol{h} \tag{8}$$

Substituting the expression (7) for the plastic multiplier in eqs. (3) and (4), we obtain:

$$\dot{\boldsymbol{\sigma}} = \boldsymbol{D}^{ep} \dot{\boldsymbol{\epsilon}} \qquad\qquad \dot{\boldsymbol{q}} = \boldsymbol{H}^p \dot{\boldsymbol{\epsilon}} \tag{9}$$

where:

$$\boldsymbol{D}^{ep} := \boldsymbol{D}^e - \frac{\mathscr{H}(\dot{\gamma})}{K_p} \left(\boldsymbol{D}^e \, \frac{\partial g}{\partial \boldsymbol{\sigma}} \right) \otimes \left(\frac{\partial f}{\partial \boldsymbol{\sigma}} \, \boldsymbol{D}^e \right) \tag{10a}$$

$$\boldsymbol{H}^p := \frac{\mathscr{H}(\dot{\gamma})}{K_p} \boldsymbol{h} \otimes \left(\frac{\partial f}{\partial \boldsymbol{\sigma}} \boldsymbol{D}^e \right) \tag{10b}$$

where $\mathscr{H}(x)$ is the Heaviside step function, equal to one if $x > 0$ and zero otherwise, and K_p is provided by eq. $(8)_1$.

3.2 State update

Let $\mathbb{I} = \bigcup_{n=0}^{N} [t_n, t_{n+1}]$ be a partition of the time interval of interest into time steps. It is assumed that at time $t_n \in \mathbb{I}$ the state of the material $(\boldsymbol{\sigma}_n, \boldsymbol{q}_n)$ is known at any quadrature point in the adopted finite element discretization. Also, let:

$$\{\boldsymbol{\epsilon}_i : i = 0, 1, \ldots, n+1\}$$

be the prescribed history of $\boldsymbol{\epsilon}$ up to time t_{n+1}. The computational problem to be addressed is the update of the state variables:

$$\boldsymbol{\sigma}_{n+1}^{(k)} \to \widehat{\boldsymbol{\sigma}}\left(\boldsymbol{\epsilon}_{n+1}^{(k)}; \boldsymbol{\sigma}_n, \boldsymbol{q}_n\right) \tag{11}$$

$$\boldsymbol{q}_{n+1}^{(k)} \to \widehat{\boldsymbol{q}}\left(\boldsymbol{\epsilon}_{n+1}^{(k)}; \boldsymbol{\sigma}_n, \boldsymbol{q}_n\right) \tag{12}$$

for a *given* increment $\Delta\boldsymbol{\epsilon}_{n+1}^{(k)} := \boldsymbol{\epsilon}_{n+1}^{(k)} - \boldsymbol{\epsilon}_n$, relative to the global iteration (k), through the integration of the system of ordinary differential equations (ODEs) (2)–(5) or (9) provided by the elastoplastic constitutive equations. Note that the evolution problem defined by eqs. (2)–(5) belongs to the category of the so–called *stiff differential–algebraic systems* – see [HW91] for details – for which *implicit* methods are ideally suited. In the evolution problem governed by eqs. (9), the algebraic constraint posed by eqs. (5) has been linearized by imposing the consistency condition and then removed. This format is therefore best suited for the application of *explicit* methods.

Whenever the existence of a free energy function $\psi = \psi\left(\boldsymbol{\epsilon}^e\right)$ can be postulated, the stress tensor is linked to the elastic strain tensor by the relation:

$$\boldsymbol{\sigma}(\boldsymbol{\epsilon}^e) = \frac{\partial \psi}{\partial \boldsymbol{\epsilon}^e}\left(\boldsymbol{\epsilon}^e\right) \tag{13}$$

and thus can be considered a *dependent* quantity. As such, $\boldsymbol{\sigma}$ can be replaced in the set of state variables by the elastic strain tensor $\boldsymbol{\epsilon}^e$. The evolution equations (11) and (12) can then be recast in the following format:

$$\boldsymbol{\epsilon}_{n+1}^{e(k)} \to \widehat{\boldsymbol{\epsilon}}^e\left(\boldsymbol{\epsilon}_{n+1}^{(k)}; \boldsymbol{\epsilon}_n^e, \boldsymbol{q}_n\right) \tag{14}$$

$$\boldsymbol{q}_{n+1}^{(k)} \to \widehat{\boldsymbol{q}}\left(\boldsymbol{\epsilon}_{n+1}^{(k)}; \boldsymbol{\epsilon}_n^e, \boldsymbol{q}_n\right) \tag{15}$$

3.3 Consistent linearization of the stress update algorithm

In a standard finite element context, the starting point for the solution of a static equilibrium problem is the weak form of the balance of momentum equation, which, for the problem at hand, is stated as follows. Find the unknown function $\boldsymbol{u}(\boldsymbol{x})$ such that, for any test function (variation) $\boldsymbol{\eta}(\boldsymbol{x})$ satisfying homogeneous boundary conditions on the appropriate part of the boundary, the following non–linear functional equation is satisfied:

$$\mathscr{G}\left(\boldsymbol{u}, \boldsymbol{\eta}\right) = \int_\Omega \nabla^s \boldsymbol{\eta} \cdot \boldsymbol{\sigma}\left(\boldsymbol{u}\right)\, dV - \int_\Omega \rho\, \boldsymbol{\eta} \cdot \boldsymbol{b}\, dV - \int_{\Gamma_t} \boldsymbol{\eta} \cdot \boldsymbol{t}\, dA = 0 \tag{16}$$

In the above equation, non–linearity stems from the non–linear dependence of the stress tensor on $\boldsymbol{u}$ induced by the constitutive equation. The iterative solution via Newton's method of the non–linear algebraic problem resulting after the introduction of a standard finite element discretization, requires the linearization of the non–linear

functional $\mathscr{G}$ with respect to the independent field $\boldsymbol{u}$:

$$D_{\boldsymbol{u}}\mathscr{G}\left(\boldsymbol{u}_{n+1}^{(k)},\boldsymbol{\eta}\right)\left[\delta\boldsymbol{u}_{n+1}^{(k)}\right]=\int_{\Omega}\left\{\nabla^{s}\boldsymbol{\eta}\cdot\left(\widetilde{\boldsymbol{D}}\right)_{n+1}^{(k)}\nabla^{s}\left(\delta\boldsymbol{u}\right)_{n+1}^{(k)}\right\}dV \tag{17}$$

in which:

$$\left(\widetilde{\boldsymbol{D}}\right)_{n+1}^{(k)}:=\frac{\partial\boldsymbol{\sigma}_{n+1}^{(k)}}{\partial\boldsymbol{\epsilon}_{n+1}^{(k)}} \tag{18}$$

The fourth–order tensor $\widetilde{\boldsymbol{D}}_{n+1}^{(k)}$ is the so–called *consistent tangent stiffness matrix* to the update procedure defined by eqs. (11) and (12) or (14) and (15), *i.e.*, by the stress–point algorithm, see [ST85]. This quantity heavily depends on the adopted integration algorithm, and its accurate evaluation is crucial to achieve the quadratic convergence when using Newton–Raphson method to solve iteratively the global discrete equilibrium equations.

3.4 Explicit adaptive methods

Starting from the pioneering work of Sloan [Slo87], a significant amount of work has been devoted to the development of explicit stress–point algorithms for infinitesimal plasticity, based on the use of Runge–Kutta methods of various order. The key point in the application of classical methods to the solution of the differential–algebraic evolution problem posed by eqs. (2)–(4) and (5) is the removal of the algebraic constraint by its linearization through the consistency condition (6), in order to obtain the system of ODEs of eqs. (9).

Due to their conditional stability, explicit integration methods have been developed in connection with adaptive time–stepping strategies employing variable substep sizes. Adaptive time–stepping is usually implemented in two possible ways, see [SB92b]:

a) by comparing the solutions obtained with the same time step size with two explicit methods of different order (*embedded Runge–Kutta methods*);

b) by comparing the solutions obtained with the same algorithm using different step sizes (typically, a single step of size h and two consecutive steps of size $h/2$).

Methods of the first group have been used in the works of Sloan and coworkers [Slo87, SB92a, SAS01, PSS08] and Tamagnini *et al.* [TVCD00]. A method of the second group based on the repeated use of the simple Forward Euler algorithm has been adopted by Fellin, Ostermann and Mittendorfer [FO02, FMO09]. In the following, we will focus our attention on these last two works, which, differently from the others mentioned, address the point of computing the consistent tangent stiffness matrix as a part of the integration algorithm.

3.4.1 Substepping, time rescaling and consistent linearization

Let $\mathbb{I} = \bigcup_{n=0}^{N} [t_n, t_{n+1}]$ be a partition of the time interval of interest $[t_0, t_{\text{fin}}]$ into time steps of amplitude $\Delta t_{n+1} = t_{n+1} - t_n$. As the material behavior is rate–independent, it is possible to rescale the time axis by introducing the following non–dimensional time factor:

$$T = \frac{(t - t_n)}{(t_{n+1} - t_n)} = \frac{(t - t_n)}{\Delta t_{n+1}} \qquad T \in [0, 1] \tag{19}$$

The (unit) non–dimensional time increment can then be divided in m substeps of size:

$$\Delta T_{k+1} = T_{k+1} - T_k = \frac{t_{k+1} - t_k}{\Delta t_{n+1}} \qquad \text{provided that:} \qquad \sum_{k=1}^{m} \Delta T_k = 1 \tag{20}$$

Considering that, during the time step $[t_n, t_{n+1}]$ the strain rate is assumed constant, we can write:

$$\dot{\boldsymbol{\epsilon}} = \frac{\Delta \boldsymbol{\epsilon}_{n+1}}{\Delta t_{n+1}} \qquad \frac{d\boldsymbol{\epsilon}}{dT} = \dot{\boldsymbol{\epsilon}} \frac{dt}{dT} = \Delta \boldsymbol{\epsilon}_{n+1} \tag{21}$$

and thus rewrite the evolution equations (9) as:

$$\frac{d\boldsymbol{\sigma}}{dT} = \boldsymbol{D}^{ep}(\boldsymbol{\sigma}, \boldsymbol{q}) \Delta \boldsymbol{\epsilon}_{n+1} = \boldsymbol{\xi}(\boldsymbol{\sigma}, \boldsymbol{q}, \Delta \boldsymbol{\epsilon}_{n+1}) \qquad \boldsymbol{\sigma}\big|_{T=0} = \boldsymbol{\sigma}_n \tag{22a}$$

$$\frac{d\boldsymbol{q}}{dT} = \boldsymbol{H}^{p}(\boldsymbol{\sigma}, \boldsymbol{q}) \Delta \boldsymbol{\epsilon}_{n+1} = \boldsymbol{\eta}(\boldsymbol{\sigma}, \boldsymbol{q}, , \Delta \boldsymbol{\epsilon}_{n+1}) \qquad \boldsymbol{q}\big|_{T=0} = \boldsymbol{q}_n \tag{22b}$$

where the strain increment $\Delta \boldsymbol{\epsilon}_{n+1}$ is to be considered a given data. As indicated by eq. (18), the consistent tangent stiffness emerging from the linearization of the algorithm employed to integrate eqs. (22) in the interval $[0, 1]$, with the initial conditions given in eqs. $(22a)_2$ and $(22b)_2$, measures the changes in the updated value of $\boldsymbol{\sigma}$ (*i.e.*, $\boldsymbol{\sigma}_{n+1}$) for an infinitesimal change of the prescribed strain increment, that is:

$$\widetilde{\boldsymbol{D}}_{n+1} = \frac{\partial \boldsymbol{\sigma}_{n+1}}{\partial \boldsymbol{\epsilon}_{n+1}} = \frac{\partial \boldsymbol{\sigma}_{n+1}}{\partial \Delta \boldsymbol{\epsilon}_{n+1}} \tag{23}$$

where the superscript (k) has been dropped to ease the notation. By deriving eqs. (22) with respect to $\Delta \boldsymbol{\epsilon}_{n+1}$ we obtain:

$$\frac{d}{dT}\left(\frac{\partial \boldsymbol{\sigma}}{\partial \Delta \boldsymbol{\epsilon}_{n+1}}\right) = \frac{\partial \boldsymbol{\xi}}{\partial \boldsymbol{\sigma}} \frac{\partial \boldsymbol{\sigma}}{\partial \Delta \boldsymbol{\epsilon}_{n+1}} + \frac{\partial \boldsymbol{\xi}}{\partial \boldsymbol{q}} \frac{\partial \boldsymbol{q}}{\partial \Delta \boldsymbol{\epsilon}_{n+1}} + \frac{\partial \boldsymbol{\xi}}{\partial \Delta \boldsymbol{\epsilon}_{n+1}} \tag{24a}$$

$$\frac{d}{dT}\left(\frac{\partial \boldsymbol{q}}{\partial \Delta \boldsymbol{\epsilon}_{n+1}}\right) = \frac{\partial \boldsymbol{\eta}}{\partial \boldsymbol{\sigma}} \frac{\partial \boldsymbol{\sigma}}{\partial \Delta \boldsymbol{\epsilon}_{n+1}} + \frac{\partial \boldsymbol{\eta}}{\partial \boldsymbol{q}} \frac{\partial \boldsymbol{q}}{\partial \Delta \boldsymbol{\epsilon}_{n+1}} + \frac{\partial \boldsymbol{\eta}}{\partial \Delta \boldsymbol{\epsilon}_{n+1}} \tag{24b}$$

By setting:

$$\widetilde{\boldsymbol{D}} = \frac{\partial \boldsymbol{\sigma}}{\partial \Delta \boldsymbol{\epsilon}_{n+1}} \qquad \widetilde{\boldsymbol{G}} = \frac{\partial \boldsymbol{q}}{\partial \Delta \boldsymbol{\epsilon}_{n+1}} \tag{25}$$

eqs. (24) provide the following evolution equations for $\widetilde{\boldsymbol{D}}$ and $\widetilde{\boldsymbol{G}}$:

$$\frac{d\widetilde{\boldsymbol{D}}}{dT} = \frac{\partial \boldsymbol{\xi}}{\partial \boldsymbol{\sigma}}\,\widetilde{\boldsymbol{D}} + \frac{\partial \boldsymbol{\xi}}{\partial \boldsymbol{q}}\,\widetilde{\boldsymbol{G}} + \boldsymbol{D}^{ep} \qquad \widetilde{\boldsymbol{D}}\big|_{T=0} = \boldsymbol{0} \tag{26a}$$

$$\frac{d\widetilde{\boldsymbol{G}}}{dT} = \frac{\partial \boldsymbol{\eta}}{\partial \boldsymbol{\sigma}}\,\widetilde{\boldsymbol{D}} + \frac{\partial \boldsymbol{\eta}}{\partial \boldsymbol{q}}\,\widetilde{\boldsymbol{G}} + \boldsymbol{H}^{p} \qquad \widetilde{\boldsymbol{G}}\big|_{T=0} = \boldsymbol{0} \tag{26b}$$

The ordinary differential equations (22) and (26), integrated over the dimensionless time interval $[0, 1]$ with the prescribed initial conditions, will yield, at the end of the integration process ($T = 1$), the updated values of the state variables $(\boldsymbol{\sigma}_{n+1}, \boldsymbol{q}_{n+1})$. The final integrated value of $\widetilde{\boldsymbol{D}}$ at $T = 1$ will be the tangent stiffness consistent with the numerical integration algorithm adopted to solve the evolution problem. This approach to the consistent linearization of the integration algorithm has been proposed by Fellin and Ostermann [FO02].

In view of the analytical difficulties in computing the derivatives of the functions $\boldsymbol{\xi}$ and $\boldsymbol{\eta}$ with respect to $\boldsymbol{\sigma}$ and $\boldsymbol{q}$ for realistic constitutive models, Fellin and Ostermann suggest to replace the RHS of eqs. (26a) and (26b) with the following approximation, obtained by numerical differentiation:

$$\frac{d\widetilde{\boldsymbol{D}}_{kl}}{dT} \simeq \frac{1}{\vartheta}\left\{\boldsymbol{\xi}\left(\boldsymbol{\sigma} + \vartheta\widetilde{\boldsymbol{D}}_{kl}, \boldsymbol{q} + \vartheta\widetilde{\boldsymbol{G}}_{kl}, \Delta\boldsymbol{\epsilon}_{n+1} + \vartheta\widetilde{\boldsymbol{I}}_{kl}\right) - \boldsymbol{\xi}\left(\boldsymbol{\sigma}, \boldsymbol{q}, \Delta\boldsymbol{\epsilon}_{n+1}\right)\right\} \tag{27a}$$

$$\frac{d\widetilde{\boldsymbol{G}}_{kl}}{dT} \simeq \frac{1}{\vartheta}\left\{\boldsymbol{\eta}\left(\boldsymbol{\sigma} + \vartheta\widetilde{\boldsymbol{D}}_{kl}, \boldsymbol{q} + \vartheta\widetilde{\boldsymbol{G}}_{kl}, \Delta\boldsymbol{\epsilon}_{n+1} + \vartheta\widetilde{\boldsymbol{I}}_{kl}\right) - \boldsymbol{\eta}\left(\boldsymbol{\sigma}, \boldsymbol{q}, \Delta\boldsymbol{\epsilon}_{n+1}\right)\right\} \tag{27b}$$

for $k = 1, 2, 3$ and $l = 1, 2, 3$, with the initial conditions:

$$\widetilde{\boldsymbol{D}}_{kl}\big|_{T=0} = \boldsymbol{0} \qquad \widetilde{\boldsymbol{G}}_{kl}\big|_{T=0} = \boldsymbol{0} \qquad \forall\,(k, l) = 1, 2, 3 \tag{28}$$

In eqs. (27) and (28), the quantities $\widetilde{\boldsymbol{D}}_{kl}$, $\widetilde{\boldsymbol{G}}_{kl}$ and $\widetilde{\boldsymbol{I}}_{kl}$ are defined as:

$$\widetilde{\boldsymbol{D}}_{kl} := \frac{\partial \boldsymbol{\sigma}}{\partial \Delta\epsilon_{kl,n+1}} \qquad \widetilde{\boldsymbol{G}}_{kl} := \frac{\partial \boldsymbol{q}}{\partial \Delta\epsilon_{kl,n+1}} \qquad \widetilde{\boldsymbol{I}}_{kl} = (\delta_{ik}\delta_{jl})\boldsymbol{e}_i \otimes \boldsymbol{e}_j \tag{29}$$

If Voigt notation is adopted to represents second–order and fourth–order tensors, with the following index mapping:

$(ij)/(kl)$	11	22	33	12	23	31
α/β	1	2	3	4	5	6

then the quantities in eq. (29) can be interpreted as the β–th column vectors of the Voigt matrices $\widetilde{\boldsymbol{D}}$, $\widetilde{\boldsymbol{G}}$ and $\widetilde{\boldsymbol{I}}$, this last being the Voigt representation of the fourth–order identity tensor.

3.4.2 Adaptive time integration

Let the unknowns of the evolution problem – $\boldsymbol{\sigma}$, $\boldsymbol{q}$, $\widetilde{\boldsymbol{D}}$ and $\widetilde{\boldsymbol{G}}$ – be collected into a single vector:

$$\boldsymbol{y} = \left\{ \boldsymbol{\sigma}^T, \boldsymbol{q}^T, \widetilde{\boldsymbol{D}}_{11}^T, \widetilde{\boldsymbol{D}}_{22}^T, \dots \widetilde{\boldsymbol{D}}_{31}^T, \widetilde{\boldsymbol{G}}_{11}^T, \widetilde{\boldsymbol{G}}_{22}^T, \dots, \widetilde{\boldsymbol{G}}_{31}^T \right\}^T \tag{30}$$

in which the stress $\boldsymbol{\sigma}$ and the eventual tensorial internal variables collected in $\boldsymbol{q}$ are represented in Voigt notation as 6–dimensional vectors and the matrices $\widetilde{\boldsymbol{D}}$ and $\widetilde{\boldsymbol{G}}$ are stored columnwise. Then, the ODEs of eqs. (22) and (27) can be recast in the following standard format:

$$\frac{d\boldsymbol{y}}{dT} = \boldsymbol{f}(\boldsymbol{y}) \qquad T \in [0,1] \qquad \boldsymbol{y}\big|_{T=0} = \boldsymbol{y}_0 \tag{31}$$

in which the vector $\boldsymbol{f}$ collects the RHSs of eqs. (22) and (27). Eq. (31) could be integrated by means of different adaptive explicit algorithms with error control, such as Forward Euler with Richardson extrapolation [FO02, FMO09], or various types of embedded Runge–Kutta schemes of different orders [Slo87, TVC00, SAS01]. Here, we discuss in detail the implementation of the second–order adaptive substepping scheme based on the simple Forward Euler method coupled with Richardson extrapolation, first proposed by Fellin and Ostermann [FO02], for its good properties of simplicity, robustness and accuracy.

Let $[T_k, T_{k+1}] \in [0,1]$ a generic substep of size ΔT_{k+1}, and let $\boldsymbol{y}_k$ the known value of $\boldsymbol{y}$ at the beginning of the step. Using the Forward Euler method, the following first approximation to $\boldsymbol{y}_{k+1}$ is obtained:

$$\boldsymbol{v} = \boldsymbol{y}_k + \Delta T_{k+1} \boldsymbol{f}(\boldsymbol{y}_k) \tag{32}$$

A second approximation to $\boldsymbol{y}_{n+1}$ is obtained by applying the Forward Euler method to two steps of size $\Delta T_{k+1}/2$:

$$\boldsymbol{w} = \boldsymbol{y}_k + \frac{\Delta T_{k+1}}{2} \boldsymbol{f}(\boldsymbol{y}_k) + \frac{\Delta T_{k+1}}{2} \boldsymbol{f}\left\{ \boldsymbol{y}_k + \frac{\Delta T_{k+1}}{2} \boldsymbol{f}(\boldsymbol{y}_k) \right\} \tag{33}$$

both $\boldsymbol{v}$ and $\boldsymbol{w}$ are first–order approximations to $\boldsymbol{y}_{k+1}$ but a straightforward Taylor expansion shows that:

$$\boldsymbol{y}_{n+1} = 2\boldsymbol{w} - \boldsymbol{v} + \mathcal{O}(\Delta T_{k+1}^2) \tag{34}$$

i.e., the difference $2\boldsymbol{w} - \boldsymbol{v}$ is a second–order approximation to the local solution.

The norm:

$$EST := \|\boldsymbol{w} - \boldsymbol{v}\|_{\max} \qquad \|\boldsymbol{w} - \boldsymbol{v}\|_{\max} := \max_{i=1,\dots,n_y} \left| \frac{w_i - v_i}{s_i} \right| \tag{35}$$

with s_i a suitable scaling factor, is an asymptotically correct estimate for the local integration error of $\boldsymbol{w}$. Setting the quantity TOL as the user–supplied tolerance, the

comparison between TOL and EST provides an indicator of the accuracy of the numerical integration procedure and an estimate of the optimal substep to be used. In particular:

a) If $EST < TOL$: the substep is accepted, with $\boldsymbol{y}_{k+1}$ given by eq. (34). The next substep size can be increased according to the relation:

$$\Delta T_{k+2} = \Delta T_{k+1} \min \left\{ r_I, \max \left(r_D, 0.9 \sqrt{\frac{TOL}{EST}} \right) \right\} \tag{36}$$

b) If $EST \geq TOL$: the substep is rejected, and the integration step repeated with a smaller substep size given by:

$$\Delta T_{k+1} \leftarrow \Delta T_{k+1} \min \left\{ r_I, \max \left(r_D, 0.9 \sqrt{\frac{TOL}{EST}} \right) \right\} \tag{37}$$

In eqs. (36) and (37), the coefficient 0.9 multiplying the square root of TOL/EST is a "safety factor" accounting from the approximation introduced in the error estimation, while r_I and r_D represent the maximum increase and decrease in the step size allowed. Typically they are set to $r_I = 2.0$ and $r_D = 0.2$.

3.4.3 Drift correction and other computational aspects in explicit integration

When using explicit integration algorithms, the updated state variables $(\boldsymbol{\sigma}_{k+1}, \boldsymbol{q}_{k+1})$ may violate the consistency condition, so that:

$$f_{k+1} = f(\boldsymbol{\sigma}_{k+1}, \boldsymbol{q}_{k+1}) > FTOL$$

with $FTOL$ a prescribed error tolerance for the consistency condition. This situation, which corresponds to a stress state $\boldsymbol{\sigma}_{k+1}$ outside the final yield surface, is commonly known in computational plasticity as *yield surface drift*. The reason for this pathology is that, in explicit methods, the algebraic constraint imposed by eq. $(5)_2$ is linearized, and thus enforced in a weak form. The extent of this violation depends on the accuracy of the integration scheme, so it could be reduced by adopting stringent error tolerances on the adaptive substepping scheme. Nonetheless, in order to prevent error accumulation, it is highly recommendable to implement a drift correction algorithm at the end of each substep, particularly for complex constitutive models.

Different types of drift correction algorithms have been proposed in literature. A detailed discussion on the advantages and drawbacks of some of the more widely used strategies for drift correction, focusing on their application to plasticity models developed for soils, can be found in the works of [PG85, SAS01].

In addition to drift correction, the adoption of explicit integration methods in classical plasticity – where there is a non–smooth transition between elastic and plastic behavior along a predefined stress–path – requires particular attention for those time integration steps which:

a) start from an elastic state and – if elastic response is maintained for the entire step – end outside the current yield surface;

b) start from a plastic state (on the current yield surface) and crosses the yield surface once before ending up on a new plastic state;

c) start from an elastic state and end on another elastic state, crossing the yield surface twice during the path from the initial to the final state.

Situations of type (a) are quite common, particularly when relatively large integration steps are used. Situations of type (b) may occur in presence of relatively small elastic domains – *e.g.*, in models for sands with rotational hardening, where the yield surface is a cone with a small opening. Both these issues have been addressed in [SAS01]. Situations of type (c) may occur when the yield surface is non–convex. While the opportunity of adopting a non–convex yield surface is questionable on both theoretical and experimental grounds, the treatment of this case has been effectively addressed by Pedroso *et al.* [PSS08].

3.5 Implicit Generalized Backward Euler method

Implicit algorithms based on the concepts of operator split and closest point projection return mapping, as discussed for example in [SH87, SG91], have been applied to computational geomechanics in a number of works, among which we mention [BL90, Bor91, ARS92, MWA97, JS97].

The starting point for this approach is the exploitation of the additive structure of the governing equations of the differential–algebraic problem eqs. (2)–(5) to split the update processes into two consecutive steps, as detailed in the following section.

3.5.1 Operator split and product formula algorithm

The constitutive equation of infinitesimal plasticity are amenable to the *elastic–plastic operator split* of the original problem of evolution, into an *elastic predictor* problem and a *plastic corrector* problem, as shown in Tab. 1 [SH87, SH98]. Note that in Tab. 1, exploiting the existence of a free energy function and thus of the elastic constitutive equation (13), the elastic constitutive equation in rate–form has been replaced by the additive split of the strain rate: $\dot{\boldsymbol{\epsilon}}^e = \dot{\boldsymbol{\epsilon}} - \dot{\boldsymbol{\epsilon}}^p$.

Starting from this operator split, a product formula algorithm is constructed as follows. First, the elastic predictor problem is solved and a so–called *trial elastic state* is obtained. Then, the constraints (5) are checked for the trial state, and if they are violated, the trial state is taken as the initial condition for the plastic corrector problem.

3.5.2 Problem 1: elastic predictor

From the physical point of view, the elastic predictor problem can be derived from the original problem of evolution by *freezing* the plastic flow (i.e., setting $\dot{\gamma} = 0$), and taking an incremental *elastic* step which ignores the constraints placed on the stress

	Global	*Elastic predictor*	*Plastic corrector*
Evolution eqs.	$\dot{\boldsymbol{\epsilon}} = \nabla^s(\dot{\boldsymbol{u}})$	$\dot{\boldsymbol{\epsilon}} = \nabla^s(\dot{\boldsymbol{u}})$	$\dot{\boldsymbol{\epsilon}} = \boldsymbol{0}$
	$\dot{\boldsymbol{\epsilon}}^e = \dot{\boldsymbol{\epsilon}} - \dot{\gamma}\dfrac{\partial g}{\partial \boldsymbol{\sigma}}$	$\dot{\boldsymbol{\epsilon}}^e = \dot{\boldsymbol{\epsilon}}$	$\dot{\boldsymbol{\epsilon}}^e = -\dot{\gamma}\dfrac{\partial g}{\partial \boldsymbol{\sigma}}$
	$\dot{\boldsymbol{q}} = \dot{\gamma}\boldsymbol{h}$	$\dot{\boldsymbol{q}} = \boldsymbol{0}$	$\dot{\boldsymbol{q}} = \dot{\gamma}\boldsymbol{h}$
Initial conds.	$\boldsymbol{\epsilon}^e(t_n) = \boldsymbol{\epsilon}^e_n$	$\boldsymbol{\epsilon}^e(t_n) = \boldsymbol{\epsilon}^e_n$	$\boldsymbol{\epsilon}^e\Big\vert_{(\dot{\gamma}=0)} = \boldsymbol{\epsilon}^{e,\mathrm{tr}}_{n+1}$
	$\boldsymbol{q}(t_n) = \boldsymbol{q}_n$	$\boldsymbol{q}(t_n) = \boldsymbol{q}_n$	$\boldsymbol{q}\Big\vert_{(\dot{\gamma}=0)} = \boldsymbol{q}^{\mathrm{tr}}_{n+1}$
Constraints	$f(\boldsymbol{\sigma}, \boldsymbol{q}) \leq 0$ $\dot{\gamma} \geq 0$ $f(\boldsymbol{\sigma}, \boldsymbol{q})\dot{\gamma} = 0$	none	$f(\boldsymbol{\sigma}, \boldsymbol{q}) \leq 0$ $\dot{\gamma} \geq 0$ $f(\boldsymbol{\sigma}, \boldsymbol{q})\dot{\gamma} = 0$

Table 1: Operator split of the evolution problem of infinitesimal plasticity, formulated in terms of strain rates.

state by the yield function. The solution of the predictor stage (*trial state*) in terms of elastic strains is given by the following geometric update:

$$\boldsymbol{\epsilon}^{e,\mathrm{tr}}_{n+1} = \boldsymbol{\epsilon}^e_n + \boldsymbol{\epsilon}_{n+1} - \boldsymbol{\epsilon}_n \tag{38}$$

As for the internal variables, since they do not change during an elastic process, the trivial solution for their trial values is:

$$\boldsymbol{q}^{\mathrm{tr}}_{n+1} = \boldsymbol{q}_n \tag{39}$$

Finally, the trial state of stress is obtained from $\boldsymbol{\epsilon}^{e,\mathrm{tr}}_{n+1}$ by a simple function evaluation:

$$\boldsymbol{\sigma}^{\mathrm{tr}}_{n+1} := \frac{\partial \psi}{\partial \boldsymbol{\epsilon}^e}\left(\boldsymbol{\epsilon}^{e,\mathrm{tr}}_{n+1}\right) \tag{40}$$

At the end of the elastic predictor stage, the trial state is checked for consistency with the yield locus. If:

$$f^{\mathrm{tr}}_{n+1} := f\left(\boldsymbol{\sigma}^{\mathrm{tr}}_{n+1}, \boldsymbol{q}_n\right) \leq 0$$

the trial state satisfies the constraints imposed by the Kuhn–Tucker conditions. The process is then declared *elastic* and the trial state represents the actual final state of the material. If, on the contrary, $f^{\mathrm{tr}}_{n+1} > 0$, the process is declared *plastic*, and consistency is restored by solving the plastic corrector problem.

3.5.3 Problem 2: plastic corrector

If $f_{n+1}^{\mathrm{tr}} > 0$, the trial state lies outside the yield locus, and thus violates the constraints. Consistency is then restored by solving the plastic corrector problem, which takes place at *fixed total strain* ($\dot{\boldsymbol{\epsilon}} = \mathbf{0}$). Since the objective of the plastic corrector stage is to map the trial state back to the yield surface, the algorithms performing such task are commonly referred to as *return mapping algorithms*.

Typically, the plastic corrector problem is solved numerically by integrating the corresponding system of ODEs by an implicit *Backward Euler* scheme, taking the trial state as the new initial condition:

$$\boldsymbol{\epsilon}_{n+1}^{e} = \boldsymbol{\epsilon}_{n+1}^{e,\mathrm{tr}} - \Delta\gamma_{n+1} \left(\frac{\partial g}{\partial \boldsymbol{\sigma}} \right)_{n+1} \tag{41}$$

$$\boldsymbol{q}_{n+1} = \boldsymbol{q}_{n} + \Delta\gamma_{n+1} \boldsymbol{h}_{n+1} \tag{42}$$

As $\Delta\gamma_{n+1} > 0$, the constraints of eq. (5) reduce to:

$$f_{n+1} = f(\boldsymbol{\sigma}_{n+1}, \boldsymbol{q}_{n+1}) = 0 \tag{43}$$

Equations (41)–(43) provide a system of $7 + n_{\mathrm{int}}$ non–linear algebraic equations in the $7 + n_{\mathrm{int}}$ unknowns $\boldsymbol{\epsilon}_{n+1}^{e}$, $\Delta\gamma_{n+1}$, and $\boldsymbol{q}_{n+1}$, which can be solved iteratively by Newton's method, at the Gauss point level.

Let:

$$\boldsymbol{x}_{n+1} := \left\{ \boldsymbol{\epsilon}_{n+1}^{eT} \quad \boldsymbol{q}_{n+1}^{T} \quad \Delta\gamma_{n+1} \right\}^{T} \in \mathbb{R}^{7+n_{\mathrm{int}}} \tag{44}$$

be a vector containing the the unknowns of the problem and

$$\widetilde{\boldsymbol{x}}_{n+1} := \left\{ \boldsymbol{\epsilon}_{n+1}^{eT} \quad \boldsymbol{q}_{n+1}^{T} \right\}^{T} \qquad \text{so that:} \qquad \boldsymbol{x}_{n+1} = \left\{ \widetilde{\boldsymbol{x}}_{n+1}^{T} \quad \Delta\gamma_{n+1} \right\}^{T}$$

The return mapping equations (41)–(43) require the vanishing of the following *residual vector*:

$$\boldsymbol{R}_{n+1}\left(\boldsymbol{x}_{n+1}\right) := \begin{Bmatrix} \boldsymbol{r}_{n+1}^{\epsilon} \\ \boldsymbol{r}_{n+1}^{q} \\ f_{n+1} \end{Bmatrix} := \begin{Bmatrix} -\boldsymbol{\epsilon}_{n+1}^{e} + \boldsymbol{\epsilon}_{n+1}^{e,\mathrm{tr}} - \Delta\gamma_{n+1}\boldsymbol{Q}_{n+1} \\ -\boldsymbol{q}_{n+1} + \boldsymbol{q}_{n+1}^{\mathrm{tr}} + \Delta\gamma_{n+1}\boldsymbol{h}_{n+1} \\ f_{n+1} \end{Bmatrix} = \mathbf{0} \tag{45}$$

where $\boldsymbol{Q}_{n+1} = (\partial g / \partial \boldsymbol{\sigma})_{n+1}$. The steps required for the iterative solution of eq. (45) via Newton's method are outlined in Tab. 2.

A first difficulty in applying the procedure outlined in Tab. 2 is that Step 3 requires the inversion of a $(7 + n_{\mathrm{int}}) \times (7 + n_{\mathrm{int}})$ square matrix. By observing that the last component of the residual vector $\boldsymbol{R}_{n+1}^{(j)}$ does not depend on $\Delta\gamma_{n+1}$, the resulting linearized system of equation can be reduced in size by one via static condensation. However, the inversion of the resulting tangent operator in closed form can still be

1. Initialize:

$$\boldsymbol{\epsilon}^{e}_{n+1} = \boldsymbol{\epsilon}^{e,\mathrm{tr}}_{n+1} \qquad \boldsymbol{q}_{n+1} = \boldsymbol{q}^{\mathrm{tr}}_{n+1} \qquad \Delta\gamma_{n+1} = 0$$

2. Check for convergence:

$$\text{IF: } \left\{ \begin{array}{c} \left\| \boldsymbol{r}^{\epsilon(j)}_{n+1} \right\| < TOL_{\epsilon} \cdot \left\| \boldsymbol{\epsilon}^{e,\mathrm{tr}}_{n+1} \right\| \\ \left\| \boldsymbol{r}^{q(j)}_{n+1} \right\| < TOL_{q} \cdot \left\| \boldsymbol{q}^{\mathrm{tr}}_{n+1} \right\| \\ f^{(j)}_{n+1} < TOL_{f} \end{array} \right\} \text{ THEN exit, ELSE:}$$

3. Find update at local iteration (j):

$$\delta\boldsymbol{x}^{(j)}_{n+1} = -\left[\left(\frac{\partial \boldsymbol{R}}{\partial \boldsymbol{x}} \right)^{(j)}_{n+1} \right]^{-1} \boldsymbol{R}^{(j)}_{n+1}$$

4. Update state variables and plastic multiplier:

$$\boldsymbol{x}^{(j+1)}_{n+1} = \boldsymbol{x}^{(j)}_{n+1} + \delta\boldsymbol{x}^{(j)}_{n+1}$$

5. Set: $j \leftarrow j + 1$, GO TO 2.

Table 2: Iterative solution of the plastic corrector problem.

very difficult, especially in presence of a large number of internal variables (*i.e.*, in the case of anisotropic hardening models). In the most difficult cases, this problem can be solved by resorting to symbolic computation tools (as, *e.g.*, MATHEMATICA) or by numerical methods, as in [TCN02].

Another classical problem in the application of the implicit Backward Euler algorithm to complex, three–invariants plasticity models lies in the need of computing the second gradients of the plastic potential function $\partial^2 g/\partial\boldsymbol{\sigma}\otimes\partial\boldsymbol{\sigma}$ and the derivatives with respect to $\boldsymbol{\sigma}$ and $\boldsymbol{q}$ of the hardening function $\boldsymbol{h}$. In the most complex situations, this task can be performed by resorting to numerical differentiation, as suggested, *e.g.*, in [PFRFH00].

3.5.4 Formulation of the corrector step in principal elastic strain space

A considerable simplification in the application of the implicit Backward Euler algorithm to complex plasticity models can be obtained in the case of isotropic–hardening plasticity, by formulating the return mapping stage in principal elastic strain space. By exploiting the spectral decomposition of the tensors $\boldsymbol{Q}_{n+1}$, $\boldsymbol{\epsilon}^e_{n+1}$ and $\boldsymbol{\epsilon}^{e,\mathrm{tr}}_{n+1}$, eq. (41) transforms into:

$$\sum_{A=1}^{3}\left(\epsilon^e_A\right)_{n+1}\boldsymbol{n}^{(A)}_{n+1}\otimes\boldsymbol{n}^{(A)}_{n+1}=\sum_{A=1}^{3}\left(\epsilon^{e,\mathrm{tr}}_A\right)_{n+1}\boldsymbol{n}^{(A),\mathrm{tr}}_{n+1}\otimes\boldsymbol{n}^{(A),\mathrm{tr}}_{n+1}-\Delta\gamma_{n+1}\sum_{A=1}^{3}\left(\frac{\partial g}{\partial\sigma_A}\right)_{n+1}\boldsymbol{n}^{(A)}_{n+1}\otimes\boldsymbol{n}^{(A)}_{n+1}\tag{46}$$

in which $\boldsymbol{n}^{(A)}_{n+1}$ and $\boldsymbol{n}^{(A),\mathrm{tr}}_{n+1}$ are the A–th unit eigenvectors of $\boldsymbol{\epsilon}^e_{n+1}$ and $\boldsymbol{\epsilon}^{e,\mathrm{tr}}_{n+1}$. Then, it follows at once that:

$$\boldsymbol{n}^{(A)}_{n+1}=\boldsymbol{n}^{(A),\mathrm{tr}}_{n+1}\tag{47}$$

and:

$$\left(\epsilon^e_A\right)_{n+1}=\left(\epsilon^{e,\mathrm{tr}}_A\right)_{n+1}-\Delta\gamma_{n+1}\left(\frac{\partial g}{\partial\sigma_A}\right)_{n+1}\tag{48}$$

for A = 1, 2 or 3. Note that, as the trial elastic strain is known, so are its principal directions. Therefore, the only unknown quantities to be determined remain the three principal elastic strains $(\epsilon^e_A)_{n+1}$, the n_{int} internal variables $\boldsymbol{q}_{n+1}$ and the plastic multiplier $\Delta\gamma_{n+1}$. Introducing for convenience the following vector notation:

$$\widehat{\boldsymbol{\epsilon}}^e:=\begin{Bmatrix}\epsilon^e_1\\ \epsilon^e_2\\ \epsilon^e_3\end{Bmatrix}\qquad\widehat{\boldsymbol{\epsilon}}^{e,\mathrm{tr}}:=\begin{Bmatrix}\epsilon^{e,\mathrm{tr}}_1\\ \epsilon^{e,\mathrm{tr}}_2\\ \epsilon^{e,\mathrm{tr}}_3\end{Bmatrix}\qquad\widehat{\boldsymbol{\sigma}}:=\begin{Bmatrix}\sigma_1\\ \sigma_2\\ \sigma_3\end{Bmatrix}\qquad\widehat{\boldsymbol{Q}}:=\begin{Bmatrix}\partial g/\partial\sigma_1\\ \partial g/\partial\sigma_2\\ \partial g/\partial\sigma_3\end{Bmatrix}\tag{49}$$

the return mapping problem in principal elastic strain space can be recast as follows:

$$\widehat{\boldsymbol{\epsilon}}^{e}_{n+1} = \widehat{\boldsymbol{\epsilon}}^{e,\mathrm{tr}}_{n+1} - \Delta\gamma_{n+1}\widehat{\boldsymbol{Q}}_{n+1} \tag{50a}$$

$$\boldsymbol{q}_{n+1} = \boldsymbol{q}^{\mathrm{tr}}_{n+1} + \Delta\gamma_{n+1}\boldsymbol{h}_{n+1} \tag{50b}$$

$$f_{n+1} := f(\widehat{\boldsymbol{\sigma}}_{n+1}, \boldsymbol{q}_{n+1}) = 0 \tag{50c}$$

The iterative solution of the return mapping equations (50) follows a scheme similar to that in Tab. 2. The number of equations to be solved is now reduced by 3. Moreover, only the evaluation of the (3×3) matrix:

$$\nabla\nabla g = \frac{\partial^2 g}{\partial\hat{\boldsymbol{\sigma}} \otimes \partial\hat{\boldsymbol{\sigma}}} \tag{51}$$

is now required to compute the tangent operator $\partial\boldsymbol{R}/\partial\boldsymbol{x}$.

3.5.5 Consistent tangent stiffness

One of the advantages of the proposed algorithm is the possibility of evaluating the consistent tangent operators *in closed form*, as shown in the following.

In the *global* iteration process, any (infinitesimal) variation in the total strain increment induces, by definition, an equal variation in the trial elastic strain:

$$d\boldsymbol{\epsilon} = d\boldsymbol{\epsilon}^{e,\mathrm{tr}} \tag{52}$$

where the subscript $n+1$ and the superscript (k) have been omitted to ease the notation. Moreover, the return mapping equations associate to each trial elastic strain a well defined elastic strain tensor, obtained as a result of the local iteration process. Therefore, for an infinitesimal variation of $\boldsymbol{\epsilon}^{e,\mathrm{tr}(k)}_{n+1}$ one has:

$$d\boldsymbol{\epsilon}^{e} = \boldsymbol{L}\, d\boldsymbol{\epsilon}^{e,\mathrm{tr}} \tag{53}$$

On the other hand, from the hyperelastic constitutive equation, we have:

$$d\boldsymbol{\sigma} = \left(\frac{\partial^2\psi}{\partial\boldsymbol{\epsilon}^{e} \otimes \partial\boldsymbol{\epsilon}^{e}}\right) d\boldsymbol{\epsilon}^{e} = \boldsymbol{D}^{e}\, d\boldsymbol{\epsilon}^{e} = \boldsymbol{D}^{e}\boldsymbol{L}\, d\boldsymbol{\epsilon}^{e,\mathrm{tr}} = \boldsymbol{\Xi}\, d\boldsymbol{\epsilon}^{e,\mathrm{tr}} \tag{54}$$

By virtue of the definition (18) and of the identity (52), the tensor $\boldsymbol{\Xi}$ is the required consistent tangent stiffness tensor. Differentiation of the return mapping equations (45) yields:

$$\boldsymbol{A}\, d\widetilde{\boldsymbol{x}} = \boldsymbol{T}\, d\boldsymbol{\epsilon}^{e,\mathrm{tr}} - d(\Delta\gamma)\boldsymbol{U} \tag{55}$$

where:

$$d\widetilde{\boldsymbol{x}} := \left\{ d\boldsymbol{\epsilon}^{eT} \quad d\boldsymbol{q}^{T} \right\}^{T} \qquad \boldsymbol{A} := \begin{bmatrix} \boldsymbol{I} + \Delta\gamma\, \boldsymbol{A}_{\sigma}\boldsymbol{D}^{e} & +\Delta\gamma\, \boldsymbol{A}_{q} \\ -\Delta\gamma\boldsymbol{B}_{\sigma}\boldsymbol{D}^{e} & \boldsymbol{I}_{q} - \Delta\gamma\boldsymbol{B}_{q} \end{bmatrix} \tag{56}$$

$$\boldsymbol{T} := \begin{bmatrix} \boldsymbol{I} & \boldsymbol{0}_q^T \end{bmatrix}^T \qquad \boldsymbol{U} := \left\{ \boldsymbol{Q}^T, -\boldsymbol{h}^T \right\}^T \tag{57}$$

$$\boldsymbol{A}_\sigma := \frac{\partial \boldsymbol{Q}}{\partial \boldsymbol{\sigma}} = \frac{\partial^2 g}{\partial \boldsymbol{\sigma} \otimes \partial \boldsymbol{\sigma}} \qquad \boldsymbol{A}_q := \frac{\partial \boldsymbol{Q}}{\partial \boldsymbol{q}} = \frac{\partial^2 g}{\partial \boldsymbol{\sigma} \otimes \partial \boldsymbol{q}} \tag{58}$$

$$\boldsymbol{B}_\sigma := \frac{\partial \boldsymbol{h}}{\partial \boldsymbol{\sigma}} \qquad \boldsymbol{B}_q := \frac{\partial \boldsymbol{h}}{\partial \boldsymbol{q}} \tag{59}$$

and $\boldsymbol{I}_q$ and $\boldsymbol{0}_q$ are the identity matrix in $\mathbb{R}^{n_{\text{int}}}$ and the zero $(n_{\text{int}} \times 6)$ matrix. The variation in the plastic multiplier $d(\Delta\gamma)$ can be evaluated by enforcing the consistency condition $df_{n+1}^{(k)} = 0$. Defining:

$$\boldsymbol{P} := \boldsymbol{D}^e \frac{\partial f}{\partial \boldsymbol{\sigma}} \qquad \boldsymbol{W} := \frac{\partial f}{\partial \boldsymbol{q}} \qquad \boldsymbol{V} := \left\{ \boldsymbol{P}^T, \boldsymbol{W}^T \right\} \tag{60}$$

the consistency condition reads:

$$\boldsymbol{V}\, d\widetilde{\boldsymbol{x}} = 0 \tag{61}$$

Solving eq. (55) for $d\widetilde{\boldsymbol{x}}$, substituting the result in eq. (61) and solving for $d(\Delta\gamma)$, the plastic multiplier increment is obtained as:

$$d(\Delta\gamma) = \frac{1}{\boldsymbol{V} \cdot \left[\boldsymbol{A}^{-1}\right] \boldsymbol{U}}\, \boldsymbol{V} \cdot \left[\boldsymbol{A}^{-1}\right] \boldsymbol{T}\, d\boldsymbol{\epsilon}^{e,\text{tr}} \tag{62}$$

From eqs. (55) and (62) we obtain:

$$\begin{aligned} d\boldsymbol{\sigma} = \boldsymbol{D}^e\, d\boldsymbol{\epsilon}^e &= \boldsymbol{D}^e \boldsymbol{T}^T\, d\widetilde{\boldsymbol{x}} \\ &= \left\{ \boldsymbol{D}^e \boldsymbol{T}^T \left[\boldsymbol{A}^{-1} - \frac{(\boldsymbol{A}^{-1}\boldsymbol{U}) \otimes (\boldsymbol{V}\boldsymbol{A}^{-1})}{(\boldsymbol{V} \cdot \boldsymbol{A}^{-1}\boldsymbol{U})} \right] \boldsymbol{T} \right\} d\boldsymbol{\epsilon}^{e,\text{tr}} \end{aligned} \tag{63}$$

By comparing eq. (63) with (54) the expression for the consistent tangent stiffness tensor follows:

$$\widetilde{\boldsymbol{D}}_{n+1}^{(k)} = \boldsymbol{\Xi}_{n+1}^{(k)} = \boldsymbol{D}^e \boldsymbol{T}^T \left[\boldsymbol{A}^{-1} - \frac{(\boldsymbol{A}^{-1}\boldsymbol{U}) \otimes (\boldsymbol{V}\boldsymbol{A}^{-1})}{(\boldsymbol{V} \cdot \boldsymbol{A}^{-1}\boldsymbol{U})} \right]_{n+1}^{(k)} \boldsymbol{T} \tag{64}$$

Note that the consistent tangent stiffness is, in general, *non symmetric*, even in the case of associative flow rule ($f \equiv g$).

4 Stress–point algorithms for finite deformation multiplicative plasticity

4.1 Evolution equations

The evolution equations of finite deformation multiplicative plasticity for isotropic materials are briefly summarized below, see [OT21] for details. Let the deformation

gradient $\boldsymbol{F}$ be multiplicatively decomposed into an elastic part $\boldsymbol{F}^e$ and a plastic part $\boldsymbol{F}^p$:

$$\boldsymbol{F} = \boldsymbol{F}^e \boldsymbol{F}^p \tag{65}$$

Recalling the expression for the spatial velocity gradient $\boldsymbol{l} = \nabla \boldsymbol{v} = \dot{\boldsymbol{F}} \boldsymbol{F}^{-1}$ and defining accordingly the the *elastic* and *plastic velocity gradients* as:

$$\boldsymbol{l}^e := \dot{\boldsymbol{F}}^e \boldsymbol{F}^{e-1} \qquad \overline{\boldsymbol{L}}^p := \dot{\boldsymbol{F}}^p \boldsymbol{F}^{p-1} \qquad \boldsymbol{l}^p := \boldsymbol{F}^e \overline{\boldsymbol{L}}^p \boldsymbol{F}^{e-1} \tag{66}$$

it is easy to show that:

$$\boldsymbol{l} = \boldsymbol{l}^e + \boldsymbol{l}^p \tag{67}$$

i.e., the multiplicative decomposition of the deformation gradient is consistent with an additive split of the spatial velocity gradient. From the spatial elastic and plastic velocity gradients, $\boldsymbol{l}^e$ and $\boldsymbol{l}^p$, the *elastic* and *plastic rates of deformation* and *spins* can be defined as:

$$\boldsymbol{d}^e := \operatorname{sym}(\boldsymbol{l}^e) \qquad \boldsymbol{w}^e := \operatorname{skw}(\boldsymbol{l}^e) \tag{68}$$

$$\boldsymbol{d}^p := \operatorname{sym}(\boldsymbol{l}^p) \qquad \boldsymbol{w}^p := \operatorname{skw}(\boldsymbol{l}^p) \tag{69}$$

In the following, consistently with the assumption of material isotropy, we will assume that the plastic spin $\boldsymbol{w}^p$ is always equal to zero, and $\boldsymbol{l}^p = \boldsymbol{d}^p$, as in [Sim98].

Then let us assume that the material possesses a *free energy function* per unit reference volume of the form:

$$\psi = \psi(\boldsymbol{b}^e) = \bar{\psi}(\overline{\boldsymbol{C}}^e) = \hat{\psi}(\lambda_1^e, \lambda_2^e, \lambda_3^e) \tag{70}$$

where $\boldsymbol{b}^e$ be the left elastic Cauchy–Green strain tensor, $\overline{\boldsymbol{C}}^e$ is the right elastic Cauchy–Green strain tensor, and λ_A^e, with $A = 1, 2, 3$ are the principal elastic stretches, eigenvalues of $\boldsymbol{F}^e$. The Kirchhoff stress tensor is linked to the elastic strains by the following alternative hyperelastic constitutive equations:

$$\boldsymbol{\tau} = 2 \frac{\partial \psi}{\partial \boldsymbol{b}^e} \boldsymbol{b}^e \qquad \boldsymbol{\tau} = 2\, \boldsymbol{F}^e \frac{\partial \bar{\psi}^e}{\partial \overline{\boldsymbol{C}}^e} \boldsymbol{F}^{eT} \tag{71}$$

To incorporate irreversible behavior, let us assume the existence of an elastic domain:

$$\mathbb{E} := \left\{ (\boldsymbol{\tau}, \boldsymbol{q}) \;\middle|\; f(\boldsymbol{\tau}, \boldsymbol{q}) \leq 0 \right\} \tag{72}$$

defined via a suitable yield function $f(\boldsymbol{\tau}, \boldsymbol{q})$ depending on Kirchhoff stress and a vector $\boldsymbol{q}$ (of dimension n_{int}) of scalar internal variables, accounting for the effects of the previous loading history.

Adopting the left elastic Cauchy–Green tensor $\boldsymbol{b}^e$ and the internal variables $\boldsymbol{q}$ as the main state variables, the problem of evolution of non–associative multiplicative plas-

ticity can be cast in the following form:

$$\dot{\boldsymbol{b}}^e = \boldsymbol{l}\boldsymbol{b}^e + \boldsymbol{b}^e\boldsymbol{l}^T + \mathscr{L}_v[\boldsymbol{b}^e] \tag{73}$$

$$\boldsymbol{d}^p = \dot{\gamma}\frac{\partial g}{\partial \boldsymbol{\tau}} \tag{74}$$

$$\mathscr{L}_v[\boldsymbol{b}^e] = -2\,\mathrm{sym}\,(\boldsymbol{d}^p\boldsymbol{b}^e) = -2\dot{\gamma}\,\frac{\partial g}{\partial \boldsymbol{\tau}}\boldsymbol{b}^e \tag{75}$$

$$\dot{\boldsymbol{q}} = \dot{\gamma}\boldsymbol{h}(\boldsymbol{\tau}, \boldsymbol{q}) \tag{76}$$

where $\mathscr{L}_v[\boldsymbol{b}^e]$ is the Lie derivative of $\boldsymbol{b}^e$, $\dot{\gamma} \geq 0$ is the plastic multiplier, $g(\boldsymbol{\tau}, \boldsymbol{q})$ is the plastic potential and $\boldsymbol{h}$ is the hardening function for the internal variables $\boldsymbol{q}$. Note that the Kirchhoff stress tensor, appearing as an argument of the yield function f and of the plastic potential g, can be considered a derived quantity by virtue of the constitutive equation $(71)_1$.

The yield function f and the plastic multiplier $\dot{\gamma}$ are subjected to the Kuhn–Tucker complementarity conditions:

$$\dot{\gamma} \geq 0 \qquad\qquad f(\boldsymbol{\tau}, \boldsymbol{q}) \leq 0 \qquad\qquad \dot{\gamma} f(\boldsymbol{\tau}, \boldsymbol{q}) = 0 \tag{77}$$

as well as to the consistency condition:

$$\dot{\gamma}\dot{f} = \dot{\gamma}\left(\frac{\partial f}{\partial \boldsymbol{\tau}} \cdot \dot{\boldsymbol{\tau}} + \frac{\partial f}{\partial \boldsymbol{q}} \cdot \dot{\boldsymbol{q}}\right) = 0 \tag{78}$$

requiring that the state of the material remains on the yield surface ($f = 0$) whenever plastic loading occurs ($\dot{\gamma} > 0$).

Eq. (73) shows that the rate of change of the elastic left Cauchy–green tensor is the sum of two contributions, the second of which – the Lie derivative of $\boldsymbol{b}^e$ – is associated to the development of plastic deformations. Eq. (74) is the non–associative flow rule for the plastic rate of deformation $\boldsymbol{d}^p$, while eq. (75) provides the link between $\boldsymbol{d}^e$ and the Lie derivative of $\boldsymbol{b}^e$. The evolution equation for the internal variables $\boldsymbol{q}$ is provided by the non–associative hardening law (76).

Differentiating the hyperelastic constitutive equation $(66)_2$ and taking into account that:

$$\boldsymbol{d} = \boldsymbol{d}^e + \boldsymbol{d}^p \qquad \boldsymbol{d}^e = \boldsymbol{F}^{e-T}\left(\frac{1}{2}\dot{\overline{\boldsymbol{C}}}^e\right)\boldsymbol{F}^{e-1} \qquad \boldsymbol{w}^e = \boldsymbol{w} - \boldsymbol{w}^p = \boldsymbol{w}$$

the following expression for the Jaumann rate of Kirchhoff stress is obtained:

$$\overset{\nabla}{\boldsymbol{\tau}} = \mathbb{a}^e\,(\boldsymbol{d} - \boldsymbol{d}^p) = \mathbb{a}^e\left(\boldsymbol{d} - \dot{\gamma}\frac{\partial f}{\partial \boldsymbol{\tau}}\right) \tag{79}$$

where:

$$\mathbb{a}^e_{ijkl} = \mathbb{c}^e_{ijkl} + \tau_{ik}\delta_{jl} + \tau_{il}\delta_{jk} \tag{80}$$

and:

$$\mathbb{c}^e_{ijkl} = \mathbb{C}^e_{ABCD} F^e_{iA} F^e_{jB} F^e_{kC} F^e_{lD} \qquad \mathbb{C}^e_{ABCD} = 4\,\frac{\partial^2 \bar{\psi}^e}{\partial \overline{C}_{AB} \partial \overline{C}_{CD}} \tag{81}$$

Substituting eqs. (76) and (79) in eq. (78) – after noting that

$$\frac{\partial f}{\partial \boldsymbol{\tau}} \cdot \dot{\boldsymbol{\tau}} = \frac{\partial f}{\partial \boldsymbol{\tau}} \cdot \overset{\nabla}{\boldsymbol{\tau}}$$

since, by isotropy, $\boldsymbol{\tau}$ and $\partial f / \partial \boldsymbol{\tau}$ commute – and solving for the plastic multiplier, the following expression for $\dot{\gamma}$ is obtained:

$$\dot{\gamma} = \frac{1}{\widehat{K}_p} \left\langle \frac{\partial f}{\partial \boldsymbol{\tau}} \cdot \mathbf{a}^e \boldsymbol{d} \right\rangle \tag{82}$$

in which:

$$\widehat{K}_p := \frac{\partial f}{\partial \boldsymbol{\tau}} \cdot \mathbf{a}^e \frac{\partial g}{\partial \boldsymbol{\tau}} - \frac{\partial f}{\partial \boldsymbol{q}} \cdot \boldsymbol{h} > 0 \tag{83}$$

The elastoplastic constitutive equation in rate–form then reads

$$\overset{\nabla}{\boldsymbol{\tau}} = \mathbf{a}^{ep} \boldsymbol{d} \qquad \mathbf{a}^{ep} = \mathbf{a}^e - \frac{\mathscr{H}(\dot{\gamma})}{\widehat{K}_p} \left(\mathbf{a}^e \frac{\partial g}{\partial \boldsymbol{\tau}} \right) \otimes \left(\mathbf{a}^e \frac{\partial f}{\partial \boldsymbol{\tau}} \right) \tag{84}$$

where $\mathbf{a}^{ep}$ is the elastoplastic continuum tangent stiffness of the material and $\mathscr{H}(x)$ is the Heaviside step function, equal to one if $x > 0$ and zero otherwise.

4.2 State update

Let $\mathbb{I} = \bigcup_{n=0}^{N} [t_n, t_{n+1}]$ be a partition of the time interval of interest into time steps. It is assumed that at time $t_n \in \mathbb{I}$ the state of the material $(\boldsymbol{b}^e_n, \boldsymbol{q}_n)$ is known at any quadrature point in the adopted finite element discretization. Also, let:

$$\{\boldsymbol{F}_i : i = 0, 1, \ldots, n+1\}$$

be the prescribed history of $\boldsymbol{F}$ up to time t_{n+1}. The computational problem to be addressed is the update of the state variables:

$$\boldsymbol{b}^{e(k)}_{n+1} \to \widehat{\boldsymbol{b}}^e \left(\boldsymbol{F}^{(k)}_{n+1}; \boldsymbol{b}^e_n, \boldsymbol{q}_n \right) \tag{85}$$

$$\boldsymbol{q}^{(k)}_{n+1} \to \widehat{\boldsymbol{q}} \left(\boldsymbol{F}^{(k)}_{n+1}; \boldsymbol{b}^e_n, \boldsymbol{q}_n \right) \tag{86}$$

for a *given* deformation gradient $\boldsymbol{F}^{(k)}_{n+1}$, through the integration of the system of ODEs (73)–(77) provided by the elastoplastic constitutive equations. Note that the evolution problem defined by (73)–(77) belongs to the category of the so–called *stiff differential–algebraic systems* due to the algebraic constraints of eqs. (77) – see [HW91] for details. At the end of the update process, the Kirchhoff stress tensor $\boldsymbol{\tau}_{n+1}$ at time t_{n+1} can be evaluated from $\boldsymbol{b}^e_{n+1}$ by means of the hyperelastic constitutive equation $(71)_1$.

4.3 Consistent linearization of the stress update algorithm

In a standard finite element context, the starting point for the solution of a static equilibrium problem is the weak form of the balance of momentum equation, which, for the problem at hand, is stated as follows. Find the unknown deformation $\boldsymbol{\varphi}_{n+1} = \boldsymbol{X} + \boldsymbol{u}_{n+1}$ such that, for any test function (variation) $\boldsymbol{\eta}$ satisfying homogeneous boundary conditions on the appropriate part of the boundary, the following non–linear functional equation is satisfied:

$$\mathscr{G}(\boldsymbol{\varphi}_{n+1}, \boldsymbol{\eta}) = \mathscr{G}^{\text{int}}(\boldsymbol{\varphi}_{n+1}, \boldsymbol{\eta}) - \mathscr{G}^{\text{ext}}_{n+1} = \int_{\mathcal{B}} \boldsymbol{\tau}(\boldsymbol{\varphi}_{n+1}) \cdot (\nabla \boldsymbol{\eta})\, dV - \mathscr{G}^{\text{ext}}_{n+1} = 0 \quad (87)$$

The iterative solution via Newton's method of the non–linear algebraic problem resulting after the introduction of a standard finite element discretization, requires the linearization of the non–linear functional $\mathscr{G}$ with respect to the independent field $\boldsymbol{\varphi}_{n+1}$ in the direction $\delta\boldsymbol{u}$:

$$D_u \mathscr{G}^{\text{int}}(\boldsymbol{\varphi}^{(k)}_{n+1}, \boldsymbol{\eta})[\delta\boldsymbol{u}] = \int_{\mathcal{B}} \left\{ \nabla^s \boldsymbol{\eta} \cdot (\widetilde{\mathfrak{c}})^{(k)}_{n+1}\, \nabla^s \delta\boldsymbol{u} \right\} dV + \int_{\mathcal{B}} \left\{ \boldsymbol{\tau}^{(k)}_{n+1} \cdot (\nabla \delta\boldsymbol{u})^T (\nabla \boldsymbol{\eta}) \right\} dV \quad (88)$$

in which:

$$\widetilde{\mathfrak{c}}_{ijkl} = \widetilde{\mathbb{C}}_{ABCD} F^e_{iA} F^e_{jB} F^e_{kC} F^e_{lD} \quad (89)$$

and:

$$\widetilde{\mathbb{C}}^{(k)}_{n+1} = \left(2 \frac{\partial \boldsymbol{S}}{\partial \boldsymbol{C}} \right)^{(k)}_{n+1} \qquad \text{with} \qquad \boldsymbol{S} := \boldsymbol{F}^{-1} \boldsymbol{\tau} \boldsymbol{F}^{-T} \qquad \boldsymbol{C} := \boldsymbol{F}^T \boldsymbol{F} \quad (90)$$

In eq. (88), the fourth–order tensor $\widetilde{\mathfrak{c}}$ is the so–called *spatial algorithmic tangent stiffness tensor*, obtained from the *material algorithmic tangent stiffness tensor* $\widetilde{\mathbb{C}}$ by the pull–back operation (89). This last quantity represents the variation of the updated second Piola–Kirchhoff stress tensor $\boldsymbol{S}^{(k)}_{n+1}$ associated to the infinitesimal change of the right Cauchy–Green deformation tensor $\boldsymbol{C}^{(k)}_{n+1}$ induced by the infinitesimal perturbation of the deformation field $\delta\boldsymbol{u}$. As such, the tensor $\widetilde{\mathbb{C}}^{(k)}_{n+1}$ is strongly dependent on the adopted integration algorithm [ST85]. Its accurate evaluation is crucial to achieve the quadratic convergence when using Newton–Raphson method to solve iteratively the global discrete equilibrium equations.

4.4 IMPLEX algorithm

In finite–deformation plasticity, explicit methods have not been so widely used as in infinitesimal plasticity. Notable exceptions are represented by the works of refs. [SO85, RFPH97, BRB16]. More recently, Monforte *et al.* [MCC$^+$19] extended the

IMPLicit–EXplicit (IMPLEX) algorithm proposed by Oliver *et al.* [OHC08] to increase the robustness and efficiency of classical fully–implicit return mapping algorithms to finite deformations. Applications of the IMPLEX method to computational geomechanics problems are reported in [MCC$^+$19, MGA$^+$21, OCT21, HS21].

The basic structure of the IMPLEX algorithm consists in a two–step solver:

1. *Extrapolation step*: the boundary–value problem is computed using an extrapolated value of the plastic multiplier increment.
2. *Correction step*: the final converged state is computed at each integration point using the displacement field obtained in Step 1. The resulting final plastic multiplier is then used for the next extrapolation step.

In a typical time step $[t_n, t_n + 1] \in \mathbb{I}$, the extrapolation step updates the state variables to their so–called IMPLEX values:

$$(\tilde{\boldsymbol{b}}^e_{n+1}, \tilde{\boldsymbol{q}}_{n+1})$$

obtained through explicit integration of the evolution equations by assuming a constant plastic multiplier increment:

$$\widetilde{\Delta\gamma}_{n+1} = \frac{\Delta t_{n+1}}{\Delta t_n}\,\Delta\gamma_n$$

To obtain an explicit update for $\boldsymbol{b}^e$, we observe that eq. $(66)_2$ provides an evolution equation for $\boldsymbol{F}^p$ in the form:

$$\dot{\boldsymbol{F}}^p = \overline{\boldsymbol{L}}^p \boldsymbol{F}^p = \left\{ \boldsymbol{F}^{e-1} \left(\dot{\gamma} \frac{\partial g}{\partial \boldsymbol{\tau}} \right) \boldsymbol{F}^e \right\} \boldsymbol{F}^p \tag{91}$$

By adopting an explicit exponential mapping to integrate the evolution equation (91) we have:

$$\boldsymbol{F}^p_{n+1} = \exp\left\{ \Delta\gamma_{n+1} \boldsymbol{F}^{e-1}_n \left(\frac{\partial g}{\partial \boldsymbol{\tau}} \right)_n \boldsymbol{F}^e_n \right\} \boldsymbol{F}^p_n \tag{92}$$

from which, replacing $\Delta\gamma_{n+1}$ with the *known* extrapolated plastic multiplier $\widetilde{\Delta\gamma}_{n+1}$, we finally obtain, after some algebra:

$$\tilde{\boldsymbol{b}}^e_{n+1} = \boldsymbol{f}_{n+1} \exp\left\{ -\widetilde{\Delta\gamma}_{n+1} \left(\frac{\partial g}{\partial \boldsymbol{\tau}} \right)_n \right\} \boldsymbol{b}^e_n \exp\left\{ -\widetilde{\Delta\gamma}_{n+1} \left(\frac{\partial g}{\partial \boldsymbol{\tau}} \right)_n \right\}^T \boldsymbol{f}^T_{n+1} \tag{93}$$

where $\boldsymbol{f}_{n+1} = \boldsymbol{F}_{n+1} \boldsymbol{F}^{-1}_n = \boldsymbol{1} + \nabla_n \boldsymbol{u}_{n+1}$ is the relative deformation gradient. The details of the derivation of eq. (93) are provided, for example, in [OCT21]. Using the elastic constitutive equation $(71)_1$, the derived Kirchhoff stress $\tilde{\boldsymbol{\tau}}_{n+1} = \boldsymbol{\tau}(\tilde{\boldsymbol{b}}^e_{n+1})$ is then obtained. Analogously, from the evolution equations (76), the following IMPLEX values for the internal variables are obtained:

$$\tilde{\boldsymbol{q}}_{n+1} = \boldsymbol{q}_n + \widetilde{\Delta\gamma}_{n+1} \boldsymbol{h}_n \tag{94}$$

According to eq. (94), the IMPLEX internal state variables depend only on known quantities, while $\tilde{\boldsymbol{b}}^e_{n+1}$ and $\tilde{\boldsymbol{\tau}}_{n+1}$ depend also on the unknown displacement field at the end of the step, $\boldsymbol{u}_{n+1}$. This field is determined by solving the global discretized equilibrium equations. In solving the global equilibrium problem, the global stiffness matrix coming from the linearization of the internal force vector can be computed using the elastic tangent stiffness tensor of eq. (81), since the plastic flow is independent of the displacement field.

Once the extrapolation step is completed, the correction step is performed at constant spatial configuration (*i.e.*, constant $\boldsymbol{u}_{n+1}$) to determine more accurate values of the state variables at the end of the step ($\boldsymbol{b}^e_{n+1}, \boldsymbol{q}_{n+1}$). In the original IMPLEX method [OCW$^+$07] this step is carried out by implicit numerical integration of the evolution equations. In the method proposed by [MCC$^+$19], an explicit adaptive scheme with substepping and error control is adopted to update the left elastic Cauchy–Green tensor and the internal variables. For a typical substep $[t_k, t_{k+1}] \in [t_n, t_{n+1}]$ we thus have:

$$\boldsymbol{b}^e_{k+1} = \boldsymbol{f}_{k+1} \exp\left\{-\Delta\gamma_{k+1}\left(\frac{\partial g}{\partial \boldsymbol{\tau}}\right)_k\right\} \boldsymbol{b}^e_k \exp\left\{-\Delta\gamma_{k+1}\left(\frac{\partial g}{\partial \boldsymbol{\tau}}\right)_k\right\}^T \boldsymbol{f}^T_{k+1} \quad (95)$$

and:

$$\boldsymbol{q}_{k+1} = \boldsymbol{q}_k + \Delta\gamma_{k+1}\boldsymbol{h}_k \quad (96)$$

The plastic multiplier appearing in the above equations is provided by the explicit integration of eq. (82):

$$\Delta\gamma_{k+1} = \Delta t_{k+1}\dot{\gamma}_k = \frac{1}{(\widehat{K}_p)_k}\left(\frac{\partial f}{\partial \boldsymbol{\tau}}\right)_k \cdot \mathfrak{a}^e_k \nabla^s_k\left(\Delta \boldsymbol{u}_{k+1}\right) \quad (97)$$

where $\nabla^s_k\left(\Delta \boldsymbol{u}_{k+1}\right)$ is the symmetric part of the spatial gradient of the displacement increment within the substep. The final value of the plastic multiplier at the end of the step ($t = t_{n+1}$) is then used for the extrapolation stage of the next computational step.

4.5 Implicit Generalized Backward Euler method

Until the beginning of the '80, computational methods for finite deformation elastoplasticity relied on models based on the additive decomposition of the rate of deformation tensor, see [OT21] in this volume. Therefore, they remained restricted to small elastic strains. Early works on computational applications of finite deformation plasticity models based on the multiplicative decomposition of the deformation gradient are presented, *e.g.*, in [AD79, SO85, Sim85]. For the case of isotropic plasticity, a very important contribution has been given by the work of Simo [Sim92] where he advocated the use of principal elastic logarithmic strains as primary state variables, in connection to an hyperelastic characterization of the elastic behavior of the material, to formulate an implicit Backward Euler elastic predictor–plastic corrector algorithm with the same structure of the corresponding integration scheme of infinitesimal plasticity. Applications of this approach to computational geomechanics are reported in

	Global	*Elastic predictor*	*Plastic corrector*
Evol. eqs.	$\dot{\boldsymbol{f}} = \boldsymbol{l}\boldsymbol{f}$ $\dot{\boldsymbol{b}}^e = \boldsymbol{l}\boldsymbol{b}^e + \boldsymbol{b}^e\boldsymbol{l}^T - 2\dot{\gamma}\,\dfrac{\partial g}{\partial \boldsymbol{\tau}}\boldsymbol{b}^e$ $\dot{\boldsymbol{q}} = \dot{\gamma}\boldsymbol{h}$	$\dot{\boldsymbol{f}} = \boldsymbol{l}\boldsymbol{f}$ $\dot{\boldsymbol{b}}^e = \boldsymbol{l}\boldsymbol{b}^e + \boldsymbol{b}^e\boldsymbol{l}^T$ $\dot{\boldsymbol{q}} = \boldsymbol{0}$	$\dot{\boldsymbol{f}} = \boldsymbol{0}$ $\dot{\boldsymbol{b}}^e = -2\dot{\gamma}\,\dfrac{\partial g}{\partial \boldsymbol{\tau}}\boldsymbol{b}^e$ $\dot{\boldsymbol{q}} = \dot{\gamma}\boldsymbol{h}$
Init. conds.	$\boldsymbol{b}^e(t_n) = \boldsymbol{b}^e_n$ $\boldsymbol{q}(t_n) = \boldsymbol{q}_n$	$\boldsymbol{b}^e(t_n) = \boldsymbol{b}^e_n$ $\boldsymbol{q}(t_n) = \boldsymbol{q}_n$	$\boldsymbol{b}^e\Big\vert_{(\dot{\gamma}=0)} = \boldsymbol{b}^{e,\mathrm{tr}}_{n+1}$ $\boldsymbol{q}\Big\vert_{(\dot{\gamma}=0)} = \boldsymbol{q}^{\mathrm{tr}}_{n+1}$
Constr.	$f(\boldsymbol{\tau},\boldsymbol{q}) \le 0$ $\dot{\gamma} \ge 0$ $f(\boldsymbol{\tau},\boldsymbol{q})\dot{\gamma} = 0$	none	$f(\boldsymbol{\tau},\boldsymbol{q}) \le 0$ $\dot{\gamma} \ge 0$ $f(\boldsymbol{\tau},\boldsymbol{q})\dot{\gamma} = 0$

Table 3: Operator split of the evolution problem of multiplicative plasticity, formulated in terms of elastic deformation rates.

the works of [SM93, BT98, CAS98, SSS02, OT20]. In the remainder of this section, we focus on this class of stress–point algorithms following closely the work of [OT20].

4.5.1 Operator split and product formula algorithm

For the implicit numerical integration of the evolution equations (73)–(77), we proceed as in the case of infinitesimal plasticity by adopting the *operator split* shown in Tab. 3, suggested by the additive structure of the evolution problem.

Again, computational strategy is to solve the elastic predictor problem first, with initial conditions provided by $(\boldsymbol{b}^e_n, \boldsymbol{q}_n)$, obtaining the so–called *trial solution* $(\boldsymbol{b}^{e,\mathrm{tr}}_{n+1}, \boldsymbol{q}^{\mathrm{tr}}_{n+1})$. Then, if the constraints posed by the complementarity conditions are violated, solve the plastic corrector problem using the trial solution as initial conditions. The attractiveness of this strategy stands in the geometric interpretation which can be given to each Problem, as detailed below.

4.5.2 Problem 1: elastic predictor

The evolution equations of the elastic predictor problem are obtained from the original problem by assuming that no dissipative processes take place ($\dot{\gamma} = 0$) and ignoring the constraint placed on the state variables by the yield function.

From a geometric point of view, during the elastic predictor stage, the update of the current configuration from $\mathcal{S}_n$ to $\mathcal{S}_{n+1}$ takes place at fixed intermediate configuration (modulo a rigid body rotation), with $\boldsymbol{F}^{p,\mathrm{tr}}_{n+1} = \boldsymbol{F}^{p}_{n}$. Thus we have:

$$\boldsymbol{F}_{n+1} = \boldsymbol{f}_{n+1}\boldsymbol{F}_n = \boldsymbol{F}^{e,\mathrm{tr}}_{n+1}\boldsymbol{F}^{p}_{n} \qquad \Rightarrow \qquad \boldsymbol{F}^{e,\mathrm{tr}}_{n+1} = \boldsymbol{f}_{n+1}\boldsymbol{F}^{e}_{n} \tag{98}$$

From this last result and the (trivial) evolution equation for $\boldsymbol{q}$ of the elastic predictor problem (see Tab. 3), the complete trial state is obtained:

$$\boldsymbol{b}^{e,\mathrm{tr}}_{n+1} = \boldsymbol{f}_{n+1}\boldsymbol{b}^{e}_{n}\boldsymbol{f}^{T}_{n+1} \qquad\qquad \boldsymbol{q}^{\mathrm{tr}}_{n+1} = \boldsymbol{q}_n \tag{99}$$

Then, the trial Kirchhoff stress is evaluated via the hyperelastic constitutive equation $(71)_1$ as $\boldsymbol{\tau}^{\mathrm{tr}}_{n+1} = \boldsymbol{\tau}(\boldsymbol{b}^{e,\mathrm{tr}}_{n+1})$.

It is worth noting that, due to its formulation in terms of kinematics, the elastic predictor problem can be solved exactly. The trial value of $\boldsymbol{b}^e$ at the end of the step is just the geometric update (actually, the push–forward) of $\boldsymbol{b}^e_n$ to the current configuration $\mathcal{S}_{n+1}$ via the relative deformation gradient.

4.5.3 Problem 2: plastic corrector

If the trial state satisfies the constraint posed by the Kuhn–Tucker conditions, *i.e.*:

$$f^{\mathrm{tr}}_{n+1} := f\left(\boldsymbol{b}^{e,\mathrm{tr}}_{n+1}, \boldsymbol{q}^{\mathrm{tr}}_{n+1}\right) \leq 0$$

then the trial state provides the exact update of the material state sought after. Otherwise, the intermediate configuration needs to be modified in order to restore the consistency with the yield surface:

$$f_{n+1} = f\left(\boldsymbol{b}^{e}_{n+1}, \boldsymbol{q}_{n+1}\right) = 0 \tag{100}$$

where $\boldsymbol{b}^e_{n+1}$ and $\boldsymbol{q}_{n+1}$ are the solution of the differential–algebraic plastic corrector problem. Since $\dot{\boldsymbol{f}} = \boldsymbol{0}$ in this case, the plastic corrector problem is formulated on a fixed current configuration $\mathcal{S}_{n+1}$.

The numerical solution of the plastic corrector problem is typically obtained by adopting an implicit strategy such as the Backward Euler method. In particular, the structure of the evolution equation for $\boldsymbol{b}^e$ suggest the use of the following exponential approximation, see [Sim92]:

$$\boldsymbol{b}^{e}_{n+1} = \exp\left\{-2\Delta\gamma_{n+1}\left(\frac{\partial g}{\partial \boldsymbol{\tau}}\right)_{n+1}\right\}\boldsymbol{b}^{e,\mathrm{tr}}_{n+1} \tag{101}$$

where $\Delta\gamma_{n+1}$ is the increment of the plastic multiplier associated to the plastic deformations, to be determined as part of the solution.

Finally, using the Backward Euler algorithm to integrate the evolution equation for $\boldsymbol{q}$, we obtain:

$$\boldsymbol{q}_{n+1} = \boldsymbol{q}^{\mathrm{tr}}_{n+1} + \Delta\gamma_{n+1}\boldsymbol{h}_{n+1} = \boldsymbol{q}_n + \Delta\gamma_{n+1}\boldsymbol{h}_{n+1} \tag{102}$$

In principle, the system of $(6 + n_{\text{int}} + 1)$ non–linear algebraic equations (101) and (102) can be solved to provide the unknowns $\boldsymbol{b}^e_{n+1}$, $\boldsymbol{q}_{n+1}$ and $\Delta\gamma_{n+1}$. However, as first shown by Simo [Sim92], the solution of the plastic corrector problem can be significantly simplified by exploiting the isotropy of the material response, as shown in the following.

4.5.4 Plastic corrector problem in principal logarithmic elastic strains space

Due to the assumption of material isotropy, the tensor $(\partial g/\partial \boldsymbol{\tau})_{n+1}$ has the same principal directions of $\boldsymbol{\tau}$ and hence of $\boldsymbol{b}^e_{n+1}$, due to eqs. (70) and $(71)_1$. Therefore, the spectral decomposition of the tensors $\boldsymbol{b}^e_{n+1}$, $(\partial g/\partial \boldsymbol{\tau})_{n+1}$ and $\boldsymbol{b}^{e,\text{tr}}_{n+1}$ appearing in eq. (101) read:

$$\boldsymbol{b}^e_{n+1} = \sum_{A=1}^{3} \left(\lambda^e_{A,n+1}\right)^2 \boldsymbol{n}^{(A)}_{n+1} \otimes \boldsymbol{n}^{(A)}_{n+1} \tag{103a}$$

$$\left(\frac{\partial g}{\partial \boldsymbol{\tau}}\right)_{n+1} = \sum_{A=1}^{3} \left(\frac{\partial g}{\partial \tau_A}\right)_{n+1} \boldsymbol{n}^{(A)}_{n+1} \otimes \boldsymbol{n}^{(A)}_{n+1} \tag{103b}$$

$$\boldsymbol{b}^{e,\text{tr}}_{n+1} = \sum_{A=1}^{3} \left(\lambda^{e,\text{tr}}_{A,n+1}\right)^2 \boldsymbol{n}^{(A),\text{tr}}_{n+1} \otimes \boldsymbol{n}^{(A),\text{tr}}_{n+1} \tag{103c}$$

where the quantities $\lambda^{e,\text{tr}}_A$ and $\boldsymbol{n}^{(A),\text{tr}}$ denote the trial principal elastic stretches (eigenvalues of $\boldsymbol{F}^{e,\text{tr}}$) and the unit eigenvectors of $\boldsymbol{b}^{e,\text{tr}}$, respectively, while the scalars $\partial g/\partial \tau_A$ are the derivatives of the plastic potential functions with respect to the principal values of $\boldsymbol{\tau}$.

Rewriting eq. (101) as:

$$\exp\left\{2\Delta\gamma_{n+1}\left(\frac{\partial g}{\partial \boldsymbol{\tau}}\right)_{n+1}\right\} \boldsymbol{b}^e_{n+1} = \boldsymbol{b}^{e,\text{tr}}_{n+1} \tag{104}$$

and incorporating the spectral decompositions (103), it easy to show that:

a) the principal directions of $\boldsymbol{b}^e_{n+1}$ coincide with the (known) principal directions of $\boldsymbol{b}^{e,\text{tr}}_{n+1}$:

$$\boldsymbol{n}^{(A)}_{n+1} = \boldsymbol{n}^{(A),\text{tr}}_{n+1} \qquad (A = 1, 2, 3) \tag{105}$$

b) the principal values of the three tensors $\boldsymbol{b}^e_{n+1}$, $(\partial g/\partial \boldsymbol{\tau})_{n+1}$ and $\boldsymbol{b}^{e,\text{tr}}_{n+1}$ are related by the following equations:

$$\left(\lambda^e_{A,n+1}\right)^2 = \exp\left\{-2\Delta\gamma_{n+1}\left(\frac{\partial g}{\partial \tau_A}\right)_{n+1}\right\} \left(\lambda^{e,\text{tr}}_{A,n+1}\right)^2 \tag{106}$$

with A = 1, 2, 3.

The result in eq. (106) is particularly relevant since, taking the natural logarithm of both sides, we obtain:

$$\varepsilon^e_{A,n+1} = \varepsilon^{e,\mathrm{tr}}_{A,n+1} - \Delta\gamma_{n+1}\left(\frac{\partial g}{\partial \tau_A}\right)_{n+1} \tag{107}$$

where:

$$\varepsilon^{e,\mathrm{tr}}_{A,n+1} := \ln(\lambda^{e,\mathrm{tr}}_{A,n+1}) \qquad\qquad \varepsilon^{e}_{A,n+1} := \ln(\lambda_{A,n+1})$$

Introducing the following vector notation:

$$\hat{\boldsymbol{\varepsilon}}^{e,\mathrm{tr}} := \begin{Bmatrix} \varepsilon^{e,\mathrm{tr}}_1 \\ \varepsilon^{e,\mathrm{tr}}_2 \\ \varepsilon^{e,\mathrm{tr}}_3 \end{Bmatrix} \qquad \hat{\boldsymbol{\varepsilon}}^{e} := \begin{Bmatrix} \varepsilon^{e}_1 \\ \varepsilon^{e}_2 \\ \varepsilon^{e}_3 \end{Bmatrix} \qquad \hat{\boldsymbol{Q}} := \begin{Bmatrix} \partial g/\partial \tau_1 \\ \partial g/\partial \tau_2 \\ \partial g/\partial \tau_3 \end{Bmatrix}$$

The system of algebraic equations governing the return mapping problem formulated in principal logarithmic elastic strains space takes the following form:

$$\hat{\boldsymbol{\varepsilon}}^{e}_{n+1} = \hat{\boldsymbol{\varepsilon}}^{e,\mathrm{tr}}_{n+1} - \Delta\gamma_{n+1}\hat{\boldsymbol{Q}}_{n+1} \tag{108a}$$

$$\boldsymbol{q}_{n+1} = \boldsymbol{q}_n + \Delta\gamma_{n+1}\boldsymbol{h}_{n+1} \tag{108b}$$

$$f_{n+1} = f\left(\boldsymbol{b}^e_{n+1}, \boldsymbol{q}_{n+1}\right) = 0 \tag{108c}$$

This set of (3+n_{int}+1) non–linear algebraic equations can be solved using Newton's method to obtain the updated state at the end of the step and the plastic multiplier increment, as shown in Tab. 4.

As noted by [Sim92], the use of the exponential algorithm in connection with the choice of formulating the plastic corrector problem in principal logarithmic elastic strain space leads to an algebraic system of equations which are formally similar to the Generalized Backward Euler algorithm of infinitesimal plasticity, see eqs. (50).

4.5.5 Consistent tangent stiffness

By differentiating the expression for $\boldsymbol{\tau}_{n+1}$ provided by the spectral decomposition of Tab. 4, the following expression for the spatial consistent tangent stiffness tensor $\widetilde{\mathfrak{C}}$ of eq. (89) is obtained (see [Sim98]):

$$\widetilde{\mathfrak{C}} = \sum_{A=1}^{3}\sum_{B=1}^{3} \hat{d}_{AB}\, \boldsymbol{m}^A \otimes \boldsymbol{m}^B - \sum_{A=1}^{3} 2\tau_A\, \boldsymbol{m}^A \\ + \sum_{A\neq B} \left\{ \frac{\tau_A(\lambda^{e,\mathrm{tr}}_B)^2 - \tau_B(\lambda^{e,\mathrm{tr}}_A)^2}{(\lambda^{e,\mathrm{tr}}_A)^2 - (\lambda^{e,\mathrm{tr}}_B)^2} \right\} \boldsymbol{M}^{AB} \tag{109}$$

1. Determine the trial principal elastic stretches $\lambda_{A,n+1}^{e,\mathrm{tr}}$ and the principal eigenvectors $\boldsymbol{n}_{n+1}^{(A),\mathrm{tr}}$ via the spectral decomposition of $\boldsymbol{b}_{n+1}^{e,\mathrm{tr}}$.
2. Set:
$$\boldsymbol{n}_{n+1}^{(A)} = \boldsymbol{n}_{n+1}^{(A),\mathrm{tr}}$$
for A = 1, 2, 3.
3. Solve the system of nonlinear algebraic equations:
$$\begin{aligned}\boldsymbol{R}_{\varepsilon} &:= -\hat{\boldsymbol{\varepsilon}}_{n+1}^{e} + \hat{\boldsymbol{\varepsilon}}_{n+1}^{e,\mathrm{tr}} - \Delta\gamma_{n+1}\hat{\boldsymbol{Q}}_{n+1} = \boldsymbol{0}\\ \boldsymbol{R}_{q} &:= -\boldsymbol{q}_{n+1} + \boldsymbol{q}_{n} + \Delta\gamma_{n+1}\boldsymbol{h}_{n+1} = \boldsymbol{0}\\ R_{f} &:= -f\left(\boldsymbol{b}_{n+1}^{e}, \boldsymbol{q}_{n+1}\right) = 0\end{aligned}$$
via Newton's method, to obtain the updated state variables at the end of the step.
4. Recover $\boldsymbol{b}_{n+1}^{e}$ and τ_{n+1} using the spectral decomposition and the hyperelastic constitutive equation:
$$b_{A,n+1}^{e} = \exp\left(2\varepsilon_{A,n+1}^{e}\right) \qquad \boldsymbol{b}_{n+1}^{e} = \sum_{A=1}^{3} b_{A,n+1}^{e}, \boldsymbol{n}_{n+1}^{(A)} \otimes \boldsymbol{n}_{n+1}^{(A)}$$
$$\tau_{A,n+1} = \left(\frac{\partial\psi}{\partial\varepsilon_{A}^{e}}\right)_{n+1} \qquad \boldsymbol{\tau}_{n+1} = \sum_{A=1}^{3} \tau_{A,n+1}, \boldsymbol{n}_{n+1}^{(A)} \otimes \boldsymbol{n}_{n+1}^{(A)}$$

Table 4: Solution strategy for the plastic corrector problem of isotropic multiplicative plasticity.

where:

$$\boldsymbol{m}^A := \boldsymbol{n}^{(A)} \otimes \boldsymbol{n}^{(A)} \quad \boldsymbol{m}^{AB} := \boldsymbol{n}^{(A)} \otimes \boldsymbol{n}^{(B)} \quad \boldsymbol{m}^{BA} := \boldsymbol{n}^{(B)} \otimes \boldsymbol{n}^{(A)}$$

$$\boldsymbol{M}^{(AB)} := \boldsymbol{m}^{AB} \otimes \boldsymbol{m}^{AB} + \boldsymbol{m}^{AB} \otimes \boldsymbol{m}^{BA}$$

The quantities $\hat{d}_{AB}$ in eq. (109), defined as:

$$\hat{d}_{AB} := \frac{\partial \tau_A}{\partial \varepsilon_B^{e,\mathrm{tr}}} \tag{110}$$

are the components of the (3×3) matrix $\hat{\boldsymbol{d}} := \partial\hat{\boldsymbol{\tau}}/\partial\hat{\boldsymbol{\varepsilon}}^{e,\mathrm{tr}}$ of tangent moduli in principal strain space. In presence of repeated eigenvalues for $\boldsymbol{b}^{e,\mathrm{tr}}$, the third term on the RHS of eq. (109) becomes singular. The singularity can be easily eliminated as shown in [Ogd84], Ch. 6.

For the case at hand, the exact calculation of the matrix $\hat{\boldsymbol{d}}$ is possible only if, during the current time step, the loading process is elastic. When the plastic deformations occur, the Kirchhoff stress tensor is a function of $\boldsymbol{b}^e_{n+1}$ which is determined numerically via the algorithm of Tab. 4. In such conditions, the evaluation of $\hat{\boldsymbol{d}}$ requires the linearization of the integration algorithm and proceeds as follows.

In terms of principal values of Kirchhoff stresses and principal elastic logarithmic strains, the hyperelastic constitutive equation reads:

$$\tau_A = \frac{\partial\hat{\psi}}{\partial\varepsilon^e_{A,n+1}} \qquad \text{or, in vector format} \qquad \hat{\boldsymbol{\tau}} = \frac{\partial\hat{\psi}}{\partial\hat{\boldsymbol{\varepsilon}}^e} \tag{111}$$

where $\hat{\boldsymbol{\tau}} := \{\tau_1, \tau_2, \tau_3\}^T$. From this equation we have:

$$\hat{\boldsymbol{d}}^{(k)}_{n+1} = \left(\frac{\partial\hat{\boldsymbol{\tau}}}{\partial\hat{\boldsymbol{\varepsilon}}^e}\right)^{(k)}_{n+1} \left(\frac{\partial\hat{\boldsymbol{\varepsilon}}^e}{\partial\hat{\boldsymbol{\varepsilon}}^{e,\mathrm{tr}}}\right)^{(k)}_{n+1} = (\hat{\boldsymbol{D}}^e)^{(k)}_{n+1} \left(\frac{\partial\hat{\boldsymbol{\varepsilon}}^e}{\partial\hat{\boldsymbol{\varepsilon}}^{e,\mathrm{tr}}}\right)^{(k)}_{n+1} \tag{112}$$

where:

$$(\hat{\boldsymbol{D}}^e)^{(k)}_{n+1} := \left(\frac{\partial\hat{\boldsymbol{\tau}}}{\partial\hat{\boldsymbol{\varepsilon}}^e}\right)^{(k)}_{n+1} = \left(\frac{\partial^2\hat{\psi}}{\partial\hat{\boldsymbol{\varepsilon}}^e \otimes \partial\hat{\boldsymbol{\varepsilon}}^e}\right)^{(k)}_{n+1} \tag{113}$$

is the (3×3) elastic tangent stiffness matrix in principal directions. Now, let us define:

$$\boldsymbol{x}^{(k)}_{n+1} := \begin{Bmatrix} (\hat{\boldsymbol{\varepsilon}}^e)^{(k)}_{n+1} \\ \boldsymbol{q}^{(k)}_{n+1} \\ \Delta\gamma^{(k)}_{n+1} \end{Bmatrix} \qquad \hat{\boldsymbol{K}}^{e(k)}_{n+1} := \Big[\hat{\boldsymbol{D}}^e \quad \boldsymbol{0}_{(3\times n_{\mathrm{int}})} \quad \boldsymbol{0}_{(3\times1)}\Big]^{(k)}_{n+1} \tag{114}$$

as the vector of unknown state variables and plastic multiplier increment, and a auxiliary matrix containing the elastic stiffness matrix, eq. $(112)_2$ can be rewritten in the

following alternative form:

$$\hat{\boldsymbol{d}}_{n+1}^{(k)} = \hat{\boldsymbol{K}}_{n+1}^{e(k)} \left(\frac{\partial \boldsymbol{x}}{\partial \hat{\boldsymbol{\varepsilon}}^{e,\mathrm{tr}}} \right)_{n+1}^{(k)} \tag{115}$$

The derivative $\partial \boldsymbol{x} / \partial \hat{\boldsymbol{\varepsilon}}^{e,\mathrm{tr}}$ measures the variation in the converged solution of the iterative algorithm used to solve the plastic corrector problem for an infinitesimal change in the relative displacement gradient $\boldsymbol{f}_{n+1}$, and thus in $\hat{\boldsymbol{\varepsilon}}_{n+1}^{e,\mathrm{tr}}$. This quantity can be obtained by linearizing the plastic corrector problem equations of Tab. 4.

Let:

$$\boldsymbol{x}_{n+1}^{(k),\mathrm{tr}} := \begin{Bmatrix} (\hat{\boldsymbol{\varepsilon}}^{e,\mathrm{tr}})_{n+1}^{(k)} \\ \boldsymbol{q}_n \\ 0 \end{Bmatrix} \quad \boldsymbol{R}_{n+1}^{(k)} := \begin{Bmatrix} -\hat{\boldsymbol{\varepsilon}}_{n+1}^{e} + \hat{\boldsymbol{\varepsilon}}_{n+1}^{e,\mathrm{tr}} - \Delta\gamma_{n+1} \hat{\boldsymbol{Q}}_{n+1} \\ -\boldsymbol{q}_{n+1} + \boldsymbol{q}_n + \Delta\gamma_{n+1} \boldsymbol{h}_{n+1} \\ -f\left(\boldsymbol{b}_{n+1}^{e}, \boldsymbol{q}_{n+1}\right) \end{Bmatrix} \tag{116}$$

be the vector of trial values for the problem unknowns and the residual vector of the plastic corrector problem. Then, let:

$$\boldsymbol{g}_{n+1}^{(k)} := \boldsymbol{x}_{n+1}^{(k),\mathrm{tr}} - \boldsymbol{R}_{n+1}^{(k)} = \begin{Bmatrix} (\hat{\varepsilon}^{e})_{n+1}^{(k)} + \Delta\gamma_{n+1}^{(k)} \, (\hat{\boldsymbol{Q}}^{*})_{n+1}^{(k)} \\ \boldsymbol{q}_{n+1}^{(k)} - \Delta\gamma_{n+1}^{(k)} \boldsymbol{h}_{n+1}^{(k)} \\ f_{n+1}^{(k)} \end{Bmatrix} \tag{117}$$

be the difference between $\boldsymbol{x}_{n+1}^{(k),\mathrm{tr}}$ and the residual vector $\boldsymbol{R}_{n+1}^{(k)}$ of eq. (116), *i.e.*, the only part of the residual vector which actually depends on the problem unknowns. Then the governing equations of the plastic corrector problem in Tab. 4 can be recast as follows:

$$\boldsymbol{g}\left(\boldsymbol{x}_{n+1}^{(k)}\right) = \boldsymbol{x}_{n+1}^{(k),\mathrm{tr}} \tag{118}$$

Deriving both sides of eq. (118) with respect to $\hat{\boldsymbol{\varepsilon}}^{e,\mathrm{tr}}$, we have:

$$\left(\frac{\partial \boldsymbol{g}}{\partial \boldsymbol{x}} \right)_{n+1}^{(k)} \left(\frac{\partial \boldsymbol{x}}{\partial \hat{\boldsymbol{\varepsilon}}^{e,\mathrm{tr}}} \right)_{n+1}^{(k)} = \left(\frac{\partial \boldsymbol{x}^{\mathrm{tr}}}{\partial \hat{\boldsymbol{\varepsilon}}^{e,\mathrm{tr}}} \right)_{n+1}^{(k)} \tag{119}$$

Noting that:

$$\left(\frac{\partial \boldsymbol{g}}{\partial \boldsymbol{x}} \right)_{n+1}^{(k)} = - \left(\frac{\partial \boldsymbol{R}}{\partial \boldsymbol{x}} \right)_{n+1}^{(k)} = -\boldsymbol{J}_{n+1}^{(k)} \tag{120}$$

$$\left(\frac{\partial \boldsymbol{x}^{\mathrm{tr}}}{\partial \hat{\boldsymbol{\varepsilon}}^{e,\mathrm{tr}}} \right)_{n+1}^{(k)} = \begin{Bmatrix} \boldsymbol{I}_3 \\ \boldsymbol{0}_{(n_{\mathrm{int}}+1 \times 3)} \end{Bmatrix} =: \boldsymbol{T} \tag{121}$$

and considering that the Jacobian matrix $\boldsymbol{J}_{n+1}^{(k)}$ is non–singular if the plastic corrector problem is well–posed, we obtain:

$$\left(\frac{\partial \boldsymbol{x}}{\partial \hat{\boldsymbol{\varepsilon}}^{e,\mathrm{tr}}}\right)_{n+1}^{(k)} = -\left(\boldsymbol{J}^{-1}\right)_{n+1}^{(k)} \boldsymbol{T} \tag{122}$$

and, finally:

$$\hat{\boldsymbol{d}}_{n+1}^{(k)} = -\hat{\boldsymbol{K}}_{n+1}^{e(k)} \left(\boldsymbol{J}^{-1}\right)_{n+1}^{(k)} \boldsymbol{T} \tag{123}$$

The evaluation of the RHS of eq. (123) is relatively easy as the inverse of the Jacobian matrix needs to be computed for the iterative solution of the local plastic corrector problem.

References

[AD79] J. H. Argyris and J. S. Doltsinis. On the large strain inelastic analysis in natural formulation part I: Quasistatic problems. *Comp. Meth. Appl. Mech. Engng.*, 20(2):213–251, 1979.

[ARS92] H. Alawaji, K. Runesson, and S. Sture. Implicit integration in soil plasticity under mixed control for drained and undrained response. *Int. J. Num. Anal. Meth. Geomech.*, 16:737–756, 1992.

[BL90] R. I. Borja and S. R. Lee. Cam–clay plasticity, part I. implicit integration of elastoplastic constitutive relations. *Comp. Meth. Appl. Mech. Engng.*, 78:49–72, 1990.

[Bor91] R. I. Borja. Cam–clay plasticity, part II. implicit integration of constitutive equation based on a non–linear elastic stress predictor. *Comp. Meth. Appl. Mech. Engng.*, 88:225–240, 1991.

[BRB16] K. C. Bennett, R. A. Regueiro, and R. I. Borja. Finite strain elastoplasticity considering the eshelby stress for materials undergoing plastic volume change. *International Journal of Plasticity*, 77:214–245, 2016.

[BT98] R. I. Borja and C. Tamagnini. Cam–clay plasticity, part III: Extension of the infinitesimal model to include finite strains. *Comp. Meth. Appl. Mech. Engng.*, 155:73–95, 1998.

[CAS98] C. Callari, F. Auricchio, and E. Sacco. A finite-strain cam-clay model in the framework of multiplicative elasto-plasticity. *Int. J. of Plasticity*, 14(12):1155–1187, 1998.

[dPO11] E. A. de Souza Neto, D. Peric, and D. R. J. Owen. *Computational methods for plasticity: theory and applications*. John Wiley & Sons, 2011.

[FMO09] W. Fellin, M. Mittendorfer, and A. Ostermann. Adaptive integration of constitutive rate equations. *Comp. & Geotechnics*, 36(5):698–708, 2009.

[FO02] W. Fellin and A. Ostermann. Consistent tangent operators for constitutive rate equations. *Int. J. Num. Anal. Meth. Geomech.*, 26(12):1213–1233, 2002.

[HS21] L. Hauser and H. F. Schweiger. Numerical study on undrained cone penetration in structured soil using g-pfem. *Comp. & Geotechnics*, 133:104061, 2021.

[Hug84] T. J. R. Hughes. Numerical implementation of constitutive models: rate–independent deviatoric plasticity. In S. Nemat-Nasser, R. Asaro, and G. Hegemier, editors, *Theoretical Foundations for Large Scale computations of Non Linear Material Behavior*, pages 29–57, Horton, Greece, 1984. Martinus Nijhoff Publisher, Dordrecht.

[HW91] E. Hairer and G. Wanner. *Solving Ordinary Differential Equations II. Stiff and Differential–Algebraic Problems, 2nd. Ed.* Springer Verlag, New York, 1991.

[JS97] B. Jeremić and S. Sture. Implicit integration in elastoplastic geotechnics. *Mech. Cohesive–Frictional Materials*, 2:165–183, 1997.

[MCC+19] L. Monforte, M. O. Ciantia, J. M. Carbonell, M. Arroyo, and A. Gens. A stable mesh–independent approach for numerical modelling of structured soils at large strains. *Comp. & Geotechnics*, 116:103215, 2019.

[MGA+21] L. Monforte, A. Gens, M. Arroyo, M. Mánica, and J. M. Carbonell. Analysis of cone penetration in brittle liquefiable soils. *Comp. & Geotechnics*, 134:104123, 2021.

[MWA97] E. J. Macari, S. Weihe, and P. Arduino. Implicit integration of elastoplastic constitutive models for frictional materials with highly non–linear hardening functions. *Mech. Cohesive–Frictional Materials*, 2:1–29, 1997.

[OCT21] K. Oliynyk, M. O. Ciantia, and C. Tamagnini. A finite deformation multiplicative plasticity model with non–local hardening for bonded geomaterials. *Comp. & Geotechnics*, 137, 2021.

[OCW+07] J. Oliver, J. C. Cante, R. Weyler, C. González, and J. Hernández. Particle finite element methods in solid mechanics problems. *Computational Methods in Applied Sciences*, 7:87–103, 2007.

[Ogd84] R. Ogden. *Nonlinear Elastic Deformations*. Ellis Horwood, Chichester, 1984.

[OHC08] J. Oliver, A. E. Huespe, and J. C. Cante. An implicit/explicit integration scheme to increase computability of non-linear material and contact/friction problems. *Comp. Meth. Appl. Mech. Engng.*, 197(21-24):1865–1889, 2008.

[OT20] K. Oliynyk and C. Tamagnini. Finite deformation hyperplasticity theory for crushable, cemented granular materials. *Open Geomechanics*, 2:1–33, 2020.

[OT21] K. Oliynyk and C. Tamagnini. Finite deformation plasticity. In C. Tamagnini and D. Mašín, editors, *Constitutive modelling of soils*. ALERT Geomaterials, 2021. This volume.

[PFRFH00] A. Perez-Foguet, A. Rodriguez-Ferran, and A. Huerta. Numerical differentiation for non-trivial consistent tangent matrices: an application to the mrs-lade model. *Int. J. Num. Meth. Engng.*, 48:159–184, 2000.

[PG85] D. M. Potts and A. Gens. A critical assessment of methods of correcting for drift from the yield surface in elasto-plastic finite element analysis. *Int. J. Num. Anal. Meth. Geomech.*, 9(2):149–159, 1985.

[PSS08] D. M. Pedroso, D. Sheng, and S. W. Sloan. Stress update algorithm for elastoplastic models with nonconvex yield surfaces. *Int. J. Num. Meth. Engng.*, 76(13):2029–2062, 2008.

[RFPH97] A. Rodríguez-Ferran, P. Pegon, and A. Huerta. Two stress update algorithms for large strains: accuracy analysis and numerical implementation. *Int. J. Num. Meth. Engng.*, 40(23):4363–4404, 1997.

[SAS01] S. W. Sloan, A. J. Abbo, and D. Sheng. Refined explicit integration of elastoplastic model with automatic error control. *Engineering Computations*, 18(1):121–154, 2001.

[SB92a] S. W. Sloan and J. R. Booker. Integration of tresca and mohr–coulomb constitutive relations in plane strain elastoplasticity. *Int. J. Num. Meth. Engng.*, 33(1):163–196, 1992.

[SB92b] J. Stoer and R. Bulirsch. *Introduction to numerical analysis, 2nd ed.* Springer Verlag, New York, 1992.

[SG91] J. C. Simo and S. Govindjee. Non–linear B–stability and symmetry preserving return mapping algorithms for plasticity and viscoplasticity. *Int. J. Num. Meth. Engng.*, 31:151–176, 1991.

[SH87] J. C. Simo and T. J. R. Hughes. General return mapping algorithms for rate–independent plasticity. In C.S. Desai et al., editors, *Constitutive Laws for Engineering Materials*, Horton, Greece, 1987. Elsevier Science Publishing.

[SH98] J. C. Simo and T. J. R. Hughes. *Computational inelasticity*, volume 7. Springer Science & Business Media, 1998.

[Sim85] J. C. Simo. On the computational significance of the intermediate configuration and hyperelastic stress relations in finite deformation elastoplasticity. *Mechanics of Materials*, 4(3-4):439–451, 1985.

[Sim92] J. C. Simo. Algorithms for static and dynamic multiplicative plasticity that preserve the classical return mapping schemes of the infinitesimal theory. *Comp. Meth. Appl. Mech. Engng.*, 99(1):61–112, 1992.

[Sim98] J.C. Simo. Numerical analysis and simulation of plasticity. *Handbook of numerical analysis*, 6:183–499, 1998.

[Slo87] SW Sloan. Substepping schemes for the numerical integration of elastoplastic stress–strain relations. *Int. J. Num. Meth. Engng.*, 24(5):893–911, 1987.

[SM93] J. C. Simo and G. Meschke. A new class of algorithms for classical plasticity extended to finite strains. application to geomaterials. *Computational Mechanics*, 11(4):253–278, 1993.

[SO85] J. C. Simo and M. Ortiz. A unified approach to finite deformation elastoplastic analysis based on the use of hyperelastic constitutive equations. *Comp. Meth. Appl. Mech. Engng.*, 49(2):221–245, 1985.

[SSS02] L. Sanavia, B. A. Schrefler, and P. Steinmann. A formulation for an unsaturated porous medium undergoing large inelastic strains. *Computational Mechanics*, 28(2):137–151, 2002.

[ST85] J. C. Simo and R. L. Taylor. Consistent tangent operators for rate independent elasto–plasticity. *Comp. Meth. Appl. Mech. Engng.*, 48:101–118, 1985.

[TCN02] C. Tamagnini, R. Castellanza, and R. Nova. A Generalized Backward Euler algorithm for the numerical integration of an isotropic hardening elastoplastic model for mechanical and chemical degradation of bonded geomaterials. *Int. J. Num. Anal. Meth. Geomech.*, 26:963–1004, 2002.

[TVC00] C. Tamagnini, G. Viggiani, and R. Chambon. A review of two different approaches to hypoplasticity. In D. Kolymbas, editor, *Constitutive Modelling of Granular Materials*, pages 107–145. Springer, Berlin, 2000.

[TVCD00] C. Tamagnini, G. Viggiani, R. Chambon, and J. Desrues. Evaluation of different strategies for the integration of hypoplastic constitutive equations: Application to the CLoE model. *Mech. Cohesive–Frictional Materials*, 5:263–289, 2000.

Macroelement modelling

Claudio di Prisco & Luca Flessati

Politecnico di Milano

In the current engineering practice, displacement-based design approaches are progressively gaining popularity in the solution of soil structure interaction problems. In case of geo-structures, a reliable estimation of displacements can be obtained by performing finite element numerical analyses in which a sufficiently sophisticated constitutive relationship for the soil is adopted. An alternative approach consists in following an upscaling procedure aimed at defining a constitutive relationship between generalized stress and strain variables. In this chapter the authors intend to discuss the concepts on which these alternative approaches (known in literature as macroelement models) are based on.

1 Introduction

In case of soil-structure interaction (SSI) problems, the assessment of displacement is done by performing numerical (finite element or finite difference) analyses, considering both the structure and the surrounding soil. Since the soil mechanical behaviour is non-linear, anholonomous and irreversible, relatively complex constitutive relationships have to be employed to obtain reliable results. An alternative approach consists in lumping structure and surrounding soil into a "macroelement" (ME), whose behaviour is governed by a constitutive law, defining a relationship between a (low number) of generalized stress and strain variables considered representative for the global system response.

In the last thirty years, the ME approach was successfully employed for different soil-structure interaction problems, such as shallow foundations ([NM91], [MN97], [GHB99], [CPD01] [GKM08] [ST09] [PFdP16] [FdPC21]), offshore foundations and wind turbines ([MH01], [BH03], [CRB06]), buried pipelines ([CdPGN09]), rock boulders impacting on soil strata ([dPV06]), pile foundations ([LKET16]), earth embankments ([dPFFG20]), tunnel cavities and faces ([dPFFL18], [dPFP20], [dPF21]). These generalized constitutive relationships (representing a sophisticated evolution of standard elastic springs) can be very simply introduced in standard structural finite element codes, allowing the solution of fully coupled soil-structure

interaction problems, without solving a fully coupled geo-structural problem and consequently dramatically increasing computational times and costs.

In this chapter, the authors intend to put in evidence (i) the similarities of the ME approach with the upscaling procedures commonly adopted for soil constitutive modelling (§2) and (ii) the fundamental ingredients necessary for the formulation of ME models (§3 and §4).

2 The upscaling procedure in SSI problems

As was clearly shown by "micro-experimental" and discrete element numerical test results concerning granular media, the mechanical response of the representative elementary volume (REV) (Figure 1a), perturbed by means of surface forces applied on its boundaries, essentially depends on both "micro" geometry (grain dimension/shape and void spatial distribution, etc) and mechanical behaviour of grains. To avoid the description of all the micro mechanical processes taking place in the REV, the response of the material is usually described at the "macro" scale in terms of average static (stresses) and kinematic (strain) variables. Under the hypothesis of neglecting body forces (gravity), both stresses and strains are assumed to be uniform and work conjugated. As is well-known, up to '80s, constitutive relationships have been phenomenologically conceived by assuming specimens tested in the laboratory to be coincident with REVs.

In case of SSI problems (e.g. shallow foundations as sketched in Figure 1b), perturbations are applied on the boundary of the domain (stress distributions or displacement field) and the system response depends on both system geometry and soil mechanical behaviour described at the macroscale: a boundary value problem has to be solved and the constitutive relationship at the upscaled level ("mega" scale) has to be defined in terms of forces and displacements. With respect to the REV case, in SSI problems the state of stress/strain is not uniform in the considered spatial domain.

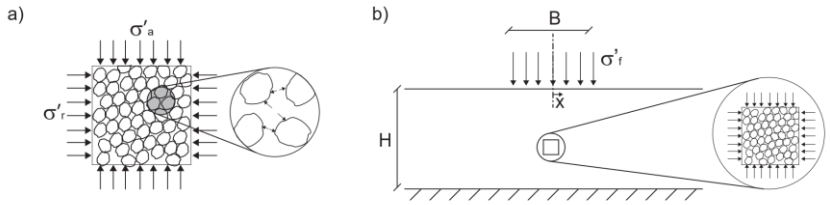

Figure 1: Upscaling procedure: a) for REVs and b) for SSI problem

With reference to Figure 1b, the generalized force applied on the *B*-width foundation (V) and the associated displacement (v) can be defined as it follows:

$$V = \int_{-B/2}^{B/2} \sigma'_f(x)dx \qquad v = \frac{\int_{-B/2}^{B/2} \sigma'_f(x)v^*(x)dx}{V} \tag{1}$$

being $\sigma'_f(x)$ the stress applied to and $v^*(x)$ displacements of (in general depending on coordinate x of Figure 1b) the foundation.

3 One-dimensional case

To emphasise the theoretical bases of the approach, in this paragraph a structural problem is first considered and then (§3.1 and §3.2) geotechnical applications are discussed.

As is well-known, the structural response of a L-long beam characterized by a moment of inertia I, subject to a progressively increasing vertical load (V) applied in the middle (Figure 2a) may be upscaled by employing a suitable elastic-perfectly plastic constitutive relationship for the beam cross section (Figure 2b), defined in terms of bending moment (M) and curvature (χ), being M_0 the maximum bending moment, EI the bending stiffness and E the material Young modulus. The balance of momentum implies the external work $W_e = Vv$ (being v the displacement in the point of application of V), to be equal to the internal work (W_i). The expression for W_i changes according to the value of V applied to the beam: (i) initially, when the response is elastic W_i is associated with the elastic beam bending, (ii) subsequently ($V = V_y$) a plastic hinge develops in point A of Figure 2c, the response becomes elastic plastic and W_i is given by the sum of the elastic work and the plastic work dissipated by the plastic hinge and (iii) finally, for $V = V_f$, a second hinge develops in point B of Figure 2d, W_i becomes equal to the plastic work dissipated by the two plastic hinges and the system collapses.

From the equality $W_e = W_i$ (the analytical derivation is hereafter omitted for the sake of brevity) the incremental generalized constitutive relationship (Figure 2e) reads:

$$d\bar{V} = \begin{cases} d\bar{v} & \bar{V} < \bar{V}_y \\ \frac{7}{16} d\bar{v} & \bar{V}_y < \bar{V} < \bar{V}_f \\ 0 & \bar{V} = \bar{V}_y \end{cases}, \tag{2}$$

where d stands for increment, the non-dimensional generalized stress and strain variables are defined $\bar{V} = V/(M_0/L)$ and $\bar{v} = (v/v_{el})V_f/(M_0/L)$, respectively, being v_{el} the elastic displacement for $V = V_f$ and $\bar{V}_y = 16/3$, whereas $\bar{V}_f = 6$ are the non-dimensional load values corresponding to V_y and V_f, respectively. The employment of non-dimensional variables is particularly convenient: Equation 2 is unique, independently on both geometry and material mechanical properties. The

"structural hardening", taking place for $\bar{V}_y < \bar{V} < \bar{V}_f$, is due to the static redundancy of the system.

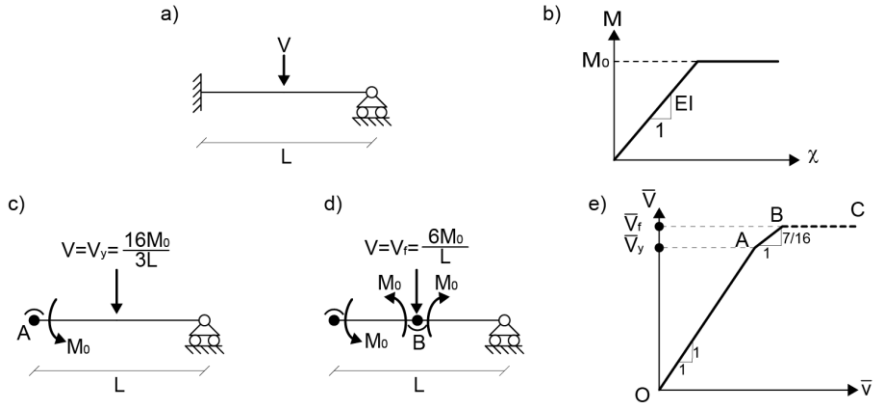

Figure 2: Elastic plastic beam: a) geometry, b) M-χ upscaled constitutive relationship, c) developing of first plastic hinge, d) developing of the second plastic hinge and e) $\bar{V} - \bar{v}$ relationship

3.1 Undrained response of shallow foundations on normally-consolidated clays

Analogously to what done for elastic-plastic beams, in this section, an elastic-plastic upscaled constitutive model [FdPC21], capable of simulating the undrained mechanical behaviour of shallow foundation foundations positioned on a H-thick normally-consolidated clay stratum behaving according to the Modified Cam Clay (MMC) constitutive relationship, is discussed. The B-width foundation (Figure 1a), is assumed to be rigid and to be loaded only by means of a uniform effective stress σ'_f. The vertical effective stresses at the foundation plane, hereafter named σ'_{f0}, are assumed to be constant. A discussion on the influence of variations in σ'_{f0} on the definition of generalized constitutive relationships is reported in [PFdP16]. Two non-dimensional static/kinematic variables are introduced:

$$\bar{V} = \frac{V}{S_u B} \qquad \bar{v} = \frac{v}{v_{el}} \frac{V_{lim,u}}{S_u B}, \tag{3}$$

being $V = (\sigma'_f - \sigma'_{f0})B$, S_u the undrained strength (corresponding to a depth equal to *B/2*) calculated by integrating the MCC constitutive equations under triaxial compression undrained stress paths, $V_{lim,u}$ the undrained limit load and v_{el} the elastic displacement corresponding to $V = V_{lim,u}$. To calculate v_{el} [FdPC21] suggests to employ an elastic solution, in which the elastic properties are evaluated at *B*/2 depth.

In [FdPC21] the undrained limit load is shown to be dependent on both geometry and material mechanical properties. By interpreting numerical finite element analyses results, the following expression is proposed:

$$V_{lim,u} = \left[\sigma'_{f0}(N_q^* - 1) + \frac{1}{2}B\gamma' N_\gamma^*\right] B \,, \tag{4}$$

where N_q^* and N_γ^* are undrained MCC bearing capacity coefficients, depending on MCC constitutive parameters (being M, κ and λ the slope of the critical state line, the unloading line inclination and the virgin load line inclination, respectively), as is shown in Figure 3.

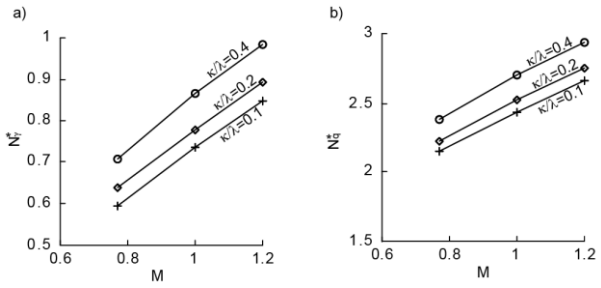

Figure 3: Variation of N_q^* and N_γ^* with M, κ and λ (adapted from [FdPC21])

Owing to the non-dimensional variable definitions, in the $\bar{V} - \bar{v}$ plane, the initial branch of the load settlement curves is independent of the geometry and soil mechanical properties ([FdPC21]). The initial slope is not elastic, since irreversible strains develop beneath the foundation edge from the onset of the loading process, as is testified by the contours of irreversible deviatoric strains of Figure 4a, corresponding to point A of Figure 4b.

To reproduce the mechanical response of the system, a non-dimensional strain hardening elastic-plastic constitutive relationship is adopted. The generalized strains ($\bar{v} = \bar{v}_u$, where u stands for undrained) are given by the sum of a reversible/elastic ($\bar{v}_u^{el}$) and an irreversible/plastic ($\bar{v}_u^{pl}$) part. The elastic law is defined as: $\bar{v}_u^{el} = \bar{V}/K_u^{el}$, being K_u^{el} the elastic undrained stiffness. For the plastic law, the failure surface (F_u), the yield function (f_u), the plastic potential (g_u) and the hardening rule have to be defined:

$$F_u = \bar{V} - \bar{V}_{lim,u} \qquad f_u = g_u = \bar{V} - \bar{V}_u \qquad d\bar{V}_u = \alpha_u \left(1 - \frac{\bar{V}}{\bar{V}_{lim,u}}\right) d\bar{v}_u^{pl} \,, \tag{5}$$

being $\bar{V}_u$ the hardening variable, $\bar{V}_{lim,u} = V_{lim,u}/(S_u B)$ the non-dimensional limit load, whereas α_u a non-dimensional constitutive parameter.

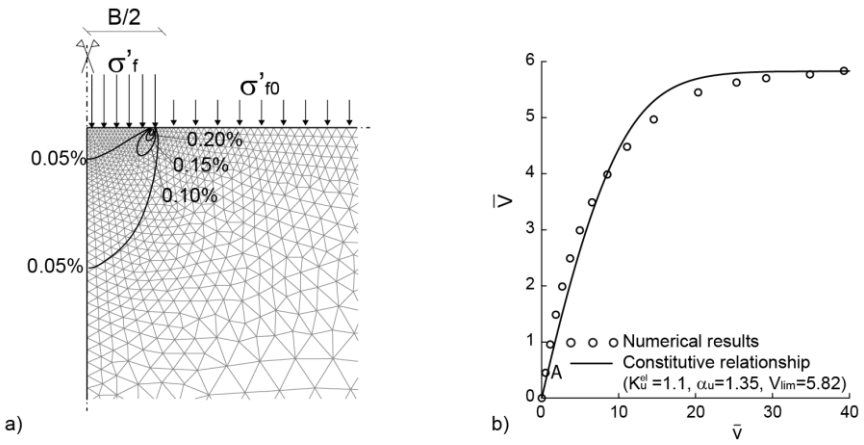

Figure 4: a) Contour of irreversible deviatoric strains (only a portion of the domain is represented) and b) non-dimensional load settlement curves (adapted from [FdPC21]) (B=2m, σ'_{f0}=20kPa, M=1, $\kappa = 0.05$, λ/κ =0.2, γ'=10kN/m^3, H/B=5)

By employing (i) both standard flow rule and consistency conditions, (ii) the elastic law and (iii) the generalized strain additivity, the constitutive relationship can be written as:

$$d\bar{v} = \left(\frac{1}{K_u^{el}} + \frac{1}{\alpha_u}\frac{\bar{V}_{lim,u}}{\bar{V}_{lim,u}-\bar{V}}\right) d\bar{V} \,, \tag{6}$$

that in case of $\bar{V}$=0 reduces to:

$$\frac{d\bar{V}}{d\bar{v}} = \frac{K_u^{el}\alpha_u}{K_u^{el}+\alpha_u} \,. \tag{7}$$

The numerical results have been used by the authors to calculate once and for all K_u^{el}, α_u and $\bar{V}_{lim,u}$ (Equation 3), whereas the initial value of the hardening variable, in case of normally consolidated clays, is imposed to be nil. The comparison between the numerical results and the constitutive law prediction is reported in Figure 4b. The use of the upscaled model substitutes the employment of a finite element code for the evaluation of footing settlements and allows to abruptly reduce computational times and costs

3.2 Partially drained response of shallow foundations on normally-consolidated clays

In this section, the extension of the model discussed in §3.1 to partially drained cases is presented. The model can be employed both to analyse the influence of

loading rate on the foundation response and to estimate settlements developing after the end of the foundation loading. The model is defined by employing non-dimensional variables: the static and kinematic variables coincide with those adopted in the undrained case (Equation 5) and the non-dimensional time is defined as:

$$T = \frac{c_{v2}t}{B^2} \qquad c_{v2} = \frac{kE}{2\gamma_w(1+\nu)(1-2\nu)}, \tag{8}$$

where t stands for time, k for isotropic soil permeability, γ_w for water unit weight, ν for Poisson ratio and E for the Young modulus calculated at a $B/2$ depth.

This model is based on the rheological scheme of Figure 5, where a spring in series with a plastic slider (A) represent the undrained response, whereas a spring in series with a plastic slider (B) in parallel with a viscous damper (C) represent the drained response. The undrained elastic response, the undrained yield function and plastic potential are the same of the model of §3.1. On the contrary, the undrained hardening rule is modified as it follows:

$$d\bar{V}_u = \alpha_u \left(1 - \frac{\bar{V}}{\bar{V}_{lim}}\right) d\bar{v}_u^{pl} + d\bar{V}_d \qquad \bar{V}_{lim} = \bar{V}_{lim,u} + \beta_d \bar{v}_d^{pl}, \tag{9}$$

being $\bar{V}_d$ the drained hardening variable, $\bar{v}_d^{pl}$ the drained plastic displacements and β_d a model parameter. Equations 11 introduces a drained-undrained coupling. In fact, the hardening of $\bar{V}_d$ partially inhibits the $\bar{V}_u$ hardening. At the same time, the consolidation process taking place in the foundation soil, associated with an increase in effective stresses, induces (drained) settlements and an increase in undrained strength. For this reason in Equation 11, any increment in $\bar{v}_d^{pl}$ induces an increment in $\bar{V}_{lim}$.

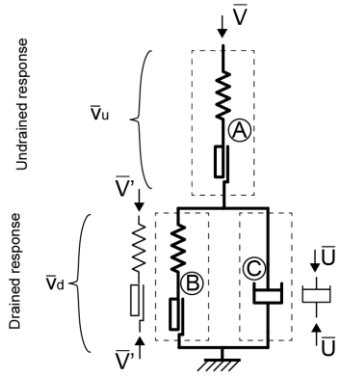

Figure 5: Rheological scheme

The drained elastic law is defined as: $\bar{v}_d^{el} = \bar{V}'/K_d^{el}$, being $\bar{v}_d^{el}$ the elastic drained displacements, $\bar{V}'$ the non-dimensional force acting on the drained spring and slider (Figure 5) and K_d^{el} a constitutive parameter. The yield function (f_d) and the plastic

potential (g_d) are defined as: $f_d = g_d = \bar{V}' - \bar{V}_d$. The hardening function for $\bar{V}_d$ is inspired to that employed to describe the characteristic curves for deep tunnel cavities and faces ([dPFFL18], [dPFP20]):

$$d\bar{V}_d = \left[\frac{\exp\left(\frac{\bar{V}_d}{\alpha_d}\right)}{K_d^{ep}} - \frac{1}{K_d^{el}}\right]^{-1} d\bar{v}_d^{pl}\,, \tag{10}$$

being K_d^{ep} and α_d two non-dimensional constitutive parameters.

For the viscous damper (C of Figure 5), the following expression is adopted:

$$U = \eta \frac{d\bar{v}_d}{dT}\,, \tag{11}$$

being U the non-dimensional force acting on the damper and η a non-dimensional constitutive parameter.

Even in this case, the 8 parameters (K_u^{el}, α_u, K_d^{el}, K_d^{ep}, α_d, η, β_d, $\bar{V}_{lim,u}$) are calculated once and for all by using hydro-mechanical coupled numerical analyses results. As is evident from Figure 6, for all the cases considered the agreement between finite element numerical results and model predictions is very satisfactory.

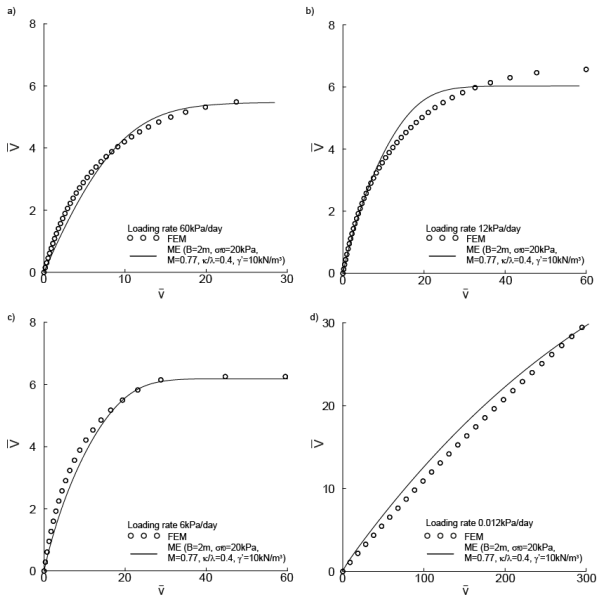

Figure 6: Validation of the generalized constitutive relationship for different loading rate values

4. Multi-dimensional case

The macroelement theory was originally conceived for rigid strip footings positioned on horizontal homogeneous granular material strata under inclined and eccentric loads [NM91]. In this case, three generalized stress variables (the vertical load component V, the horizontal load component H and the overturning moment M) and the corresponding three generalized strain variables (vertical displacement v, horizontal displacement u and foundation rotation θ) are considered. The stress and strain variables are collected into three-dimensional vectors, named $\boldsymbol{Q}$ and $\boldsymbol{q}$, respectively. Under three-dimensional loading conditions, both $\boldsymbol{Q}$ and $\boldsymbol{q}$ become six-dimensional ([GKM08], [ST09]).

Analogously to the case presented in §3.1, an elastic-plastic strain-hardening constitutive relationship is generally employed. Generalized strains are given by the sum of a reversible/elastic ($\boldsymbol{q^{el}}$) and an irreversible/plastic ($\boldsymbol{q^{pl}}$) part. The elastic law is expressed as $\dot{\boldsymbol{q}}^{el} = \boldsymbol{C}^{el}\dot{\boldsymbol{Q}}$, being $\boldsymbol{C}^{el}$ the elastic compliance matrix, usually assumed to be diagonal. The three non-nil terms of $\boldsymbol{C}^{el}$ can be calculated, for instance, by employing the expressions reported in [G91].

The failure mechanisms developing beneath the foundation severely depend on the applied combination of generalized stress variables. As a consequence, for the failure locus an interaction domain has to be introduced ([BT79], [GB88], [NM91], [BG94], [GHB99]). For the sake of brevity, hereafter only the expression proposed in [NM91] is considered:

$$F = \left(\frac{H}{\mu V_{lim}}\right)^2 + \left(\frac{M}{\psi B V_{lim}}\right)^2 + \left(\frac{V}{V_{lim}}\right)^2 \left(1 - \frac{V}{V_{lim}}\right)^{2\beta} \quad , \tag{12}$$

being V_{lim} the limit load under vertical loads, whereas μ, ψ and β are non-dimensional constitutive parameters. In Figure 7, the curves associated with Equation 14 are compared with the small scale laboratory experimental test results of [NM91].

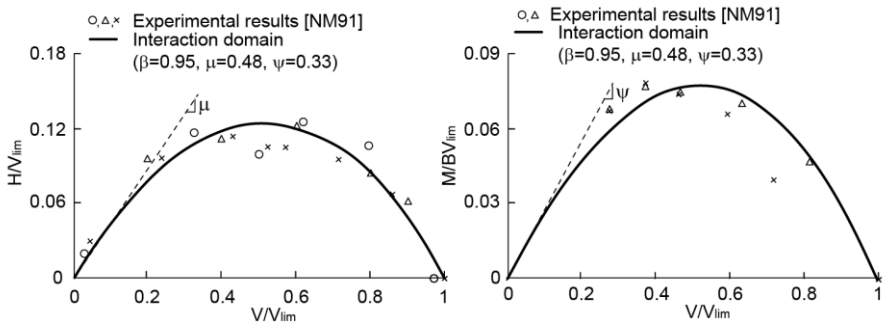

Figure 7: Interaction domain proposed in [NM91]

In [NM91] the yield locus f is homothetic with F and its size is governed by the hardening variable V_c, evolving according to:

$$dV_c = \left(1 - \frac{V_c}{V_{lim}}\right) R_0^p (dv^p + \alpha du^p + \gamma B d\theta^p) , \tag{13}$$

being α and γ two non-dimensional constitutive parameters, whereas R_0^p, analogous to α_u of Equation 5, represents the initial plastic stiffness. The plastic potential g does not coincide with f, in order to nullify vertical upward displacements when pure sliding occurs.

In [NM91] the model parameters were calibrated on the basis of experimental test results. More recently, an alternative approach, consisting in employing numerical analyses (e.g. finite element or discrete element) results, has become very common.

In the last three decades, many authors have suggested different formulations, for macroelements employed to reproduce the mechanical behaviour of shallow footings characterized by different embedment values and under cyclic loading. In case of seismic actions anisotropic hardening rules ([CPD01], [CPS09]) and hypoplastic constitutive relationships [ST09] were proposed.

5 Conclusions

In this chapter, the authors presented an upscaling procedure that can be employed for the solution of soil-structure interaction problems. This procedure consists in lumping the structure and its surrounding soil in a unique macroelement, individuating suitable static and kinematic variables representative for the system response and introducing a generalized constitutive relationship. By adopting this approach, once the constitutive law is both defined and calibrated by using either experimental test or numerical analysis results, the solution of a complex soil-structure interaction problem becomes the integration of a constitutive relationship, with negligible computational times.

References

[BG94] Butterfield, R., & Gottardi, G. (1994). A complete three-dimensional failure envelope for shallow footings on sand. Géotechnique, 44(1), 181-184.

[BH03] Byrne, B. W., & Houlsby, G. T. (2003). Foundations for offshore wind turbines. Philosophical Transactions of the Royal Society of London. Series A: Mathematical, Physical and Engineering Sciences, 361(1813), 2909-2930.

[BT79] Butterfield, R. & Ticof, J. Discussion: design parameters for granular soils IN proceedings 7th European conference on Soil Mechanics, Foundation Engineering pages 259-262 (4) Brighton, 1979

[CRB06] Cassidy, M. J., Randolph, M. F., & Byrne, B. W. (2006). A plasticity model describing caisson behaviour in clay. Applied Ocean Research, 28(5), 345-358.

[CPS09] Chatzigogos, C. T., Pecker, A. & Salencon, J. (2009). Macroelement modeling of shallow foundations. Soil Dynam. Earthquake Engng 29, No. 5, 765–781.

[CdPGN09] Cocchetti, G., di Prisco, C., Galli, A., & Nova, R. (2009). Soil–pipeline interaction along unstable slopes: a coupled three-dimensional approach. Part 1: Theoretical formulation. Canadian Geotechnical Journal, 46(11), 1289-1304.

[CPD01] Cremer, C., Pecker, A., & Davenne, L. (2001). Cyclic macro-element for soil–structure interaction: material and geometrical non-linearities. International Journal for Numerical and Analytical Methods in Geomechanics, 25(13), 1257-1284.

[dPF21] di Prisco, C. & Flessati, L. (2021a) A generalized constitutive relationship for undrained soil structure interaction problems, Lecture Notes in Civil Engineering, 125, pp. 398–405

[dPFFG20] di Prisco, C., Flessati, L., Frigerio, G. & Galli, A. (2020a) Mathematical modelling of the mechanical response of earth embankments on piled foundations, Géotechnique 70(9), pp. 755–773 DOI https://doi.org/10.1680/jgeot.18.P.127

[dPFFL18] di Prisco, C., Flessati, L., Frigerio, G. & Lunardi, P. (2018) A numerical exercise for the definition under undrained conditions of the deep tunnel front characteristic curve. Acta Geotechnica, 13 (3) 635–649. doi:10.1007/s11440-017-0564-y

[dPFP20] di Prisco, C., Flessati, L., Porta, D. (2020) Deep tunnel fronts in cohesive soils under undrained conditions: a displacement-based approach for the design of fibreglass reinforcements Acta Geotechnica, 15 (4), pp. 1013-1030. DOI: 10.1007/s11440-019-00840-8

[dPV06] di Prisco, C. & Vecchiotti, M. (2006). A rheological model for the description of boulder impacts on granular strata Géotechnique 56, No. 7, 469–482

[FdPC21] Flessati, L., di Prisco, C. & Callea, F. (2020) Numerical and theoretical analyses of settlements of strip shallow foundations on normally-

consolidated clays under partially drained conditions, Géotechnique in press doi.org/10.1680/jgeot.19.P.348

[G91] Gazetas G. Foundations vibrations. In Foundation Engineering Handbook, Chapter 15, Fang H-Y (ed.). van Nostrand Reinhold: New York, 1991.

[GB88] Georgiadis, M., & Butterfield, R. (1988). Displacements of footings on sand under eccentric and inclined loads. Canadian Geotechnical Journal, 25(2), 199-212.

[GHB99] Gottardi, G., Houlsby, G. T., & Butterfield, R. (1999). Plastic response of circular footings on sand under general planar loading. Géotechnique, 49(4), 453-470.

[GKM08] Grange, S., Kotronis, P., & Mazars, J. (2008). A macro-element for a circular foundation to simulate 3D soil–structure interaction. International Journal for Numerical and Analytical Methods in Geomechanics, 32(10), 1205-1227.

[LKET16]Li, Z., Kotronis, P., Escoffier, S., & Tamagnini, C. (2016). A hypoplastic macroelement for single vertical piles in sand subject to three-dimensional loading conditions. Acta Geotechnica, 11(2), 373-390.

[MH01] Martin, C. M., & Houlsby, G. T. (2001). Combined loading of spudcan foundations on clay: nu-merical modelling. Géotechnique, 51(8), 687-699.

[MN97] Montrasio, L., & Nova, R. (1997). Settlements of shallow foundations on sand: geometrical effects. Géotechnique, 47(1), 49–60. doi:10.1680/geot.1997.47.1.49

[NM91] Nova, R., & Montrasio, L. (1991). Settlements of shallow foundations on sand. Géotechnique, 41(2), 243-256.

[PFdP16] Pisanò, F., Flessati, L., & di Prisco, C. (2016). A macroelement framework for shallow foundations including changes in configuration. Géotechnique, 66(11), 910-926.

[ST09] Salciarini, D., & Tamagnini, C. (2009). A hypoplastic macroelement model for shallow foundations under monotonic and cyclic loads. Acta Geotechnica, 4(3), 163-176.

Laboratoire 3SR / Bâtiment Galilée
CS 40700
38 058 Grenoble cedex 9
France

ISBN 978-2-9561359-7-5

Fon: +33 (0) 456 528 621
Fax: +33 (0) 476 827 043
president@alertgeomaterials.eu
http://alertgeomaterials.eu

ALERT Doctoral School 2021

Constitutive Modelling in Geomaterials

Editors: C. Tamagnini, D. Mašín

Herle

Fundamentals of constitutive modelling for soils

Tamagnini & Oliynyk

The theory of plasticity in constitutive modeling of rate–independent soils

Mašín

Hypoplasticity and other incrementally non-linear modelling approaches

Mašín

Modelling non-linearity, small-strain stiffness and cyclic loading

Mašín

Meta-stable structure, breakage and thermal effects

di Prisco & Flessati

Time and rate dependence

Oliynyk & Tamagnini

Finite deformation plasticity

Tamagnini & Oliynyk

Numerical implementation of elastoplastic models in the Finite Element Method

di Prisco & Flessati

Macroelement modelling

ISBN 978-2-9561359-7-5